A Nuclear Magnetic Resonance and Quasielastic Neutron Scattering Study of Hydrogen Diffusion in Metal-Hydrogen Systems

Karl Jon Barnfather MSc

A thesis submitted to the University of Warwick
for admission to the degree of Doctor of Philosophy.

Department of Physics
December 1992

PALE BROKEN PRINT

For Louise Colette Hollings

Acknowledgements

I wish to express my sincere thanks to the many people who have assisted me in my studies at Warwick University and elsewhere whilst studying for and preparing this thesis.

Many thanks to my supervisor, Dr Graham Styles, whose assistance whilst I was a student and subsequently, during the preparation of this thesis has been invaluable. I wish to express my gratitude also to the late Professor Eddie Seymour who instructed and assisted me in my early days of postgraduate life and left an impression of an admirable scientist. I am also grateful to Dr Jose Dianoux of the ILL, Grenoble, for his help in performing experiments on both the IN6 and IN10 spectrometers. Thanks also to Dr David Fort of Birmingham University for his assistance with some of the single crystal metal samples.

I am also indebted to those who have assisted me with their technical expertise, including Barrie Sheffield, once of the nmr group, Roger Buckle, and Derek Naylor. There are also a great many more people in the nmr group and generally at Warwick whose assistance and friendship I most gratefully acknowledge. My days here were most rewarding, enjoyable and memorable.

Without doubt the person who deserves the most thanks is Louise Hollings. She has tolerated my procrastination, has assisted in the preparation of this thesis and has provided immeasurable support.

Declaration

This thesis is submitted to the University of Warwick as substantial fulfillment of the requirements of my application for the degree of Doctor of Philosophy. The work presented has not been submitted in any thesis to any other institution and is the result of my own study, under the supervision of Dr G A Styles, at the Physics Department, Warwick University, unless specifically acknowledged.

I am pleased further to declare that part of the work presented is published as follows:

Styles G.A., Seymour E.F.W., Barnfather K.J., Schone H. and Sholl C.A., Journal of the Less-Common Metals, **129**345-353(1987).

Barnfather K.J., Seymour E.F.W., Styles G.A., Diancux A.J., Barnes R.G. and Torgeson D.R., Zeitschrift fur Physikalische Chemie Neue Folge, Bd. **164**S.935-940(1989).

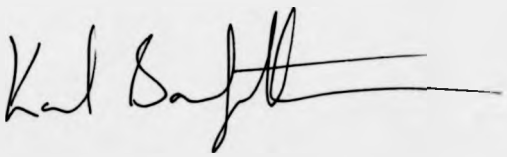

Kari Jon Barnfather

Abstract

The result of work investigating hydrogen diffusion in a variety of Metal-Hydrogen systems using both the nmr and qns techniques is presented.

Chapter 1 provides a description of the uses and general character of MeH systems and is intended as a pragmatic introduction. In addition, diffusion theory is discussed and again general theory relevant to later work is presented regarding the properties of hydrogen diffusion within metal lattices. Chapter 2 gives an exposition on both the fundamental theory of the techniques used and detailed theoretical results which describe the effect of hydrogen diffusion on various observable parameters; primarily the nuclear spin-lattice relaxation time T_1 and the neutron scattering function $S(Q,\omega)$. Chapter 3 describes the experimental apparatus and procedures used for both the nmr and neutron scattering studies as well as for sample preparation.

Chapter 4 sets out the results of an nmr study of single crystal samples of β-NbH_x, β-VH_x and α-YH_x. Individual theoretical treatments of the expected anisotropy of the hydrogen Knight shift and spin-lattice relaxation rate due to the dipole-dipole interaction are presented for each of the systems. The T_1 results obtained for a single domain sample of β-$NbH_{0.75}$ are in excellent agreement with theory, however it is not possible to determine the exact nature of the diffusion mechanism except to predict that it is likely to be an isotropic mechanism rather than a one dimensional mechanism such as intra-chain. A T_1 anisotropy is also observed in two single crystal samples of β-VH_x. In the case of a single domain sample the orientational dependence of the results is in good agreement with theory and the anisotropy of $T_{1\,[001]//B_o}$ / $T_{1\,[001]\perp B_o}$=17% is in excellent agreement with the maximum predicted 16%. The results tend to confirm the theoretical methods used and the diffusion mechanism suggested by earlier qns studies. For a single crystal of α-$YH_{0.17}$, again excellent agreement with theory is observed in the form of the T_1 angular dependence. An anisotropy of $T_{1\,[001]//B_o}$ / $T_{1\,min}$=85% is observed which greater than predicted by three theoretical diffusion mechanisms. The magnitude of and errors in the results do not enable any determination of the true diffusion mechanism in the α-YH system.

Chapter 5 presents a study of the high temperature T_1 anomaly which is an unexpected reduction in the relaxation time at temperatures where the Korringa (or conduction electron) mechanism is expected to dominate. Richards' model of large anharmonic vibration of hydrogen at neighbouring interstitial sites which was suggested as an explanation of the anomaly is described. The results of a qns study of $Nb_{0.75}V_{0.25}H_{0.20}$ and $YH_{1.97}$ powdered samples, which display the T_1 phenomenon, are then presented. The study measures hydrogen diffusion coefficients for both samples in the temperature regime of the anomaly, which finds that hydrogen diffusion in both samples exhibit the usual Arrhenius temperature dependence. For the α-phase alloy system E_a =0.16 ± 0.02 eV and D_o =1.76 (±0.4) x 10^{-4} cms^{-1}, and for the sub-stoichiometric dihydride sample E_a =0.33 ± 0.09 eV and D_o =0.70 (±0.4) x 10^{-4} cms^{-1}. The conclusion is that Richards' model does not hold and other possible models are discussed including sub-lattice melting and hydrogen pairing.

Chapter One
Hydrogen in Metals

1.1 Introduction

The number of applications of metal hydrides and the diversity of research into their properties have become very considerable. Initially discovered in the 19th century as a phenomenon whereby metals absorbed hydrogen gas which enabled hydrogen purification, the field has grown to be of major international interest [1.1]. At present metal-hydrides find application, inter alia, in materials technology, for example in pure metal powder formation, and in purification of hydrogen itself to be used as a carrier gas in chemical vapour deposition manufacture of semiconductors. Hydrogen as fuel is also an important application for which MeH_x systems can be used simply for hydrogen storage. Technologically, metal-hydrides could play a major role in the future as means of energy storage and in nuclear fusion reactors. Other potential applications which are receiving current investigation, as recently reported [1.2, 1.21], include refrigeration, heat pumps, solid-state and liquid electrolyte batteries, compressors and air-conditioners. All of these, of course, would be 'greener' than their current equivalents, so that we find that the so-called hydrogen economy is receiving popular attention because of its environmental attractiveness.

It is apparent, however, that whilst an inexhaustible supply of H_2 exists this source is not in itself a source of energy, the H_2O dissociation energy merely being returned on combustion of H_2, and it is as a means of transferable energy storage that MeH systems will be used. One such use is to power motor vehicles, a test fleet of which have been running in Germany since 1976. The results of a study of a further test fleet which began in 1984 have been reported [1.3] and are very promising. However, it is fundamental research on these systems which makes development possible. Of great importance in this case, in order to achieve comparable performance to petrol vehicles, are firstly the absorption/desorption characteristics of the material and secondly the bulk diffusion of the hydrogen in the metal lattice. The work presented here is a study of the latter property of metal hydrogen systems, that is the fundamental physical properties of the hydrogen as it moves around the host metal lattice.

Much fundamental research has been carried out on these systems, however, due to the diversity of systems into which H can be implanted (for example, high T_c superconductors and pure transition metals) by various means, and due to the diversity of phenomenon observed (for example electronic, magnetic and structural phase transitions), it is not practical to provide an exhaustive review of hydrogen in metals per se. Instead, a description of some general properties of relevance to the later work is given and the reader is referred to several review texts and conference proceedings for a wider treatment [1.1 to 1.7, 1.21].

1.2 Formation and Structure

Metal-hydrides can be formed in a variety of ways, such as ion implantation, electrochemical doping and gaseous deposition. The latter technique is used to prepare our samples and is described here. Note that the term metal hydride whilst not always strictly correct is used generically in this text for all hydrogen concentrations.

One of the reasons Me-H systems make good storage media is that the basic gaseous absorption is a reversible chemical reaction and desorption can give off H_2 at almost constant pressure, unlike gaseous release from a pressurised cylinder. Figure 1.1 shows a schematic representation of a typical PCT curve (pressure, composition and temperature) for an Me-H system which absorbs hydrogen exothermically. The plateaus between A and B show the constant pressure desorption region which exists for compositions of mixed phase. At low concentrations hydrogen is absorbed into a solid-solution or α-phase where approximately linear distortion of the metal lattice occurs and there is no, or only slight, hydrogen ordering at room temperature (but see section 4.3 on α-YH_x). At these low H to Me ratios (x) the pressure composition dependence is approximately described by Sieverts' law

$$P=K_s x^2 \qquad \{1.1\}.$$

That is, the composition is proportional to the square root of the equilibrium hydrogen pressure. At point A in figure 1.1 the solid-solution phase is saturated and regions of ordered hydride phase begin to form. Between A and B a mixture of α and β phase exists, here Gibbs phase rule, C-P+2=F, predicts that the pressure remains constant as there is only one degree of freedom, F. C is the number of components (H and Me)

and P the number of phases (H_2, α and β). At B the composition is an entirely ordered hydride phase and to increase the H concentration above B requires an increase in hydrogen pressure. The ordered phase can occur at various compositions. For example, for Y it is a dihydride phase YH_2 where the single phase exists approximately for $1.8 \leq x \leq 2.1$ at 300K, whilst for Nb it is the monohydride NbH_1 where the single phase region exists for $0.72 \leq x \leq 1.05$ at 300K. In fact this representation is very much a simplification of real systems as many different phases can occur (see for example chapter 4).

A schematic representation of the absorption potentials from gas phase to bulk is shown in figure 1.2, where the enthalpy of dissolution is ∂H_{∞}; for $\partial H_{\infty} < 0$ the reaction is exothermic. For the dilute phases of the systems studied here ∂H_{∞} = -0.88, -0.33 and -0.27 eV/atom for Y, Nb and V respectively. The relatively large value for Y means that hydrogen is readily absorbed at low H_2 pressure which causes a problem in accurately calculating the concentration of a single crystal α-phase, as discussed in section 4.3. However, another factor in the reaction kinetics is the adsorption energy, E_{ad}, which for certain metals can be large and cause the reaction to go relatively slowly. Surface impurities (such as oxygen or nitrogen) can also hinder adsorption. Both these problems can be overcome by either etching samples to remove impurities at the surface and/or coating with a metal such as Pd which has a low E_{ad}.

A simplistic view of the atomic structure of these systems can be achieved if we regard the metal lattice as comprising space-filling hard-sphere atoms of equal radius R. Then, for the fcc structure, for example, the atoms fill 74% of space whilst interstitial sites take up the remaining 26%. In this case two types of interstitial are identified, see figure 1.3, as the tetrahedral or T-site and the octahedral or O-site. The former is coordinated by 4 metal atoms and has a radius of 0.225R whilst the latter is coordinated by six metal atoms and has a radius of 0.414R. In the fcc structure there are two T-sites and one O-site per metal atom. Similarly, these figures are presented for the bcc and hcp structures in table 1.1. This model can be used to get a basic idea of the behaviour of hydrogen in a lattice. Drawing a very naive analogy of hydrogen diffusion to that of a small ball-bearing in a stack of billiard balls gives an idea of paths within a lattice, although in reality this requires a detailed potential structure analysis. From table 1.1 it is possible to see that the close-packed structures have fewer but larger interstitial sites than the bcc structure.

This suggests that they may be more stable at large H concentrations, which is the case as MeH_3 systems can be formed in, for example, YH_3 (hcp) and LaH_3 (fcc) [1.4]. The bcc structure has smaller interstices but in greater number and it is found that these systems cannot absorb much hydrogen before a distortion of the lattice occurs, generally distortion is to bct (tetragonal) or bco (orthorhombic). Distances between various sites are given in table 1.2 in terms of the metal lattice unit cell constant a. In the case of the bcc metal it is found that the T-sites form six and the O-sites three distinct inter-penetrating bcc lattices (a_H=a). For an fcc metal lattice the T-sites form a single, simple cubic structure (a_H=a/2) and the O-site form an fcc lattice (a_H=a) [1.5]. In the case of the systems studied greater atomic structure detail is given in the relevant section.

Table 1.1 Some structural information using the hard-sphere model.

Structure	% space	No. of T-sites to Me atoms	No. of O-sites to Me atoms	T-site radius	O-site radius
fcc	26	2	1	0.225R	0.414R
bcc	32	6	3	0.291R	0.115R
hcp	26	2	1	0.225R	0.414R

Table 1.2 Interstices structures and nearest neighbour site distances, with number of sites at that distance in brackets, for a bcc and fcc metal lattice of lattice constant a.

Metal lattice	T-site lattice	O-site lattice	T-T distance	T-Me dist.	O-O dist.	O-Me dist.
bcc	6bcc	3bcc	$\sqrt{2}$ a/4 (4)	$\sqrt{5}$ a/4 (4)	a/2 (4)	a/2 (2), $\sqrt{2}$ a/2 (4)
fcc	sc (a/2)	fcc	a/2 (6)	$\sqrt{3}$ a/4 (4)	a/$\sqrt{2}$ (12)	a/2 (6)

In introducing the general characteristics of MeH systems we briefly consider their electronic structure. Whilst ionic and covalent hydrides form from compounds of elements from the left and right hand side of the periodic table respectively, the model is not so simple for the transition metal-hydrides. This subject is still attracting much theoretical study in order to interpret experimental observations [1.8] and is of course

important in order to understand many of the physical phenomenon observed. The structure can generally be described as one where the hydrogen interacts with the metal atom and causes a lowering of the metal s-states near the hydrogen due to the attractive potential of the proton whilst the hydrogen electron is drawn into empty states near the Fermi level of the metal; these are typically d-states. This effectively leaves the hydrogen as a proton with a build up of charge cloud around it and for this reason it is often referred to simply as a proton.

1.3 Diffusion

Many natural phenomena are due to the diffusion of particles which can occur because of an imbalance within a system, for example in concentration, temperature or electrical potential. In these cases the movement of the average indistinguishable particle is described by Fick's laws [1.9] from which one can obtain the chemical diffusion coefficient D_c. However, we are primarily interested here in diffusion of a single distinguishable particles in dynamic equilibrium. In this case the atomic motion is described by the tracer diffusion coefficient D_t which, after Einstein [1.10], is defined as

$$D_t=\frac{\langle r^2(t)\rangle}{6t} \qquad (1.2)$$

where the numerator is the mean squared distance moved by a particle in three dimensional space in time t. This result was obtained for particles able to move freely in space. Similarly, Markov [1.11] considered a random walk model where particles moved in a given direction before a collision and afterwards in a direction completely independent of it, thus $\langle r_n^2\rangle=n\langle r_1^2\rangle$, where n is a number of collisions. Neither of these treatments exactly matches the classical model for diffusion of hydrogen in metals.

The hydrogens occupy discrete sites separated by fixed distances l and diffusion takes place by individual atoms jumping over a potential barrier to a neighbouring site. Now equation 1.2 can be written as

$$D_t=\frac{l^2}{6\tau} \qquad (1.3)$$

where $l=\langle r_1^2 \rangle$ and τ is the average time for each jump (t/n). If we assume that particle flight between sites is instantaneous then τ is the dwell time at each site τ_d which we can define as

$$\tau_d = A\exp(E_a/kT) \qquad \{1.4\}$$

where A is a constant which depends, for example, on τ_o (which is the mean jump attempt time) and a probability factor for a site being vacant, and E_a is the activation energy. Similarly, we have the Arrhenius expression for the diffusion coefficient given this classical, thermally activated process where

$$D = D_o\exp(-E_a/kT) \qquad \{1.5\}.$$

We now need to develop the model of Markovian random walk, which is only valid in our systems for very low hydrogen concentrations, to one where interactions between particles are accounted for. On a basic level two particles must not be allowed to occupy the same site nor diffuse through one another. Other factors are that once a jump has occurred a vacancy definitely exists at the initial site and in the short term this must mean that a reverse jump has a higher jump probability than the average jump. Also, interactions beyond nearest-neighbour blocking to next-nearest-neighbour sites and beyond need to be considered allowing for both H-H and H-Me interactions. These factors can be incorporated into {1.3} by means of the tracer correlation factor f_t, as introduced by Bardeen and Herring [1.12 and 13], such that

$$D = \frac{f_t\, l^2}{6\tau} \qquad \{1.6\}.$$

It should be noted that there are basically two different ways of determining particle diffusion coefficients; one by direct measurement such as by permeation, Gorsky effect (both of which measure D_c), pulsed-field-gradient nmr or qns ($Q<1/l$), the other is to measure τ, for example by relaxation time nmr studies or qns studies ($Q\sim1/l$). Thus f_t is not always important unless one is trying to make accurate comparison of values of D or τ between different techniques or an accurate value of l needs to be determined. Hence f_t is often taken as unity when presenting data. See chapter 2 for a description of both nmr and qns and for reviews of all these techniques see [1.7].

By way of example of characteristics of hydrogen in metals it is worth noting the large range of hydrogen diffusivity, $10^{-12} \leqslant D \leqslant 10^{-5}$ cm^2s^{-1}, at room temperature such that $10^{-4} \leqslant \tau \leqslant 10^{-11}$ s and typically, E_a might be in the order of 0.1eV. This is compared to host metal atom self-diffusion coefficients of $D < 10^{-20}$ cm^2s^{-1} and $E_a \sim 2eV$. Similarly, no other interstitial atom, for example O or N, diffuses as rapidly as hydrogen.

Given site blocking and the enhanced reverse jump effect at finite concentrations it can be seen that f_t is time dependent and less than or equal to one. Many calculations of f_t have been carried out, initially these were only for the monovacancy limit where the result can be obtained exactly, that is as $c \rightarrow 1$ where f_t is found to equal 0.65211, 0.72722 and 0.78146 for sc, bcc and fcc diffusional lattices respectively [1.14]. However, these values are also only valid in the regime where τ is measured over many jumps. Later, general expressions evolved for a range of concentrations calculated using a variety of methods, for example Fedders and Sankey [1.15] used a multiple scattering method whilst Tahir-Kheli and Elliot [1.16] used Green's functions expansions. These calculations show that as the concentration increases from 0, where $f_t=1$, so f_t decreases, approaching its monovacancy value. This area has been well reviewed by Faux [1.17] who goes on to use Monte Carlo calculations to predict the time-dependence of f_t. It is shown that in the limit of infinitesimally short measurement time, ie no jumps, $f_t=1$ at any concentration and thereafter asymptotically approaches its finite concentration dependent value. Data presented by Faux shows that typically after 8 attempted jumps the value of f_t is approximately within 8% of its asymptotic value.

The effects of different diffusion models on observable nmr and qns parameters is further discussed in chapter 2 along with further models. We have so far only considered one mechanism for inter-site diffusion, that of over-barrier hopping. It is generally considered that in fact four diffusion mechanism regimes exist at different temperatures [1.18 and 19]. These are shown in figures 1.4 & 1.5 and are; coherent tunneling, incoherent tunneling, over-barrier hopping, and fluid-like diffusion.

Adopting the small-polaron model for hydrogen within the metal lattice, the hydrogen state is obtained as a solution to Schrodinger's equation where the hydrogen is surrounded by interactions from metal atoms. A

minimum energy configuration is achieved by relaxation of the metal lattice and the creation of a self-trapped hydrogen state at an interstitial.

At very low temperatures, of the order of 1 Kelvin, the interstitial thermal energy is very much less than the over-barrier activation energy, $kT \ll E_a$, and diffusion may only occur through coherent tunneling. The diffusivity in this regime may be expressed as

$$D=\langle v^2/\tau \rangle \qquad \{1.7\}$$

where v is the particle velocity and τ the lifetime of the coherent state. Naturally, the coherency length must be greater than the inter-site distance l. As T tends to 0K the diffusivity would increase as the number of phonons decreased; the other lifetime factors are perturbations such as impurities and dislocations. This regime has not been observed experimentally despite studies of μ^+ in both Al and Cu, and Fukai suggests that a coherent over-barrier mode may exist instead [1.19].

At higher temperatures the diffusion mechanism is one of incoherent transitions, that is where the coherence of the metal lattice phonons is lost, regime B of figure 1.5. This process can be separated into two further regimes, nonadiabatic and adiabatic for lower and higher temperatures respectively. In a single phonon event the potential of a neighbouring site is raised until the proton state in the self-trapped site is matched by the vacant neighbour. At this point a tunneling event may occur as shown in figure 1.5. The transition can be described with regard to a tunneling transition matrix element J which in a simple form can be written as

$$J=\frac{h^2}{\pi ml}\left[\frac{8\pi ml^2V_o}{h^2}\right]^{3/4}\exp\left\{\frac{-2}{\pi}\left(\frac{8\pi^2ml^2V_o}{h^2}\right)^{1/2}\right\} \qquad \{1.8\}$$

where Kehr assumes a simple 1D periodic potential such that $V_o \gg h\nu_l$ where ν_l is the vibrational frequency of the proton, $\nu_l=(V_o/2ml^2)^{1/2}$, and m is the particle mass [1.19]. Now in the regime that $J < h\nu_D$ the transition is via excited states since the hydrogen cannot follow the metal lattice motion, and hence nonadiabatic. The minimum period of motion of the metal atoms is $\sim 1/\nu_D$ (ν_D is the Debye frequency) which is shorter than the time for the hydrogen to adjust to displacements h/J. Here the thermally activated jump frequency is written as

$$\nu \sim (J^2/T^{1/2})\exp(-\partial E/kT) \qquad \{1.9\}$$

where ∂E is the energy difference between the ground state of the H in the interstitial and the energy state at the saddle-point in the presence of the phonon. The second incoherent transition regime occurs where $J > h\nu_D$ and the transitions occur adiabatically. The jump frequency can be written

$$\nu \propto \nu_0 \exp(-\partial E/kT) \qquad (1.10)$$

where $\nu_0 \sim \nu_D$ and is independent of particle mass.

At higher temperatures where $kT > h\nu_D$ and $h\nu_1$, classical over-barrier jumps occur as previously described. However, here the ν_0 factor of (1.10) is ν_1 and it is thus proportional to $1/\sqrt{m}$. Generally the energy requirements for the classical model are not met by MeH systems near room temperature and therefore the diffusion mechanism is one of incoherent tunneling. The actual mechanism can be determined from experimental observations, for example of the isotope dependence of the prefactor in equations 1.9 and 1.10. Because of the structure of interstices in bcc systems, as discussed in section 1.2, it might be that the lower activation energy and shorter inter-site distances give rise to greater diffusivity in bcc systems compared with fcc. This is apparently the case given the results of a study of $Pd_xCu_yH_z$ in the bcc phase and a quenched fcc phase [1.20]. Further to this, it also appears that the predominant mechanism in bcc systems is adiabatic incoherent tunneling whist for fcc systems it is nonadiabatic [1.18]. However, this is dependent on the exact temperature and composition of the system.

At the highest temperatures the hydrogen is believed to diffuse through a fluid-like mechanism, as shown schematically in figure 1.5 mechanism D. In this regime the hydrogen are no longer localised but undergo long range diffusion wherein τ_d is less than the time of flight over many sites.

In the temperature regimes used in the nmr study in chapter 4 it is apparent that either adiabatic incoherent transitions or classical over-barrier hopping occur and in both cases the diffusion can be described by the Arrhenius expression where only the prefactor is different. The work presented later is a study of two different aspects of hydrogen diffusion; firstly the variation of nmr parameters in single crystal samples with crystal orientation and temperature with the aim of resolving diffusion paths through the lattice, and secondly a study of hydrogen diffusion at

high temperatures in order to interpret some anomalous nmr results in a variety of powdered systems.

References

1.1 Gibb Jr T R P, 'Primary Solid Hydrides', Progress in Inorganic Chemistry, **3**,315-509,(1962).

1.2 Metal-Hydrogen Systems fundamentals and applications, Stuttgart Conference Proceedings, Zeitsschrift fur Physikalische Chemie Neue Folge, Bd. 163 & 164 (1989).

1.3 Topler J & Feucht K, Zeitsschrift fur Physiskalische Chemie Neue Folge, Bd. 164, 1451-1461 (1989).

1.4 Libowitz G G & Maeland A J, 'Hydrides', Chapter 26, Handbook on the Physics and Chemistry of Rare Earths, Eds Gschneider Jr K A & Eyring L, North Holland Publishing Company, 1979.

1.5 Fast J D, 'Interactions of metals and gases', Vol. 2, MacMillan, 1971.

1.6 Metal-Hydrogen Systems, Banff Conference Proceedings 1990, to be published.

1.7 Alefeld G and Volkl J, 'Hydrogen in Metals', Vols. 1 & 2, Topics in Applied Physics, Vols. 28 & 29, Springer-Verlag, 1978.

1.8 Gupta M, Zeitsschrift fur Physiskalische Chemie Neue Folge, Bd. 163,517-520,(1989).

1.9 Kittel C, 'Introduction to Solid State Physics', Wiley, 1976.

1.10 Einstein A, Ann Physik, **17**, 549, (1905).

1.11 Markov A A, Wahrschienlichkeitsrchung Leipzig, 1912.

1.12 Bardeen J, Imperfections in Nearly Perfect Crystals, Wiley, 1949.

1.13 Bardeen J and Herring C, Imperfections in Nearly Perfect Crystals, Wiley, 1952.

1.14 LeClaire A D, Physical Chemistry, An Advanced Tretise, Editors Eyring H, Henderson D and Jost W, p261, chapter 10, (1970).

1.15 Fedders P. A. and Sankey O. F., **19**, 5938-47, Phys. Rev. B, (1978).

1.16 Tahir-Kheli R. A. and Elliott R. J., **27**, 844-57, Phys. Rev. B, (1983).

1.17 Faux D, PhD Birmingham University, (1987).

1.18 Fukai Y & Sugimoto H, Advances in Physics, **34** no.2, 263-326 (1985).

1.19 Kehr K W, p198-226, Vol. 1 of [1.7].

1.20 Volkl J, Bauer H C., Freudenberg U, Kokkinidis K, Lang G, Steinhauser K A and Alefeld G, 'Internal Friction and Ultrasonic

Attenuation in Solids', Editors Hasiguti R R and Mikoshiba N, University of Tokyo Press, 485 (1977).

1.21 International Symposium on Metal-Hydrogen Systems, Banff 1990 conference proceedings, J Less-Comm Metals, **172-174** (1991).

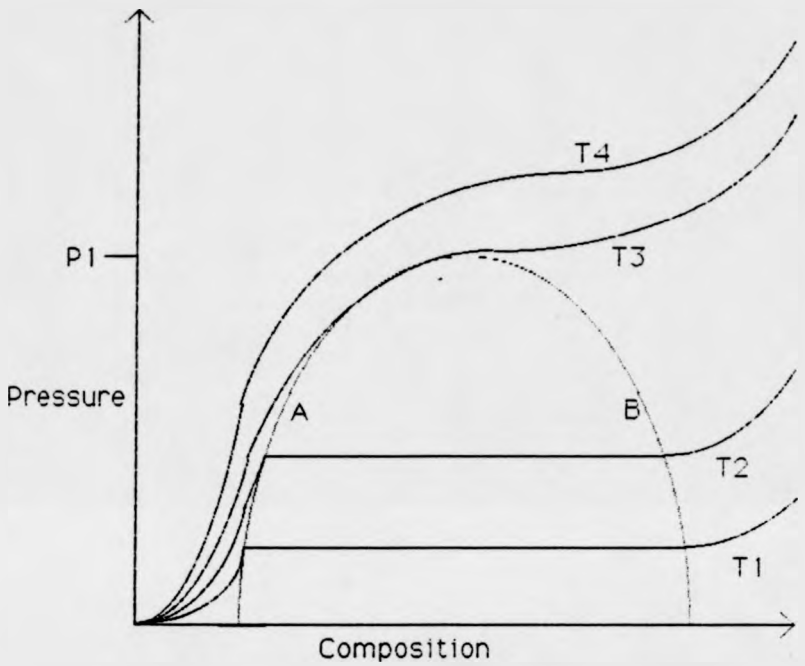

Figure 1.1 Schematic representation of pressure versus composition isotherms in a 'typical' metal-hydrogen system, where T4>T3>T2>T1. The mixed phase region is enclosed by the dotted line and P1 and T3 are therefore critical temperature and pressure values which need to be maintained in order to form a single crystal ordered-phase hydride (see chapter 4).

Figure 1.2 The absorption process represented schematically in terms of the potential energies from gas to surface to bulk. Ediss is the dissociation energy of the H2 molecule. Ead the adsorption potential. Esb the surface to bulk energy barrier, Ea the classical diffusion activation energy and ∂H∞ the enthalpy of dissolution.

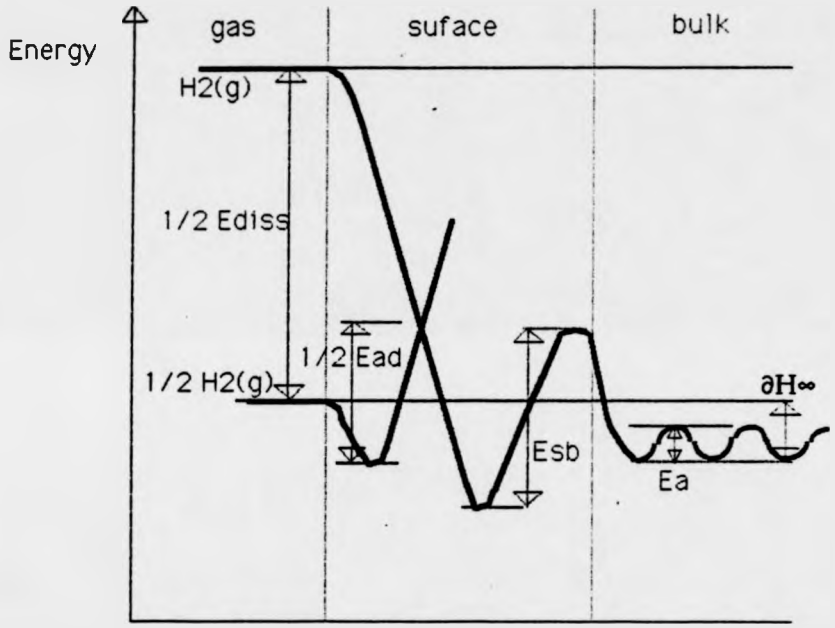

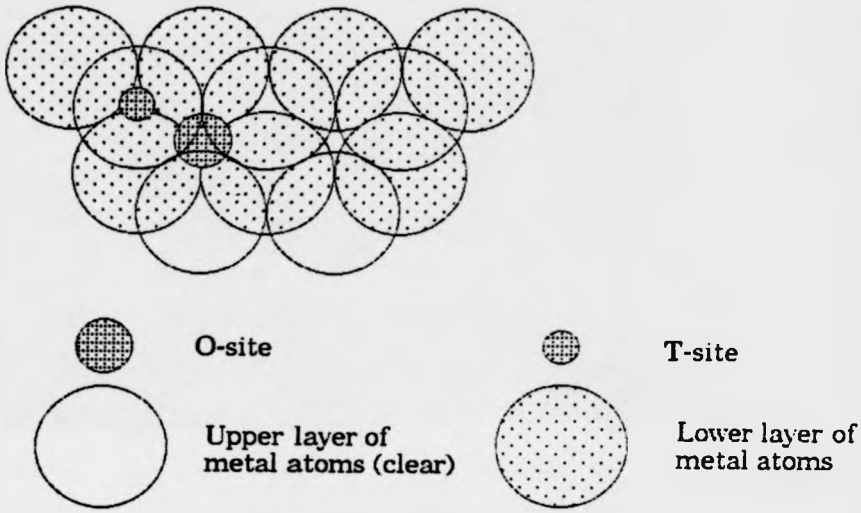

Figure 1.3 A simplistic view of an fcc metal lattice showing the interstial O and T-sites.

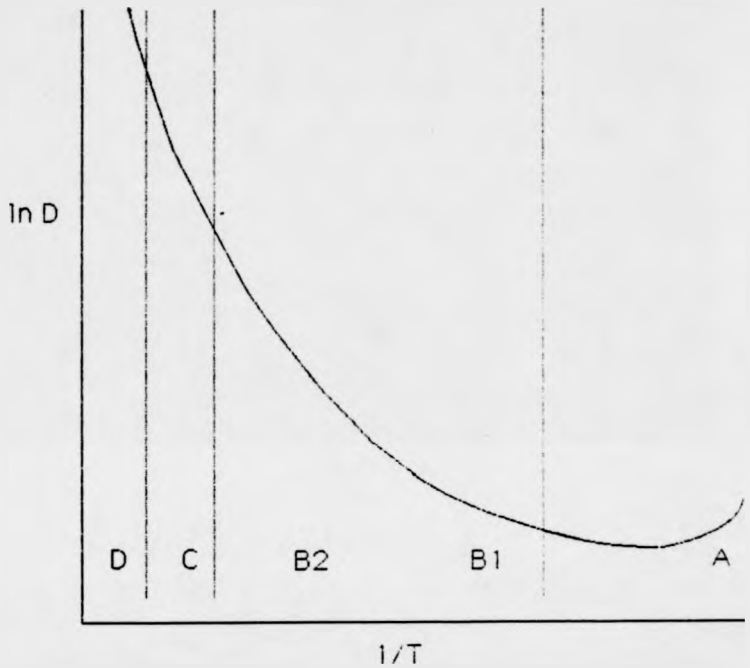

Figure 1.4 Schematic representation of the possible behaviour of hydrogen diffusivity with temperature, four regimes descibed in the text are predicted to exist and may or may not occur for a given system. The regimes D, C, B2, B1, and A correspond to the diffusion mechanisms shown in figure1.5.

Figure 1.5 Schematic diagrams of the diffusion mechanisms which occur with increasing temperature A to D.

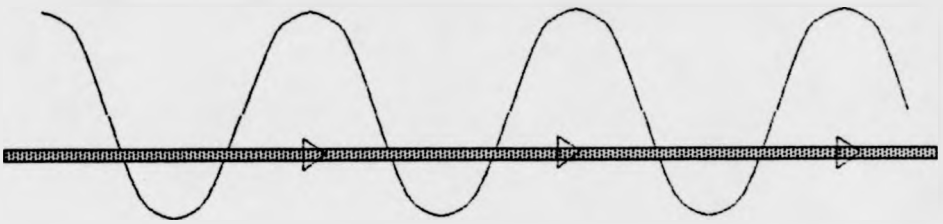

Diffusion mechanism A; coherent tunneling at very low temperatures.

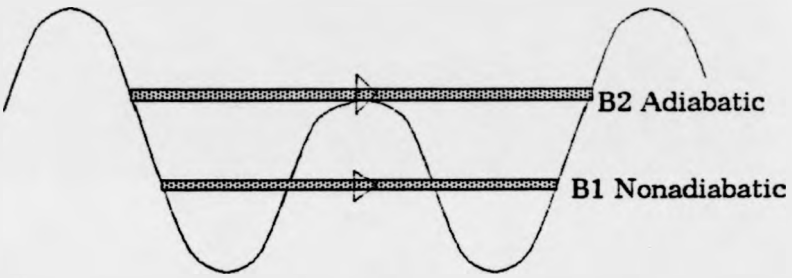

Diffusion mechanism B; adiabatic and nonadiabatic incoherent transitions.

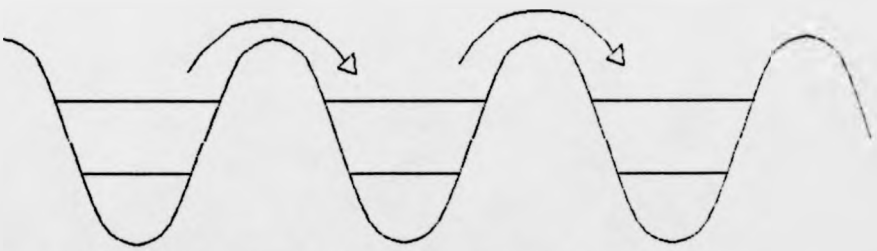

Mechanism C; thermally activated over-barrier jumps.

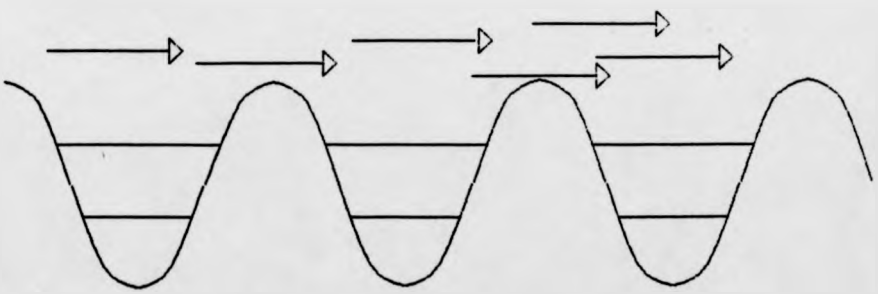

Mechanism D; fluid-like diffusion.

Chapter Two
A Theoretical Basis

2.1 Nuclear Magnetic Resonance

This chapter gives the theoretical basis for both the nmr and qns techniques. The emphasis is on the nmr theory which is developed from the basic interactions of the nuclear spin with its environment to the treatment of nuclear spin relaxation, particularly that caused by translational diffusion. A treatment of the effects of the conduction electron interaction with the nuclear spin is also given. The theoretical developments in the derivation of the nuclear spin relaxation rates due to translational diffusion for a variety of diffusion models with applicability to a range of metal-hydrogen systems are discussed. Similar developments in the treatment of qns results have occurred and while a less rigorous review is given, its applicability to metal-hydrides is emphasized.

2.1.1 Basic Principles of NMR

The nuclear spin Hamiltonian can be expanded into many terms and those relevant to the understanding and interpretation of results presented later in this thesis are described individually here. For a more comprehensive treatment of nmr the works of Abragam [2.1] and Slichter [2.2] are recommended.

The Hamiltonian may be written as

$$H=H_z+H_{rf}+H_d+H_{hf}+H_q+H_p+... \qquad (2.1)$$

where the terms on the right are the Zeeman, rf, dipole, hyperfine, quadrupole and paramagnetic terms respectively. The principal term is the Zeeman interaction H_z, that of the spins with the externally applied magnetic field. The other terms, generally being weaker in an nmr experiment, can be treated as perturbations. They give rise to the phenomena of excitation and relaxation as well as causing shifts in the Zeeman energy levels.

The large externally applied magnetic field B_o causes a splitting of the otherwise degenerate spin energy levels. The coupling of the nuclear spin magnetic moment μ with B_o creates $2I+1$ energy states, where I is an

eigenvalue of the angular momentum operator **I** and $\mu=\gamma\hbar\mathbf{I}$, where γ is the gyromagnetic ratio. The Zeeman Hamiltonian can be written as

$$H_z=-\mu.B_o=-\gamma\hbar B_o I_z=-\gamma\hbar B_o m \qquad \{2.2\}$$

since B_o is taken to define the z axis and m=I,I-1.....-I. The interaction eigenvalues have an energy difference of $h\nu=\gamma\hbar B_o$ or $\omega_o=\gamma B_o$ where ω_o is the angular Larmor precession frequency. The energy levels thus created are populated according to Boltzmann statistics which generates a net equilibrium magnetization of the macroscopic spin system $M_o=\mu_p\chi B_o$, where μ_p and χ are the absolute permeability and the magnetic susceptibility of the system respectively.

In an nmr experiment transitions between the discrete quantum levels are induced using a linearly oscillating radio frequency, rf. field $2B_1\cos\omega_1 t$ generated by a coil surrounding the sample with its cylinder axis perpendicular to B_o. This field can be regarded in terms of two counter rotating components of magnitude B_1 where only the component rotating in the same sense as the nuclear precession is significant. The rf term of the Hamiltonian can be written as

$$H_{rf}=-\gamma\hbar B_1\{I^+\exp(-i\omega t)+I^-\exp(i\omega t)\} \qquad \{2.3\}$$

where I^+ and I^- are raising and lowering operators which can be expressed in terms of the x and y components of the nuclear spin such that $I^+=(I_x+iI_y)$ and $I^-=(I_x-iI_y)$. The rf field has an angular frequency ω such that if we transform to a frame of reference also rotating about the z axis with the same angular frequency we obtain an effective magnetic field $B_{eff}=B_o-\omega/\gamma+B_1$. Applying an rf field $\omega=\omega_o$, ie at resonance, gives $B_{eff}=B_1$ and the magnetisation precesses about the latter. The magnetisation may be rotated through a specific angle Θ from the z axis by applying B_1 for a time t where $\Theta=\gamma B_1 t$. Using this vector model it can be seen that the maximum signal occurs when $\Theta=\frac{\pi}{2}$ given t is sufficiently short that no relaxation occurs and since the detection coil is placed perpendicular to B_o, see figure 2.1a.

In a somewhat similar manner relaxation can be brought about by interactions with the nuclear spins where these processes have a frequency component at ω_o (see section 2.1.2a). It is convenient to describe relaxation of the magnetisation using the vector model. The relaxation times T_1 and T_2 govern respectively the growth of the z magnetisation

vector back to equilibrium (hence longitudinal or spin-lattice relaxation time) and the decay of the magnetisation in the x-y plane (hence transverse or spin-spin relaxation time). Details of how a T_1 measurement is made are shown in figures 2.1b & c using the vector model described. The measurement is achieved using a 180°-τ-90° pulse sequence since successive values of τ from 0 to about $5T_1$ give a virtually complete magnetisation recovery curve. The z magnetisation for a pulse interval τ of such an inversion-recovery pulse sequence is described by the expression

$$M_z=M_o(1-2\exp(-\tau/T_1)) \qquad \{2.4\}$$

assuming equilibrium is restored between the successive 90° and 180° pulses.

So far we have discussed only external interactions. The importance of nmr however stems from the information which can be gleaned about the nuclear environment and its dynamical properties which are manifest as perturbations of the Zeeman interaction as a result of interactions of the nuclei with their surroundings. Firstly we shall consider the nuclear dipole-dipole interaction H_d which contributes to both T_1 and T_2 processes and is given by

$$H_d=(\gamma_i\gamma_j\hbar^2/r_{ij}^3)\{\mathbf{I}_i.\mathbf{I}_j-3(\mathbf{I}_i.\mathbf{r}_{ij})(\mathbf{I}_j.\mathbf{r}_{ij})/(r_{ij}^2)\} \qquad \{2.5\}$$

where i and j are two spins separated by $\mathbf{r}_{ij}$. Equation 2.5 can be rewritten in terms of nuclear spin operators such that

$$H_d=\Sigma_q A_{ij}^q F_{ij}^q \qquad \{2.6\}$$

for $-2\leq q\leq 2$ and where the second rank nuclear spin operators A_{ij} can be written as

$$A_{ij}^{\circ}=(\gamma_i\gamma_j\hbar^2/2)(3I_{iz}I_{jz}-\mathbf{I}_i.\mathbf{I}_j) \qquad \{2.7a\}$$

$$A_{ij}^{\pm1}=(3\gamma_i\gamma_j\hbar^2/2)(I_{iz}I_j^{\pm}+I_i^{\pm}I_{jz}) \qquad \{2.7b\}$$

$$A_{ij}^{\pm2}=(3\gamma_i\gamma_j\hbar^2/4)I_i^{\pm}I_j^{\pm} \qquad \{2.7c\}$$

with $A^q_{ij}=A^q_{ji}=A^{-q*}_{ij}$, while the geometrical lattice functions F^q_{ij} are second rank tensor operators which describe the spatial dependence of the dipole-dipole interaction and can be written

$$F^0_{ij}=d_0(Y_{20}(\Theta,\phi)/r^3_{ij})=(1-3\cos^2\Theta)/r^3_{ij} \quad (2.8a)$$

$$F^{\pm1}_{ij}=d_1(Y_{21}(\Theta,\phi)/r^3_{ij})=\sin\Theta\cos\Theta\exp(\pm i\phi)/r^3_{ij} \quad (2.8b)$$

$$F^{\pm2}_{ij}=d_2(Y_{22}(\Theta,\phi)/r^3_{ij})=\sin^2\Theta\exp[\pm 2i\phi]/r^3_{ij} \quad (2.8c)$$

where $d_0^2=16\pi/5$, $d_1^2=8\pi/15$, $d_2^2=32\pi/15$ and $Y_{2q}(\Theta,\phi)$ are normalised second order spherical harmonics in which Θ and ϕ are the polar angles which define the direction of $\mathbf{r}_{ij}$.

These expressions give valuable insight into the interaction and its effect on relaxation. For example term a of (2.7), where q=0, contributes to T_2 processes since the Zeeman energy of the system is conserved for like spins i and j. That is, the dipole Hamiltonian for q=0 commutes with the Zeeman Hamiltonian and is therefore a secular term. This term represents the phenomenon of spin diffusion, for example, which sets a lower limit on T_2, the rigid lattice value T_{2rl}, and causes the finite width of resonance lineshapes at low temperatures. Terms b and c contribute to T_1 since the Zeeman energy is not conserved. These terms generate a frequency component for the interaction at ω_o and $2\omega_o$, for like spins i and j only and, as will be seen in the next section, the relaxation depends on the so-called spectral density function $J(\omega)$ at these specific frequencies.

The nucleus also experiences a magnetic interaction due to the conduction electrons known as the hyperfine interaction which can be written as

$$H_{hf}=\frac{16}{3}\pi\mu_B\gamma_n\hbar\mathbf{I}.\mathbf{S}(r)\partial(r)-2\mu_B\gamma_n\hbar\mathbf{I}[(\mathbf{S}/r^3)-3r(\mathbf{S}.r)/r^5]-\gamma_n\hbar e/mc(\mathbf{I}.\mathbf{l}/r^3) \quad (2.9)$$

where μ_B is the Bohr magneton, **S** the electron spin and **l** the orbital angular momentum [2.3]. The first term above is the Fermi contact interaction due to s-state conduction electrons which have a finite

probability density at the nucleus. Note that d-state conduction electrons in the metal can have an s-like nature at the hydrogen on interstitial sites [2.4]. An indirect contact interaction also exists, for transition and rare earth metals in particular where the d or f state conduction electrons induce polarisation of the inner closed shell s electrons. This is known as core polarisation and the hyperfine field produced is antiparallel to the unpaired d or f electrons mediating the polarisation. The time dependence of these interactions produces an effective nuclear spin relaxation mechanism where the exchange of energy produces a change in the itinerant electron wave number which is in good thermal contact with the lattice [2.5]. The time averaged effect of these interactions is to cause an isotropic shift in the nuclear resonance frequency, the Knight shift. The second term of {2.9} is the dipolar interaction which can generate an anisotropic Knight shift (except in cubic metals) and also provides a relaxation mechanism. The third term is due to the orbital motion of the conduction electrons induced by the applied magnetic field.

Additional effects of electronic origin arise from paramagnetic or diamagnetic fields from valence and core electrons which produce chemical shifts (σ) and relaxation. These contributions are assumed in what follows to be negligible and indeed it is found that the only three terms which are important for transition metal-hydrides are the s contact, the d core-polarisation and orbital terms.

A shift in the resonance frequency of a nuclear species in a metal (ν_m) relative to a reference diamagnetic salt (ν_{ref}) occurs due to a non-zero average component of the hyperfine field parallel to B_0. This was first observed by Knight [2.6] and the Knight shift is defined as

$$K=(\nu_m - \nu_{ref})/\nu_{ref} \qquad \{2.10\}$$

at constant field (note $\sigma=\nu_{ref} - \nu_{sample})/\nu_{ref}$ generally). The theoretical calculation of K is complex since contributions arise from the many-bodied electron system which is difficult to model, however, in its simplest form when determined only by s electrons the Knight shift can be expressed as

$$K=\frac{8}{3}\pi\chi_\rho\langle\psi_s(0)^2\rangle \qquad \{2.11\}$$

where χ_ρ is the Pauli paramagnetic spin susceptibility per atom and $\langle\psi_s(0)^2\rangle$ is the square of the s wave function at the nucleus averaged over the Fermi surface.

The complete first order anisotropic Knight shift may be defined using the nomenclature of Torgeson et al [2.7] as

$$K=K_{iso}+K_{ax}(3\cos^2\Theta-1)+K_{an}(1-\cos2\Theta)\cos^2\phi \qquad (2.12)$$

where $K_{iso}=(K_x+K_y+K_z)/3$, $K_{ax}=(2K_z-K_x-K_y)/6$ and $K_{an}=(K_y-K_x)/2$. the x, y, z form an orthogonal set of crystal axes and Θ and ϕ are the polar angles defining the orientation of the principal crystallographic symmetry axis z relative to B_0. In the case of cubic symmetry the diagonal elements of the Knight shift tensor K_x, K_y and K_z are such that the shift has no angular dependence, that is $K_z/2=K_x=K_y$, whilst for axial symmetry $K_x=K_y$ and hence only a Θ dependence exists.

The last two terms of equation 2.1 are respectively the electric quadrupole interaction and the interaction with paramagnetic impurities which it is important to be aware of in our systems. Only a brief description is given here.

Nuclei with a spin I>1/2 possess an electric quadrupole moment Q which interacts with the electric field gradients at the nucleus giving rise both to relaxation and shifts. The Hamiltonian H_q can be written in a similar form to that of the dipole interaction, viz.

$$H_q=\Sigma_m Q^m V^m \qquad (2.13)$$

where $-2\leq m\leq 2$ and the second rank tensor operators are now

$$Q^0=(-eQ/8I(2I-1))(3I_z^2-I^2), \qquad (2.14a)$$

$$Q^{\pm1}=(-3eQ/8I(2I-1))(I_zI^{\pm}+I^{\pm}I_z), \qquad (2.14b)$$

$$Q^{\pm2}=(-3eQ/16I(2I-1))(I^{\pm})^2 \qquad (2.14c)$$

and the electric field gradient components are

$$V^0=-2V_{zz}, \qquad (2.15a)$$

$$V^{\pm1}=2(V_{zx}\pm iV_{zy})/3, \qquad (2.15b)$$

$$V^{\pm2}=4(((V_{xx}-V_{yy})/2)\pm iV_{xy})/3 \qquad (2.15c).$$

The accepted definition for the field gradient tensor V_{ab} is to define an orthogonal principal axis system x', y', z' such that $|V_{z'z'}|\geq|V_{y'y'}|\geq$

$|V_{x'x'}|$ with $eq = V_{z'z'}$ and with an asymmetry parameter $\eta = (V_{x'x'} - V_{y'y'})/V_{z'z'}$ such that $0 < \eta < 1$. If the field gradient at the nuclear site has cylindrical symmetry then $\eta = 0$ while for materials having cubic symmetry the quadrupole interaction reduces to zero. Even in this case the temporal and spatial dependence of the nuclear environment due to nuclear or vacancy diffusion, for example, will give rise to fluctuations in the electric field gradients which provide a relaxation mechanism.

The term H_p of {2.1} is that due to paramagnetic impurity ions within a sample. Gd^{3+} and Mn^{2+} for example possess large magnetic moments due to unpaired f and d shell valence electrons respectively. As such they can provide a strong relaxation mechanism which is well recognised and indeed used for a variety of purposes such as doping diamagnetic liquids to accurately produce desired relaxation times. Since these elements are only present in our sample in low concentrations (<100ppm) we can assume that they do not interact with one another and that they interact with nuclei via a short range transferred contact interaction to nearest neighbour sites and a long range dipole-dipole interaction. In this way it is possible to characterise their effect on the observed system [2.9]. It is especially important to be aware of possible effects of these interactions where one desires accurate diffusion parameters and only the highest purity materials should be studied to avoid unwanted paramagnetic effects. It has been wrongly suggested by Fujita [2.10] that nmr results which show a significant change in the spin-lattice relaxation rate in the presence of about 20ppm paramagnetic impurity imply that the hydrogen. once activated, goes into a fluid-like diffusion mode enabling each proton to come within close proximity of the impurity nuclei. In fact the rapid diffusion is by spin diffusion, originally described by Bloembergen [2.11], and not the hydrogen itself.

2.1.2 Nuclear Spin Relaxation

In the previous section a review of the interactions of the nuclear spin with its surroundings has been given. The aim of this work is to obtain information on the hydrogen diffusion mechanism which can be gleaned from the relaxation rates. It is therefore necessary to present the relaxation effects due to the interactions discussed showing how these are modulated through particle diffusion.

2.1.2a The Dipole-Dipole Interaction

A variety of mathematical formalisms exist to describe relaxation where one is essentially looking at the quantum mechanical transition probability between states a and b of energy difference $\hbar\omega_{ab}$. The transition probability W can be expressed as

$$W_{ab} = |(a|A|b)|^2 J(\omega_{ab}) \qquad \{2.16\}$$

where A is an interaction operator and $J(\omega_{ab})$ is the spectral density at ω_{ab}. The total relaxation rate R of a system can generally be expressed as a linear sum of spectral densities $R = J_i(\omega_i)$ where the $J_i(\omega_i)$ are evaluated at specific frequencies ω_i. The number of terms in $J(\omega)$ and the frequencies ω_i depend on the details of the motion, the interactions that are being modulated and the specific relaxation rate being measured. The determination of $J(\omega)$ is a very important and complex problem since it depends on several dynamical processes and measurements are made on many-body systems where one observes an ensemble of interacting particles.

The spectral density is defined as the Fourier transform of a correlation function $G^q(\tau)$ by

$$J^q(\omega) = \int_{-\infty}^{\infty} G^q(\tau)\exp(-i\omega\tau)d\tau \qquad \{2.17\}.$$

The correlation function can be written as an ensemble average of the spatial operators $F^q_{ij}(t)$ of the dipole-dipole interaction as given in equation 2.8 such that

$$G^q(\tau) = \Sigma_{ij} \langle F^q_{ij}(t) F^q_{ij}(t+\tau) \rangle \qquad \{2.18\}$$

where $G(\tau)$ is independent of t. It can then be shown that the relaxation rates of a spin I due to the nuclear dipole-dipole interaction between like and unlike spins have the following form

$$T_1^{-1} = \frac{3}{2} D_l [J^1(\omega_o) + J^2(2\omega_o)] +$$
$$D_u [\frac{1}{12} J^0(\omega_o - \omega_s) + \frac{3}{2} J^1(\omega_o) + J^1(\omega_s) + \frac{3}{8} J^2(\omega_o + \omega_s)] \qquad \{2.19a\}$$

$$T_2^{-1}=\frac{3}{8}D_l[J^0(0)+10J^1(\omega_o)+J^2(2\omega_o)]+$$

$$D_u[\frac{1}{6}J^0(0)+\frac{1}{24}J^0(\omega_o-\omega_s)+\frac{3}{4}J^1(\omega_o)+\frac{3}{2}J^1(\omega_s)+\frac{3}{8}J^2(\omega_o+\omega_s)] \quad \{2.19b\}$$

where $D_l=\gamma^4\hbar I(I+1)$, $D_u=\gamma_I^2\gamma_S^2\hbar^2S(S+1)$ and ω_o and ω_s are the I and S spin resonance frequencies respectively. A third relaxation time sometimes used in the study of diffusion is $T_{1\rho}$ which is the spin-lattice relaxation time in the B_1 field when the nuclear magnetism is locked by B_1. The magnetism is therefore precessing relative to the laboratory frame with frequency ω_1 and the relaxation rate is correspondingly

$$T_{1\rho}^{-1}=\frac{3}{8}D_l[J^0(2\omega_1)+10J^1(\omega_o)+J^2(2\omega_o)] \quad \{2.19c\}$$

for the like-like spin interaction only. Interpretation of $T_{1\rho}$ is similar to that of T_1, however, as is apparent, $T_{1\rho}$ is sensitive to much slower diffusional processes than T_1 at a given temperature and frequency ω_o.

It may be shown that the relaxation rates due to the quadrupole interaction have a similar form to {2.19} and are

$$T_1^{-1}=\frac{2}{30}D_Q[J^1(\omega_o)+4J^2(2\omega_o)] \quad \{2.20a\}$$

$$T_2^{-1}=\frac{3}{40}D_Q[3J^0(0)+5J^1(\omega_o)+2J^2(2\omega_o)] \quad \{2.20b\}$$

$$T_{1\rho}^{-1}=\frac{3}{40}D_Q[3J^0(2\omega_1)+5J^1(\omega_o)+2J^2(2\omega_o)] \quad \{2.20c\}$$

where $D_Q=(\frac{e^2qQ}{\hbar})^2((2I+3)/I^2(2I-1))$ and $J^q(\omega)$ is still defined by {2.17}, now however, $G^q(\tau)=\Sigma_{ij}<V_{ij}^q(t)V_{ij}^q(t+\tau)$.

These equations thus define a formal set of relationships for the relaxation rates of a spin system due to the dipole-dipole interaction in terms of spectral density functions. In order to obtain the details required of the diffusion mechanism from experimental relaxation rate data it is necessary to model the correlation and hence spectral density functions.

2.1.2b The BPP model

Possibly the simplest form for the correlation function is that adopted by Bloembergen, Purcell and Pound [2.12]. First we develop equation 2.18 specifically for the dipole interaction between particles undergoing translational diffusion, then

$$G^q(\tau)=cd_q^2\Sigma_{ij}\left(\frac{Y_{2q}(\Theta,\phi)}{r_i^3}\,\frac{Y^*_{2q}(\Theta,\phi)}{r_j^3}\right)P(r_i,r_j,t) \qquad \{2.21\}$$

where c is the ratio of nuclei to available lattice sites and $P(\mathbf{r}_i,\mathbf{r}_j,t)$ is the probability of a pair of spins being separated by $\mathbf{r}_i$ at t=0 and $\mathbf{r}_j$ after a time t. The BPP model assumes the form of the correlation function to be

$$G^q(\tau)=G^q(0)\exp(-\tau/\tau_c) \qquad \{2.22\}$$

where τ_c is the characteristic correlation time of the random diffusion and is of the order of the time taken for a dipole to move through a distance sufficient to significantly alter the local B field. That this form may be reasonably valid is evident since from {2.18} we know that $G(0)=\langle F_{ij}^2(\tau)\rangle$ at $\tau=0$ and for $\tau\rightarrow\infty$, $G(\tau)\rightarrow 0$. The BPP model meets these conditions and generates a Lorentzian form for $J(\omega)$. From {2.17} for example

$$J^1(\omega)=G^1(0)\frac{2\tau_c}{1+\omega_o^2\tau_c^2} \qquad \{2.23\}$$

as shown in figure 2.2. For the H-H interaction τ_c may be approximated by $\tau_c=\tau_d/2$, where τ_d is the dwell time on a lattice site, since both hydrogens are moving and we assume the jump time is negligible in comparison with the interstitial dwell period. Note that in the case of Me-H interactions we can generally assume the host metal nuclei are stationary and thus $\tau_c\approx\tau_d$. The temperature dependence of τ_d for a thermally activated process is given by the Arrhenius relation. From {2.23} the spectral density has a maximum for $\tau_c\approx 1/\omega_o$ at a given ω_o and constant $G^q(0)$. This is reflected in the relaxation rates shown schematically in figure 2.3. We can also define two limits for T_1

$$T_1 \propto \tau_c \quad \text{for } \omega_o\tau_c << 1 \quad \text{High Temperature Limit} \qquad \{2.24a\}$$

$$T_1 \propto \frac{1}{\omega_o^2 \tau_c} \quad \text{for } \omega_o\tau_c >> 1 \quad \text{Low Temperature Limit} \qquad \{2.24b\}$$

Case a corresponds to rapid diffusion relative to the Larmor frequency in the high temperature (or low frequency) limit, and case b to slow diffusion in the low temperature (or high frequency) limit. We can see at this stage that a study of diffusion mechanisms might best be achieved in the low temperature regime where only a few diffusive steps occur in the Larmor period. $J(\omega)$ and hence T_1 are therefore sensitive to the microscopic detail of the diffusive process and not just some average as in the high temperature regime. Note that T_2 also contains this information but it is less readily obtained due to the additional $J^0(0)$ term in the relaxation rate. Also note that this analysis is only valid for $\tau_c < \{\delta\omega_d^2\}^{-1/2}$, where $\delta\omega_d^2$ is the rigid lattice linewidth due to the dipole interaction.

In using the BPP model we make specific assumptions about the jump probability function $P(r_i,r_j,t)$ in equation 2.21. This function can be written as $P(r_i,r_j,t)=\sum_s \omega_s(t,\tau)P_s(r_i,r_j)$ where $\omega_s(t,\tau)$ gives the probability that two spins perform s jumps in a time interval t and τ is the mean time between jumps, $P_s(r_i,r_j)$ is the probability of a given spin pair separation after s jumps. This model does not depend on the initial or final absolute positions of the spins but only on relative displacements. For a random jump process then

$$\omega_s(t,\tau)=(s!)^{-1}(t/\tau)^s\exp(-t/\tau) \qquad \{2.25\}$$

which is a Poisson distribution. The BPP model is equivalent to taking only s=0, thus generating {2.22}, and it therefore ignores any detail of the jump processes. Nevertheless the BPP model does generate a reasonable approximation to the form of the relaxation rates versus correlation time and as such has been used extensively to obtain values for jump activation energies. However, it is a rather simplistic model which has been improved in recent years in order to obtain more precise and detailed information about diffusion correlation times and processes, as discussed in the next section.

2.1.2c Further Modelling of the Correlation Function

Since the BPP model there have been many theoretical developments of the dipole-dipole correlation function due to translational diffusion. These have often involved the use of rather unrealistic models for the hydrogen diffusion in order to simplify the mathematical treatment.

Much of the work is based on the random walk model which assumes a particle simply hops randomly from one site to another independently of site occupation and taking no account of interactions with other particles. The model has a number of inherent drawbacks including the possibility that two particles may hop through one another. Hence the use of this model is only an approximation even at low hydrogen concentrations.

Torrey and later Resing and Torrey [2.13 - 5] were the first to use a random walk model and also attempt to cater for the discrete nature of the lattice sites. The particle motion was assumed to be random and completely isotropic and only jumps of a fixed length l were allowed. A particle is therefore able to hop from a given site to any point on the surface of a sphere of radius l centred at that site. A correlation function normalisation constant k is accurately determined at $\tau=0$ giving accurate values in the low frequency limit. However, the isotropic diffusion model does not account for pair correlations and is thus most accurate at low c. It is best suited to hydrogen motion between sites with a large coordination number for example O-sites in an fcc lattice which have 12 near neighbour sites forming an interstitial fcc lattice.

By way of an aside it might be noted that in all of these papers, tabulated results of T_1 and T_2 are given for a range of $\omega\tau$ and only for cubic systems. This method of presentation is that generally adopted in all such theoretical works. It is for this reason that the BPP model remains widely used in laboratory practice for fitting data. However, a recent improvement by Sholl [2.16], who has introduced a new analytical form for the theoretical relaxation rates, may become more widely used. This is of course only applicable in any case to polycrystalline samples.

Wolf [2.17] used a similar model to Torrey for a vacancy diffusion mechanism applicable in the limit $c_H \rightarrow 1$ where the vacancy concentration $c_v \rightarrow 0$. However, he found that the two parameters l and k were insufficient to cater for the lattice detail and the neglect of pair correlation gave

significant errors. Wolf went on to develop a more accurate monovacancy theory [2.18] based on the vacancy encounter model of Eisenstadt and Redfield [2.19]. The encounter model allows for the increased probability of mutual jumps between a particle and a vacancy once an exchange has taken place. The effects of this on the diffusion coefficient have been accurately calculated by Bardeen and Herring [2.20] and Lidiard [2.21], for example the diffusion coefficient for the fcc lattice is 0.78 that of the random walk model value when the encounter correlations are allowed for, as discussed in section 1.3. Wolf only dealt with the high concentration limit $c_H \rightarrow 1$ and ignored the detail of an encounter, only taking into account the final relative displacement of particles. He derives the correlation functions as a series expansion taking the first 10 to 20 terms and then averaging over all orientations to obtain the relaxation rate in the polycrystalline case [2.22-23].

At about this time Sholl and Barton [2.24-26] developed a similar mathematical technique using a random walk model for cubic lattices. The relaxation rates are calculated for specific crystal orientations by performing a threefold numerical integration to determine $P(r_i,r_j,t)$ incorporating some 7000 neighbouring spins [2.27]. The differences between the predictions of Sholl and those of Wolf, who allows for about 1330 nearest neighbour spin interactions, are minimal at low temperatures and are expected to be greatest in the high temperature regime where Wolf's analysis is less accurate since many diffusional jumps occur in the Larmor period.

Barton and Sholl [2.28-34, 2.14] subsequently went on to make use of the reciprocal space formalism and mean field theory initially developed by Fedders and Sankey [2.35]. The mean field theory extends the simple hopping model used in the random walk methods by disallowing multiple site occupancy and introducing a blocking factor $(1-c_H)$ in the determination of jump probabilities. The theory is accurate for $c_H \rightarrow 0$ and in the high frequency, low temperature limit $\omega\tau \gg 1$ except at $c \rightarrow 1$. The reason for discrepancies in the theory is that it still does not account for all pair correlations nor does it account for a spin leaving a site and thus giving that site an occupation probability of 0 since the model still assigns a probability of $(1 - c_H)$. Again, accuracy in the low temperature limit is expected since very few jumps are involved and hence correlation effects are not prevalent.

Fedders and Sankey used the theory to obtain relaxation rates for particles making nearest neighbour jumps on a simple cubic lattice taking into account both like and unlike interactions. They also developed a multiple scattering theory applicable for any c_H and $\omega\tau$ though only exact for the limits $c_H \rightarrow 0$ and $c_H \rightarrow 1$. Although possibly the best theory to date, it has a rather complex concentration dependence and a simple representation of results, for example as data tables, is not readily obtained. Using the mean field theory however, Barton and Sholl [2.28] produced one of the most comprehensive papers in this area by presenting results for sc, fcc and bcc lattices for all $\omega\tau$ and c, including the exact spatial correlation effects in the low temperature limit.

A further development was made by Bustard [2.36] who described an independent spin-pair model and used Monte Carlo methods to derive diffusional effects on T_1 for 1st and 3rd nearest neighbour jumps on a simple cubic lattice. These findings were compared to nmr results for γ-$TiH_{1.5}$ by Bustard et al [2.37], who showed that the hydrogen diffuses between the nearest neighbour T-sites which form a simple cubic lattice within the fcc Ti lattice. Diffusion coefficients predicted from T_1 versus temperature results were also shown to be in good agreement with direct measurements made using an nmr pulsed field gradient technique. The independent spin-pair model however does not account for correlations between pairs of spins, whilst it does account for spin correlations within a pair. Further approximations exist in the method of fitting which results in a systematic error of the order of 6% compared with the monovacancy calculations at high concentration. The Monte Carlo method shows much promise for application to specific jump models and is potentially applicable to many particles interacting on a specific lattice. It has been developed in recent years by Faux et al [2.33] but still falls short of its potential which could be realised with faster computers and/or longer CPU time to enable the use of larger and more complex models with greater statistical accuracy. The results presented by Faux et al are for all $\omega\tau$ and c (except $c \rightarrow 1$) with least accuracy in the high temperature regime. Faux and Ross [2.36] use this method to obtain tracer and chemical diffusion coefficients which are compared with experimental results for NbH_x and TaH_x ($0.5 < x > 0.6$). They allow for multiple blocking to second and third nearest neighbours, deriving results for a range of c and comment on the significance of blocking models due to H-H interactions for diffusion. A treatment of the effect of nearest neighbour interactions between hopping

particles on T_1 has also been presented which allow for I-I coupling over a range of concentrations for sc and fcc lattices [2.39]. The effect of hopping to second-nearest neighbour sites is presented by Faux [2.64] for the case of a bcc lattice allowing for both H-H and H-Me interactions. Faux concludes from the agreement of his calculations with previous experimental results for $NbH_{0.6}$ that 60% of hydrogens hop to second-nearest neighbour sites.

The problem of long range blocking is of vital importance in developing mathematical hopping models to sufficient accuracy in determining the true diffusional properties of hydrogen in crystalline solids. In 1982 Fedders [2.40] showed that even simple nearest neighbour blocking effects relaxation due to diffusion on a sc lattice. MacGillivray and Sholl [2.30] considered the case of interactions in the high frequency limit which simplifies the calculation since few jumps are involved. Richards [2.41] has developed a theoretical model accounting for particle interactions which in the extreme case only allows particle hopping in the presence of a pair of vacancies at near neighbour sites. The second nearest vacancy effectively reduces the otherwise infinite barrier potential at the saddle point between particle and first nearest neighbour vacancy. Thus a greatly reduced particle hopping rate occurs at high concentration $c_H \rightarrow 1$ where this model is potentially applicable.

In summary, therefore, it can be seen that a good deal of progress has been made in describing diffusion mechanisms in metal hydrides and their effecton nuclear spin relaxation. Most experimental studies have to date dealt with powder samples and there is much potential in single crystal studies since we have seen that theoretical results involve averaging to obtain polycrystalline relaxation rates. A more quantitative analysis of the orientation dependence of relaxation rates is given in the next section.

2.1.2d T_1 Anisotropy

The nuclear spin relaxation rates due to the dipole interaction depend on the orientation of the crystal with respect to the static magnetic field. This orientation dependence was first expressed by Eisenstadt and Redfield [2.19] for cubic systems and has since been developed by various authors, the most recent being Sholl [2.32] who derives expressions for all 32 crystal point group symmetries. Sholl gives the angular dependence of the spectral density functions independent of diffusion and for the I-I type interaction only. These expressions are derived using transformation properties of the relevant spherical harmonics in terms of rotation

matrices $R^2_{q',q}(\Theta,\phi)$ where Θ and ϕ are the polar angles of the magnetic field direction relative to an orthogonal set of axes fixed in relation to the crystal and the $R_{q',q}$ form a 5x5 rotation matrix **R**. Sholl derives a general expression for all crystal classes in terms of the independent elements of two 5x5 matrices **R** and **J**. As a result of crystal symmetry this expression includes at most 15 elements (for the triclinic class), and can be reduced to only 2 elements for cubic systems. The definition of the axes used in this derivation by Sholl are for example, for orthorhombic and cubic classes x, y, z axes along orthogonal crystal axes, and for hexagonal the z axis is parallel to the six fold symmetry axis with x and y axes arbitrary.

The relaxation rates are given explicitly in terms of functions of the polar angles Θ and ϕ and independent parameters A_i, where $i \leq 15$. For the cubic and hexagonal crystal classes the correlation functions have the form

cubic $$A_1+A_2(\sin^2 2\Theta+\sin^4\Theta\sin^2 2\phi) \qquad \{2.26\}$$

hexagonal $$A_1+A_2\sin^2\Theta+A_3\sin^4\Theta \qquad \{2.27\}$$

but a more complete derivation and results for other crystal classes are given by Sholl [2.32]. Note that for hexagonal systems the relaxation rates are independent of ϕ and hence assignment of the x and y axes in the six fold symmetry plane can be arbitrary as previously stated. The spin lattice relaxation rate for cubic systems can then be written as

$$T_1^{-1}=B\{A_1+A_2(\sin^2 2\Theta+\sin^4\Theta\sin^2 2\phi)\}, \qquad \{2.28a\}$$

where $B=(4\pi/5)\gamma^4\hbar^2 I(I+1)(\mu_o/4\pi)$ and

$$A_1=(8\pi/15)(J_{11}(\omega_o)+2J_{00}(2\omega_o)+2J_{11}(2\omega_o)), \qquad \{2.28b\}$$

$$A_2=(4\pi/15)(J_{00}(\omega_o)-J_{11}(\omega_o)-J_{00}(2\omega_o)+J_{11}(2\omega_o)) \qquad \{2.28c\}.$$

Similarly for hexagonal systems we have

$$T_1=B(A_1+A_2\sin^2\Theta+A_3\sin^4\Theta), \qquad \{2.29a\}$$

where

$$A_1=(8\pi/15)(J_{11}(\omega_o)+4J_{22}(2\omega_o)), \qquad \{2.29b\}$$

$$A_2=(4\pi/15)(J_{00}(\omega_o)-5J_{11}(\omega_o)+2J_{22}(\omega_o)+8J_{11}(2\omega_o)+8J_{22}(2\omega o)), \qquad \{2.29c\}$$

$$A_3=(4\pi/15)(4J_{11}(\omega_o)-3J_{00}(\omega_o)-J_{22}(\omega_o)-4J_{11}(2\omega_o)+3J_{00}(2\omega_o)+J(2\omega_o)) \quad \{2.29d\}.$$

The $J_{qq}(\omega)$ are elements of the matrix **J** and their theoretical evaluation is complex since they are dependent on frequency, temperature, spin concentration and the diffusional processes discussed in the previous section. Conversely, the A_i may be determined experimentally and may be used to deduce details of the diffusional process.

In the low frequency limit many diffusional jumps occur in the Larmor period and hence $J_{nn}(\omega_o)=J_{nn}(2\omega_o)$. We can then write

$$T_1^{-1}=B(2J_{00}+3J_{11}) \qquad \{2.30\}$$

for cubic systems and

$$T_1^{-1}=B\{(J_{11}+4J_{22})+(3/2)(J_{00}+J_{11}-2J_{22})\sin^2\Theta\} \qquad \{2.31\}$$

for hexagonal systems.

For the cubic system we note that in this limit $T_1^{-1}=T_2^{-1}=T_{1\rho}^{-1}$ and they are all isotropic. For hexagonal systems however this is not the case and some anisotropy remains through the Θ dependence. The angular averages of the relaxation rates are all equal. For lower order crystal symmetry groups the anisotropy is reduced and the expressions for T_1^{-1} involve fewer independent parameters.

As one might expect it is in the low temperature limit that one gets the largest anisotropy. The anisotropy is conveniently expressed in terms of a ratio of the extrema, which for cubic systems is

$$\zeta=1+\frac{4A_2}{3A_1} \qquad \{2.32\}$$

In general authors have either published theoretically calculated spherical average values of relaxation rates, $(R_n)_{poly}$, or $(R_n)_{poly}$ and $(R_n)_{001}$ which are the relaxation rate for a polycrystal and for B_o parallel to a <001> direction respectively. In the latter case there is sufficient information to calculate rates at other orientations since from {2.28}

$A_1=(R_1)_{001}$ and $A_2=5/4\{(R_1)_{poly}-(R_1)_{001}\}$ and hence $\zeta=1+5/3\{((R_1)_{poly}/(R_1)_{001})-1\}$. The orientation of the extrema are <001> and <111> directions where $\Theta=\phi=0$ and $\Theta=54.7°$, $\phi=45°$ respectively. Which of these pairs of angles corresponds to the maximum R_1 and which the minimum depends on the sign of A_2 which is determined by the structure. Figure 2.4 shows the predicted orientation dependence of R_1 for sc, bcc and fcc lattices over a complete range of $\omega\tau$. These results were derived using the above expression from the Barton and Sholl mean field calculations [2.28]. They show the expected isotropic relaxation in the high temperature regime and the approach to maximum anisotropy in the low temperature limit. Note also the difference in relaxation rates between the crystal classes which results from the differences in coordination number.

While the greatest anisotropy ratio ζ occurs in the low temperature limit it is worth noting that using random walk calculations for nearest and 3rd nearest neighbour hopping models on a simple cubic lattice the greatest difference $\partial\zeta$ between the models occurs for $\omega\tau\approx1$ as shown by Styles et al [2.42] and not $\omega\tau\gg1$. This value of $\partial\zeta$ is some 8.6% suggesting that to identify jump models from experimental results requires very accurate data as shown in table 2.1. Site occupation is potentially far easier to determine in the fcc host metal lattices for example since the O-sites form an fcc lattice and the T-site a simple cubic lattice.

Table 2.1 The predicted anisotropy for a range of $\omega\tau$ in a simple cubic lattice from different models

$y=\omega\tau$	ζ_{nn}^{MF}	ζ_{nn}^{RW}	ζ_{3nn}^{RW}	ζ^{RW}
0.1	1.025	1.017	1.015	0.002
0.3	1.129	1.093	1.060	0.033
0.6	1.281	1.224	1.155	0.069
1.0	1.402	1.362	1.276	0.086
2.0		1.525	1.454	0.071
5.0	1.570	1.616	1.579	0.037
$\gg1$	1.583	1.639	1.615	0.024

We have made use of the T_1 anisotropy phenomena in confirming the diffusion path for hydrogen which jumps between nearest neighbour O-sites in α'-PdH_x. This was possible since a T_1 anisotropy $\zeta=0.94$ was observed in line with a predicted value of 0.95 for diffusion on a bcc lattice and not comparable with $\zeta=1.29$ predicted for an sc array [2.42].

For hexagonal systems few theoretical results exist. Sholl [2.44] has published some calculations using the random walk model for particles on a simple hexagonal structure, potentially applicable to hydrogen O-site occupation in hexagonal close packed metal lattices where the I-I interaction dominates. Two jump probabilities, ω_1 and ω_2, are considered for jumps to any one of the six neighbouring sites in the hexagonal ab plane and to one of the two sites along the c axis respectively. For three dimensional isotropic motion $6\omega_1+2\omega_2=1$ and, by introducing a parameter u, the jump model is made anisotropic since $\omega_1=1/8(1+u/3)$ and $\omega_2=1/8(1-u)$. Hence u=1 conveniently defines 2D motion in the hexagonal plane while u=-3 produces 1D motion along the c axis. Results of spherically averaged R_1 for a range of $\omega\tau$ and different u are published for several c/a ratio. Figure 2.5 shows that for 1D motion an enhanced relaxation occurs at low $\omega\tau$ compared with 2 and 3D motion. This effect is increased for smaller c/a since nearest neighbour distances are decreased in the c direction. A value of c/a=0.8 is roughly that for the O-site lattice which form a simple hexagonal structure in a hcp metal lattice where typically c/a≈1.6. Further potentially useful observations for hexagonal systems are discussed by Sholl.

Use is made of T_1 anisotropy in chapter 4 to investigate diffusion mechanisms and some theoretical predictions of the T_1 orientation dependence for different specific jump models are presented for the relevant system studied.

2.1.2e Conduction Electrons

The hyperfine field produced at the nucleus due to conduction electrons has been discused in section 2.1.1 and it is known to produce an effective relaxation mechanism. In 1950 Korringa [2.45] derived an analytical expression for the relaxation produced in a simple metal where only the s-contact interaction is found to be responsible for both the Knight shift and the nuclear T_1. The Korringa relation is

$$K^2T_1T=S \qquad (2.33)$$

where T is the absolute temperature and S the Korringa constant

$$S=(\gamma_e/\gamma_n)^2(\hbar/4\pi k_B) \qquad (2.34)$$

where γ_e is the electron gyromagnetic ratio. However this expression is found to be too simplistic for most metals [2.3]. Narath [2.46] derived

similar expressions incorporating further parameters, including enhancement factors to allow for electron-electron interactions and d-core polarisation, again finding that T_1T equals a constant.

In transition metal-hydrides the hyperfine field is predominantly due to three effects, as described earlier, and we can write the consequent spin-lattice relaxation rate as

$$T_1^{-1}=4\pi\hbar\gamma^2kT\{(H_{hf}^{s}N_s(E_F))^2+(H_{hf}^{d}N_d(E_F))_q^2+(H_{hf}^{o}N_d(E_F))_p^2\} \quad \{2.35\}$$

where H_{hf}^{s}, H_{hf}^{d} and H_{hf}^{o} are the s-contact, the d-core polarisation and d-orbital hyperfine fields at the nucleus. $N_s(E_F)$ and $N_d(E_F)$ are the s and d density of states at the Fermi level (E_F) and p and q are reduction factors dependent on the nature of the symmetry of the d-states at the Fermi level. The analysis assumes an absence of electron state admixing (ie between s and d levels) and that two distinct s and d bands exist. Note that the first term of {2.35} should be for all s-like electrons in the case of hydrogen nuclei at interstitial sites, especially since the intrinsic hyperfine field of the hydrogen 1s orbital is small [2.46]. In fact it is predominantly the transition metal d electron which is predicted to be responsible for the proton spin relaxation [2.4]. For some pure metals such as Mo and Pd the three terms make comparable contributions to T_1 [2.47].

Experimental observation of relaxation produced by these interactions can yield valuable information about the electronic structure of a system, especially in conjunction with Knight shift results. However in metal hydrides it only becomes the dominant relaxation mechanism at high and low temperatures since the nuclear dipolar mechanism, modulated by diffusion, controls the relaxation rate at intermediate temperatures with a maximum when $\omega_o\tau_c\approx1$ as described earlier. It is only approximately a decade in $\omega\tau$ away from the dipolar maximum that T_{1e}^{-1} becomes significant, but it should always be considered since the measured total rate includes a contribution from this source.

Earlier in this chapter the Knight shift was shown to be anisotropic, the anisotropy depending on the nuclear site symmetry and electronic structure, and, in the absence of cubic symmetry, an anisotropy also occurs in both the dipolar and orbital hyperfine contributions to T_{1e}. In 1967 Narath [2.48] derived the angular dependence of T_{1e} for a hexagonal

close packed system through the transformation properties of spherical tensor terms in the relevant hyperfine interactions using a rotation matrix method similar to that used by Sholl [2.32] discussed earlier. In the absence of s-d admixing and using a tight binding model Narath showed that

$$T_1^{-1} = 4\pi\hbar\gamma^2 k_B T \ \Sigma_i N_i^2 (K_i^1 + K_i^2 \sin^2\Theta) \qquad (2.36)$$

where the sum over i is for all hyperfine interactions with $N_s = N_s(E_F) H_{hf}^s$. $N_d = N_d(E_F) H_{hf}^d$ and $N_{dip} = N_{orb} = N_d(E_F) H_{hf}^{orb}$. The K_i are reduction factors and $K_s^2 = K_d^2 = 0$, ie the s-contact and d-core polarisation terms are isotropic as previously stated. The other K factors are derived by Narath in terms of d-state symmetry operators ($K_s^1 = 1$) showing that the K_{dip}^n are very small making the dipolar term negligible. The only significant anisotropy therefore arises from the $K_{orb}^2 \sin^2\Theta$ term. Narath did not actually observe any anisotropy since he made measurements on a powdered Ti sample and took an average value of $2/3K_{orb}^2$. His results were also complicated by the quadrupole interaction for both Ti isotopes. He was therefore only able to speculate on the relative contributions from each mechanism to the overall relaxation process.

Fradin in 1968 [2.49] observed a T_{1e} anisotropy in hcp metallic Sc, finding that $(T_1T)^{-1} = 1.25 - 0.58\sin^2\Theta$ $(sK)^{-1}$. From his result he was able to set a limit on the likely contributions concluding that the s-contact and d-core polarisation terms cancel leaving a dominant orbital hyperfine interaction where $K_{orb}^1/-K_{orb}^2 \leq 2.155$.

Seymour and Sholl have recently performed some theoretical calculations to derive the anisotropy of T_{1e} for all crystal classes [2.50]. As seen with Narath's result for hcp systems it transpires that the T_{1e} angular contribution for a given point group is the same as that for the high temperature limit of the nuclear dipole-dipole relaxation due to translational diffusion. This is physically reasonable since the itinerant electron velocity is naturally much greater than that of either the metal or

the hydrogen nuclei and one is therefore always in the low correlation time regime.

2.2 Neutron Scattering

2.2.1 Introduction

The neutron eluded detection until 1933 when it was discovered by J. Chadwick several years after its sub-atomic counterparts the electron and proton. It is precisely the properties which made it elusive then that now make it such a useful tool in the study of matter. The overall charge neutrality of the neutron enable it to penetrate a significant depth into solids since it interacts only via the short-range strong force. At thermal energies (100-1000K) the neutron has a de Broglie wavelength of the order of interatomic spacings in solids which leads to diffraction phenomena in scattering experiments. These neutron energies and momenta are also similar to collective atomic excitations in solids, phonons for example, and hence inelastic scattering can occur with large observable changes in the neutron energy and momentum. The neutron also has a magnetic dipole moment and spin I=1/2 which enables the study of magnetic structure and excitations. The theory of neutron scattering is described in detail elsewhere, for example [4.49 & 4.50], and only a brief introduction is given here followed by an explanation of quasielastic neutron scattering, qns, and its use in determining details of particle diffusion.

In a scattering event we have for a neutron of wavelength λ and mass m

$$\hbar\omega = E_i - E_f = \frac{\hbar}{2m}(|\mathbf{k}_i|^2 - |\mathbf{k}_f|^2) \qquad (2.37)$$

$$\hbar\mathbf{Q} = \hbar(\mathbf{k}_f - \mathbf{k}_i) \qquad (2.38)$$

where $|k| = 2\pi/\lambda$ and $\hbar\omega$ is the change in neutron energy, the subscripts i and f denote incident and final energy states respectively, and $\hbar Q$ is the momentum transfer. The scattering angle Θ is given by the cosine rule, as shown in figure 2.6, viz.

$$Q^2 = k_i^2 + k_f^2 - 2k_i k_f \cos\Theta \qquad (2.39).$$

The basic characteristic which describes the sample nuclei is the scattering cross-section σ which is defined as the number of neutrons scattered per unit time divided by the incident neutron flux Φ. For the

simple case of scattering from a single fixed nucleus it can be shown that $\sigma=4\pi b^2$, where b is a characteristic nuclear scattering length which is isotope dependent. For an overall sample, however, the number of neutrons scattered through a solid angle $d\Omega$ in the direction Θ, ϕ with an energy between E and E+dE per second divided by $\Phi d\Omega dE$ is known as the partial differential cross-section (pdcs), see figure 2.7. The derivation of satisfactory expressions for the pdcs requires the use of rigorous scattering theory but approximations can be made to the procedure if a specific system is being studied or a less than general result is required. It should be noted that there are two fundamentally different types of neutron scattering cross-section known as the coherent and incoherent terms. If a sample consisted of only one isotope, which had zero spin, then the scattered neutrons from each nucleus would all possess the same amplitude and phase, the overall scattered wave would thus be a result of the interference of the scattered neutrons from different nuclei and therefore dependent only on the relative position of the nuclei; this is coherent scattering. Incoherent scattering arises from nuclear spin and isotope fluctuations throughout a sample which give rise to variation in the amplitude and phase of the scattered neutron waves from nucleus to nucleus. In theory this could average the scattered amplitude to zero thus losing all information from interference effects leaving only information about the motion of the nuclei. In the case of hydrogen, ^1H has a very large incoherent scattering cross-section σ_i=79.9 barns (1barn=10^{-28} m^2) at thermal energies due to the dependence of the neutron interaction on the relative direction of the proton spin. ^1H also has a low coherent cross-section σ_c=1.76 barns in contrast to deuterium which has σ_c=5.59 and σ_i=2.04barns. This variation in cross-section between the two isotopes is very useful in determining properties of metal hydrides where one might put either pure ^1H or ^2D into the metal and thus determine dynamical or structural properties from both incoherent and coherent scattering. Several reviews exist dealing specifically with the study of metal hydrogen systems using neutron scattering techniques to which the reader is referred for full details [2.53-57].

The pdcs for both types of scattering can be expressed as

$$\left(\frac{d^2\sigma}{d\Omega d\omega}\right)_{inc}=[\langle b^2\rangle - \langle b\rangle^2]\frac{k_f}{k_i}S_{inc}(\mathbf{Q},\omega) \qquad \{2.40\}$$

and

$$\left(\frac{d^2\sigma}{d\Omega d\omega}\right)_{coh} = \langle b \rangle^2 \frac{k_f}{k_i} S_{coh}(\mathbf{Q},\omega) \qquad (2.41)$$

where $\langle b \rangle^2 = (1/N)\sum_{i=1}^{N} b_i^2$ and $\langle b \rangle = (1/N)\sum_{i=1}^{N} b_i$ and the equations hold if the sample contains a random distribution of N nuclei with scattering lengths b_i. The scattering functions $S(\mathbf{Q},\omega)$ contain all the useful information concerning the scattering sample. For inelastic scattering, $S(\mathbf{Q},\omega)$ can be derived using perturbation theory to determine transition probabilities of the system. For the case of a simple cubic Bravais lattice in a harmonic one phonon approximation one obtains

$$S_{inc}(\mathbf{Q},\omega) = \left[\frac{\hbar F(\hbar\omega/k_B T)}{2M|\omega|}\right] Q^2 g(\omega) \exp(-Q^2\langle u^2 \rangle) \qquad (2.42)$$

where $g(\omega)$ is the phonon density of states, M is the nuclear mass and the thermal population factor is

$$F(x) = (\exp(x)-1)^{-1} + 1/2\,(1 \pm 1) \qquad (2.43)$$

which allows for phonon creation and annihilation events. The Debye-Waller factor $\exp(-Q^2\langle u^2 \rangle)$ determines the intensity of the zero phonon processes where $\langle u^2 \rangle$ is the mean-square amplitude of vibration of the nuclei. Equation 2.42 is generally applicable to hydrogen scattering in metal-hydrides, despite them not always forming a Bravais lattice, where M corresponds to the hydrogen mass for optical modes and the metal atom mass for acoustic modes. For dilute hydrides the optical vibrations are considered as localised modes between a hydrogen and neighbouring metal atoms rather than as a collective excitation. Note that one-phonon processes dominate for $Q^2\langle u^2 \rangle \leq 0.1$ which generally requires Q of the order of 2 to 4Å^{-1} and also that the effect of diffusion is not included in this factor, although it is expected to be small [2.53].

The scattering function has been described for inelastic interactions for the incoherent term. Besides inelastic and elastic scattering a third regime exists known as quasielastic neutron scattering which arises from small energy changes in the neutron due to reorientational or translational motion of the scattering system which is observed as a broadening of the elastic peak. A more useful approach in deriving the form of the scattering function for our purpose, the study of hydrogen diffusion, is that given by Van Hove [2.57]. He presented the following expressions

$$S_{coh}(\mathbf{Q},\omega)=1/2\pi\iint\exp\{i(\mathbf{Q}\cdot\mathbf{r}-\omega t)\}G(\mathbf{r},t)d\mathbf{r}dt \qquad (2.44)$$

$$S_{inc}(\mathbf{Q},\omega)=1/2\pi\iint\exp\{i(\mathbf{Q}\cdot\mathbf{r}-\omega t)\}G_s(\mathbf{r},t)d\mathbf{r}dt \qquad (2.45)$$

where the $G(\mathbf{r},t)$ are complex quantum mechanical functions such that the real part is equivalent to the classical space-time correlation time and the imaginary part describes local variations in the density of nuclei due to the interaction with the neutron. For distinguishable particles such as ^1H the correlation function $G(\mathbf{r},t)$ can be expanded as

$$G(\mathbf{r},t)=G_s(\mathbf{r},t)+G_d(\mathbf{r},t) \qquad (2.46)$$

the so-called self and distinct terms respectively. The former describes the probability of finding a given particle at the origin at a time t=0 then displaced by $\mathbf{r}$ at time t later, while the latter gives the probability of finding any other particle at $\mathbf{r}$ at time t. In a neutron experiment typically, using a specific diffusion model, one derives the form of the correlation function which is then transformed to obtain $S(\mathbf{Q},\omega)$ which is fitted to the experimental data.

A first analysis of $G_s(\mathbf{r},t)$ considers macroscopic continuous tracer diffusion described by $D_t=l^2/6t$ and assumes a delta function source at t=0 which it can be shown [2.51] generates a Lorentzian form for the scattering function

$$S_{inc}(\mathbf{Q},\omega)=(1/\pi\hbar)\frac{D_tQ^2}{\omega^2+(D_tQ^2)^2} \qquad (2.47)$$

which has a full width at half-maximum $E_{FWHM}=2\hbar D_tQ^2$, as shown in figure 2.8. Thus, as stated above, fitting experimentally observed $S(Q,\omega)$ over a range of Q one is able to determine the tracer diffusion coefficient as shown schematically in figure 2.9. However, the continuous diffusion model can only be assumed if the jump step is very small relative to the overall particle displacement during the measurement which means that Q must be small. As scattering can be observed at greater Q this region of reciprocal space will yield information about the microscopic nature of the diffusion process and indeed much work has been done in the area both experimentally and theoretically as discused in the next section. In this regime equation 2.47 no longer holds and the scattering function is no longer found to be Lorentzian and its half-width decreases below the

predicted $D_t Q^2$ value. A similar relation holds for the chemical diffusion coefficient in terms of $S_{coh}(\mathbf{Q},\omega)$ where one might consider macroscopic diffusion governed by $D_c = l^2/6t$.

2.2.2 Development of the Scattering Function

Derivation of the form of the correlation functions to be used in the neutron scattering function for metal-hydrides closely follows the methods described in section 2.1.2 b and c for nmr. Indeed one can express the self-correlation function as

$$G_s(\mathbf{r},t) = \sum_{n=0}^{\infty} R_n(\mathbf{r}) T_n(t) \qquad (2.48)$$

where $R_n(\mathbf{r})$ is the probability that a particle at the origin at t=0 is at a point $\mathbf{r}$ after n jumps and $T_n(t)$ is the probability that a particle has taken n jumps at time t. Assuming a random walk diffusion model over discrete particle sites with separation $\mathbf{l}$ then the jump factor $T_n(t)$ is described by a Poisson distribution and $T_o(t) = \exp(-t/t_o)$ is the probability of no jumps after time t. The $R_n(\mathbf{r})$ are n-fold convolutions of $R_1(\mathbf{r}) = 1/m \sum_l d(\mathbf{r}-\mathbf{l})$ which is the probability distribution after one jump. Here m is the number of different possible nearest neighbour jump vectors $\mathbf{l}$ to the equivalent sites on a Bravais lattice. Despite the inadequacies of the random-walk model it is the basis of the so-called Chudley-Elliot model [2.59] which generates the following form for $S_{inc}(\mathbf{Q},\omega)$

$$S_{inc}(\mathbf{Q},\omega) = \frac{F(\mathbf{Q})/\tau_o}{\omega^2 + |F(\mathbf{Q})/\tau_o|^2} \qquad (2.49)$$

which has a FWHM of $G = 2F(\mathbf{Q})/\tau_o$ where $F(\mathbf{Q}) = 1 - 1/m \sum_l \exp\{i(\mathbf{Q}.\mathbf{l})\}$. This model is identical to that in the Torrey analysis of nmr T_1 discussed in section 2.1.2c.

Experimental studies of α-PdH_x, first carried out by Skold and Nelin [2.60] (for a review of subsequent studies see for example [2.54]), have given results in excellent agreement with the random walk model and show that the hydrogens jump between nearest neighbour O-sites. This particular system is ideal for this study since the α-phase necessarily has a low hydrogen concentration and the O-sites form an fcc structure in the the fcc host lattice. The predicted behaviour of the qns half-width versus Qa/2 for scattering along specific crystallographic directions in an fcc structure of lattice constant a is shown in figure 2.10. The two sets of graphs are for O-

O and T-T nearest neighbour hopping paths based on the Chudley-Elliot model. They show the distinct difference in qns half-widths predicted from the two jump models; for a powdered sample an average of the crystallographic results is necessary for each jump model.

Development of mathematical representations of the scattering has progressed along the lines of that described earlier for nmr T_1 studies. Improvements in the theoretical jump models were necessary to allow for increased concentration and therefore jump correlation effects. Also necessary was an extension from the simple Bravais lattice structures to more complex systems such as T-site hopping in a bcc host lattice where six inequivalent T-sites exist. This work, carried out by Blaesser and Peretti [2.61] and later by Rowe et al [2.62], involved deriving $S_{inc}(\mathbf{Q}, \omega)$ as a sum of six Lorentzians each having a different Q dependence. The result at low Q reduced to a single Lorentzian with half-width proportional to DQ^2 since again the details of the microscopic diffusion mechanism vanish and the macroscopic continuous diffusion model is applicable. Further extension of these models to allow for next-nearest neighbour hopping and hopping on non-cubic arrays have been carried out. For example Lottner et al [2.63] found good agreement with experimental results and a near neighbour T-T jump model for NbH_x at low temperatures. but at high temperatures it was necessary to extend the model to include next-nearest neighbour jumps.

Extensive use has been made of the Monte Carlo method to determine $S_{inc}(\mathbf{Q}, \omega)$ for a variety of jump models in different systems. As pointed out previously this method is particularly useful in allowing for correlation effects such as site blocking. A review of this subject has been presented by Ross [2.56].

References

2.1 Abragam A., 'Principles of Nuclear Magnetism', OUP, 1961.

2.2 Slichter C.P., 'Principles of Magnetic Resonance', Harper and Row, 1964.

2.3 Carter G.C., Bennett L.H. and Kahan D.J., 'Metallic Shifts in NMR', Progress in Materials Science vol. 20, Pergamon Press, 1977.

2.4 Bowman Jr. R.C., Hyperfine Interactions, **24-26**583-606,(1985).

2.5 Bloembergen N. and Rowland T.J., Acta Met., **1**, 731 (1953).

2.6 Knight W.D., Phys. Rev., **76**,1259 (1949).

2.7 Torgeson D R, Schoenberger R J and Barnes R G, J. Magn Res, **68**, 85-94,(1986).
2.8 Cohen M H and Reif F; in Solid State Physics, edited by Seitz F and Turnbull D, Academic Press Inc, New York, Vol 5, 1957.
2.9 Belhoul M., Phd Thesis, University of Warwick, 1983.
2.10 Fujita S., Phys. Stat. Sol. (b), **143**443-451(1987).
2.11 Bloembergen N., Physica, **15**,386(1949).
2.12 Bloembergen N, Purcell E M, and Pound R V, Phys Rev,**73**679-712, (1948).
2.13 Torrey H C,Phys Rev, **92** 962,(1953).
2.14 Torrey H C, Phys Rev, **96**, 690,(1954).
2.15 Resing H A and Torrey H C, Phys Rev. 131, 1102-1104, (1963).
2.16 Sholl C A, J Phys C,**21**, 319-24,(1988).
2.17 Wolf D, Z Naturforsch, **26a**,1816(1971).
2.18 Wolf D, Phys Rev B,**10**,2710-23,(1974).
2.19 Eisenstadt M and Redfield A G, Phys Rev, **132**,635-43,(1963).
2.20 Bardeen J and Herring C; in Imperfections in Nearly Perfect Crystals John Wiley & Sons Inc, New York, 1952.
2.21 Lidiard A B; in Handbuch der Physik, edited by Flugge S, Springer-Verlag, Berlin, Vol 20, 327, 1957.
2.22 Wolf D, J Magn Reson, **17**,1-19,(1975).
2.23 Wolf D, J Phys C, **10**,3545-57,(1977).
2.24 Sholl C A, J Phys C, **7**,3378-3386,(1974).
2.25 Sholl C A, J Phys C, **8**,1737-1741,(1975).
2.26 Barton W A and Sholl C A, J Phys C, **9**,4315-4328,(1976).
2.27 Barton W A and Sholl C A, J Phys C, **11**,4405-4418,(1978).
2.28 Barton W A and Sholl C A, J Phys C,**13**,2579-95,(1980).
2.29 Sholl C A, J Phys C, **14**,1479-90,(1981).
2.30 MacGillivray I R and Sholl C A, J Phys C, **16**,5659-5669,(1983).
2.31 MacGillivray I R and Sholl C A, J Phys C, **18**,1691-703,(1985).
2.32 Sholl C A, J Phys C, **19**,2547-2555,(1986).
2.33 Faux D A, Ross D A and Sholl C A, J Phys C, **19**,4115-4133,(1986).
2.34 MacGillivray I R and Sholl C A, J Phys C, **19**,4771-4779,(1986).
2.35 Fedders P A and Sankey O F, Phys Rev B, **18**,5938-47,(1978).
2.36 Bustard L D, Phys Rev B, **22**, 1-11,(1980).
2.37 Bustard L D, Cotts R M and Seymour E F W, Phys Rev B,**22**,12-20, (1980).
2.38 Faux D A and Ross D K, J Phys C, **20**,1441-57,(1987).
2.39 Faux D A and Hall C K, J Phys C, **21**,3967-3981,(1988).

2.40 Fedders P A, Phys Rev B, **25**, 78, (1982).
2.41 Richards P M, Phys Rev B, **33**,3064-3075,(1986).
2.42 Styles G A, Seymour E F W, Barnfather K J, Sholl C A and Schone H E, J Less-Common Metals, **129**,345-353,(1987).
2.43 Schone H E, Seymour E F W, Styles G A and Sholl C A, J Less-Common Metals, **118**,201-215,(1986).
2.44 Sholl C A, J Less-Common Metals, **129**,335-343,(1987).
2.45 Korringa J, Physica, **16**, 601,(1950).
2.46 Narath J, J Appl Phys, **41**, 1122,(1970).
2.47 Narath A; in Hyperfine Interactions, edited by Freeman A J and Frankel R B, New York, Academic Press, 1967.
2.48 Narath J, Phys. Rev, **162**,320,(1967).
2.49 Fradin F Y, Phys Lett, **28A**, 441-2,(1968).
2.50 Seymour E F W and Sholl C A, J Phys Condensed Matter, **1**, 8529, (1989).
2.51 Squires G.L., Introduction to Thermal Neutron Scattering, CUP, 1978.
2.52 Lovesey S.W., Theory of Neutron Scattering from Condensed Matter, OUP, 1984.
2.53 Springer T., Hydrogen in Metals 1, Editors Alefeld G. and Volkl J., Springer-Verlag, 1978, p75-98.
2.54 Skold V.,Hydrogen in Metals 1, Editors Alefeld G. and Volkl J., Springer-Verlag, 1978, p267-286.
2.55 Springer T. and Richter D., Methods in Experimental Physics 23B, Neutron Scattering, Editors Price D.L. and Skold K., Academic Press, 1987.
2.56 Ross D.K., Z. Phys. Chem. N.F. **164**(1989)897-906.
2.57 Van Hove L., Phys. Rev. **95**(1954)249.
2.58 Rowe J.M., Rush J.J., de Graf L.A. and Ferguson G.A., Phys. Rev. Lett.**29**(1972)1250.
2.59 Chudley C.T. and Elliott R.J., Proc. Phys. Soc. **77**(1961)353.
2.60 Skold K. and Nellin G., J. Phys. Chem. Sol. **119**(1960)863.
2.61 Blaesser G. and Peretti J., Proc. Int . Conf. Vacancies and Interstitials in Metals, KFA Julich, **2**(1968)836.
2.62 Rowe J.M., Skold K., Flotow H.E. and Rush J.J., J. Phys. Chem. Sol. **32**(1971)41.
2.63 Lottner V., Heim A. and Springer T., Z. Phys. B. **32**(1979)157.
2.64 Faux D A, J Phys : Condens Matter, **3**,2201-2205,(1991).

Figure 2.1a is a schematic representation of the vector model which shows that an ensemble of spins with magnetic moments μ precess about B_o to produce a net magnetisation M_o. Applying a field B_1 with angular frequency ω_o, seen here in the rotating frame x' and y', causes the magnetisation to precess about B_1.

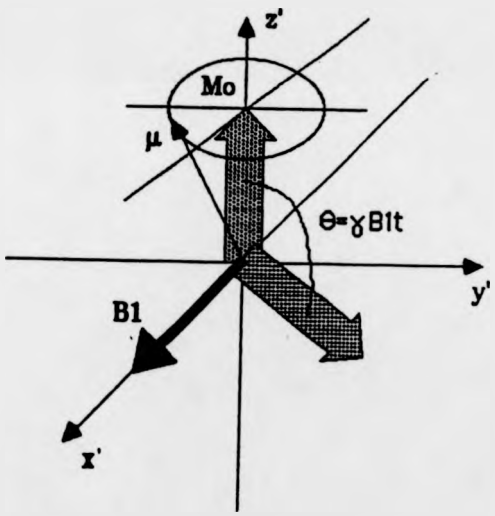

Figure 2.1b shows a 180°-τ-90° pulse sequence for three τ, τ'>τ">τ"'. $M_z=M_0$ before the 180° pulse is applied, and after the pulse the z magnetisation then recovers according to equation 2.4 (as shown by the light shaded arrow). M_z is detected by applying a 90° pulse thus putting it in the plane of the coil.

Figure 2.1c shows a graph of magnetisation recovery against time for the 180°-τ-90° sequence shown in part b.

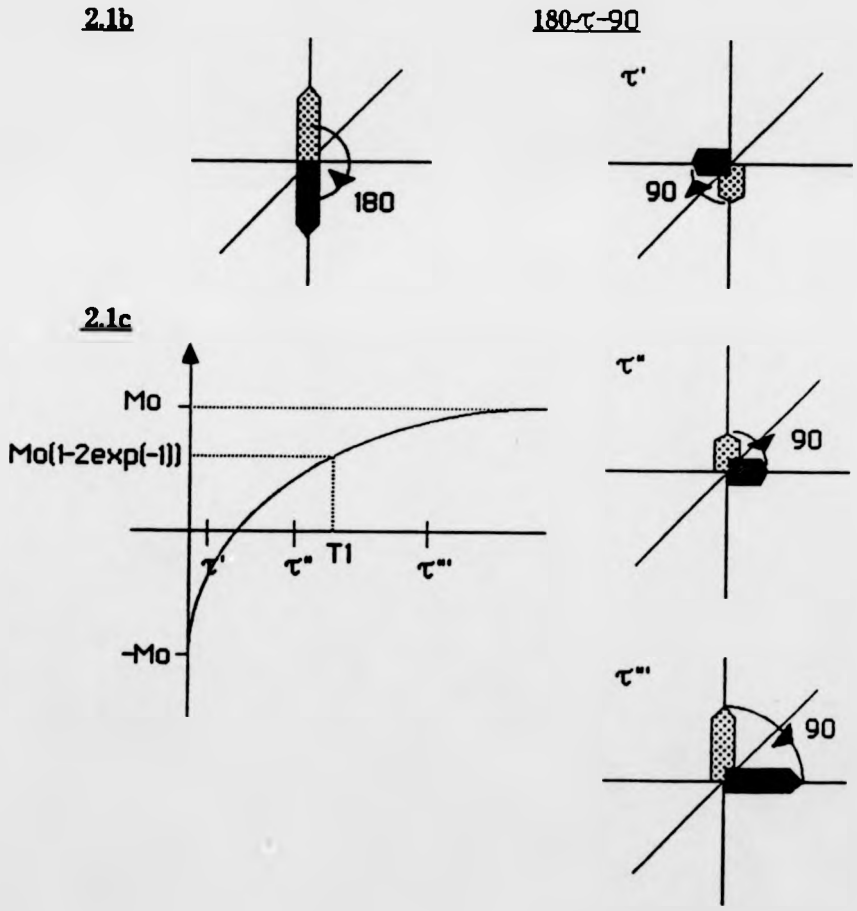

Figure 2.2 A schematic diagram of the spectral spectral density versus frequency. The functional dependence is Lorentzian, as expressed in equation 2.13, distorted here by the logarithmic scale. The curves represent decreasing correlation time of the interaction from left to right, in other words increasing temperature due to the Arrhenius relation since $\tau_c \propto \tau_d$.

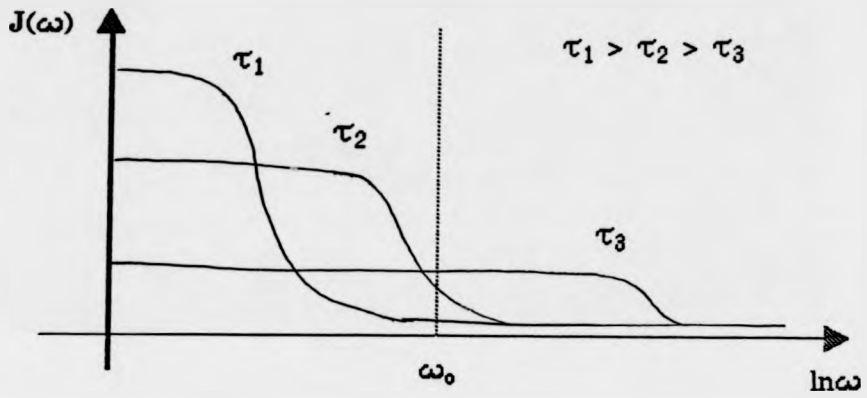

Figure 2.3 A schematic representation of the relaxation times, measured at fixed ω_0, versus τ for the dipole-dipole interaction described by the BPP model. Figure 2.2 shows that a minimum in T_1 is generated when $\omega_0\tau_c \approx 1$. Also shown is the increase in T_2 above the rigid lattice value for decreasing τ.

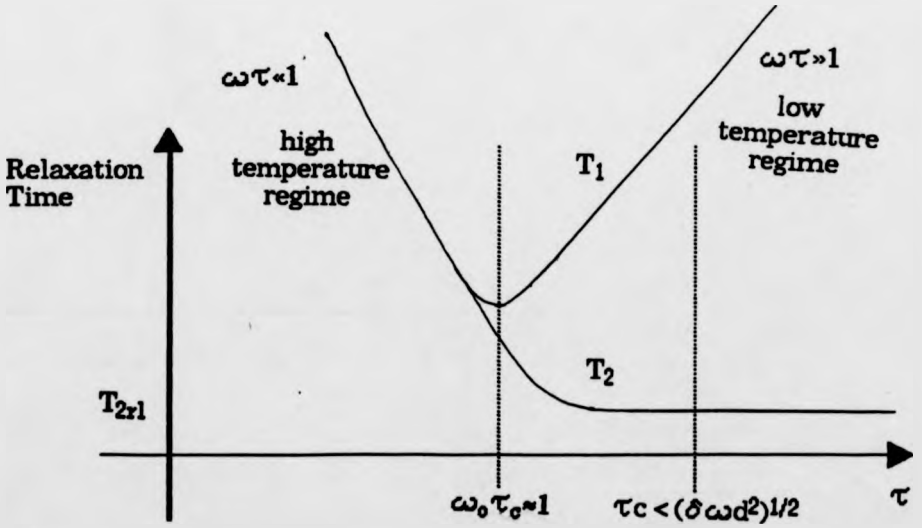

Figure 2.4 The T_1 orientational dependence is shown here for fcc, bcc and sc lattices. These results are derived using equation 2.28 and the mean field results of Barton and Sholl [2.28].

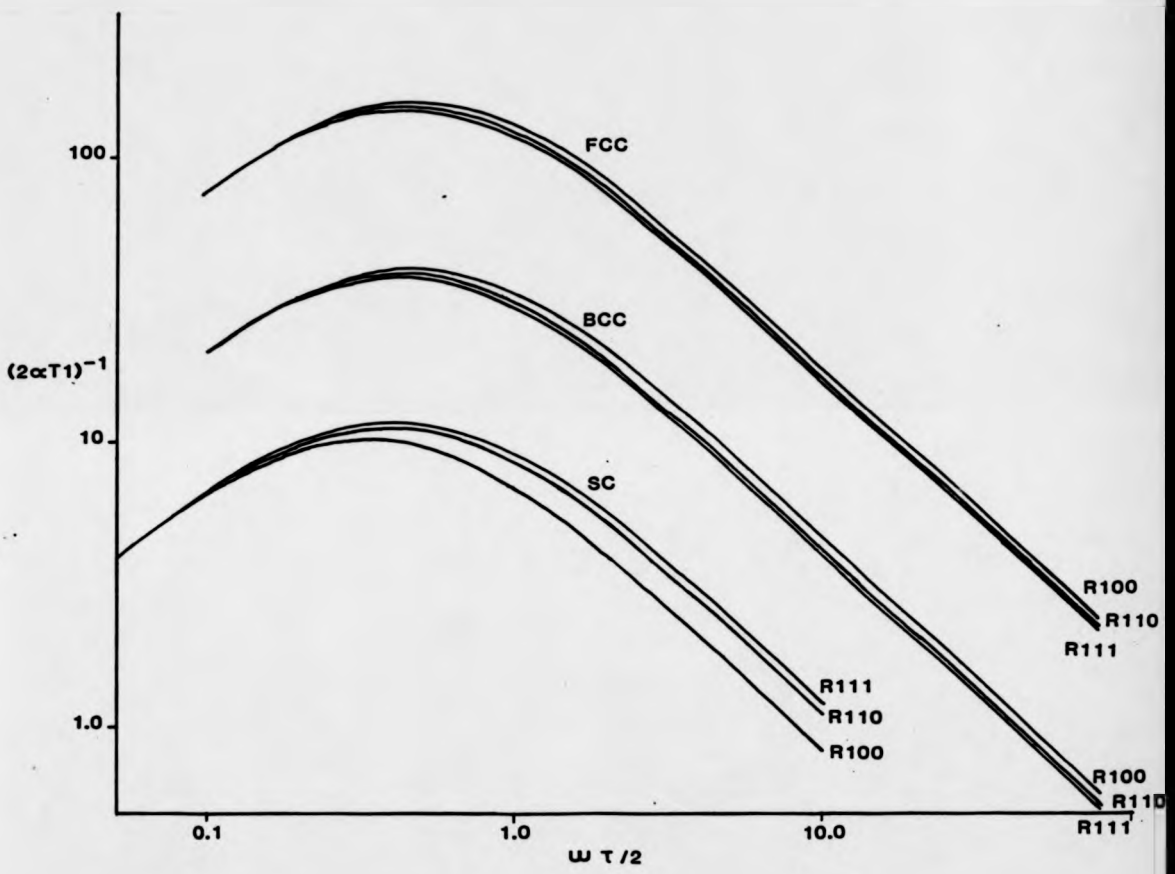

Figure 2.5 The dependence of T_1 on $\omega\tau$ in a hexagonal system for different diffusion models (u=3, 0, -1) and c/a ratio (c/a=1.2, 0.8), after Sholl [2.44]. The upper set of lines are for c/a = 0.8, and the models are represented by

_____ u=0, ____ ____ ____ ____ u=-3, and __ __ __ __ u=1.

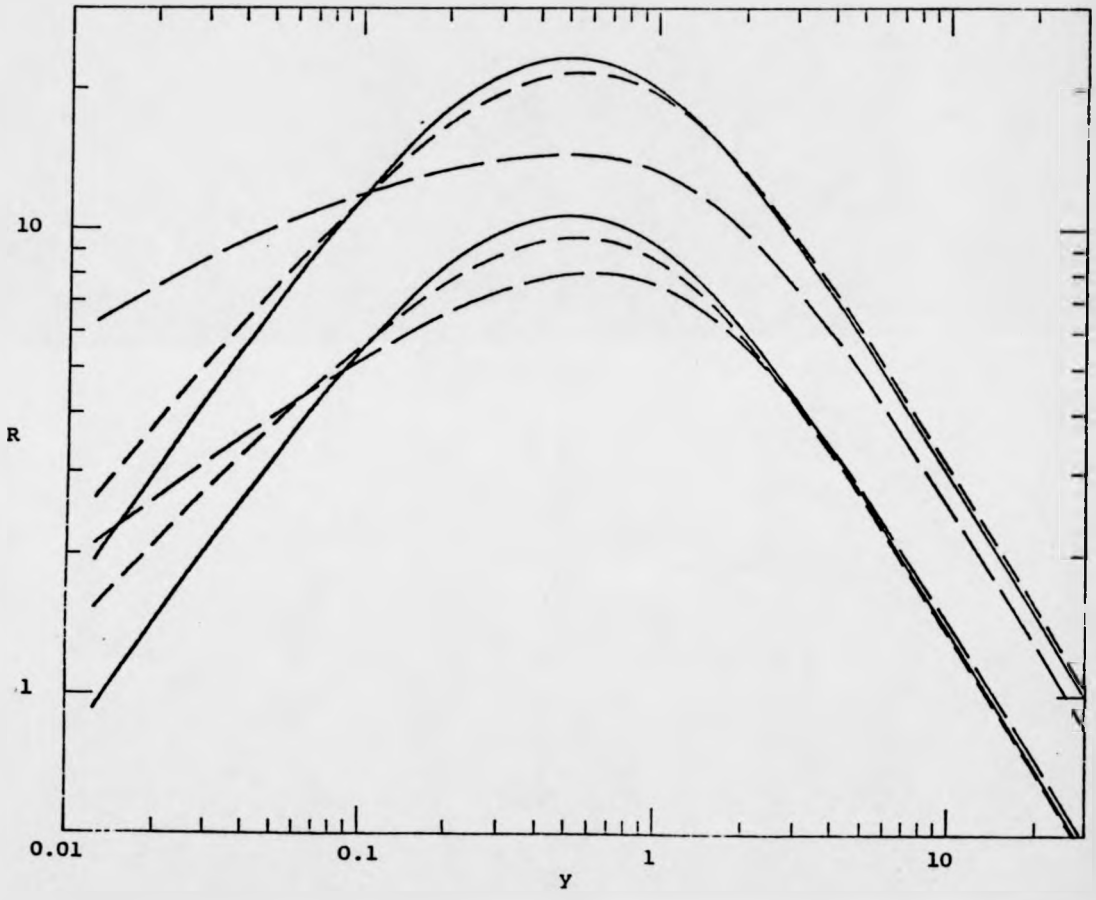

Figure 2.6 A simple representation of a neutron scattering event which can be described by the cosine rule given in equation 2.39.

Figure 2.7 A schematic representation to show the partial differential scattering cross-section which is defined in equations 2.40 & 41.

Figure 2.8 A sketch of a quasielastic lineshape generated by the diffusing particles. It is Lorentzian in shape as expressed by equation 2.49.

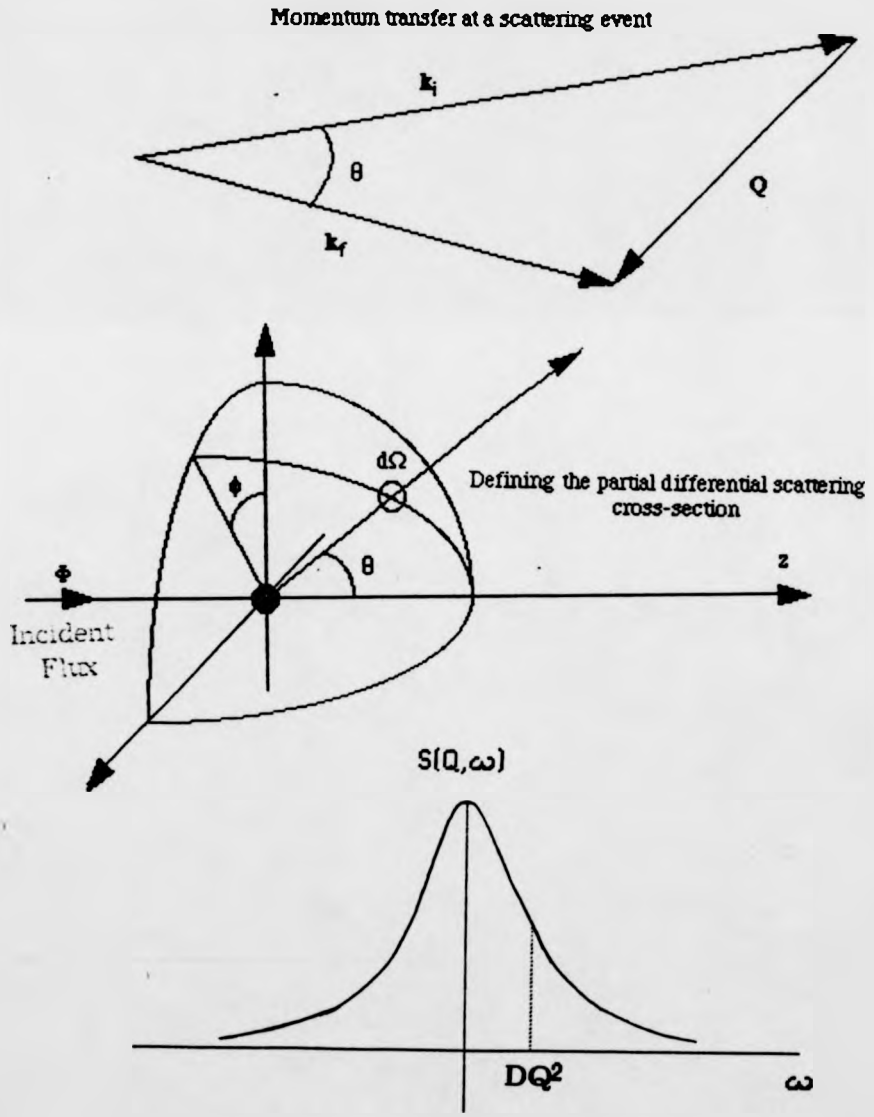

Figure 2.9 The theoretical results from a qns experiment, as represented by equation 2.49, where E_{FWHM} is plotted against Q^2 in (a), whilst in (b) $S(Q,\omega)$ is shown, in this figure D =2 x 10^{-5} cm^2s^{-1}. Adapted from Squires [2.51].

Figure 2.10 The qns peak width for random diffusion on an fcc lattice at different crystallographic directions and for two jump models: (a) T-T site and (b) O-O site jumps only. Adapted from Squires [2.51].

2.9

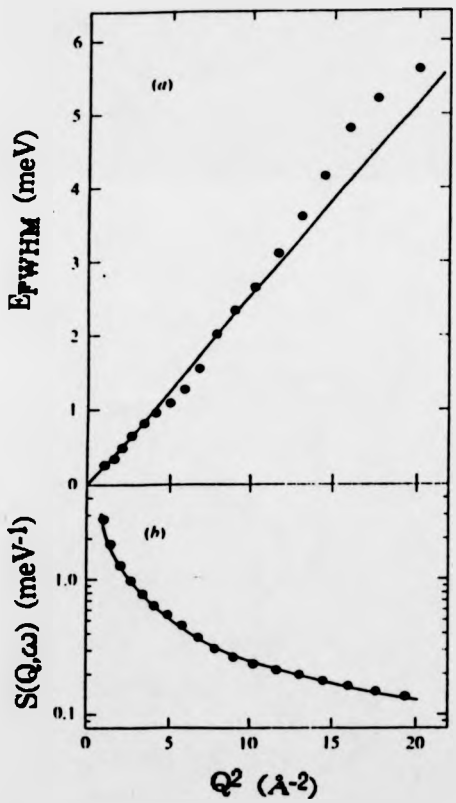

2.10

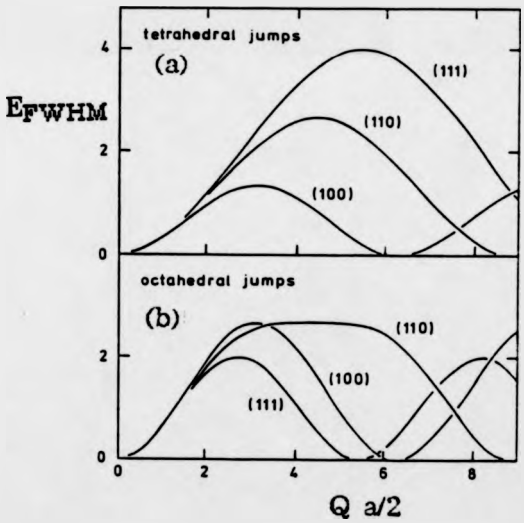

Chapter Three
Experimental Techniques and Apparatus

3.1 NMR Instrumentation and Operation

The pulsed nmr spectrometer used for this work is described below in terms of its principal components as shown in the block diagram in figure 3.1. The spectrometer is interfaced with various peripheral devices for data acquisition and processing. The equipment has been used principally to determine two nmr parameters, T_1 and the Knight shift, as a function of temperature and/or crystal orientation with respect to the static field B_o. Unless otherwise stated the equipment used was built at the Physics Department, University of Warwick.

3.1.1 The Pulsed NMR Spectrometer

The spectrometer can be regarded as six distinct units; an rf generator section, a pulse programmer, a transmitter, a probe, a receiver and an electromagnet.

RF Generator

The oscillator unit contains seven different tuned crystal circuits which generate continuous rf of $1V_{pp}$ amplitude at frequencies of 4.8, 9.8, 14.8, 19.8, 29.8, 39.8 and 49.8 MHz. The highest frequency was changed at a late stage during this work to 47.0 MHz in order to avoid interference problems. The selected frequency is channelled to 4 output ports; two going to the phase shifters, a third to the phase sensitive detector in the receiver and the other can be used as a reference. The phase shifters are independently variable and introduce a time delay which allows a phase change over several cycles of the rf. The continuous rf from the phase shifters then enter two gates which generate pulses of variable width and separation from each channel. This depends on the effective open and close commands generated by the pulse programmer unit. The gate outputs are merged by the combiner before amplification in the transmitter unit.

Pulse Programmer

The unit is based on the design of Conway and Cotts [3.1] and is capable of producing up to four independent pulse trains. The programmer consists of a 10MHz clock module and up to four channel modules together with an auto-increment module based on the design of Adduci et al [3.2].

The main clock determines how often a pulse sequence is repeated, this repetition period being variable between 1μs and 999s. Each module takes its time base from the 10MHz clock and generates an output pulse, of variable width between approximately 500ns and a few seconds, which is used to open the rf gate. A start pulse for each module which initiates that module's pulse train can be taken from the main clock, the previous module or the auto-increment module. Each module can generate either a single pulse or a cycle of pulses at a fixed interval. The output start pulse from each module can be generated a preset time after each input start pulse or after each pulse in the train from that module. Trigger pulses are available for starting oscilloscope sweeps or gating a signal averager with preset delays after each channel's output pulse. The auto-increment module takes its start pulse from the first pulse module and waits a fixed initial time t_i before generating a start pulse for a second module. subsequent pulses are delayed t_i+t_{inc}, t_i+2t_{inc}, t_i+3t_{inc} and so on until a preset final interval t_f is reached. The auto-increment module then resets its delay to t_i before repeating the sequence.

Transmitter

The rf pulses generated by the pulse programmer are amplified in three separate stages. The first stage is a Power Labs. Inc. 110MHz wideband rf amplifier which produces a pulse of amplitude approximately $50V_{pp}$. This is followed by the intermediate power amplifier which generates an output pulse of amplitude $140V_{pp}$ which is subsequently fed to the higher power amplifier. This unit has a stabilised power supply with a maximum output of 3kV. Both intermediate and high power units are tuned to the operation frequency by inserting ready made plug-ins. The output from each unit can then be optimised by adjusting continuously variable controls. The final optimum output is of the order of $500V_{pp}$. Each unit has input and output impedances of 50Ω.

Probe

The probe is connected to the transmitter via 50Ω transmission lines where the length of line from probe to receiver is $\lambda/4$ (or $3\lambda/4$ at high frequencies), as shown in figure 3.2. These lengths were determined using a Hewlett Packard 4193A Vector Impedance meter. Two sets of fast switching crossed diodes are incorporated in the circuit, these have a low impedance at high voltage and thus the rf pulse passes the series diodes to

the matching circuit whilst the parallel diodes prevent the rf pulse entering the receiver and present a high impedance to the probe through the transformer action of the $\lambda/4$ cable. After the pulse the series diodes present a large impedance, isolating the transmitter, and the small signal voltage (less than millivolts) is seen at the receiver. The probe circuit and receiver input are both matched to 50Ω. The crossed diodes should be made of four or more pairs in order to reduce the impedance in the conducting state. The coil used is specifically made for each single crystal sample at any one frequency, it is an essential element in optimising the signal. A study by Stakelon and Follstadt [3.3] showed that the largest signal that could be obtained from a conducting crystal sample was about $1/10^{th}$ that from its powdered form. The problem is caused by the skin depth effect which reduces the effect volume of sample irradiated and reduces the Q factor of the coil. In order to achieve reasonable intensities it is necessary to separate the coil and crystal by an insulating sheet of about 25μm thick, typically a coil of some 30 turns of 30 gauge wire can be used. The matching circuit is either tapped parallel-tuned for low frequencies or a tapped series-tuned circuit for high frequencies (ν>20MHz) [3.4], see figure 3.2 part a and b respectively. The variable capacitors were either laboratory-made concentric cylinder type of 5-85pF, or Jackson 21 vane 5-79pF, all with a high voltage rating of 2kV. These circuits require a sample coil of the order of 1μH inductance. The circuit is tuned and matched using a Wavetek 1060 sweep/signal generator and a hybrid tee. Typically a 90° pulse was between 1 and 2μs using this probe arrangement to study single crystals.

Receiver

The receiver consists of a pre-amplifier with a gain of 6dB followed by a series of tuned LC filters and broadband limiting amplifiers, each with a gain of 21dB, a phase sensitive detector and final video amplifier stage, figure 3.3. The filters are discrete units which are changed to match the operational frequency whilst the limiting amplifiers are broadband, 1-100MHz, with an output limit of $0.5V_{pp}$. The video amplifier has an incrementally adjustable bandwidth from 19kHz to 1.3MHz and a similarly adjustable gain between 3 and 53dB. An essential DC offset control is a final feature of the video amplifier, the range of control being dependent on gain setting. A blanking circuit in the receiver allows the output signal to be blanked for between 0 and 3μs after a separate input pulse which is generally taken from of the module trigger outputs. Thus ringdown from

both receiver and probe could be 'blanked' from the receiver output. Ringdown is generally of the order of 10-15μs after a 1-2μs rf pulse (dependent on frequency).

Magnet

The magnetic field was generated by a Varian 15" electromagnet with a pole gap of 1 3/4", it has a maximum field capability of approximately 2.5T which is stabilised using a Fieldial control unit to 1ppm. The field can be swept up or down at various rates and over various ranges.

3.1.2 Temperature Control

A system of temperature control enables stable sample temperatures between 77K and ambient room temperature to be achieved. The device is a liquid nitrogen bubble pump based on the design of Norris and Strange [3.5] and is shown in figure 3.4.

The system comprises a 25l Dewar storage vessel which pumps liquid nitrogen to a smaller intermediate Dewar flask. This pumping is achieved by sealing the Dewar and heating the liquid with a 40W coil element thus forcing the liquid through the feed pipe. A diode, which forms part of a feedback circuit with the control unit, is placed at a predetermined height in the intermediate Dewar such that when the required level of nitrogen is reached in the smaller Dewar the heating element is turned off and a two-way gas valve is opened releasing the nitrogen vapour pressure in the large Dewar. A second heating element in the smaller Dewar is used to bubble liquid nitrogen via a copper tube onto the splash plate above the sample which is shown in figure 3.5. This is achieved by pulsing the heating element on and off, the precise power setting and mark space ratio of these pulses has been found to be critical in order to achieve stable sample temperatures, both are variable and set on the control unit. Also critical are the level of the head of nitrogen in the middle Dewar and the length of piping between it and the splash plate.

The sample temperature is monitored using a T1/T2 alloy thermocouple which is placed under the surface of the splash plate and forms part of a second feedback circuit in the temperature control unit. This operates a sample on/off control; when the temperature is above the preset value the current to the intermediate Dewar heating element is pulsed on and off, when the temperature goes below the current is completely turned off.

This system is capable of achieving sample temperature stabilities of ±0.5K, this is monitored separately using a copper-constantan thermocouple placed above the sample. The sample cavity is filled with hydrogen vapour, fed from an external bladder, which prevents oxidation of the sample and condensation of water within the cavity.

The low temperature sample probe is placed in a cylindrical Dewar between the magnet poles. It is rigidly connected to the matching box, which is suspended from aluminium rails above the magnet. The matching circuit is contained within a cylindrical copper box which rests on an aluminium plate, this is marked in one degree of arc intervals enabling the entire probe to be accurately rotated in small increments through a full 360°.

3.1.3 Data Acquisition and Processing

Two nmr parameters have been measured using the above equipment. The techniques used in acquiring and processing the data are described here.

3.1.3 a Knight Shift Measurements

The spectrometer has been adapted to enable lineshape and Knight shift studies using a simple 90°-τ pulse sequence. In the experiment ω_o is held constant whilst the B field is ramped through a predetermined range dB_o centered on B_o, in a time dt as shown in figure 3.6. A 90° pulse rotates the magnetisation into the plane of the coil which generates a free induction decay (FID) signal as the magnetisation in the x-y plane dephases. The characteristic time for this dephasing is called T_2^* which results from both spin-spin relaxation and dephasing due to field inhomogeneity across the sample. The FID signal is integrated using a Princeton Applied Research boxcar integrator, the gatewidth τ_g of which is generally set to about $3T_2^*$ to prevent lineshape distortion. The integrator output is fed into the BBC microcomputer which is used to initialise B sweeps as well as record data by using the program FISWEEP [3.6]. The BBC generates a pulse which starts the magnet ramp, however dB and dt are set using the Fieldial unit itself. The B_1 pulse of 90° is used to maximise signal and consequently a delay of about $5T_1$ is left between pulses. The experiment is further optimised by setting the integrator time constant τ_{rc} according to the following expression

$$\tau_{rc} = \partial B \tau_g dt / 5 dB\tau \qquad (3.1)$$

where ∂B is the lineshape full width at half maximum. Finally the lineshape data can be transferred to a mainframe for linefitting, the program used is based on a fitting algorithm given by Bevington [3.7].

3.1.3b T_1 Measurements

T_1 measurements were made using a standard 180°-τ-90° pulse sequence or inversion recovery method [3.8] which gives the maximum possible dynamic range of magnetization signal and hence, in principle, gives the greatest accuracy in T_1. The experiment is performed using the spectrometer previously described together with other peripheral units which are interfaced as shown in figure 3.7. The pulse repetition period, τ_{rp}, is set on the main clock of the pulse programmer which generates a short pulse for channel module 1. Module 1 is set to generate a 180° pulse each time this occurs and also activates the auto-increment module. The auto-increment module operate as previously described and triggers a start pulse from module 1 which is used to activate module 2 which generates a 90° pulse.

The fast boxcar integrator [3.6] integrates the FID signal from the receiver following the 90° pulse and is thus triggered from module 2. The integrator has a continuously variable gatewidth and a discretely variable time constant between 1μs and 100ms. To obtain a linear response over all signal inputs the integrator output voltage should be made approximately equal to the input voltage. This can generally be achieved by making the gatewidth and time constant roughly equal and normally of the order of T_2^*. The integrator signal is sent to the Transiac 2108 signal averager, which has a maximum input of ±0.25V. An address advance pulse from the integrator to the averager occurs during the output signal. The averager then reads the signal and finally an internal reset trigger sets the integrator output to zero ready to sample the next FID. The averager is interfaced to a BBC microcomputer via a digital interface which allows all the averager operating parameters to be set from the microcomputer, for greater details see [3.9]. This information is input to the BBC using a user-friendly program called AUTOT1 [3.6]. When averaging is complete the data stored in the averager is transferred to the microcomputer through the digital interface. The data may then be analyzed using a fitting program called T1FIT. This uses a least squares fitting procedure based

on an algorithm described by Bevington [3.7]. The form of the magnetization recovery is assumed to be

$$Y=Y_s+M_o(1-2\exp(-\tau/T_1)) \qquad (3.2)$$

where Y_s is a dc offset and Y_s, M_o and T_1 are evaluated in the fitting procedure.

3.2 Neutron Scattering Instrumentation and Operation

A study of some metal-hydrogen systems using neutron scattering techniques was performed at the Institute Laue Langevin (ILL), Grenoble, France, on the time-of-flight (tof) spectrometers IN6 and IN10. In this section the Laue requirements of tof spectrometry are described and the specifications and operation of the above instruments are outlined. Details are also given of sample containment and data analysis methods.

3.2.1 Time-of-Flight Spectrometry

The principle of tof measurement is simply that the energy of a scattered neutron is determined by timing its flight over a known distance after scattering from a sample and thus calculating its velocity. In order to do this one requires a narrow monochromatic pulse of neutrons, each pulse being separated by a finite time interval τ much greater than the width of the pulse itself. This is essential in order to identify a detected neutron at a specific time and angle with a known incident pulse and thus determine whether this neutron gained or lost energy with respect to the incident beam energy E_o. Each set of detector counts are therefore clocked with respect to the incident pulse, and the length of time τ before the next incident pulse sets a limit on the maximum energy loss which can be observed before slow neutrons from one pulse overlap fast, high energy gain, neutrons from the next.

The ILL ^{235}U reactor operates at 57MW producing continuous thermal neutrons which are moderated using cold liquid deuterium or hot graphite sources. The beam can be monochromated using specific Bragg reflections from single crystals and subsequently pulsed using rotating choppers. Both tof spectrometers used are on the same neutron guide H15 from the ILL reactor cold source. H15 has a peak wavelength of approximately 4Å and a flux of 2×10^{19} n $cm^{-2}s^{-1}$ [3.10].

3.2.1 a Time-of-Flight Spectrometer IN6

The IN6 instrument specifications are outlined in table 3.1 and a schematic diagram is given in figure 3.8 which shows all the principal features described here [3.11]. The neutron beam is initially monochromated using three pyrolytic graphite assemblies which may be rotated to select accurately, repeatable wavelengths of 4.1, 4.7, 5.1 and 5.9Å. The spectrometer itself must also be rotated on guide rails to maintain alignment with the neutron beam. A beam shutter made of lead and boron carbide plugs is operated pneumatically in order to close off the beam, for example when changing sample. The beam is somewhat divergent from the monochromators but the divergence can be controlled using the diaphragms, the beam is then filtered using cooled Be which only transmits wavelengths greater than 4Å. The beam is collimated before passing through the two stage choppers, the suppressor and Fermi chopper. The latter is a rotating collimator used to start the basic timing signal for the detection process. The suppressor chopper is either left open or rotated at a slower speed than the Fermi chopper in order to increase the time delay between pulses. The beam then passes through monitor 1 which is a thin, low efficiency detector used to monitor the neutron flux before the beam enters the sample box. The pulsed beam passes through a defining mask and then strikes the sample which can be mounted in either a furnace or a cryostat. The box itself is evacuated and then filled with He gas to reduce scattering. Similarly the flight path to the bank of detectors is through an aluminium box filled with He. There are three rows of detectors which are curved in order to maintain a constant distance from the sample, these are filled with ^{3}He to high pressure. A pair of monitors is used to gauge the neutron beam flux on the far side of the sample. This data can be used to calculate the sample transmission coefficients which are useful, for example, to check sample properties after changing temperature.

Control of the spectrometer is extensively automated and user-friendly operational software exists on its DEC-PDP11 computer. This enables control of the electronics which handle data acquisition and storage and monitor the experiment. Whilst this control is operated as a foreground priority program, it is possible to run a background program on a second terminal enabling data inspection of current or previous runs together with some processing and comparison between data files.

Table 3.1	IN6	IN10
Beam-tube	H15	H15
Beam size at sample	3x5 cm^2	3.5x3.5 cm^2
Flux at sample	$8.9x10^4$ n $cm^{-2}s^{-1}$	$\approx 10^4$ n $cm^{-2}s^{-1}$
Wavelength λ (Å)	4.1, 4.6, 5.1, 5.9	3.27, 4.33, 6.28, 6.31, 6.53
Monochromator	Composite vertically focussed pyrolitic graphite	Various, including Si(111),Si(311),Ge(111)
Elastic energy resolution, FWHM	170μeV at 4.1Å, 50μeV at 5.9Å	≈1μeV depending on frequency
Background	0.51 counts s^{-1}	$4 - 28x10^{-3}$ counts s^{-1}
Detectors	337 elliptical ^3He	8 ^3He detectors

3.2.1 b The Backscattering Spectrometer 1N10

This spectrometer differs from 1N6 in that the scattered neutrons are backscattered by analyser crystals which gives rise to greater energy resolution, of the order of 1μeV. The instrument specifications are given in table 3.1 and a schematic diagram of its main components is shown in figure 3.9 [3.12].

The upper quarter of the neutron beam from H15 is used on IN10, this portion is guided to the monochromator mounted on a velocity drive. The beam is backscattered and reflected off an orientated graphite crystal toward the sample where about 40% of the backscattered beam remains. The neutrons pass through a chopper, which acts as the timing source for the synchronisation of the system, then through a flux monitor before entering the analyser chamber. The beam then reaches the sample which, similar to IN6, can be mounted in either a furnace or a cryostat. Each of the six analysers is an array of hexagonal single-crystal silicon slices, 0.5mm thick by 20mm diameter, with either (111) or (311) planes oriented perpendicular to the surface face. The slices are glued to the inner surface of a hollowed spherical aluminium plate with a radius of curvature of 1.5m and surface area of 50x50 cm^2. The analysers are aligned such that the neutrons are backscattered to six ^3He detectors near the sample. The analyser chamber is filled with He gas and is entirely shielded with 1mm Cd, 4mm boron carbide and 15cm of paraffin. The

instrument electronics are controlled using a PDP11 computer which offers a foreground and background inspection program mode.

3.2.2 Sample Containment

As discussed later it has been suggested that a number of possible experimental deficiencies may have led to the apparent high temperature nmr anomaly in some systems. These had to be eliminated as far as possible in the neutron work if it is to help determine the true nature of the hydrogen diffusion in these systems. Firstly it is important that on heating the sample, up to 1000°C in the case of YH_2, one ensures that there is no hydrogen loss through the vessel walls. Secondly there must be no other gaseous impurities present in the sample cell which might diffuse into the sample thus affecting hydrogen mobility. It is also desirable that the sample cell design should maximise the neutron beam cross-section used and in order to avoid the problem of multiple scattering, which would complicate data analysis, the total transmission coefficient should be about 80-90%. The coefficient can be estimated by assuming that the transmitted intensity is

$$I=I_o\exp(-dn\sigma) \qquad \{3.3\}$$

where d is the sample thickness, n is the number of nuclei per unit volume and σ is the average nuclear cross-section. The cell walls must also be sufficiently thin to avoid a significant contribution to the scattered neutron intensity while at the same time thick enough to prevent hydrogen loss from the sample. With these criteria in mind stainless steel cells of varying dimensions, depending on the spectrometer to be used and sample to be studied, were designed as shown in figure 3.10. For example the sample cavity might be 40mm by 40mm and 1-2mm thick (a, b and d respectively in figure 3.10). A device for loading and sealing the cell in an inert atmosphere is also shown in figure 3.11, its operation is described below.

The powder samples were made from very high purity material by the Ames Laboratory and were sealed in quartz tubes under a partial atmosphere of inert gas. These tubes were opened in an inert atmosphere, inside a glove bag, and the powder poured into the cell until it was completely full, thus reducing possible contamination from gaseous impurities and moisture. A very fine mesh steel gauge is placed over the top of the sample to prevent loss of the powder when the cell is evacuated.

The upper conflat is then secured to the lower half with an intervening copper o-ring, the top bolt and a second copper o-ring are screwed into place, but left loose so that the cell can be evacuated. The cell is placed inside the sealing device where it is held rigidly by support rods and the sealing device lid is placed in position. One must ensure that a good rubber o-ring seal is made and the sample cell sealing bolt is held correctly. This unit is removed from the glove bag and pumped down to a partial vacuum of the order of 0.1mbar. Transfer of the cannister from the glove bag to vacuum pump can be achieved by attaching rubber piping to the nozzle and clamping this so that the inert atmosphere remain within the cannister and cell. The sample cell is closed by rotating the sealing device lid several times until a very firm seal is made by the bolt and copper o-ring at the top of the cell. The cell can then be removed and attached to the furnace mounting where generally several thermocouples are placed in contact with its surface to ensure accurate thermometry during the neutron experiment.

3.2.3 Data Analysis

An extensive range of data correction and fitting programs exist at the ILL, some of which have been used in this work and are briefly described here. The aim of correcting raw data is to subtract neutron counts due to scattering from parts of the apparatus other than the sample, background noise is also removed and corrections are made for instrumental effects such as differing individual detector efficiencies. These operations are necessary to obtain a true value for the scattering function $S(\mathbf{Q},\omega)$. This is particularly important in qns and inelastic neutron scattering time-of-flight experiments where it is desirable to map $S(\mathbf{Q},\omega)$ over a large range of $\mathbf{Q}$

Data analysis on IN6 was carried out using two programs, Prime and CrossX [3.12], on the Dec10 computer. The purpose of Prime is to take the raw data set from the instrument and convert numbers of counts at the different detectors into a neutron intensity as a function of $\mathbf{Q}$ and ω calculated from detector angles and comparison of elastic peak positions in the monitor with those in the detectors. The program initially allows adjustment of the header settings, the header contains values for all experimental parameters such as incident wavelength and detector angles, before offering options such as raw data printout or the data evaluations just described. The option 'Monitor peak analysis and

vanadium peak evaluation' uses the monitor spectrum to find the flat background adjacent to the peak and a vanadium spectrum file, which is taken as a standard, is compared with a calibration vanadium spectrum measured on the instrument at a similar time to the sample data. The latter operation thus corrects changes in detector efficiency. The moments of the data peak and its central position may then be determined. Basically this is a calibration of the instrument preparing the data for evaluation using CrossX.

CrossX calculates the absolute cross-section by comparison with the standard vanadium specimen. The program requests the required analysis and such measured parameters as sample transmission coefficient, temperature and mass before performing computation which is based on algorithms devised by S. J. Cocking [3.14].

Analysis and fitting of IN10 data was performed on the DEC10 computer using the program ESFIT [3.15]. The data was prepared for analysis using the program 10PDP, similar in function to Prime, and ESFIT run using a command file program. The basic function of ESFIT is to take the crudely calibrated data and fit the elastic peak and quasielastic peak or peaks for given scattering angles. The elastic peak is taken as a delta function and the form of the qns line, being model dependent, can be input by the operator. A single Lorentzian is assumed for the qns lineshape in our analysis (justified by the high transmission coefficient of the samples) such that the scattering function $S(\mathbf{Q},\omega)$ is determined through its to proportionality to

$$P_5\exp(-\hbar\omega/kT)\{[P_8 f(Q_o)A_1(Q)]\partial(\omega-P_4-\mathrm{exc}(Q_o))+ \frac{1-P_8 f(Q_o)A_1(Q)}{1-A_1(Q)}\sum_{i=1}^{N}A_i(Q)L(\tau_i,\omega-P_4-\mathrm{exc}(Q_o))\}+P_6 \qquad \{3.4\}$$

where the P_n are user variable parameters. They are given an initial value and varied in an iterative process by the computer until a minimum error between fit and data is found or until a specified number of iterations have been completed. In {3.4} P_4 is used to shift the origin of spectra (zero of the energy transfer) which assumes the vanadium spectrum is perfectly centred at $\hbar\omega_o$, P_5 is an amplitude scale factor, P_6 is an energy independent background term, P_7 is a Q dependent background factor, P_8 is a weighting factor of the amount of purely elastic scattering in the data and P_9 is the ratio of fixed protons to the total number of protons. Note also

that $\exp(-\hbar\omega/kT)$ is the detailed balance correction factor whilst $exc(Q_0)$ and $f(Q)$ are respectively the energy shift correction and elastic incoherent structure factor for the spectrum considered. The least-squares fitting procedure is re-run until the user is satisfied by the goodness of fit and the data can finally be transferred or displayed to or on various storage or printing facilities. A more complete description of the above is given in reference [3.15].

3.3 Sample Preparation

Several methods exist for the preparation of metal-hydrogen systems including electrolytic doping, chemical reaction or gaseous doping, each being particularly suited to different applications. In the present study the aim was to make single crystal samples with relatively high hydrogen concentrations, as in the case of β-NbH_x for example. for which gaseous doping is appropriate. In this section only the apparatus and general procedure are described, the precise details such as etchants used in preparing an individual sample are given in the relevant section of chapter 4. All samples used in the nmr study were made at Warwick from high purity metal crystals whilst the neutron scattering samples were prepared by the Ames Laboratory by similar methods to those described here. The hydriding equipment is shown in figure 3.12 and is mainly made of copper pipe with rubber o-ring connectors and a Ti sponge was used as a reservoir for the hydrogen.

Before hydriding it is necessary to define the orientation of the crystal. This was done using the back-reflection Laue technique on a Philips PW1008/85 x-ray diffractometer using either a copper or molybdenum source, the x-ray pattern also reveals the quality of the crystal. The crystal's orientation is marked on the end surface after x-raying. The crystals are then etched using specific acid solutions to remove any surface oxide layer. After rinsing and weighing, the sample is generally placed in a quartz crucible which is loaded into the hydriding apparatus, which is pumped down to a pressure of the order of 10^{-6} mbar. The sample is then degassed by heating to around 1000°C and again reaching an equilibrium pressure of $\approx 10^{-6}$ mbar. Several cycles of degassing were sometimes performed. The sample is now ready for hydriding which is done using a volumetric method where the calibrated volume shown in figure 3.12 is loaded to a predetermined pressure of hydrogen. This pressure is generally such that the number of moles of hydrogen give the

desired MeH_x composition on completion of the hydriding process when no hydrogen gas remains. The hydrogen is obtained by heating the Ti sponge and the hydrogen produced is better than 99.9% pure. The sponge is held in refractory material such as silica tubing. The sample, at the required temperature, is then exposed to the hydrogen atmosphere. In order to calculate the volume and pressure of gas used and the temperature range to hydride it, it is essential to know the PCT characteristics of the sample. Generally a dummy run using a powder or polycrystalline sample is made before hydriding the single crystal. Since all the samples used react exothermically with hydrogen the temperature is gradually lowered until all the hydrogen is absorbed. This process can take days and sometimes repeated cycling was necessary in order to achieve the desired concentration. The hydrided sample was removed and reweighed to check on the amount of hydrogen absorbed. Further x-ray study also gave a check on the nature of the crystal sample prepared and by calculating the lattice parameter, from copper K Bragg spots, a third estimate of the hydrogen content is achieved. In general all estimates of concentration were found to be in satisfactory agreement with one another.

References

3.1 Conway J L and Cotts R M, Rev Sci Instrum. **48** 656-660.(1977).

3.2 Adduci D J, Hornung P A and Torgeson D R, Rev Sci Instrum, **47** 1503(1976).

3.3 Stakelon T S and Falstaedt D M, Rev Sci Instrum, **49** 45-49, (1978).

3.4 Murphy P D and Gerstein B C, Analysis and Computerised Design of NMR Probe Circuits, Ames Laboratory DOE, Iowa State University, 1978.

3.5 Norrris M O and Strange J H, J Sci Instrum, **2** 1106-1108, 1981.

3.6 Barnfather K.J., MSc thesis, University of Warwick, 1986.

3.7 Bevington P R, Data Reduction and Error Analysis for the Physical Sciences, McGraw-Hill, 1969.

3.8 Fukushima E and Roeder S A, A Nuts and Bolts approach to Experimental Pulse NMR, Addison-Wesley Publishing Co Ltd, Reading, Mass, 1981.

3.9 Boukraa A., MSc thesis, University of Warwick, 1989.

3.10 Neutron Research Facilities At The ILL High Flux Reactor, (yellow book), ILL 1983

3.11 Ghosh R.E., Control of IN6, ILL Report 82GH15T

3.12 Heidemann A., Users guide to IN10, ILL Report 78HE144T

3.13 Dianoux A.J., Ghosh R.E., Hepvet H. and Lechner R.E., Users Guide, ILL Report 75D16T

3.14 Cocking S.J., PhD Thesis, AERE R6897, HMSO London 1968

3.15 Bee M., Comparison of physical models with time-of-flight and backscattering experimental results, ILL Report 84BE05

Figure 3.1 A block diagram of the nmr spectrometer and peripheral apparatus.

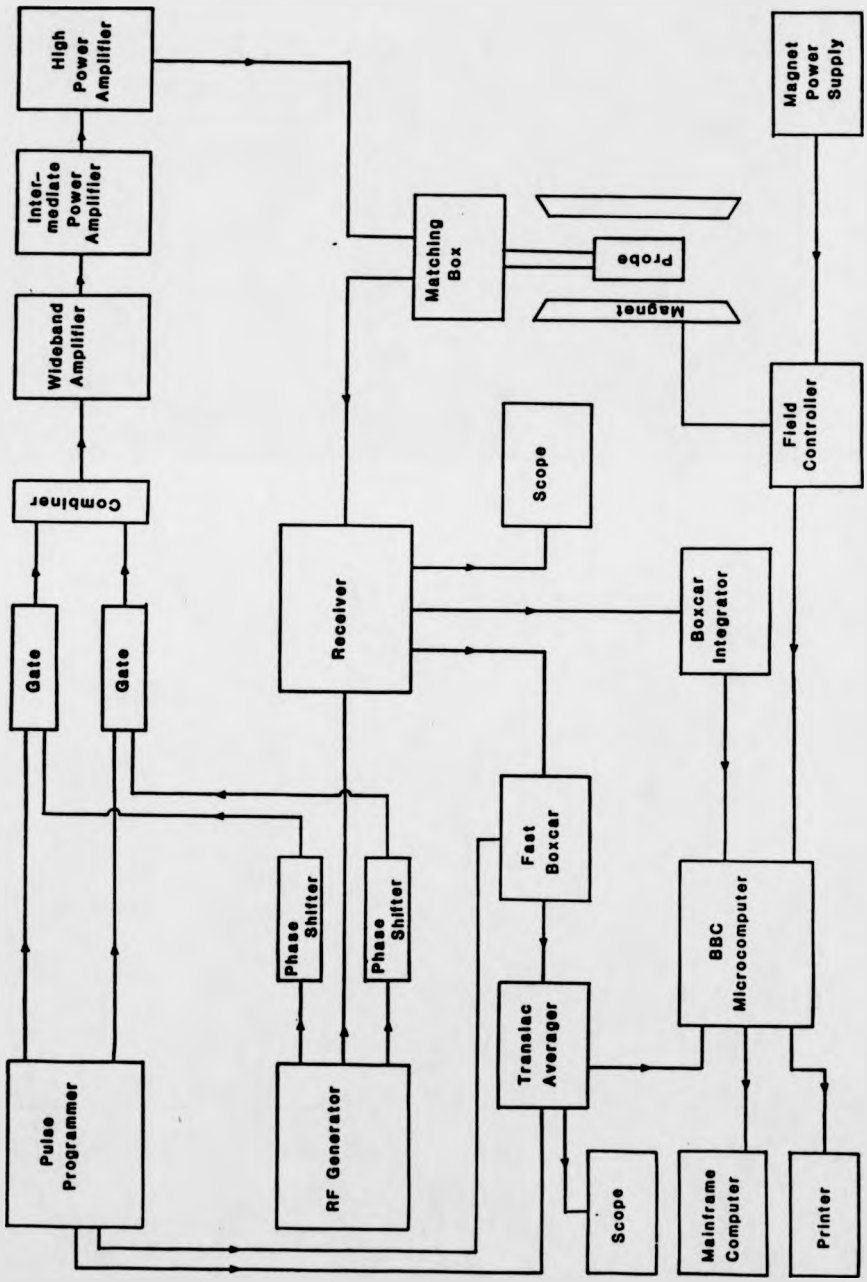

Figure 3.2 A schematic representation of the probe matching circuits, (a) shows a tapped parallel tuned circuit and (b) a tapped series tuned circuit.

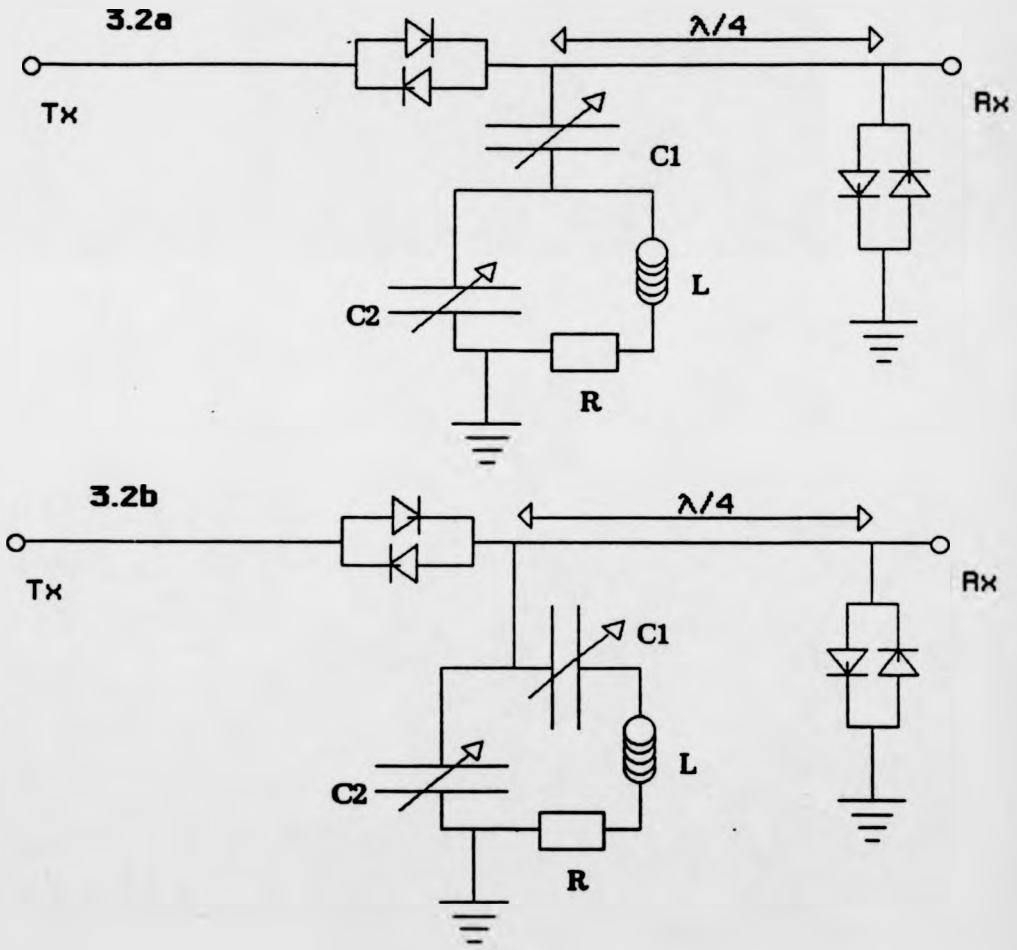

Figure 3.3 A block diagram of the receiver.

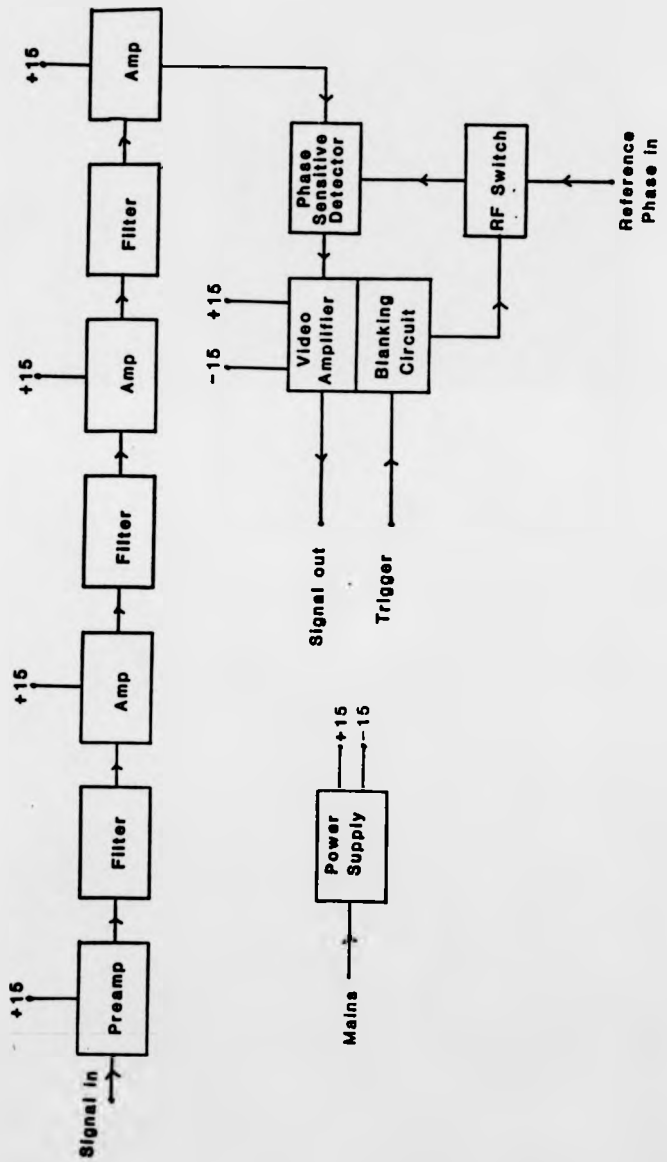

Figure 3.4 A schematic diagram of the liquid nitrogen bubble pump and sample temperature control system.

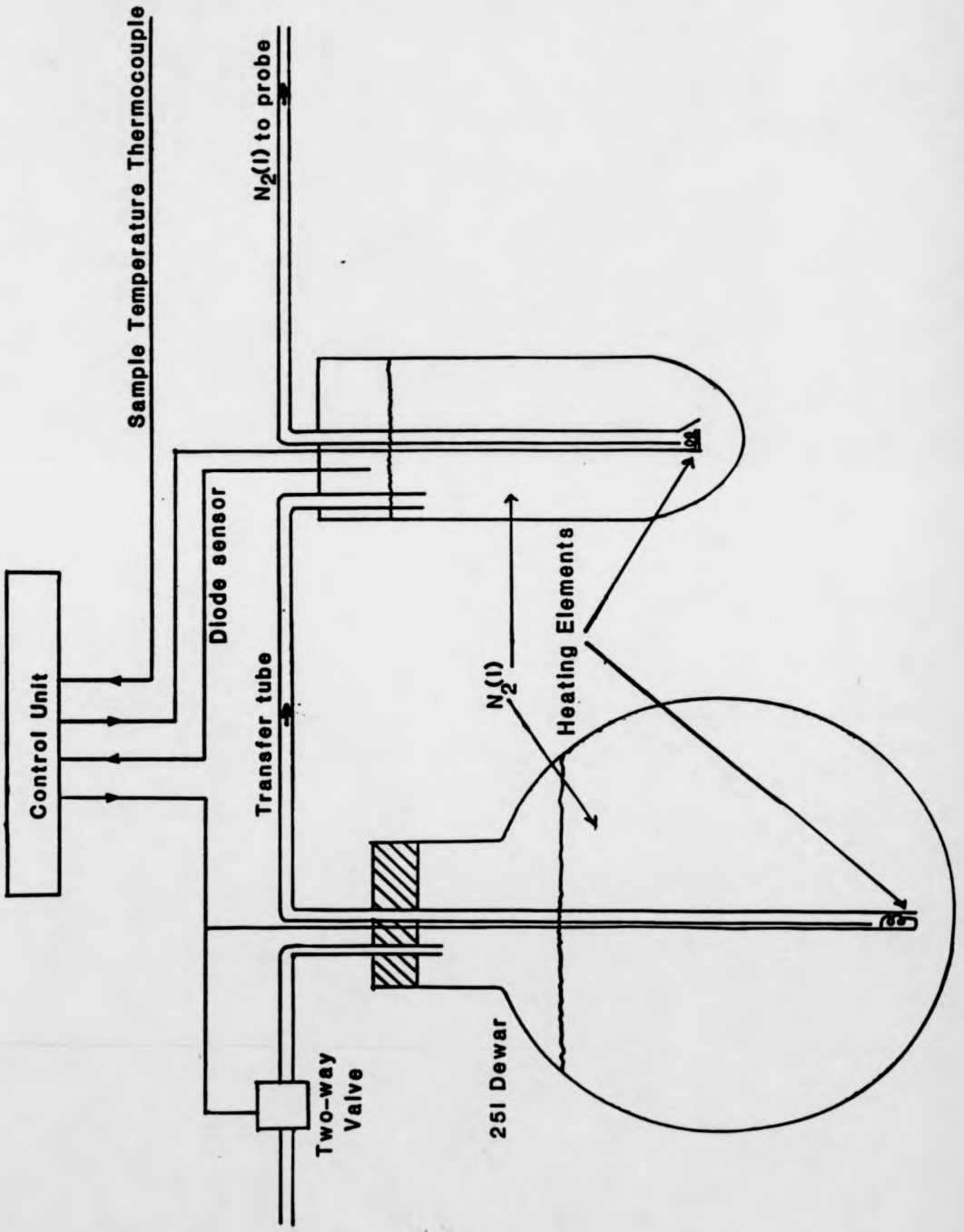

Figure 3.5 A sectional view of the low temperature probe.

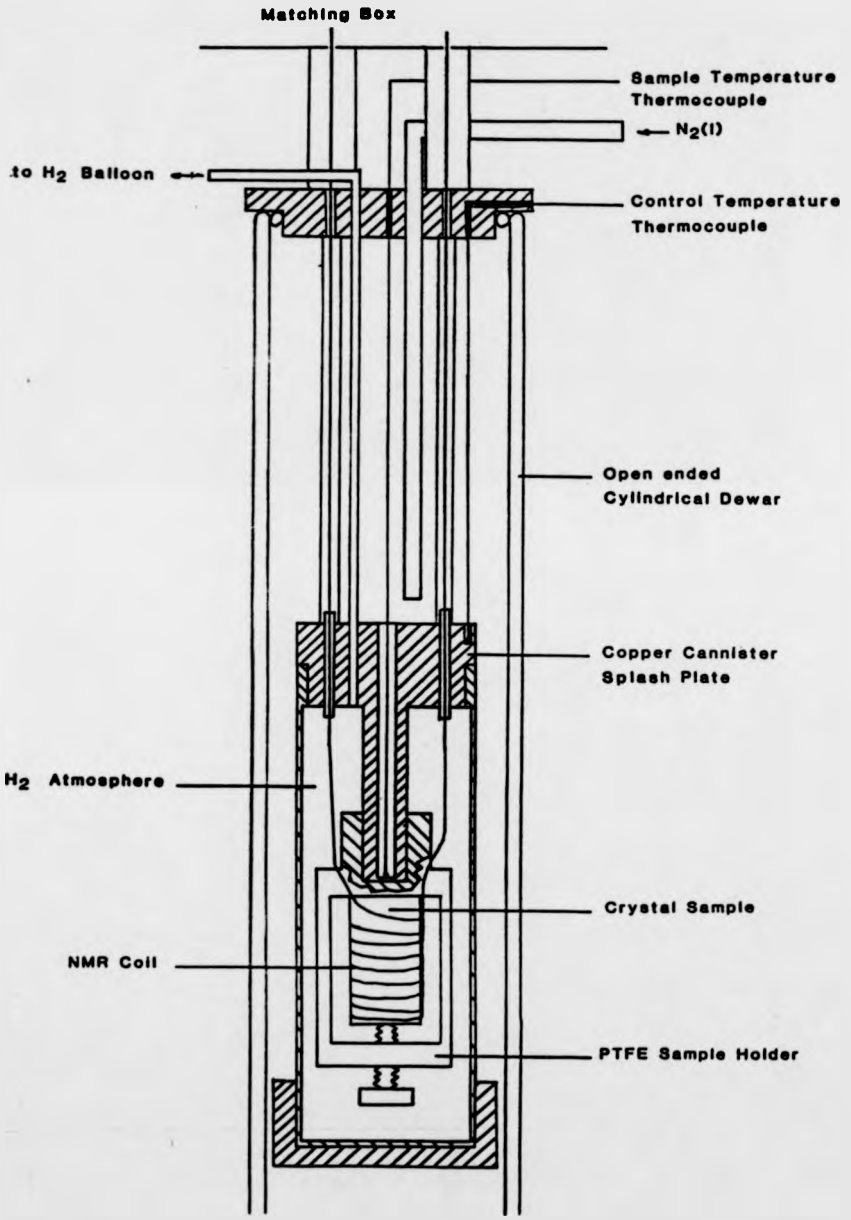

Figure 3.6 A schematic diagram of the pulse sequence and signal processing in the Knight shift study.

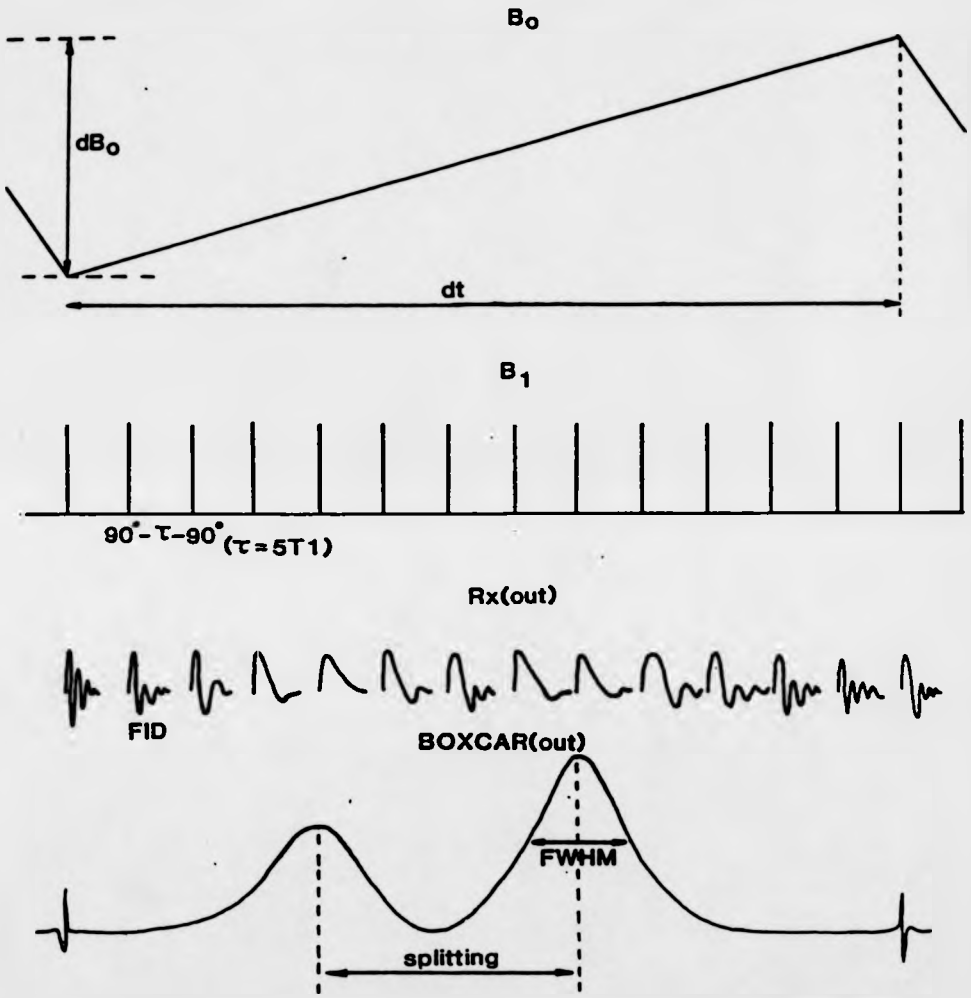

Figure 3.7 Pulse sequence modules of the nmr spectrometer configured for measurement of T_1 using a 180°-τ-90° pulse sequence.

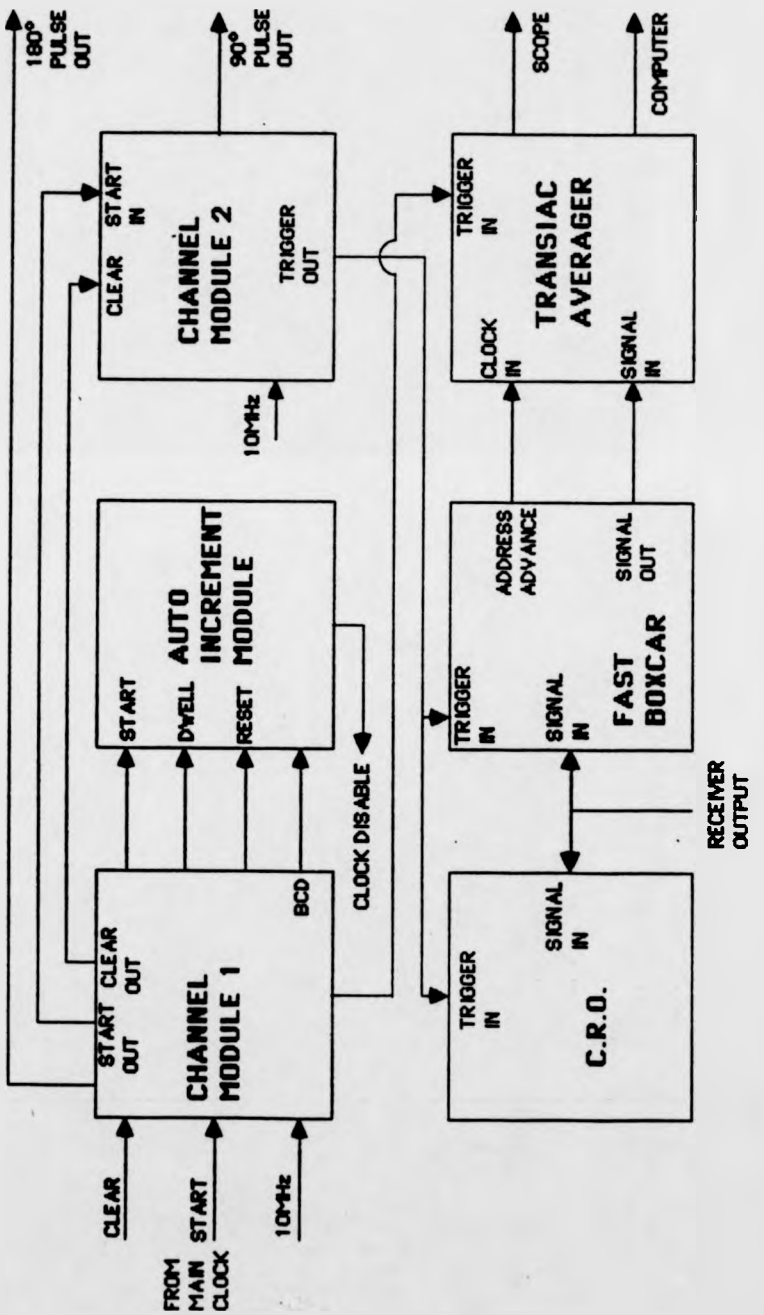

Figure 3.8 A schematic diagram of the time-of-flight spectrometer IN6.
1 Neutron guide 2 Graphite monochromators 3 Diaphragms
4 Beam shutter 5 Cooled Be filter 6 Fixed collimator
7 Suppressor chopper 8 Fermi chopper 9 Monitor 1
10 Beam mask 11 Sample 12 Support rail
13 Beam trap 14 Monitor 3 15 Monitor 2 16 Detectors

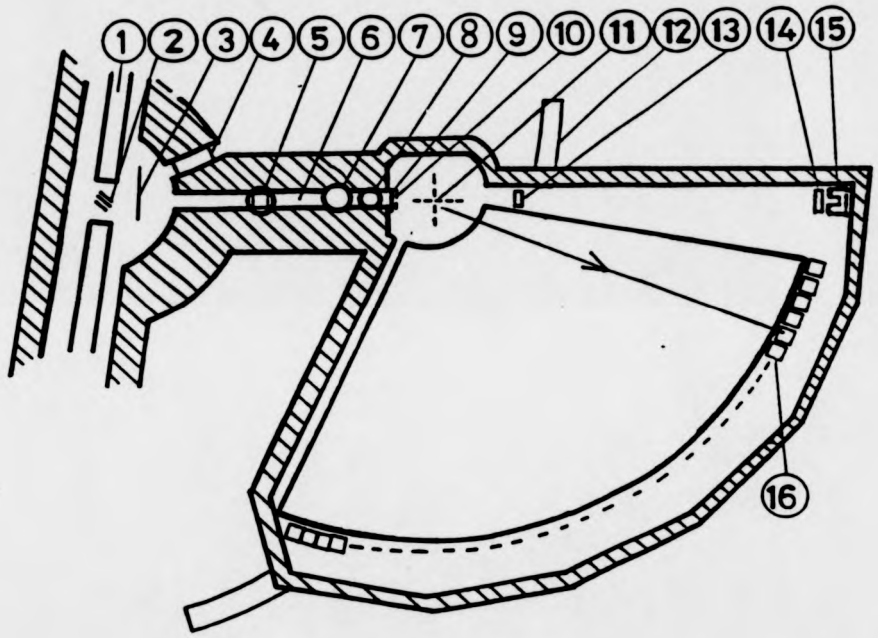

Figure 3.9 A schematic diagram of the backscattering spectrometer IN10.

1 Doppler drive	2 Monochromator crystal	3 Graphite crystal
4 Neutron guide	5 Analyser crystals	6 Monitor 2
7 Shielding	8 Paraffin shielding	9 ^{3}Hedetectors
10 Monitor 1	11 Auxiliary chopper	12 Guide rail

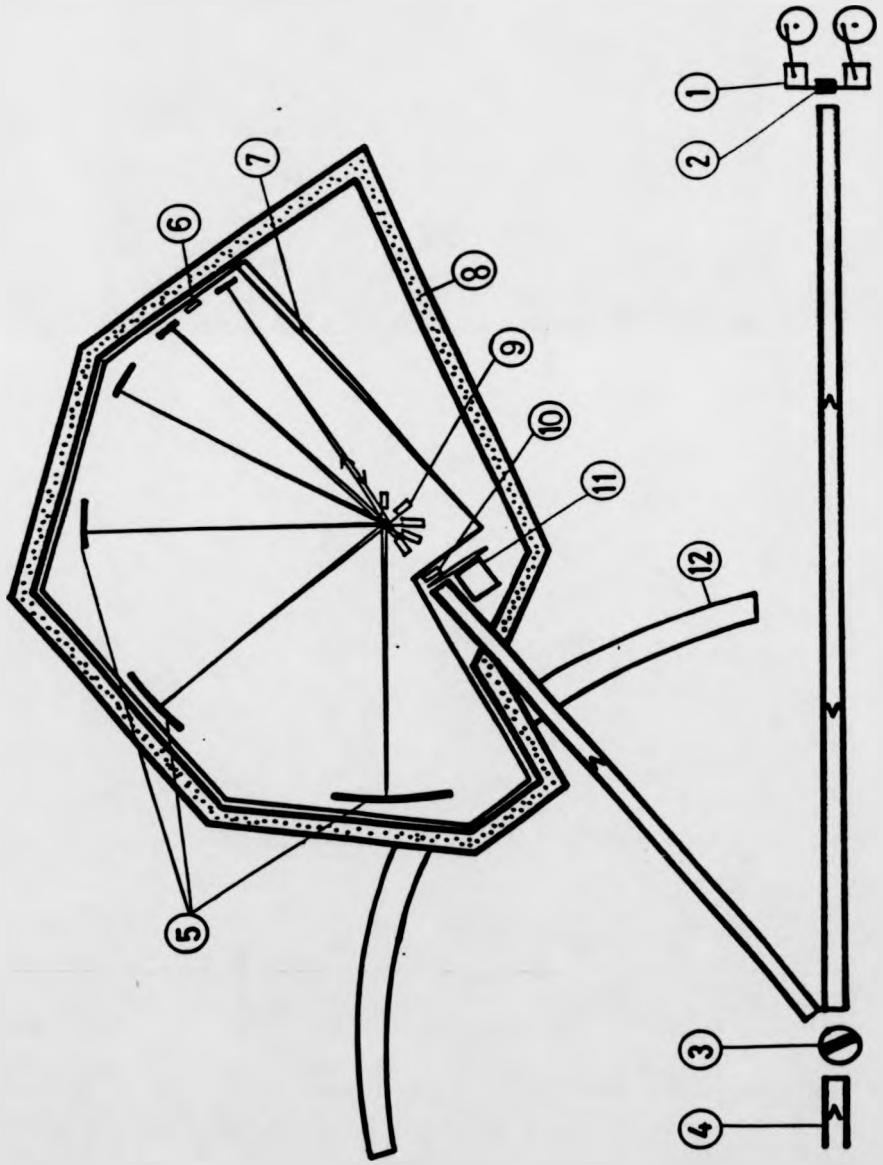

Figure 3.10 A sectional diagram of the sample cell.

1 69mm steel conflats
2 Annealed copper o-ring
3 M6 thread to connect to furnace
4 Groove to allow evacuation of cell
5 Copper o-ring
6 Steel gauze
7 Powder cavity (powder thickness perpendicular to page = d)

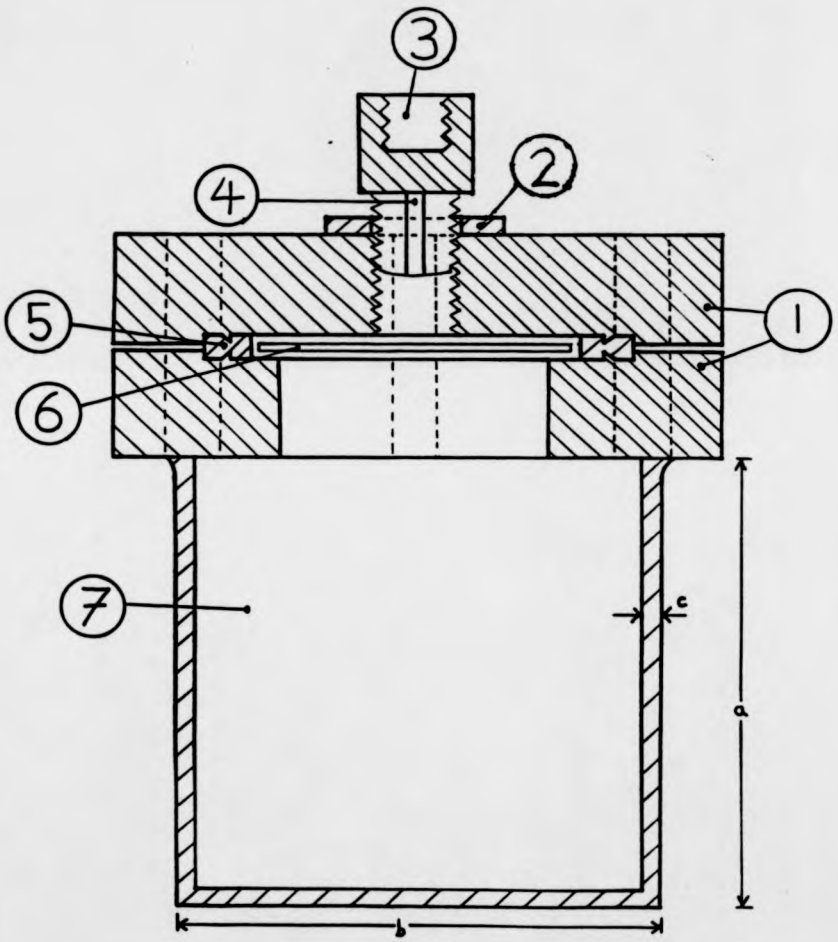

Figure 3.11 A sectional drawing of the sample holder sealing device.
1 Cavity to lock onto bolt at top of sample holder
2 Lid for sealing device
3 Turning arms
4 Rubber o-rings
5 Supports to hold and lock sample holder
6 Hose from nozzle to pumps (which is clamped in transfer from glove bag)

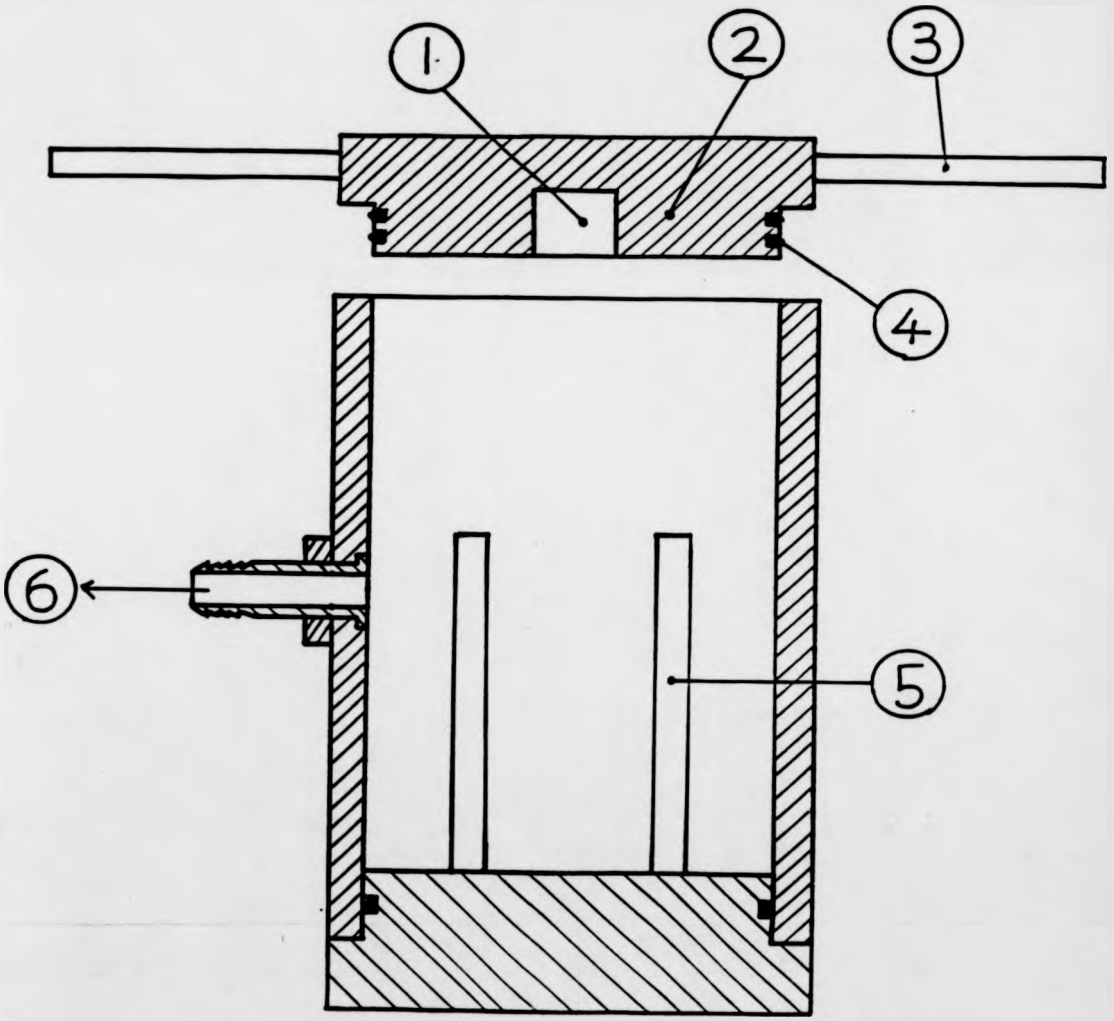

Figure 3.12 A schematic drawing of the sample hydriding rig.

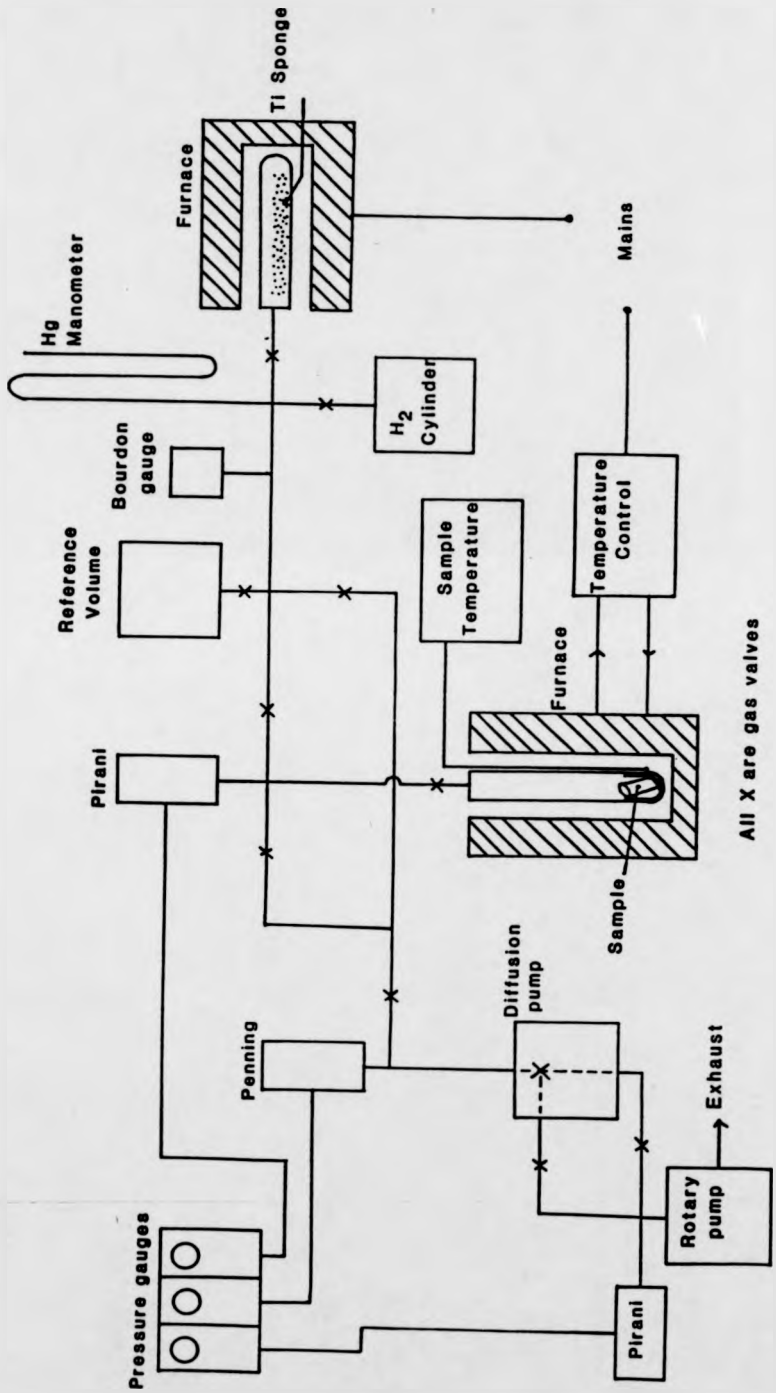

Chapter Four
NMR Study of some Single Crystal Metal-Hydrogen Systems

4.1 β-NbH_x

4.1.1 Formation and Structural Properties

The niobium-hydrogen system has been investigated extensively and its structure and thermodynamic properties are well recorded. A comprehensive phase diagram of the system exists, as shown in figure 4.1 after Köbler and Welter [4.1] who have looked specifically at the low temperature region using magnetic susceptibility studies to differentiate the phase regions of the peritectoid cascade. Reviews of the entire system with greater detail of the structure of each phase, which were not determined by the susceptibility studies of Köbler and Welter, are given in numerous papers [4.2 to 4.6].

The hydrogens move around on interstitial sites behaving like a gas in the α-phase and like a liquid in the α'-phase. The β-phase results from ordering of the hydrogens due to H-H interactions which also produces a distortion of the niobium lattice. The β-phase is an ordered solid solution of hydrogen, where the niobium atoms form a face-centred orthorhombic structure. This was determined using x-ray diffraction which also shows that the fco lattice parameters, a, b and c, vary linearly with hydrogen concentration [4.3 and references therein]. The slight distortion of the bcc niobium lattice on hydriding to this phase is shown in figure 4.2 where the fco cell parameters are a= 4.82 - 4.84Å, b= 4.86 - 4.92Å and c= 3.42 - 3.47Å with γ = 0.4 - 0.9° for x between 0.7 and 1.0 at room temperature. It is partly the large concentration of the β-phase with only a slight associated lattice distortion and the availability of relatively large niobium crystals that make it a suitable system for this nmr study.

Hydrogen has been shown to occupy an ordered subset of T-sites within the niobium lattice. This was initially observed using neutron diffraction [4.7] and later confirmed by electron microscopy [4.8] where it was shown that the hydrogens form linear chains along the <110> directions on $\{1\bar{1}2\}$ planes of the original bcc lattice, see figure 4.3. Within a single crystal of niobium, six possible hydrogen chain directions exist due to the inequivalence of T-sites within a unit cell. There are three pairs of T-sites, each pair having a principal symmetry axis parallel with either the [100], [010] or [001] original bcc niobium axes. Note that this axis system is referred to throughout, see figure 4.4. The separation of nearest T sites along one chain is $a/\sqrt{2}$ (ie along the [110] direction), and between adjacent chains it is $\sqrt{3}a/2$ and a along $[\bar{1}11]$ and [001]

directions respectively. Identical chains tend to group forming domains which vary in size depending on the formation process. The growth of the domains tends to be on {100} planes which minimises the enthalpy of formation of the ordered phase since boundaries are shared with inequivalent T-site chains which do, however, share the same principal symmetry axis. These pairs are shown in figure 4.4 as; sites 1 and 2, sites 3 and 4, and sites 5 and 6. This formation of coherent domain boundaries gives rise to twinning throughout the lattice of say 1-2-1-2-1 domain sequences as observed by Schober and Linke [4.9]. However, a single crystal of niobium once hydrided will consist of an array of all six domains unless the sample is prepared in a manner which gives an increased population of a specific domain. This causes a problem in the analysis of nmr results and is discussed later, in particular in section 4.1.6.

Figure 4.5 shows the hydrogen solubility curves and in conjunction with the phase diagram we can see that in forming a single crystal a minimum hydriding temperature of 450K must be observed in order to avoid the $\alpha+\alpha'$ region. In any event it is found that the most effective hydriding temperature is around 700-800K. The β-phase is formed on decreasing the temperature from this range which leads to decomposition of the supersaturated solution α'-phase into the ordered hydride. On exposure to the atmosphere a thin oxide layer seals the niobium surface effectively trapping the hydrogen up to temperatures of the order of 500K.

Formation of the β-phase can be achieved by gaseous doping since niobium reacts exothermically with hydrogen. It has intermediate stability in relation to other metal hydrogen systems due to a relatively low dissociation pressure at room temperature, however, it is found that a surface oxide layer readily forms effectively increasing the surface barrier potential inhibiting either absorption or desorption of hydrogen [4.3]. To remove this layer prior to hydriding a suitable etchant was found to be a mixture of $HF:HNO_3:H_2O$ in the ratio of about 1:1:6.

Theoretical Knight Shift Behaviour

From this known structure the angular dependence of the hydrogen Knight shift can be calculated. Equation 2.10 gives the general expression for the anisotropic Knight shift. Initially ignoring the lattice distortion and assuming each T-site has axial symmetry then

$$K = K_{ISO} + K_{AX}(3\cos^2\theta - 1) \qquad \{4.1\}$$

since the bcc T-site has $\bar{4}2m$ symmetry and therefore $K_x = K_y = -1/2\,K_z$. Here θ defines the angle of the T-site symmetry axis with respect to B_o. Having ignored the lattice distortion there are only three inequivalent domains whose symmetry axes are orthogonal. Rotation of a single crystal, which comprises these domains, about a [110] type direction, that is with a (110) plane in the plane of B_o, enables the orientation of [100], [111] and [110] type directions along B_o. For one of the domains this rotation will change the T-site symmetry axis from parallel to perpendicular to B_o. Thus $\theta_1 = 0°$ for $<100> // B_o$ and $\theta_1 = 90°$ for <110> parallel to B_o. For the other two domains this is not the case and it can be shown that

$$K_1 = K_{ISO} + K_{AX}(3\cos^2\theta_1 - 1) \qquad (4.2a)$$

while

$$K_{2,3} = K_{ISO} + K_{AX}\,(3/2\,\sin^2\theta_1 - 1) \qquad (4.2b).$$

Allowing for the lattice distortion means that the T-sites no longer have axial symmetry, ie $K_x \neq K_y$, and therefore

$$K_1^1 = K_1 + K_{AN}\,(\sin^2\theta_1\cos^2\phi_1) \qquad (4.3a)$$

$$K_2^1 = K_{2,3} + K_{AN}\,(1-\tfrac{1}{2}\sin^2\theta_1)(\cos^2\theta_1) \qquad (4.3b)$$

$$K_3^1 = K_{2,3} - K_{AN}(1-\tfrac{1}{2}\sin^2\theta_1)(\cos 2\theta_1) \qquad (4.3c)$$

where it is assumed that $\cos^2\theta_2 = \frac{1}{2}\sin^2\theta_1$, $\phi_2 = \theta_1$, $\cos\theta_3 = \frac{1}{2}\sin^2\theta_1$, and $\phi_3 = \frac{\pi}{2} - \theta_1$.

4.1.2 Dynamical Properties

Several studies of hydrogen diffusion in niobium have been carried out which have determined the macroscopic diffusion coefficient at various concentrations and temperatures but these studies are mainly of powder samples [4.4]. We are attempting to discover something of the microscopic detail of the diffusion process through nmr studies of single crystals and perhaps the most significant published works those of Lütgemeier et al [4.16, 4.17] who studied annealed foil samples which were nearly single crystals.

From their study of the ^2D quadrupole lineshape they predict that the deuteriums diffuse among a subset of all possible sites. The subset is defined as those sites having the same orientation of axial symmetry axes and therefore orientation of principal

components of electric field gradient. This can be deduced since they observed splitting of the ^2D spectrum from 4K up to room temperature where the deuteriums diffuse rapidly and motional averaging would be expected to take place if diffusion occurred over randomly oriented sites. From their study of hydrogen in similar annealed samples of $NbH_{0.78}$ Lütgemeier et al [4.16] obtained a value for the hydrogen jump frequency of about 10^8 Hz at 300K and an activation energy of 0.222eV. Below 150K they observed that T_1 is determined by the Korringa mechanism where T_1T=670sK.

Theoretical T_1 Behaviour

In order to determine more precisely the nature of hydrogen diffusion, Schone et al [4.10] have investigated and presented some theoretical calculations for the T_1 angular dependence in the low temperature limit for three different jump models in the β-phase. T_1, due to the dipole interaction, can be expressed in terms of a sum of spectral densities for both the like-like and like-unlike interaction: see equation 2.19 where I = 1/2, S = 9/2 and c = 0.7 to 1.0. For the unlike case (2.19b) the $J^1(\omega_s)$ term is ignored and these equations are valid if the s nuclei are quantized along B_o and not some local electric field gradient and secondly if the s spins relax rapidly in relation to the hydrogen and through mechanisms other than the dipole-dipole interaction. These conditions both hold as shown for the former requirement by muon spin-resonance line width studies [4.11] and the exponential nature of the hydrogen relaxation, and the latter requirement is also valid since the Korringa mechanism is found to dominate the niobium relaxation at similar fields and temperatures to those used here [4.12].

The specific calculations by Sholl given in [4.10] use a similar form for the correlation function presented earlier (equation 2.21) where the summations performed are over all possible hydrogen sites multiplied by a concentration factor and over all niobium sites relative to occupied hydrogen sites for the like-like and like-unlike terms respectively. The jump probability $P(r_i, r_j, t)$ is expanded to only the first two terms, considering only zero and one attempted jump. Fourier transformation of the correlation functions generates spectral densities in terms of dimensionless lattice sums $S(q)$ which incorporate the spherical harmonic and jump probability terms. The relaxation rate is expressed as

$$T_1^{-1}=(\mu_o/4\pi)^2\frac{\gamma_1^4\hbar^2I(I+1)}{a^6\omega_1^2\tau}(\lambda_L+\lambda_U) \qquad (4.4)$$

where the λ_L and λ_U are sums of the $S^{(q)}$ for different q for the like and unlike terms respectively. Some tabulated values of the $S^{(q)}$ and λ are given for specific crystal orientations in reference [4.10].

The three jump models considered are :

(i) to allow only jumps to one of the two nearest neighbour sites on the same chain;

(ii) to allow for jumps to T-sites on other chains via one of the two nearest O-sites in addition to jumps as in (i); and

(iii) to allow jumps via the four second nearest O-sites as well as all jumps in (ii).

The jump probabilities assumed in the calculations for each model and for all resultant sites are given in table 4.1. In the tables the jump probabilities are for a proton commencing at (0, 1/2, 3/4)a relative to a metal atom at the origin and for proton chains orientated in the [110] direction. The first two entries for each model result in the proton finishing on the same chain.

Table 4.1

Jump Vector	Jump Probability Model (i)	Model (ii)	Model (iii)
$(\frac{1}{2},\frac{1}{2},0)$	$\frac{1}{2}$	$\frac{1}{4}$	$\frac{1}{6}$
$(-\frac{1}{2},-\frac{1}{2},0)$	$\frac{1}{2}$	$\frac{1}{4}$	$\frac{1}{6}$
$(\frac{1}{2},-\frac{1}{2},\frac{1}{2})$		$\frac{1}{8}$	$\frac{1}{12}$
$(\frac{1}{2},-\frac{1}{2},-\frac{1}{2})$		$\frac{1}{8}$	$\frac{1}{12}$
$(-\frac{1}{2},\frac{1}{2},\frac{1}{2})$		$\frac{1}{8}$	$\frac{1}{12}$
$(-\frac{1}{2},\frac{1}{2},-\frac{1}{2})$		$\frac{1}{8}$	$\frac{1}{12}$
$(1,0,\frac{1}{2})$			$\frac{1}{12}$
$(-1,0,\frac{1}{2})$			$\frac{1}{12}$
$(0,1,-\frac{1}{2})$			$\frac{1}{12}$
$(0,-1,\frac{1}{2})$			$\frac{1}{12}$

Further, they consider a crystal containing a variety of domains and the T_1 orientational dependence for each is given graphically, see figure 4.6. Also given is the predicted experimental T_1 variation for a crystal consisting of a known relative amount of each domain,as shown in figure 4.7. The predicted T_1 anisotropy is quite large, $\{ T_1^{-1} / T_{1(\theta=90°)}^{-1} \}_{max} \approx 1.17$ for a single domain and, unfortunately, approximately the same for all three models. However, this is not the case when the anisotropy is weighted for an average over several domain orientations within one crystal; $\{ T_1^{-1} / T_{1(\theta=90°)}^{-1} \}_{max} \approx 1.04$ when all three inequivalent domains are equally populated.

This derivation uses only zero or one jump probabilities in the calculations and shows the maximum likely anisotropy in the low temperature limit. Whilst random site occupancy is assumed within a domain, a concentration factor which affects the jump time is allowed for and $\tau = \tau_o / (1-c)$ where c=x, the hydrogen concentration in this case. The concentration is again accounted for in determining the outcome of a one step jump probability along a certain direction by using the multiplicative factor (1-c). Thus hydrogen correlation effects are crudely accounted for, this model is not intended as a general result in the manner of some of those described in section 2.1.2c, but within the limits mentioned should nevertheless give accurate predictions.

4.1.3 Sample 1: $NbH_{0.76}$ Cylindrical Single Crystal.

The work and results presented in this section, 4.1.3 only, were carried out prior to the work for this PhD and have successfully been presented to the University of Warwick for the degree of MSc.

Sample Preparation

This sample was made from a cylindrical single crystal of high purity niobium made at the Ames laboratory. The crystal has dimensions of 12mm diameter and 20mm length and was grown from seed with a <110> direction along the cylinder axis. The x-raying, etching, degassing and hydriding procedures previously described were carried out except it was found that repeated cycles of degassing and hydriding were necessary in order to achieve the desired hydrogen concentration. This is thought to be due to large absorption barrier potentials created by surface gaseous impurities, such as O and N, still present after degassing because of the non-UHV conditions used:

ideally one might hope to degas at 2000K and 10^{-8} Pa instead of the 1400K and 10^{-4} Pa achieved. The impurities trap the hydrogen and inhibit permeation into the bulk [4.13], and the repeated cycling is not only thought to remove these impurities but also possibly to create surface strain dislocations which provide channels for the hydrogen to be absorbed. A sample of β-$NbH_{0.76}$ was prepared and the concentration and quality of crystal confirmed by x-ray diffraction.

NMR Experimental Details

The nmr results were obtained at 39.8MHz and about 0.9T on the spectrometer previously described. A 20 turn coil of 22 swg enamelled copper wire was wound over the complete length of crystal separated by a 50μm layer of PTFE. The coil, with sample, had an inductance of 0.6μH and a Q of 7 at 25.5MHz and was tuned to 39.8MHz using the tapped series tuned matching probe. The crystal orientation with respect to B_0 is shown in figure 4.8 where the angle of rotation, θ, is with respect to the [001] direction and B_0, and is consistent with θ_1 of equation 4.2 and that described by Schone et al [4.10].

Knight Shift Study

The Knight shift results for this sample are shown in figure 4.9 and are seen to be consistent with equations 4.2. The maximum separation of the lines is 50μT ± 2μT (55ppm ± 2ppm) when B_0 is aligned along [001], i.e. θ=0°, where both lines are clearly resolved and show a relative intensity of 2:1. That is, all three domains are equally populated. The linewidths (full-widths at half-maximum) are approximately 20μT and the observed value of K_{AX} is -16.5μT ± 0.5μT, or -17.5ppm. These results are in good agreement with a similar sample previously studied by Schone et al [4.10] where two lines were resolved having linewidths of 14ppm and where K_{AX} = -18.5ppm ± 0.5ppm. They observed a domain population of approximately the ratio 1:1.2 for domain 1 to domains 2 and 3. Their sample was a $NbH_{0.76}$ cylindrical single crystal similar to that used here and this population difference presumably arose due to a preferential domain formation during hydriding. No such preferential domain formation was present in our sample, possibly due to repeated loading and unloading of hydrogen in order to achieve the required concentration in such a large sample.

Determination of the anisotropic Knight shift given in equation 4.3 was not possible from these results except to say that it is small since at these relatively small fields the potential splitting of the lines from domains 2 and 3 remained unresolved. Torgeson et

al [4.14] however, were able to accurately resolve the complete shift by studying a powdered $NbD_{0.78}$ sample at 8T. They obtained best fit parameters to some very elegant data of K_{ISO} = -46ppm, K_{AX} = -18.7ppm, K_{AN} = -9ppm, υQ = 49.3KHz and η = 0.11.

The Knight shift results are significant in that they clearly show that the hydrogen occupy and diffuse between an ordered subset of sites in domains within the niobium lattice in agreement with the work of Lütgemeier et al discussed earlier. These results also seem to be able to explain some observations of Baden and Weiss [4.15] who studied foils of β-NbH_x for various concentrations after a variety of heat treatments on the foils. They observed three coexisting ^1H nmr lines the relative intensities of which vary depending on heat treatment. The separation of the lines is however, consistent with the domain model and gives K_{AX} = -19 ± 1ppm as discussed in [4.10]. In order for the results of Baden and Weiss to be explained in these terms however, requires most of the Nb to be crystaline with a preferred orientation within the foil during the heat treatment. This is quite reasonable and indeed consistent with known foil crystallisation behaviour [4.16]. However, Schone et al do not comment on the statement by Baden and Weiss that the relative separation of the three lines remains constant for all orientations of the foil with respect to B_o. This statement appears to refute the domain and crystallite theory and favour their trapping site theory. however, Baden and Weiss only present data for the foil perpendicular to B_o to validate their statement and not at intermediate orientations. These orientations would raise the additional problem of analysing demagnetizing effects in the lineshape and shift due to the sample geometry which will be discussed in greater detail in the next section.

T_1 Study

T_1 was measured as a function of crystal orientation and temperature. Lütgemeier et al [4.16] measured the T_1 temperature dependence of powdered NbH_x samples and observed a dipolar minimum at approximately 320K for x=0.78 where T_1=7ms measured at 44.4MHz. The study of this sample at 39.8MHz in the stated temperature region means that this study is on the low temperature side of the minimum in the correct region to analyse data in terms of the theory presented earlier. Note that this system is further favoured since hydrogen relaxation through the Korringa mechanism is weak, as suggested by the small Knight shifts and the measured $T_{1e}T$=670sK[4.16].

Figure 4.10 shows results obtained for the variation of T_1 with crystal orientation at 290K and θ=0°, 15°, 30°, 55°, 70° and 90°. The maximum anisotropy of T_1, that is $T_1[110]/T_1[001]$, is 1.02 ± 0.01. This is in good agreement with the predicted results shown in figure 4.7 in terms of both the form of the T_1 angular dependence and the magnitude of anisotropy, especially considering that these measurements are not truly in the low temperature limit. This result is also in good agreement with that found by Schone et al [4.10] for their sample with a 1:1.2 domain occupation. They observed a maximum anisotropy of ξ=1.04 at room temperature and below. The experimental accuracy in the measurements of T_1 presented here is very good. for example, T_1 = 9.2 ± 0.05ms and 9.4 ± 0.05ms for θ = 0° and 90° respectively. That is an error of less than 1% achieved through lengthy averaging, however, variation of sample temperature and B field required the collection of large numbers of data sets. This process was of course aided by the fact that T_1 is relatively short. A guide to the form of the T_1 angular dependence and the theoretical prediction are presented in figure 4.10. Despite the accuracy achieved it is not possible to determine the most likely jump model, this would require experimental errors of the order of 0.1%. The best possibility is to study the T_1 angular dependence at lower temperatures.

Figures 4.11 and 4.12 show the T_1 temperature dependence between approximately 295K and 210K for three different orientations. Maintaining a constant temperature during a complete orientation study is not readily achieved with the temperature control system used, therefore the crystal orientation was fixed at θ=0°, 56° and 90° and sets of T_1 data at various temperatures obtained. The lower temperature limit is determined by the phase transformation at approximately 190K. Best fits to this data give the apparent activation energies for the hydrogen diffusion mechanism at specified crystal orientations; cf discussion by Lütgemeier et al [4.17].

Table 4.2

Orientation, θ	Apparent Activation Energy, E_a (eV).
0°	0.223 ± 0.005
55°	0.227 ± 0.005
90°	0.231 ± 0.005

These give a true activation energy in good agreement with Lütgemeier et al [4.16] who obtained a value of E_a = 0.222 ± 0.008eV independent of hydrogen concentration for 0.3 < x < 0.78 and Zamir and Cotts [4.18] also obtained E_a=0.218eV/atom for x = 0.7 at room

temperature. Note that as one might expect, a slightly lower value has been found for $x \approx 0.7 - 0.8$ in the high temperature cubic α'-phase where $E_a \approx 0.17 \pm 0.01$eV [4.18 to 4.20].

The apparent variation in activation energy is due to a divergence in the T_1 anisotropy, that is ξ is greatest in the low temperature limit. Interpolation of the results at 216K gives $\xi = 1.13$ (±0.1) compared with 1.02 at 290K. Note that at 216K T_{1e} is approximately 3s and the corrected anisotropy is $\xi = T_1[110]/T_1[001] = (215 \pm 10)/(190 \pm 10) = 1.13 \pm 0.08$, the electronic contribution does not affect the magnitude of anisotropy since the T_{1e} contribution is too long. Also, no account is taken of an anisotropic T_{1e} contribution because of this fact and since in an axially symmetric environment there is no orientational dependence as discussed in section 2.1.2e: the orientational dependence of T_{1e} is the same as for the dipole-dipole interaction in the high temperature limit, ie isotropic in this case. Overall, these results are in good agreement with the predicted orientational dependence for this particular sample.

It is worth noting that the use of the BPP model in evaluating E_a in the low temperature regime is not valid in these systems; and as predicted theoretically, the largest anisotropy ξ is achieved approximately a decade in $\omega\tau$ away from the dipolar minimum. It is dissappointing that despite the good accuracy achieved, the latter does not permit determination of the jump model as had been hoped.

4.1.4 Sample 2: $NbH_{0.75}$ Single Crystal Disc

Following the findings discussed in the previous section several attempts were made to prepare a single domain β-NbH sample in order to remove the effect of averaging over different domain orientations. A brief description of the methods used is given below.

Sample Preparation

First, it is thought that if a single crystal presents a favourable fraction of its surface area having a (100) type plane and hydriding is achieved in one complete run, (i.e. a single exposure to hydrogen instead of the cycling found to be necessary in preparing sample 1) then one domain might be formed. For example Schone et al [4.10] explain their observed domain population ratio of 1:1.2 due to the fact that their crystal only exposed the (001) plane at the cylinder surface whilst the other planes subtended an angle between 45° and 90° to the surface. Hence domains along [110] and [1$\bar{1}$0] would be preferentially formed since these are in the plane of the surface. Schone et al also give

this as an explanation for similar relative signal intensities observed by Lütgemeier et al [4.17] for ^2D in β-NbD_x.

A device for exposing a single surface of a single crystal disc was made in accordance with figure 4.13 to be used in a high pressure hydriding system at Warwick [4.18]. Using the device it was intended that the top surface be exposed to 0.4 MPa of hydrogen, the opposite side being exposed to only the evacuated cavity. Thus it was thought that hydriding could be achieved relatively quickly and with a preferential domain formation. The device was not found to be effective because of intrinsic problems in its fabrication and use. Firstly, and most importantly, the knife edge seals at the edge of the disc caused stressing of the sample due to restriction of sample expansion under heat treatment which caused samples to crack excessively. Secondly, heating of the device also led to problems with the copper o-ring seal and threads on the various parts which either fatigue easily or fuse with cooperating parts.

A second method considered was to expose the desired surface of a sample by masking the rest of it with a non-hydridable material [4.5] and to assist hydriding by coating the desired surface with palladium black which is known to increase hydriding rates in certain cases due to its low enthalpy of absorption of hydrogen [4.19]. This method would be somewhat complex since after applying the desired coats it would also be necessary to remove them before the nmr study. This could be achieved by etching however, a further problem might be differential rates of etching of the different coating substitutes.

The method which was found to be successful was simply to cut a disc sample and expose it to a hydrogen atmosphere as previously described for sample 1. The success is thought to be due to the fact that the disc shape simply gives a greater exposure to a certain orientation due to the ratio of the surface areas of the disc faces to edge compared with the face to length ratio of a cylindrical sample. A single domain sample of $NbH_{0.75}$ was prepared by cutting, by spark-erosion, a roughly 2mm thick circular disc from a cylindrical niobium single crystal with the same orientation as sample 1. The original crystal was 12mm in diameter and 25mm long. It has a [110] cylinder axis, a purity of 99.999% and was purchased from Goodfellow Metals. This crystal disc was etched to remove damage from spark-erosion leaving approximately a 1.5mm thick, 12mm diameter disc (the disc faces were not quite parallel however, and after etching the sample had an irregular thickness of 1.5 ± 0.2mm). A schematic drawing of the crystalline disc sample is given in figure 4.14.

It was, however, again found necessary to degas and hydride the sample repeatedly before it eventually formed a β-phase composition of $NbH_{0.75}$. The concentration was confirmed by X-ray analysis which also showed the good crystalline quality of the hydrided sample. A crack developed from the outer edge to the centre of the disc along the $[1\bar{1}0]$ direction, which as has been demonstrated lies in an easy cleave plane of this phase [4.9]. The sample was subsequently found by the Knight shift measurements to contain only one type of domain with principal axis perpendicular to the [110] (disc face normal direction), that is along the [001] direction.

NMR Experimental Details

NMR measurements on this sample were made at 47MHz and approximately 1.1T. For the T_1 study the disc was held in a PTFE former which was a rectangular plate (of dimension 210 x 15 x 2mm) with a central hole to hold the disc by friction. A 9.5 turn 24 swg copper wire coil was wound around the former and tuned to 47MHz using the tapped series matching probe. A signal to noise ratio of about 1:1 was observed on the oscilloscope for a simple 90° pulse. However, this coil was found to be problematical when studying the ^1H lineshape behaviour. In order to avoid any effects due to the coil shape the crystal was mounted in a cylindrical PTFE former, split longitudinally in to two sections and having a recess for the crystal. A 7 turn 24 swg copper wire, cylindrical coil was wound on the former. The former was then mounted in the holder used for a cylindrical crystal. This arrangement obviously led to a lower signal to noise due to the decreased sample filling factor but adequate measurements were achieved as described below.

Knight Shift Study

Knight shift studies of a disc-shaped sample are complicated by an anisotropic demagnetising field effect due to the sample shape which produces an angular dependence [4.20]. It can be shown that the orientational dependent shift $S(\Theta)$ observed in such a case is:

$$S(\Theta) = K_{A\chi}(3\cos^2\Theta - 1) - \alpha\sin^2\Theta \qquad \{4.5\}$$

where $\Theta=0°$ when both the domain symmetry axis and disc faces are parallel with B_o as is the case for the sample prepared as shown in figure 4.14. The demagnetising factor α is shape dependent and varies from 0 to $4\pi\chi_v$ (in c.g.s units), where the upper limit is valid for an "infinite plate" and this sample is expected to take some

intermediate value. Calculation of this factor is somewhat complex and only readily obtainable for rather simple shapes such as ellipsoids and not the irregular, tapered disc shape of this sample.

The absolute shift relative to a standard reference of bare protons can be calculated using the following expression

$$K = K_{ISO} + S(\Theta=0) - 2K_{AX} - (\frac{4}{3})\chi_v - 25.6 \text{ (ppm)} \qquad (4.6)$$

where K_{ISO} is the observed shift relative to a ^1H signal from pure water. $4/3\chi_v$ is the Lorentz cavity field [4.22] and -25.6ppm is the molecular shielding constant for protons in water [4.23].

The factor α was determined qualitatively by orientating the [001] direction parallel to the axis of rotation of the crystal thereby removing the Knight shift component of equation 4.5. The crystal was rotated between orientations having the disc faces and crystal [110] direction parallel to B_o, and the disc face normal and crystal [1$\bar{1}$0] parallel to B_o. As stated earlier, a single ^1H line was observed and the maximum observed separation of the ^1H line in the two positions was 39 ± 2ppm. This value for the demagnetisation factor α is approximately 1/3 the value of 110ppm observed by Fukai and Kazama [4.20] for a thin (50μm) foil of $NbH_{0.771}$. From their measurements over a range of sample angles and sample concentrations they observed a non-linear decrease in volume susceptibility of the systems with increasing hydrogen concentration which was in reasonable agreement with results obtained from ordinary susceptibility studies. From this it is reasonable to predict a value of α=120ppm for a 50μm sheet sample of $NbH_{0.75}$.

Returning the crystal to the orientation shown in figure 4.14 the orientational dependence of the ^1H Knight shift was measured and the results obtained are shown in figure 4.15. The orientational dependence observed was in good agreement with the predicted form given by equation 4.5.

The observation of a single resonance line from this sample and the Knight shift orientational dependence confirms the statements made earlier about the population of domains and the orientation within the disc. It was felt that achievable accuracy in determining K_{ISO} did not warrant its study since extensive measurements of this system in more suitably shaped samples already exist [4.10, 4.14 & 4.20].

With the orientation indicated in figure 4.14 the shift observed is as shown in figure 4.15. The maximum separation of the line when Θ=0° and Θ=90° (ie [001] parallel and perpendicular to B_o respectively) was 101.6 ± 2ppm. Fitting the observed data to equation 4.5 we obtain a value for K_{AX} of -19.5 ± 2ppm in good agreement with previously quoted values. The linewidth observed was of the order of 20ppm and therefore, in similarly good agreement with previously obtained values. Again, however, a value for K_{AN} was not determinable from the data, except to say that it may be non-zero.

T_1 Study

An extensive investigation of the ^1H T_1 orientation and temperature dependence has been carried out and the results are shown in figures 4.16, 4.17 and 4.18.

Due to the problem discussed earlier of maintaining a constant sample temperature whilst rotating the sample through a range of orientations, as with sample 1 a set of T_1 measurements for one specific orientation at a time were made at various temperatures between ambient room temperature and about 217K. The data shown in figure 4.16 A, B, & C, are for Θ=0°, 35° and 90° respectively and they are shown comparitively in figure 4.16D. These are, the approximate orientations predicted to give the maximum variation in T_1 for single or multiple domain samples.

Typically, each T_1 measurement consisted of about 50 sweeps of τ, given in equation 2.4, from 0 to $5T_1$, though this was less, say 32 or 16, for longer values of T_1. Several data sets (between 4 and 9) were taken at each temperature where a stability of better than 1K was achieved during the period of gathering all data sets. The error in the fittedT_1 value for each T_1 data set was of the order of or less than 5% and the standard deviation in the average of T_1 from the gathered data was of the order of 2-3%.

The magnitude of the relaxation times is in good agreement with those obtained for sample 1 (given the increase in field, B, of study). As pointed out earlier, the gradient of T_1 v T^{-1} is meaningless in terms of determining activation energies since it incorporates a divergence in T_1 for the various orientations as the low temperature limit is reached and maximum anisotropy occurs. Nevertheless they are consistent with increasing anisotropy with decreasing temperature and are given in table 4.3.

Table 4.3

Orientation, θ	Apparent Activation Energy, E_a (eV).
0°	0.209 ± 0.005
35°	0.211 ± 0.005
90°	0.229 ± 0.005

It can be seen that despite the fact that a consistently lower value of T_1 was observed for θ=35° compared to θ=0°, the activation energies are very close to one another and $E_a(\theta=0°)$ is found to be lower. This is probably due to the more limited range of temperatures over which the θ=35° measurements were made compared to θ=0°, which means that the full effect of the anisotropy was not observed for θ=35° at very low temperatures. The value for $E_a(\theta=90°)$ is however, appropriately larger than either of the other orientations. The average is in good agreement with previously reported values of E_a, as was that obtained for sample 1.

By varying the sample orientation only slightly it was found that a constant sample temperature could be maintained across a range of angles. Accordingly a set of measurements for θ=30°, 45° and 60° were achieved, as shown in figure 4.17, at near constant temperature. Measurements were made at temperatures of 238K, 247K, and 263K. Additional T_1 values for θ=0°, 35° and 90° are shown which were obtained from interpolation of the data shown in figure 4.16.

As shown in figure 4.16d and figure 4.17 the maximum relaxation rate is achieved when the [001] direction is approximately 35° to B_0, the minimum rate occurs when θ=90° ([001] perpendicular to B_0), quite different from sample 1 but in excellent agreement with theory. Fitting Sholl's theoretical predictions for each of the three models discussed earlier to the data, as shown in figure 4.18 for T=238K, we find a good agreement between experiment and theory. The anisotropy observed at 238K is, $T_{1\,[110]} / T_{1\,(\theta=35°)} = (80 \pm 2\text{ms}) / (66 \pm 2\text{ms}) = 1.21 \pm 0.04$ which is somewhat larger than the predicted anisotropy of 1.17 but not unacceptably so. The general trend in behaviour of T_1 for different sample orientations with respect to B_0 is very good.

4.1.5 Discussion

The theory predicts a decrease in anisotropy with increased domain mixing in a sample and good experimental agreement with this was observed between samples 1 and 2, where $\zeta = 1.13 \pm 0.08$ and 1.21 ± 0.04 respectively. However, theory also shows

that whether a single domain or multiple domain sample is used the variation in anisotropy of T_1 between different diffusion mechanisms is small. It has not been possible to determine the diffusion mechanism despite the excellent agreement in form of T_1 v Θ observed as shown in figure 4.18.

In fact theory predicts the largest anisotropy for model 1, but only marginally so since the difference is less than 1%. Given the observation of a larger than predicted variation in T_1 it is tempting to conclude that the diffusion is most likely to be one dimensional in nature, that is of an intra-chain type, see table 4.1. However, this model is physically unrealistic since hydrogens undergo long range diffusion and cannot pass through one another as would be required by this constrained model. It would therefore be worth seeing what theory predicts for a larger range of diffusion models, some of which were predominantly one dimensional perhaps, but this would require a much larger number of types of jumps to be taken into account and accordingly increases the complexity of accurate prediction.

A conclusion which suggested one dimensional diffusion would contrast with unreported neutron scattering results obtained by Richter [4.25] who apparently observed only a three dimensional diffusion behaviour. The results, being so unremarkable, remain unpublished.

Unfortunately, in the case of the β-NbH_x system the anisotropic behaviour of T_1 is not sensitive to a large variation in hydrogen diffusion paths. It has been found that the achievable experimental accuracy is still not good enough with a single domain sample to determine the diffusion mechanism. On a positive note, these results are highly satisfactory and justify pursuing further study of single crystals since the theory and experiment have been found to be consistent. If a system which has equally good properties for study by nmr as the β-NbH_x system, but for which a greater variation in the theoretical predictions for T_1 behaviour for different hydrogen diffusion mechanisms exists, then this study shows that determination of the actual diffusion mechanism may be possible.

4.2 β-VH_x

4.2.1 Formation and Structural Properties

The group Va transition metals are very similar to each other in their hydriding characteristics and hydrogen alloy properties, as can be seen for example from the

review of Nb, V and Ta hydrides by Schober and Wenzl [4.26]. This similarity is reflected in the general diffusional and structural properties; for example all three can absorb large amounts of hydrogen to form an ordered dihydride phase.

The vanadium hydrogen system has been extensively investigated and several ordered phases have been observed as shown in figure 4.19 after Schober and Pesch [4.27], see also a review by Smith and Peterson [4.28]. The solid solution phase is remarkable in that it has the greatest hydrogen diffusivity of all known systems and in fact $D \approx 6 \times 10^{-5}$ cm^2s^{-1} at 330K. Also it is worth noting that there is no η phase (compare figure 4.19 with the phase diagram given by Schober and Wenzl [4.26]). This phase was speculatively introduced by Schober and Carl in 1977 [4.37] but later withdrawn in 1979 [4.27] when the original DTA evidence was discredited. However, the phase is still shown in some literature.

Two ordered phases have been found to exist in the region of the stoichiometric composition V_2H. These are shown in figure 4.19 as the monoclinic β-phase and the tetragonal ϵ phases, though they are more usually now referred to as the β_1 and β_2-phases respectively. It is the β_1-phase which is studied here, however, it is worth noting that the β_2-phase exists between approximately 175 and 197 °C for the same compositions as β_1 and is very similar to the β_1-phase except that the hydrogen ordering is less structured as would be expected at the higher temperature. Also, one of the curious properties of the vanadium-hydrogen system is the contrast in characteristics for the different hydrogen isotopes. This is reflected in their respective phase diagrams and indeed no equivalent to the hydrogen β_2-phase exists in the deuteride system.

The β_1-VH_x phase exists between concentrations $0.49 \leq x \geq 0.59$ at room temperature and is also stable for the exact concentration x=0.5 to temperatures less than 170K. The vanadium system differs from those of Nb and Ta in that the hydrogens occupy O-sites in the β-phase compared with T-site occupation in the ordered β-phases of the other two and in the α-phase of all three systems. This was first proposed by Rush and Flowtow [4.29] from inelastic neutron scattering studies and later by Arons et al [4.30] from comparison of theoretical second moment calculations with experimental ^{51}V nmr measurements in samples of both β-V_2D and β-V_2H.

As for β-NbH_x, the high concentration of hydrogen in the ordered β-phase causes the vanadium lattice to distort. The structure is monoclinic (isomorphic with β-V_2D) but there is only a slight distortion from a tetragonal structure in which the lattice

parameters of the original bcc unit cell are distorted so that c/a ≈ 1.1. Reference to the structure of the vanadium lattice is to the original bcc unit cell unless indicated with a subscript 'T' for the tetragonal cell directions and subscript 'm' for the monoclinic case. Figure 4.20 shows this structure where a, b and c are the original bcc lattice cell vectors and the monoclinic unit cell is given by $A_m \approx B_m \approx (a^2 + c^2)^{1/2}$, $C_m \approx b$. The β_1-V_2H lattice parameters are A_m=4.4566Å, B_m=4.4760Å, C_m=3.0022Å and γ_m=84.4° at 298K [4.31]. The parameters for the bcc cell are given in the narrative for figure 4.20 after Takano et al [4.42].

Marsh [4.32] has shown that the monoclinic structure has space group symmetry c2/m and not cm as described by Noda et al [4.31]. The error in the x-ray data analysis by Noda et al was a result of domain twinning which they did not allow for; Marsh suggests a twin component, 55% the size of the main crystal, existed in their sample with twinning across the ab plane. Twinning was previously observed in these systems by Wangagel et al [4.33] in an early x-ray and electron microscopy study in which they characterised the β_1 phase as being tetragonal with a twin plane of $(101)_T$. They also observed that whilst the a axis is only increased by a small amount the β-phase lattice is tilted with respect to the original bcc lattice hinting at an unusual hydrogen ordering in the system.

It is found that for the β_1-V_2H system the hydrogens occupy specific O_{Z1}-sites which form occupied $(10\bar{1})$ planes separated by a single parallel layer of predominantly vacant O_{Z2}-sites, as shown in figure 4.20 [4.35]. The O-sites of a bcc lattice can be subdivided into three categories labelled x, y, and z depending on the local symmetry of the site. The label refers to the direction of the principal symmetry axis with respect to the bcc lattice axes. There is one of each type of O-site per metal atom. The β_2-phase, which exists at higher concentrations and temperatures, is ordered in that it exhibits hydrogen occupation on O_Z-sites for a given domain however, the layering of the β_1-phase breaks down until each O_Z-site has an equal population probability. In a tetragonal β_2-V_2H sample therefore, all O_Z sites are occupied with equal probability of 1/2.

It is possible to describe three types of β-VH_x domains which may form in a bcc vanadium lattice. These domains are labelled A, B or C depending on which of the original a, b or c axes of the bcc lattice is parallel to the c_m (ie $[001]_m$ or $[001]_T$) axis of the newly formed domain, see figure 4.21.

The formation of β-V_2H has been the subject of considerable study due to its unusual characteristics, such as the existence of a second order phase transition from the β_1 to β_2-phase. A pct curve of this system is shown in figure 4.22 from which it can be seen that the vanadium system exothermically absorbs hydrogen in a similar manner to niobium (cf figure 4.5). However, in order to form the β_1-phase it is necessary to pass through a two stage transformation, viz. α (bcc) to β_2 (bct) to β_1 (monoclinic). The transitions involve shear transformations which appear to be relatively complex and which preclude readily preparing large single domain samples. For example it has been found in recent studies by Takano et al [4.42] that it is necessary to exert a uniaxial tensile stress of about 20 MPa along a [011] crystal axis parallel to the sample longitudinal axis whilst cooling the hydrided sample through the phase transition region in order to form a single domain crystal (other optimum stresses are reported for different sample orientations). Despite this, it is possible to form large single domain regions within a single crystal sample by careful heat treatment as reported by Richter et al [4.40] and discussed later.

The local O-site environment which results from the distortion in the β-phase is shown in figure 4.23. The site shown is that for an assumed body centered tetragonal lattice, to which the monoclinic lattice is a very close approximation, such that the hydrogen occupys an expanded O-site with principal symmetry axis along the z direction. This assumption has been used to analyse inelastic neutron scattering results from a single domain β-V_2H crystal where the authors were able to establish a well defined hydrogen potential up to more than 1 eV [4.39]. Through rotation of the crystal they resolved fundamental vibration energies along the three crystal axes showing that the hydrogens vibrate with higher frequency along directions where the metal atom spacing is smaller. However, more recently INS studies of β_1-V_2H, β-V_2D and β-V_2T by Rush et al [4.48] gave results which do not fit the form of the site potential described by Hempelmann et al [4.39] and they suggest a strongly anharmonic potential exists in the ab plane which is both isotope and temperature dependent.

For these Knight shift studies however, it is reasonable to assume that K is dominated by the hydrogen nearest neighbour interaction with V atoms and the O-site represented in figure 4.23 should have near axial symmetry. For a single crystal composed of three types of domain, having pseudo-tetragonal symmetry with principal symmetry axes along the x, y and z directions respectively, the variation of K for rotation about a <110> type direction will be given by equations 4.2a and 4.2b. In these equations the subscripts 1, 2 and 3 will represent domains A, B or C depending on the

exact crystal orientation. As with β-NbH however, there is a possibility of observing a slight anisotropic distortion and then equations 4.3 would hold. A recent ^{2}D nmr study of β-$VD_{0.59}$ by Salibi et al [4.36] found a significant distortion in the ^{2}D line due to an anisotropic Knight shift component. However, at this mixed β + ∂-phase composition the distortion was only observed for the ∂-phase component of the deuterium line. The measurements were made at 194K and 4.7 Tesla. The ∂-phase has an orthorhombic structure similar to β-NbH where the deuterium atoms occupy T-sites. They concluded that there was no evidence of any significant anisotropic shift in the β-phase, which is of course isomorphic with the β_1-V_2H phase.

4.2.2 Dynamical Properties

One of the earliest nmr studies of β-V_2H was reported by Zogal and Stalinski [4.44] in 1967, which showed that motional narrowing of the proton line starts to occur at about 130K in samples of $VH_{0.52}$ and $VH_{0.77}$. They observed two lines in each sample both of which narrowed to a constant value of about 100ppm in their powdered sample at temperatures above 240K. They were unable to identify the interstitial site occupancy of the hydrogens from their results but could conclude that there was a high probability that more rapid diffusion occurs within one of two sets of occupied sites.

Fukai and Kazama [4.45] later conducted an extensive nmr study of a range of VH_x powdered samples over temperatures from 90K to 550K at a time when much more was known about the structure of the system. Their study did much to improve the understanding of the nature of the β_1-β_2 phase transition which produces a distinct form to the T_1 temperature dependence and which does not fit a simple Arrhenius dependence. From their T_1 results they were able to show the variation of diffusional activation energy for the O_{Z1} and O_{Z2}-sites with composition and temperature across the phase transition from β_1 to β_2. They observed, for example, that the activation energy for the O_{Z1}-site monotonically decreased from 0.37 to 0.29 eV for x=0.486 to 0.736, whilst for O_{Z2} the activation energy increased from 0.23 to 0.29 eV over the same composition range (see also [4.43]).

Interestingly they were able to observe a relatively weak low-temperature second maxima in T_1^{-1} due to the more rapid ^{1}H diffusion on the O_{Z2}-sites. From their T_1 data they were able to extract mean jump times for diffusion on the two sub-lattices of O_Z-sites and satisfyingly found that both τ_{o1}^{-1} and τ_{o2}^{-1} were approximately equal to 2.2 x 10-

^{13} s^{-1}, where the subscript 1 or 2 refers to the type of O_Z site. Plots of the τ_2^{-1} data produced a reasonable fit to the Arrhenius expression unlike the τ_1^{-1} data. It was found that $\tau_2^{-1} = \tau_{o2}^{-1} \exp(-0.24eV/kT)$ such that by extrapolation $\tau_2^{-1} = 2 \times 10^{-10}$ s^{-1} at 400K, for example.

That the hydrogen diffusion takes place between ordered interstitial sites is confirmed by ^{2}D study of a β-V_2D sample as reported by Salibi et al [4.36]. By scaling the proton T_1 results of Hayashi et al [4.43] by the factor γ^2 they found their ^{2}D T_1 results were in good agreement with these especially for those values in the region where dipole relaxation dominates the ^{1}H results. Since γ^2 scaling can be misleading when comparing different isotope results, this study is very satisfying and leads to the conclusion that the dipole-dipole interaction is dominant in the temperature regime of 200-400K, as opposed to quadrupole or conduction electron interactions. That a T_1 maximum was observed in this region and that the structured deuterium lineshape was not averaged out confirms that the deuterium (and by analogy the hydrogen) diffuses on an ordered sub-set of sites.

Theoretical T_1 Anisotropy

The general theoretical angular dependence of the T_1 anisotropy according to Sholl [2.32] for diffusion on tetragonal and monoclinic lattices are given respectively by the expressions

$$T_1^{-1} \propto A_1 + A_2 \sin^2\Theta + A_3 \sin^4\Theta + A_4 \sin^4\Theta \cos 4\phi \; (= G) \qquad (4.7)$$

$$T_1^{-1} \propto G + \sin^2\Theta \cos 2\phi (A_5 + A_6 \sin^2\Theta) + (A_7 + A_8 \sin^2\Theta) \sin^2\Theta \sin 2\phi + A_9 \sin^4\Theta \sin 4\phi \qquad (4.8)$$

where the As contain the correlation function information as described in section 2.1.2d. In these equations Θ and ϕ describe the magnetic field direction with respect to orthogonal axes in the crystal. In the case of a monoclinic lattice the z axis is defined along the atomic site principal symmetry axis which is parallel to a two-fold axis or perpendicular to the mirror plane, and the x and y axes are arbitrary. The large number of variables in the monoclinic case contrasts with that for cubic symmetry as described by equation 2.26.

Whilst the O-sites mirror the structure of the metal atoms in these (pseudo-) body-centered systems, as has been seen in the previous discussion of the niobium hydrogen system proton diffusion is not exactly matched to general theory since hopping may be among non-structural sites (eg T- or O_{Z2}-sites in this case) and of course since the structurally occupied sites do not themselves form a Bravais lattice. One must therefore consider the specific known structural and dynamical properties in order to analyse or predict any T_1 anisotropy. Such a theoretical study has been made by Sholl in light of a detailed diffusion study of this system by Richter et al [4.40].

Richter et al [4.40] were the first to produce a single domain β-V_2H sample large enough to be usefully studied using qns to determine differential jump rates within the system. The sample was prepared using a "special heat process" to produce a single c-domain crystal, as shown in figure 4.21, having a surface area of about $5cm^2$. The crystal is substantially the same as that used in the nmr study reported by Hoke et al [4.41] which is discussed later and in this study reported in section 4.2.4 in which it is referred to as sample 4. Their analysis of qns data uses an iterative process to predict different jump rates based on a specific model for the orientational dependence of the scattering function with crystal orientation with respect to the incident neutron beam. Their method relies on the simple Chudley-Elliot model discussed in section 2.2.2 and on a pseudo-cubic treatment of the vanadium lattice. Because of the large difference in jump rates for hydrogen in the occupied plane compared to motion in the unoccupied plane, determination of hydrogen jumps rates in the system required use of both IN6 and IN10 spectrometers (described in section 3.2.1). In their analysis they allowed for four near neighbour jumps to O-sites within a plane and four to a different plane as shown in figure 4.24.

The hydrogen jump rates determined by Richter et al are shown in table 4.4, where $1/\tau_{o-u}$, $1/\tau_o$, $1/\tau_u$, and $1/\tau_{u-o}$ refer to rates for jumps from the occupied to empty plane, in the occupied plane, within the empty plane, and from unoccupied to occupied plane respectively.

Table 4.4

Temperature [K]	occupation of empty layer	$1/\tau_{o-u}$ [ns^{-1}]	$1/\tau_o$ [ns^{-1}]	$1/\tau_u$ [ns^{-1}]	$1/\tau_{u-o}$ [ns^{-1}]
390	0.04	0.15	0.04	-	3.6
400	0.051	0.24	0.05	22	4.5
410	0.064	0.53	0.08	25	7.7
420	0.08	0.9	0.16	30	10.3
430	0.11	1.67	0.35	29.6	13.5
435	0.13	1.85	0.62	-	12.4
440	0.15	2.87	-	-	16.2

Errors quoted for the above results vary for each datum but are typically of the order of 10%. It can clearly be seen that the hydrogen diffusion rate in the occupied plane is about two orders of magnitude less than in the unoccupied plane, and, not surprisingly, this difference is greatest at the lower temperatures. Additionally, the jump paths can be seen to be highly anisotropic and the dominant diffusion path is across non-structural sites All this new information is entirely consistent with the earlier nmr results of Fukai and Kazama on powdered samples and provides a firm basis for the present nmr studies of Knight shift and T_1 anisotropy in single crystal samples of β_1-V_2H.

Sholl has investigated the basic theoretical behaviour of T_1 in a single domain sample of β_1-V_2H [4.41]. Figure 4.25 shows the predicted behaviour obtained by Sholl using the jump parameters determined by Richter et al [4.40] as presented above in table 4.4. Sholl's analysis was based on a reciprocal space method to determine the spectral density functions $J(\omega)$ given in equation 2.17 for example. The jump probability function $P(\mathbf{r}_i, \mathbf{r}_j, \omega)$ (see for example equation 2.21) was assigned two terms corresponding to the two types of initial O-site occupied by a proton and each term was weighted by the probability of occupation of that type of O-site. Additionally, the analysis treated the vanadium lattice as cubic and did not consider the effect of either tetragonal or monoclinic distortion on the T_1 anisotropy.

Figure 4.25a shows the predicted dependence of T_1 on ψ, the angle between B_o and a <110> direction in the plane of hydrogens, ie ψ=0° for [$\bar{1}$10] parallel to B_o (see figure 4.21) and ψ=90° when B_o is aligned with the [001] axis also in the plane of the hydrogens as shown in figure 4.21. Figure 4.26b shows the predicted variation of T_1

with Θ, which is the angle between the [100] axis and B_0, for three different temperatures. The graphs show that a maximum in T_1 is expected for $\Theta \approx 40°$ and $\psi = 0°$. Some experimental results are also presented by Hoke et al and these are discussed later.

4.2.3 Sample 3: $VH_{0.53}$ Cylindrical Single Crystal

The preparation procedure for a β-VH_x sample was much the same as for β-NbH_x. In order to avoid the phase mixture regions it is necessary to maintain a temperature greater than 200°C but otherwise trial experiments showed that an optimum hydriding temperature range was between 320°C and 250°C. The trial attempts to hydride polycrystalline rods of V to a composition of $x \approx 0.5$ initially proved difficult however, and it was found necessary to coat the vanadium rods with a surface layer of palladium to enhance the hydrogen absorption [4.49]. This presents a possible problem in preparing a good single crystal sample in that palladium atoms may be absorbed into the vanadium surface forming a non-crystalline alloy. However, palladium is only found to be absorbed into vanadium to a concentration of less than 20% and then only when they are heated together in alloying experiments at 1200°C and quenched [4.51]. The experimental conditions used here of lower temperatures followed by gradual cooling to room temperature should therefore largely avoid the problem of Pd-V alloying. The palladium could therefore be removed by etching after hydriding the vanadium crystal.

A high purity 18g vanadium single crystal was obtained from Goodfellow metals having the same crystal orientation as the cylindrical niobium sample 1 which is shown in figure 4.8. The crystal is 12mm in diameter and 26mm in length. The crystal was degassed, to improve prospects of hydriding to a desired concentration, by David Fort at Birmingham University. The crystal was degassed down to a pressure of 1.3×10^{-7} Pa at up to 1300°C without significant evaporation of surface contaminants. The crystal was then rolled in Palladium Black which had also been degassed using the hydriding apparatus described in chapter 3 to less than 1.3×10^{-3} Pa at 800°C. The surface layer of Pd formed <0.05% by mass of the crystal and could therefore be ignored in the calculation of the resultant composition of the VH_x sample formed.

The crystal was loaded into the hydriding equipment and heated to 850°C at 1.5 Pa before exposure to hydrogen gas at a pressure of 10^5 Pa in the calibrated volume. The temperature was lowered over a period of two days to 350°C and then gradually lowered down to 210°C over the next five days. This run only produced a composition of

x≈0.35. The crystal temperature was again raised to 850°C and degassed to about 1.5 Pa. It was then exposed to hydrogen at about 10^5 Pa and the temperature lowered to 330°C over two days followed by a gradual lowering to 260°C over 3-4 days. This last cycle formed a β_1-phase sample of composition $VH_{0.53 \pm 0.01}$. On removal from the apparatus the crystal had visible surface cracks.

An etchant of HF: HNO_3: H_2O, in the ratio of volumes 20ml (at 60% concentration):10ml:15ml respectively, was used to remove the palladium layer from the sample. Subsequent x-ray analysis revealed that the sample was composed of many small crystallites and/or domains with dimensions of the order of 100μm. This was determined through repeated observation of back-reflection Laues patterns at many different points on the crystal surface. Distinct sharp reflections were observed with little overall coherent symmetry. That is, several distinct crystallites exist within the 1mm beam diameter, but no Bragg arcs were observed which would have been apparent in a largely polycrystalline or powdered sample. Because of the lack of coherent crystallinity no check of the concentration from lattice parameter measurements was possible.

NMR Experimental Details

NMR studies of the crystal were carried out at 19.8 and 47.0MHz using 32 turn, 27 swg and 14 turn, 22swg enamelled copper wire coils respectively. Coils were wound direct onto the crystal separated only by a single 50μm layer of PTFE. The length of the coils was approximately equal to that of the crystal in order to maximise the proton nmr signal. According to Fromm and Gebhardt [4.46], the resistivity of vanadium hydride depends on hydrogen concentration as ρ=1.7μΩcm/At%H. The skin depth is therefore of the order of 63μm at 19.8MHz and 41μm at 47MHz.

Knight Shift Study

The proton lineshape orientation dependence which was observed at 47MHz and 298K for the $VH_{0.53}$ sample is shown in figure 4.26. As is apparent from the figure, an anisotropy was observed in the lineshape.

The orientation dependence which is evident certainly confirms the presence of large regions of crystallinity and therefore of crystalline domains within the sample. However, analysis of the lineshapes is rather difficult due to the lack of resolution of individual lines. This is unlike the β-NbH_x multi-domain sample reported in section 4.1.3 where separate lines were clearly resolved for the distinguishable domains.

As stated earlier certain behaviour of two lines from the distinguishable domains in this sample is predicted, similar to the β-NbH_x multi-domain sample, and since measurements were made at a temperature in the motionally narrowed regime of the hydrogen line for both the O_{Z1} and O_{Z2}-site hydrogens in the β_1-phase there should only be a single line from each domain. However, the best fit to the data was obtained by fitting four (rather than two) lines. The fitted lines at the two extremes of the observed variation (which was symmetrical about the 90° orientation) are shown in figure 4.27. In the figure, part a shows the lineshape for θ=0°, ie [001] (of the original vanadium bcc lattice) parallel to B_o, and part b is θ=90°, ie [1$\bar{1}$0] parallel to B_o. The full range of the scans shown is 2mT.

The fitted lines are indicated by the letters A, B, C and D where the latter two are found to be isotropic. The anisotropic component(s) of the lineshape are unresolved but are found to be best represented by lines A and B which also vary in magnitude and which do not therefore represent a 'species' of hydrogens in themselves. Also, the behaviour of the lines A and B with orientation is not the same as predicted for this system. The fitted parameters for each line are:

Line	Linewidth (FWHM)	Shift ΔB ($B_{\theta=0°}$-$B_{\theta=90°}$/B_o)	Amplitude θ=0°	θ=90°
A	200ppm	41ppm	2.0	1.0
B	200ppm	23ppm	2.4	4.0
C	200ppm	0	0.8	0.9
D	1000ppm	0	1.0	1.0

Both lines C and D are isotropic with a relative magnitude of 1. Best fits to the anisotropic form of the line are achieved by two further lines A and B having fixed linewidths but varying amplitude and which lines shift to lower fields with an increase in angle of the [001] axis relative to B_o, as shown above by the parameter ΔB. As can also be seen from the above tabulated values some discrepancy exists in the sum of the amplitudes of the fitted data. On the whole the spectra are not as expected and are not very satisfactory due to the lack of resolution. Nevertheless, before proceeding with a study and analysis of T_1 variation in this sample it is necessary to try to at least ascribe some meaning to the spectra.

Two possibilities exist for line C which might be the result of some region of polycrystallinity of a different phase to the β_1-phase, assuming that the substantial

signal is from regions of β_1-phase which also produce anisotropic lines A and B. Alternatively, the <110> type axes could possibly form a principal symmetry axis for the sites occupied by the hydrogens, which are likely to be O-sites (or T-sites for the α-phase). This therefore seems highly unlikely both intuitively, based on the known structure of the O-sites, and from comparison with quadrupolar studies of the equivalent deuterium system [4.36] where the principal symmetry axis is predictably found to be the <001> axis. The known isotropic Knight shift is found to vary little with hydrogen concentration $x<0.6$ and for both the α and β-phase is approximately equal and about -60ppm [4.20]. Line C, if truly an isotropic line, might therefore be due to the presence of polycrystalline regions of a different phase which might have formed due to an uneven distribution of hydrogen in the sample during the hydriding process. Whilst all lines except line D have a full-width at half maximum consistent with previously reported values for this system, line D is anomalously broad. This may be due to a fraction (about 15%) of hydrogens within the skin-depth region of the sample studied existing in a range of environments due to dislocations, grain boundaries, palladium-hydrogen phase(s) or a range of vanadium-hydrogen concentration regions. This seems possible given the hydriding route (ie temperature cycling and complex phase transitions) required to form the sample.

As stated above the fitted lines A and B cannot in themselves represent a species of hydrogen unlike the two lines resolved for the β-NbH, sample 1. In addition to the amplitude discrepancy, for example the two fitted lines do not converge at $\Theta=55°$ as would be predicted. Otherwise lines B and A might be distinguishable domains of β_1-$VH_{0.53}$ in the sample, where two domains would have an orientation of $\Theta=45°$ when $\Theta_i=0°$ ([001] parallel to B_o) and one domain $\Theta=0°$, cf equations 4.2 for theβ-NbH system. Unfortunately it is not possible to give any definate interpretation of the observed anisotropy nor to provide any quantitative results for K_{AX} or K_{AN} which might exist; though it is noted that Salibi et al have previously reported that K_{AX} is negligibly small [4.36].

Due principally to the lack of resolution and also to the variety of possible explanations for the observed lineshape variations as set out above, it is not possible to characterise the sample with any certainty. Nevertheless it is apparent from the Knight shift results that some kind of crystallinity and therefore domain structure exists in the sample which is suitable for further study of its T_1 properties. It is thought that the bulk of the proton signal is likely to be from hydrogens in a β_1-phase environment from

previous success in making samples, the accuracy of determining the sample composition and given the known phase diagram of the system.

T_1 Study

Previous nmr studies (eg, Fukai and Kazama [4.45]) show that the main (ie due to O_{Z1}-site proton diffusion) dipole-dipole minimum in T_1 for the β-phase occurs between 300 and 400K when studied at between 5 to 25MHz. Indeed, Fukai and Kazama found that $\tau_{o1} = 5 \times 10^{-14} \exp(0.38eV/kT)$ such that it can be shown for example that $\omega_o\tau_c \geq 10$ for $T \leq 300K$ and 47MHz. Therefore, these proposed conditions for this study are in the low temperature regime of the dipole-dipole interaction.

However, Sholl theory [4.52] shows that the largest differences in T_1 are expected at the highest frequencies. He has shown for example, that R_{1max}/R_{1min} is 1.11 at 100 MHz. and 390K when $\Theta=0°$, and $\Theta=54.7°$ and $\psi=45°$ respectively. While $R_{1max}/R_{1min} = 1.006$ at 20 MHz and all other conditions the same. Note of course that $\omega\tau=3.2$ in the latter case and 16 for the former but that this factor of 5 does not account for the difference of the predicted anisotropy of 0.6% and 11% respectively.

Extensive measurements of T_1 at 19.8MHz did not resolve any anisotropy in T_1 with crystal orientation. At 47MHz a T_1 anisotropy was observed at about 289K which, at least, confirms the sample retains some degree of crystallinity. Figure 4.28 shows the typical form of T_1 versus Θ observed, whilst some T_1 versus reciprocal temperature data is shown in figure 4.29. The latter shows that a value of $T_{1e}T=113sK$ (±5 sK) exists for this sample in good agreement with the expected value for a sample of this concentration [4.45].

Many measurements were made on this system and on average the anisotropy of $T_{1[110]}/T_{1[001]} = 1.05$ at 289K where T_1 is in the range of about 185 to 177ms. Allowing for an isotropic conduction electron contribution to T_1 at this temperature the anisotropy of the dipole-dipole interaction component of T_1 is increased to about 8% only. The angular form of the anisotropy is in good agreement with that predicted for ψ and as shown in figure 4.25(a). This would suggest that the [001] axis is in the plane of the occupied hydrogen layers of O_{Z1}-sites and that the sample is predominantly a C-domain. Thus, ψ would be the angle between B_o and the $[1\bar{1}0]$ axis, which would also necessarily be in the plane of occupied hydrogen sites (compare figures 4.8 and 4.21). For this C-domain then, the predicted Θ dependence of T_1, shown in figure 4.25(b), would modulate the ψ effect somewhat since Θ is the angle of B_o with respect to the

[100] axis which varies from 90° when ψ=0° to 45° when ψ=90° (ie $\Theta=(\pi - \psi)/2$). Assuming A- and B-domains are also present in the sample their contribution to the form of the T_1 angular dependence for rotation of this sample leads to a much more complex situation. As with the cylindrical sample of β-$NbH_{0.76}$ (sample 1) the contributions would need to be weighted according to the relative population of each of the domains. It is apparent that even if this relative occupation of the different domain types were known, the information which could be gleaned from this sample about the hydrogen diffusional paths would be minimal. What appears to be the requirement for this complex system is a much more precisely defined, single domain sample; and preferably several, each having different orientations to enable selective rotation of crystal axes with respect to B_o.

4.2.4 Sample 4: β-V_2H Plate-like C-Domain

Towards the end of these studies, a laminar C-domain single crystal of β_1-V_2H was provided by Harlan Schone. This sample was prepared by Hempelmann using the same technique employed to prepare the sample for the neutron scattering measurements [4.40] which were discussed in section 4.2.2. The full details of this sample preparation technique have not yet been published. However, it consists of first exposing a laminar single crystal of vanadium to a hydrogen atmosphere in order to hydride to the desired composition. A special heat treatment is then used to produce large single domains. The sample is then studied using neutron diffraction to determine a region of the sample containing a large single domain and this domain is cut from the planar sample to provide a sample which is essentially a single domain. The exact composition of this sample is not known.

The sample was somewhat irregularly shaped. It had the basic configuration shown in figure 4.21 with width b=12mm, thickness d=1mm but with length l=27.5mm on one side and l=40mm on the other.

NMR Experimental Details

Measurements were made at 19.8MHz for which a coil consisting of 42 turns 27 swg wire was used. The crystal was wrapped in two layers of 50μm thick PTFE sheeting and also supported by two PTFE splints at its edges. The coil was wound around the PTFE sheeting and splints and held in place by PTFE tape. The splints were used to firmly attach the crystal to the nmr probe again using PTFE tape. This configuration

gave a coil filling factor of one third and a relatively high Q (for single crystal samples studies) of 14 was obtained at 19.8MHz with a coil inductance of 4μH.

Knight Shift Study

The plate-like sample has a width of about 12mm and depth of 1mm similar in proportion to the disc-like NbH sample studied in section 4.1.4 which has a diameter of 12mm and depth of 1.5mm and α=39ppm. Since this vanadium sample cannot be rotated in the manner described in the Knight shift section for the niobium sample in order to determine the factor α of equation 4.5, an initial estimate of α for this sample is determined from the relative values of χ_v reported by Kazama and Fukai [4.20] for each system. They report a value of $\chi_v \approx 12\times10^{-6}$ emu/cm^2 for $NbH_{0.75}$ and $\chi_v \approx 30\times10^{-6}$ emu/cm^2 for V_2H. An initial estimate of α for this sample might be of the order of 100ppm, though the true value depends on the shape and direct comparison of the two samples is limited, due especially to the irregular shape of the niobium disc sample.

For this sample the O-site principal symmetry axis is aligned with B_0 when the plate's faces are perpendicular to the field (see figure 4.21). Therefore, taking Θ=0° when the principal symmetry axis is aligned with B_0, equation 4.5 becomes

$$S(\Theta) = K_{AX}(3\cos^2\Theta - 1) - \alpha\sin^2(90-\Theta) \qquad \{4.9\}.$$

The orientational dependence of the observed proton line for this sample is shown in figure 4.30. It can be seen that a single line is observed of full-width at half-maximum of 225 (±20) ppm. The observed shift between the orientational extrema is 170 (±20) ppm. The orientational dependence of the lines is in reasonably good agreement with equation 4.9 and yields a value of α=170ppm (±20ppm). A reasonable fit to the data can also be achieved for a range of magnitudes of K_{AX} up to about 10ppm (for which α correspondingly decreases to 140ppm for K_{AX}=-10ppm, for example). The results appear therefore to confirm that the sample is a good single domain β_1-phase of approximate composition V_2H.

T_1 Study

Figure 4.31 shows the variation in T_1 with orientation of the sample relative to B_0 typically observed for sample 4. An anisotropy of $T_{1max}/T_{1min} \approx 1.10$ is typically observed, where T_1 =145 (±5) ms for Θ=0° and 160 (±5) ms for Θ=90°, when T=289K and ν_0=19.8MHz. However, allowing for an isotropic T_{1e} component of T_1, the anisotropy in the dipole-dipole component increases to 17%. In this case the angle shown in the

figure is the angle ψ which is that between the [$\bar{1}$10] axis and B_o. The relaxation rates for the ψ dependence predicted by Sholl and as observed by Hoke et al [4.41] are shown in figure 4.25(a). The angular dependence of the T_1 anisotropy observed here is in excellent agreement with the predictions of Sholl which are based on the diffusion mechanism determined by Richter et al [4.40] and are much more sophisticated than predicted by standard theory for the basic lattice structure (see equations 4.7, 4.8 and for the cubic case 2.28a).

The measurements of Hoke et al [4.41] were carried out at 83MHz and show a consistently large anisotropy of the order of 50% in the range of temperatures 390K to 315K. Hoke et al acknowledge that the observed anisotropy is about five times larger than predicted but unfortunately offer no explanation for this. Also, they do not explain their observation that the anisotropy is constant over such a large range of $\omega\tau$ which ranges from approximately unity near the dipole-dipole maximum to well into the low temperature regime. The predicted anisotropy does depend on $\omega\tau$ naturally, as discussed in the T_1 study part of section 4.2.3, but a maximum anisotropy of about 16% is predicted for certain $\omega\tau$ and orientation. The anisotropy observed here at 19.8MHz of 17% therefore appears to be in good agreement with theory. It might be construed that the experimental observation supports the theory of Sholl and thus the experimental work of Richter et al also. However, this would probably be too strong a supposition based on the limited study carried out here. Also some questions have been raised by the results found by Hoke et al which require further study.

The ideal objective of this type of study would be to extract values of τ for diffusion on each of the O_{Z1} and O_{Z2}-sites in a manner similar to Fukai and Kazama [4.45] and to observe the orientational variation of T_1 in order to determine the orientational dependence of the jump rates; that is, as achieved by the neutron scattering study of Richter et al [4.40]. This would require a large number of single domain samples, which are of course difficult to prepare, to enable a large number of accurate T_1 measurements over a range of orientations, Θ and ψ, temperatures and frequencies.

4.2.5 Discussion

The preparation of a single domain single crystal sample of β_1-V_2H has proved more difficult than for β-NbH. Accordingly, the nmr study of this vanadium phase has been somewhat limited. In the case of β-NbH it was found relatively easy to prepare a cylindrical single crystal sample suitable for nmr work and despite having a multi-domain structure the sample could provide interpretable nmr results. Indeed, a

single domain sample was also prepared after much trial and error. In the case of the vanadium-hydrogen system however, the preparation of a single crystal β_1-phase sample is complicated by an intermediate β_2-phase and second order transformations which lead to nucleation growth rather than domain propagation throughout the sample. It is known that complex growth procedures involving the application of large tensile stresses have been used in order to successfully obtain single domain β_1-phase samples with specific orientations [4.42]. The high pressure technique effectively suppresses the formation of the β_2-phase enabling a direct α to β_1-phase transformation. Furthermore, Hempelmann has developed an unpublished method of hydriding large crystals using a specific heat treatment by which he produces large single domain regions in the crystal [4.40]. The orientation of these regions is then charaterised by neutron diffraction study.

These techniques are beyond the capability of apparatus presently available at Warwick. Nevertheless, a cylindrical sample having a crystalline structure was prepared but the complex domain structure of the sample eluded interpretation since the proton nmr lines remained unresolved. Further Knight shift studies of the single domain sample at various crystal orientations revealed that axial Knight shift up to ±10ppm might exist.

The T_1 study of the single domain sample was not as complete as would really be desired and was somewhat limited by the shape and orientation of the sample. Both the cylindrical multi-domain and plate-like single domain samples revealed an anisotropy in T_1. In the case of the latter sample, this could firmly be attributed to the predicted orientational behaviour for the known orientation of the sample based on the theoretical predictions of Sholl [4.41] which are based on the anisotropic jump mechanism determined by Richter et at [4.40]. The results therefore tend to confirm both these works. But it would really be necessary to conduct a further rigorous study of this system in order to come to any firm conclusions.

4.3 α-YH_x

4.3.1 Formation and Structural Properties

Yttrium is a group III transition metal with a hexagonal close-packed structure which is capable of absorbing up to three hydrogen atoms to every metal atom. The phase diagram shown in figure 4.32 is that compiled by Khatamian and Manchester [4.53] from the large quantity of published data on the YH_x system. The phase

diagram shows that only two stoichiometric hydride phases exist, the fcc dihydride and hcp trihydride.

This system has been investigated extensively, and in recent years special attention has been paid to anomalies observed in the solid solution phase in the composition range of the present single crystal nmr study. The α-phase of YH_x is stable at room temperature up to a relatively large concentration of x=0.25, in common with other lanthanides such as scandium and lutetium, and shows a linear increase in lattice parameters a and c with hydrogen concentration. The hydrogens occupy the T-site almost exclusively.

The interest in the α-phase arises since, for example, the limiting concentration of 20% is unusually large and is constant for virtually all temperatures less than 400K. In most systems the limiting concentration decreases with decreasing temperature. Also, various resistivity anomalies have been observed in α-YH, as well as α-ScH_x and α-LuH_x which have a similar hcp structure to yttrium [4.54-4.56]. It has been proposed that the reason for the various anomalies is an ordering of the hydrogens into pairs and, at lower temperatures, into chains along the c axis of the hcp lattice [4.55,4.57,4.58]. In the case of YH_x the ordering occurs below 403K with further ordering around 173K. In the higher temperature regime the hydrogens form pairs on next nearest neighbour T-sites along the c-axis, that is across the metal atoms. Pairing of some nature had been proposed for some time but the fact that it occurs across the metal atoms accounts for the experimental nmr observations by Lichty et al [4.59] of the lack of a Pake doublet which would have been expected for pairing in the a-b plane. A schematic diagram of one of the models proposed for the long range ordering in these systems at lower temperatures is shown in figure 4.33 which shows the zig-zag ordering of pairs of hydrogens in chains along the c direction.

A schematic view of the atomic cell of the α-YH_x system is also given in figure 4.33. The main, six fold symmetry axis is along the c axis and the cell parameters can be described by $a=b\neq c$, $\alpha=\beta=90°$ and $\gamma=120°$. The T-sites form chains along the c-axis with near neighbour sites separated by c/4 and next nearest neighbours at 3c/4. The near neighbour T-sites are separated by ≈1.43Å and the Swittendick criteria would preclude near neighbour pairing.

The pct curve for the binary YH_x system is shown in figure 4.34, see also [4.60 and 4.61]. The general hydriding characteristics of this system can be seen to be similar to those of Nb and V. However, as is readily apparent from the pct curve the α-phase

composition is saturated at relatively low temperatures and pressures thereby presenting the problem of formation of crystallites of the dihydride-phase in the single crystal. In order to avoid this possibility the parameters for the gaseous absorption method of preparation of a single crystal sample were somewhat different to those for Nb and V as discussed in section 4.3.3.

4.3.2 Dynamical Properties

Several studies of the dynamical properties of the α-YH_x system have been made which are in generally good agreement with one another, and the hydrogen diffusivity is found to be Arrhenius in nature. The diffusion parameters derived from independent qns and nmr studies are respectively E_a=0.57±0.03eV and τ_o^{-1}=28.6THz [4.62], and E_a=0.51±0.02eV and τ_o^{-1}=11THz [4.59]. Anderson et al [4.62] have conducted a qns study using the IN10 instrument of a single crystal sample of $YH_{0.2}$. They determined the individual jumps rates between the different sites at temperatures in the range 593K to 695K. In common with earlier work they show that the T-T near neighbour jump rate is extremely fast compared to the overall diffusion rate. They evaluate a very low activation energy of Ea=0.09±0.02eV for this jump compared to the activation energy given above for the T-O site jump (see figure 4.33). They determine site dwell times at 593K to be; τ_{OO}=39ps, τ_{TT}=1ps, τ_{OT}=80ps, and τ_{TO}=2433ps whilst the diffusion coefficients perpendicular to and along the c-axis are respectively D_a=0.90x10^{-7} cm^{2}s^{-1} and D_c=2.48x10^{-7} cm^{2}s^{-1}. They therefore show that the diffusion rate determining step is between the T and the O-site and that a certain anisotropy in the diffusion mechanism exists, ie a preference to jump along the c-axis via O-sites, at the relatively high temperatures of their study.

In order to analyse any single crystal T_1 measurements it is necessary to have some idea of the theoretically predicted behaviour in this system. In chapter 2, theoretical expressions were given for the T_1 angular dependence in hexagonal systems due to the dipole-dipole interaction (equation 2.29) and conduction electron interactions (equation 2.36 and c.f. 2.31). For ease of reference the general form of the former is

$$T_1^{-1} \propto A+B\sin^2\Theta+C\sin^4\Theta \qquad \{4.10\}$$

whilst the latter can probably be ignored due to the axially symmetric nature of the T-site. These general studies have been developed in collaboration with Sholl [4.63] for a

specific diffusion mechanism in a hcp metal lattice from which it is possible to predict the angular dependence of the proton T_1 in the low temperature regime.

The jump model considers six T-O-T jumps from a T-site, represented by the coordinates (0,0,0), to an O-site having coordinates (-1/3,1/3,1/8), and beyond to the six T-sites surrounding the O-site; these are desribed as follows where each is assigned a probability ω_i:

(0,0,0)+	(-1/3,1/3,1/8)+	(1/3,-1/3,-1/8)=	(0,0,0)	ω_1
"	"	(-2/3,-1/3,-1/8)=	(-1,0,0)	ω_2
"	"	(1/3,2/3,-1/8)=	(0,1,0)	ω_2
"	"	(2/3,1/3,1/8)=	(1/3,2/3,1/4)	ω_3
"	"	(-1/3,-2/3,1/8)=	(-2/3,-1/3,1/4)	ω_3
"	"	(-1/3,1/3,1/8)=	(-2/3,2/3,1/4)	ω_4

where $\omega_1+2\omega_2+2\omega_3+\omega_4=1$. The ω_1 (a jump back to the original site) and ω_2 hydrogen jumps allow for motion in the same a-b plane, while ω_3 and ω_4 represent jumps to a different a-b plane (ie motion along the c-axis) as well as lateral motion in the a-b plane. It is not possible for a hydrogen simply to move linearly along the c-axis unless one or more intermediate O-O site hops occur. Whilst such jumps have been shown to occur at higher temperatures by Anderson et al [4.62] they are not accounted for here.

In two specific jump models different probabilities are assigned to individual jumps as follows:

Model 1	all $\omega_i=1/6$	all jumps equally probable, and
Model 2	$\omega_1=\omega_2=\omega_4=0$, $\omega_3=1/2$	jumps to nearest chains only.

The form of the relaxation rate given above in equation 4.10 can be determined for this model based on mean field theory to account for site blocking [4.63]. The predicted anisotropy in the magnitude of T_1 produced by each of these models is 16.9% between $\Theta=0°$ and 50.1° for model 1, and 15.4% between $\Theta=0°$ and 47.4°. Figures 4.35 and 4.36 show the R_1 dependence for the specific hydrogen jump models 1 and 2 respectively, see also table 4.5 below. The difference in the angular form and magnitude of the anisotropy predicted by the two models is fairly minimal but accurate determination of the angular dependence of T_1 for a single crystal of α-YH might provide some insight into the nature of the hydrogen diffusion.

A recent study by Hoke et al [4.41] of a single crystal sample of ScH_x has been reported. The theoretical predictions presented in that paper are for ScH scandium-hydrogen dipole-dipole interaction which dominates the relaxation in contrast to the case for α-YH_x. The theoretical predictions and experimental results presented are shown in figure 4.37.

One of the advantages of the YH system is that yttrium has a very small gyromagnetic ratio γ, and therefore relaxation of the hydrogens through the unlike dipole-dipole mechanism is negligible. This is not the case for the ScH system for which a characteristic high temperature peak in the hydrogen R_1 is observed due to the cross relaxation mechanism. A single crystal of α-ScH_{025} has been studied by Hoke et al [4.41] who present a theoretical form of the hydrogen relaxation rate quite different to that predicted here for α-YH, see figure 4.37. The diffusion model considered by them is different to that used here and allows for highly anisotropic diffusion at low temperatures which is due to rapid hopping between near neighbour T-sites.

4.3.3 Sample 5: $YH_{0.17}$ Cylindrical Single Crystal

Sample Preparation

A very high purity 15.4g boule of yttrium was obtained from the Ames laboratory. Mass spectroscopic analysis showed that the crystal had a low impurity content; less than 1ppm for most impurities. The highest concentration impurities observed by vacuum fusion analysis were; La 7ppm, Fe 17ppm, C 59ppm, N 63ppm, F 10ppm ,Cl 4ppm and H 1408ppm by weight. A large single crystal was drawn from the melt using a Y seed by David Fort of Birmingham University. From the large crystal a cylindrical sample was cut having dimensions of 22mm length by 8mm diameter. The crystal weighed 5.18g. The hcp crystal was oriented so that a crystallographic b axis, or [1120] axis in Weber notation, is aligned along the cylinder axis and the c axis, [0001], is perpendicular to this. Thus, the main crystallographic symmetry axis can be rotated with respect to the magnetic field about the cylinder axis, see figure 4.38. After x-ray analysis of the crystal the c-axis direction was marked on the end of the cylindrical sample.

Many etchants are recommended in the literature for use with yttrium, for example; lactic, phosphoric, acetic, nitric and sulphuric acids in the ratio 20:5:10:15:1, phosphoric, lactic, nitric and acetic acids in the ratio of 1:1:3:2, and a mixture of

perchloric acid and absolute methanol used with a dry ice and acetone bath. However, an easy to prepare and satisfactory etchant was found to be a mixture of high purity nitric and acetic acids in the ratio of 2:3 followed by washing first in high purity water and then in high purity acetone.

The crystal was hydrided using the apparatus and technique described in section 3.3, where the calibrated reference volume used was approximately 28 litres. This large volume was found to be necessary in order to allow reasonable assessment of the amount of hydrogen absorbed by the sample (ie an observable change in hydrogen pressure) whilst preventing the formation of the dihydride phase at the experimental temperatures. After etching and degassing the sample the calibrated volume was loaded to 5mmHg and introduced to the crystal at 1100°C. The sample temperature was lowered over a 24 hour period to ambient temperature. A sample concentration of $YH_{0.17\pm0.01}$ was obtained and confirmed through calculation of gaseous moles absorbed, crystal weight gain and x-ray analysis.

NMR Study

Having determined by x-ray analysis that a good single-phase single crystal of composition $YH_{0.17}$ had been prepared, a Knight shift and T_1 anisotropy investigation was carried out. From previous nmr data, see for example that of Lichty et al [4.61], the optimum conditions in which to work would be to use a low frequency such as 10 MHz in order to observe a dipole-dipole dependent T_1 through a large range of temperature below room temperature.

Several factors inhibited use of these low frequencies. First the coil required to tune at the 9.8 MHz frequency was a 70 turn 40 gauge copper coil having a Q of about 1 only, when mounted on the crystal and separated from it by a 50μm layer of PTFE foil as usual. Due to the skin-depth effect, the low hydrogen concentration in the sample and the low signal due to the low field, a very small and barely observable proton signal was obtained which was insufficient to enable accurate determination of T_1 to the precision known to be required for these studies.

The best signal was obtained at 47 MHz where a 14 turn coil of 22 gauge wire was used, again mounted on the crystal using a layer of PTFE. This arrangement gave a proton signal to noise ratio of about 1:1. The study required use of a tapped series tuned probe matching circuit as shown in figure 3.2b.

Knight Shift Study

A Knight shift study at 47 MHz confirmed the x-ray analysis that a good crystal had been prepared and revealed an anisotropic dependence with crystal orientation with respect to field in accordance with equation 2.12. The experimentally observed orientation behaviour is shown in figure 4.39from which it can be seen that the system is axially symmetric with K_{iso}=-58ppm and K_{ax}=-12ppm±4ppm. These results are in reasonably good agreement with those observed by Barnes et al in a high resolution powder study [4.64].

T_1 Study

Figures 4.40 to 4.42 show the experimentally observed orientational dependence of the proton spin-lattice relaxation rate for this sample at T=290K, 173K, and 77K respectively. The nature of the anisotropy at 290K is in excellent agreement with theory as discussed below. At 173 and 77K however, where the dipole-dipole interation is much weaker than the conduction electron interaction with the hydrogen nuclei, there is minimal anisotropy outside the deviation of the experimental error for the values of T_1. Nevertheless the data does enable an estimate of $T_{1e}T$ which is found to be about 160sK which compares reasonably well with that of Lichty et al [4.59] of 180sK observed for their sample of $YH_{0.2}$.

At 290K the anisotropy is greatest between $\theta \approx 45°$ and 0°, ie c-axis parallel to B_o in the latter case, where $T_{1(45°)}/T_{1(0°)} \approx 1.15$ and the typical T_1 measured 520ms/452ms. These results appear to be in very good agreement with theory as can be seen by comparing the form of the anisotropy shown in figure 4.40 with that theoretically predicted and shown in figure 4.35 and 4.36. That the angular form is in good agreement with theory is very satisfying, but as stated earlier, it does not necessarily identify any preferred diffusion mechanism since different theoretical models provide similar magnitudes of anisotropies. And indeed, in this case the magnitude of anisotropy is in fact quite dissimilar to the prediction once the conduction electron contribution to T_1 is taken into account. The maximum anisotropy of the dipole-dipole interaction contribution to T_1 is then of the order of 85%, see table 4.5.

For the sake of comparison of the experimental results with theory, the magnitude of the anisotropy has been calculated for a two dimensional diffusion model, model 3, in which only diffusion in the a-b plane is allowed; thus ω_1=1/3 and ω_2=1/3 in this

model. The ratios of anisotropies for the theoretical models and for the observed T_1 are given in table 4.5.

Table 4.5 Comparison of the observed anisotropy in the proton relaxation rate with that predicted by models 1 and 2 described earlier, and model 3 described above. For the experimental data R_1 at Θ=45° is taken as R_1 min.

	Observed T_1	T_{1d}	Model 1	Model 2	Model 3
$R_1\ \Theta$=0° / R_1 min	14%	85%	16.9%	15.4%	24.1%
$R_1\ \Theta$=90° / R_1 min	6%	34%	9.6%	13.0%	10.4%
$R_1\ \Theta$=0° / $R_1\ \Theta$=90°	8%	17%	9.9%	4.6%	12.4%
Θ_{min}	45°-55°	45°-55°	50.1°	47.4°	51.0°

The errors in the extracted values of T_{1d}^{-1} are large since there is an error of the order of 10% in each measurement of T_1. For example, it can be seen from figure 4.40 that the error bars for Θ=0° and Θ=45° almost overlap, thereby presenting the possibility that the anisotropy is in fact of the order of only a few percent.

It is clear that the predicted anisotropy from the third (two dimensional) diffusion model is the greatest and is considerably more than predicted by the other two models and might at first be attractive. However, it would be unrealistic to draw any conclusions about the diffusion mechanism from these results given the possible errors in the observed anisotropies.

4.3.4 Discussion

The results of the angular form of the T_1 anisotropy for hydrogen in this system is very satisfactorily in agreement with the theoretical prediction. This certainly confirms that firstly the theoretical analysis is a good approximation to the real system and secondly that the hydrogen diffusion mechanism is comparable to the mechanisms considered if not exactly the same. Despite arduous attempts to achieve as accurate data as possible, a precision of only ±10% in the T_1 data could be achieved for this sample at 290K. The large magnitude of anisotropy observed, a factor of between 3 and 5 greater than that theoretically predicted, does not enable any reasonable assessment of the likely diffusion mechanism at these temperatures to be given. Since the largest anisotropy is predicted by the two dimensional mechanism (model 3) this might apparently be a contender but for the errors in the magnitude of the extracted

anisotropy. It is worth noting also, that such a mechanism would be in direct contrast with the three dimensional diffusion mechanism observed by Anderson et al [4.62], albeit at much higher temperatures where no ordering occurs.

In order to overcome the problems of low signal intensity from single crystal sample of the system it would be appropriate to prepare a sample made of many single crystal discs which are aligned and mounted on top of one another to form a cylinder. This sample might enable accurate T_1 measurements to be made over a range of frequencies and temperatures. In this regard it would be interesting to look at the form of the T_1 anisotropy at higher temperatures in the high temperature regime since Sholl has shown that there may exist an asymmetric gradient in $1/T_1$ v Ln(T) for hexagonal systems [2.44]. Of course further difficulties would be experienced at higher temperatures such as evaporation of the hydrogen and loss of signal due to the Boltzmann factor. Nevertheless these are areas of possible further study.

4.4 Conclusions

The investigation of the spin-lattice relaxation rate dependence on both the temperature and crystal orientation of various single crystal samples has been presented here. Generally excellent agreement in the nature of T_1 v θ is found between theory and experiment. This enabled certain conclusions to be drawn about the nature of the hydrogen diffusion mechanism for each of the systems studied. The ability of nmr to provide exact information about hydrogen jumps in single crystals is however, somewhat doubtful unless the crystals can be better characterised and the measurement precision improved.

This situation is somewhat different to that in qns studies, several of which have been discussed here and have generally given quite precise results. The difference between nmr and qns would appear to be that the nmr T_1 is caused by many interactions which in practical terms means that only certain systems under only limited physical conditions can be studied. This also means that the observations are the result of a combination of interactions which might not be readily distinguished. Additionally, the anisotropy of T_1 can be fairly insensitive to different hydrogen jump models for the same system.

Nevertheless, nmr undoubtedly provides much useful information about these metal-hydrogen systems. This area of single crystal work should become easier for both qns and nmr studies since single domain samples are essential and are now becoming

available due to increased research in this field and improved techniques of sample preparation.

References

4.1 Köbler U and Welter J M. J Less-Common Met. **84** 225.(1982).

4.2 Smith J F, Bull. Alloy Phase Diagrams 4(1) (Jun 1983), also in Binary Alloy Phase Diagrams. Ed. Massalki T B, Am Soc for Metals, USA, (1986).

4.3 Wenzl H and Welter J-M. Current Topics in Materials Science. Vol 1 and 2. (ed) Kaldis E, North-Holland. (1978).

4.4 Alefeld G and Völkl J, in Völkl J and Alefeld G (eds). Topics in Applied Physics Vol 29, Hydrogen in Metals II, Springer-Verlag (1978).

4.5 Mueller W M, Blackledge J P and Libowitz G G. Metal Hydrides. Academic Press, 1968.

4.6 Fromm E and Gebhardt E. Gase und Kohlenstoff in Metallen, Springer Verlag. (1976).

4.7 Somenkov V A, Gurskaya A V, Zemlyanov M G, Kost M E, Chernoplekov N A and Chertkov A A. Sov Phys Solid State. **10** 1076-1082.(1968).

4.8 Schober T, Pick M A and Wenzl H. Phys Stat Sol (a). **18** 175.(1973).

4.9 Schober T and Linke U, J Less-Common Met. **44** 63 (1976).

4.10 Schone H E, Seymour E F W, Styles G A and Sholl C A. J Less-Comm Met. **118** 201-215,(1986).

4.11 Richter D, Hempelmann R, Hartmann O, Karlsson E, Norlin L O, Cox S F J and Kutner R, J Chem Phys, **79** 4564.(1983).

4.12 Zamir D, Phys Rev A, **140** 271.(1965).

4.13 Pfeiff and Wipf H. J Phys F, **6** 167.(1976).

4.14 Torgesson D R, Schoenberger R J and Barnes R G. J Magn Reson. **68** 85-94, (1986).

4.15 Baden W and Weiss A, Ber Bunsenges Phys Chem, **87** 479.(1983).

4.16 Lütgemeier H, Arons R R and Bohn H G. J Magn Reson. **8** 74.(1972).

4.17 Lütgemeier H, Bohn H G and Arons R R, J Magn Reson. **8** 80,(1972).

4.18 Boes N and Zücher H, Z Naturforsch, **31a** 754-759,(1976).

4.19 Boukra A , MSc Thesis, University of Warwick, (1990).

4.20 Fukai Y and Kazama S, J Less-Comm Metals, **53** 25-33.(1977).

4.21 Carter G C, Bennett L H and Kahan D J, Metallic Shifts in NMR,Pergammon Press, 1977.

4.22 Dickinson W C, Phys Rev, **81**,717-731,(1951).

4.23 Reid R V Jr, Phys Rev A, **11** 403,(1975).
4.24 Barnfather K J, MSc Thesis, University of Warwick, (1986).
4.25 Richter D, Private Communication.
4.26 Schober T and Wenzl H, in "Hydrogen in Metals II", Eds. Alefeld G and Völkl J, Springer Verlag, Berlin (1978).
4.27 Schober T and Pesch W, Z Phys Chem NF, **114**21-28(1979).
4.28 Smith J F and Peterson D T , Bull Alloy Phase Diagrams. **3** (1) (1982), also "Binary Alloy Phase Diagrams", Ed. Massalski T B, Am Soc for Metals, USA, 1986.
4.29 Rush J J and Flowtow H E, J Chem Phys, **48** 37-95.(1968).
4.30 Arons R R, Bohn H G and Lütegemeier H. J Phys Chem Sol. **35** 207.(1974).
4.31 Noda Y, Masumoto K, Koike S, Suzuki T and Sato S. Acta Cryst. **B42** 529-533. (1986).
4.32 Marsh R E, ,Acta Cryst, **B43**415-416.(1987).
4.33 Wangagel J, Sass S L and Batterman B W. Metallurgical Trans. **5** 105-109. (1974).
4.34 Kajitami and Hirabayashi, Z Phys Chem NF, **145**27-42(1985).
4.35 Asano H and Hirabashi M, Proc. NATO Advanced Study Institute on Metal Hydrides, Metal Hydrides, Plenum Press, Ed Bambakidis G. 81-103. (1981).
4.36 Salibi N, Ting B, Cornell D, and Norberg R E. Phys Rev B. **38** (7). 4416-38.(1988).
4.37 Schober T and Carl A, Phys Status Solidi (a).**43**. 443-449.(1977).
4.38 Asano H and Hirabashi M, Z Phys Chem NF, **114**1-19.(1979).
4.39 Hempelmann R, Richter D and Price D L, Phys Rev Letts, **58** (10). 1016-1019. (1987).
4.40 Richter D, Mahling-Ennaoui S and Hempelmann R, Z Phys Chem NF, **163** 907. (1989).
4.41 Hoke H C, Schone H E, Sholl C A, Usher S P, Barnes R G, Torgeson D R, Hempelmann R and Styles G A, J Less-Common Metals. **172-174** 603-610. (1991).
4.42 Takano S, Makita A and Kojima H, Materials Science and Engineering, **A142** 245-253,(1991).
4.43 Hayashi S, Hayamizu K and Yamamoto O, J Chem Phys, **76** 9, 4392-4397, (1982).
4.44 Zogal O J and Stalinski B, Colloque Ampere XIV, North-Holland Publ Co, (1967).
4.45 Fukai Y and Kazama S, Acta Metallurgica, **25** 59-70,(1977).

4.46 Fromm E and Gebhardt E, Gase und Kohlenstoff in Metallen. Springer Verlag, 1976.
4.47 Asano A, Abe Y, and Hirabayashi M, J Phys Soc Jpn. **41** 974,(1976).
4.48 Rush J J, Berk N F, Magerl A, and Rowe J M, Phys Rev B. **37**(10),7901-7903 (1988).
4.49 Boes N and Zuchner H, Zeit Naturforschung, **A31**,754,(1976).
4.50 Mueller W M, Blackledge J P and Libowitz G G. Metal Hydrides. Academic Press, 1968.
4.51 Greenfield and Beck, Trans AIME, **206**265-276.(1956).
4.52 Sholl C A, Private Communication to Harlan Schone, 1990.
4.53 Khatamian D and Manchester F D, Bulletin of Alloy Phase Diagrams. 8, (1987).
4.54 Daou J N, Lucasson A and Lucasson P, Solid State Commun. **19** 895.(1976).
4.55 Blaschko O, J Less-Common Metals, **172-174**237-245.(1991).
4.56 Bonnet J E, Juckum C and Lucasson A, J Phys F, **12** 699.(1982).
4.57 Blaschko O, Krexner G, Daou J N and Vajda P, Phys Rev Lett. **55** 2876.(1985).
4.58 Anderson I S, Rush J J, Udovic T and Rowe J M, Phys Rev Lett. **57** 2876.(1986).
4.59 Lichty L, Schoenberger R J, Torgeson D R and Barnes R G, J Less-Common Metals, **129**31-38,(1987).
4.60 Yannopoulos L N, Edwards R K and Wahlbeck P G, J Phys Chem. **69** 8,2510-2515,(1965).
4.61 Lundin C E and Blackledge J P, J Electrochem Soc. **109** 9, 838-841.(1962).
4.62 Anderson I, Ross K R, Bonnet J, Z Phys Chem. **164** 923.(1989).
4.63 Sholl C A, Private Correspondence.
4.64 Barnes R G, Torgeson D R,Bastow T J M, West G W, Seymour E F W and Smith M E, Z Phys Chem, **164**867-872,(1989).

Figure 4.1 Phase diagram of the NbH_x system showing temperature (K) versus composition (x), after Köbler and Welter [4.1].

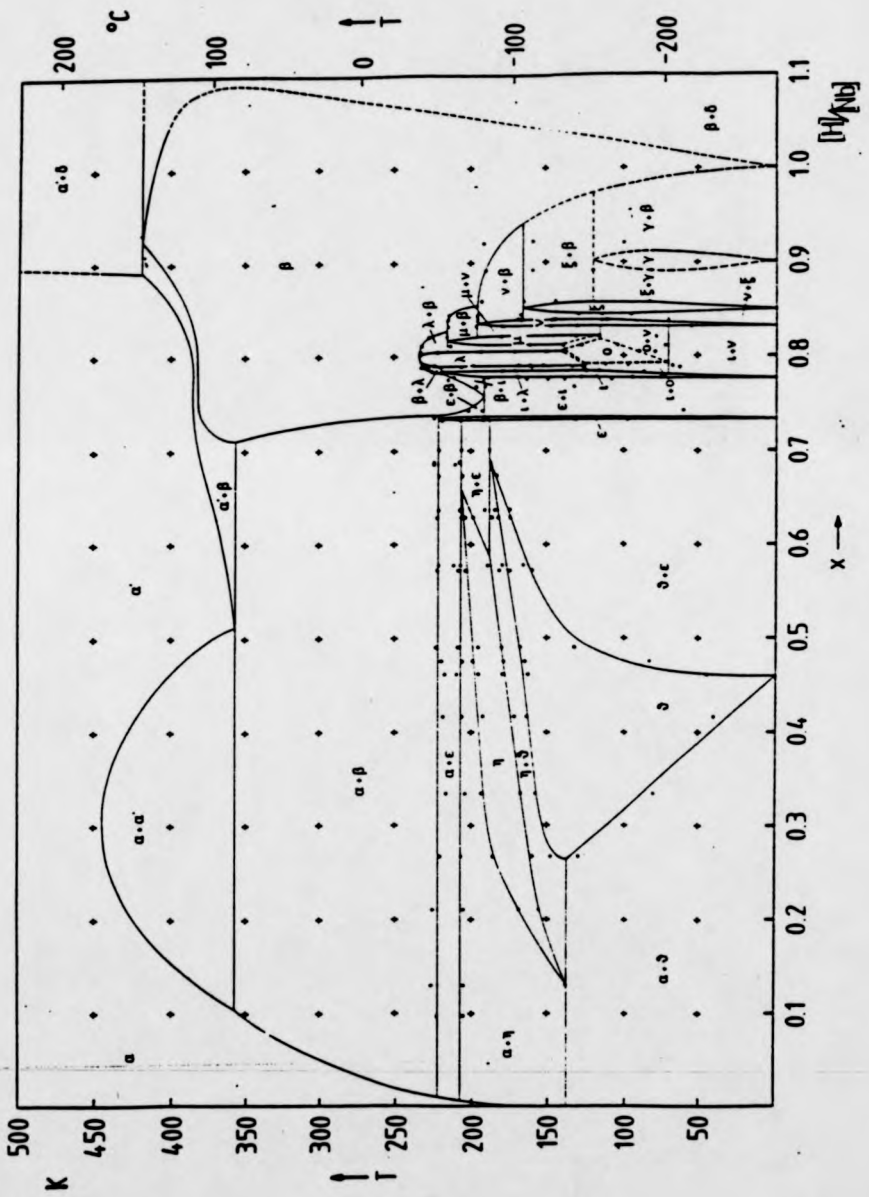

Figure 4.2 Schematic representation of the face-centered orthorhombic structure of niobium lattice in the β-phase hydride. The open circles represent the niobium atoms. The fco cell parameters are a = 4.82 - 4.84, b = 4.86 - 4.92, c = 3.42 - 3.47 Å and γ = 0.4 - 0.9° for NbH_x where $0.7 \geq x \leq 1.0$ at room temperature.

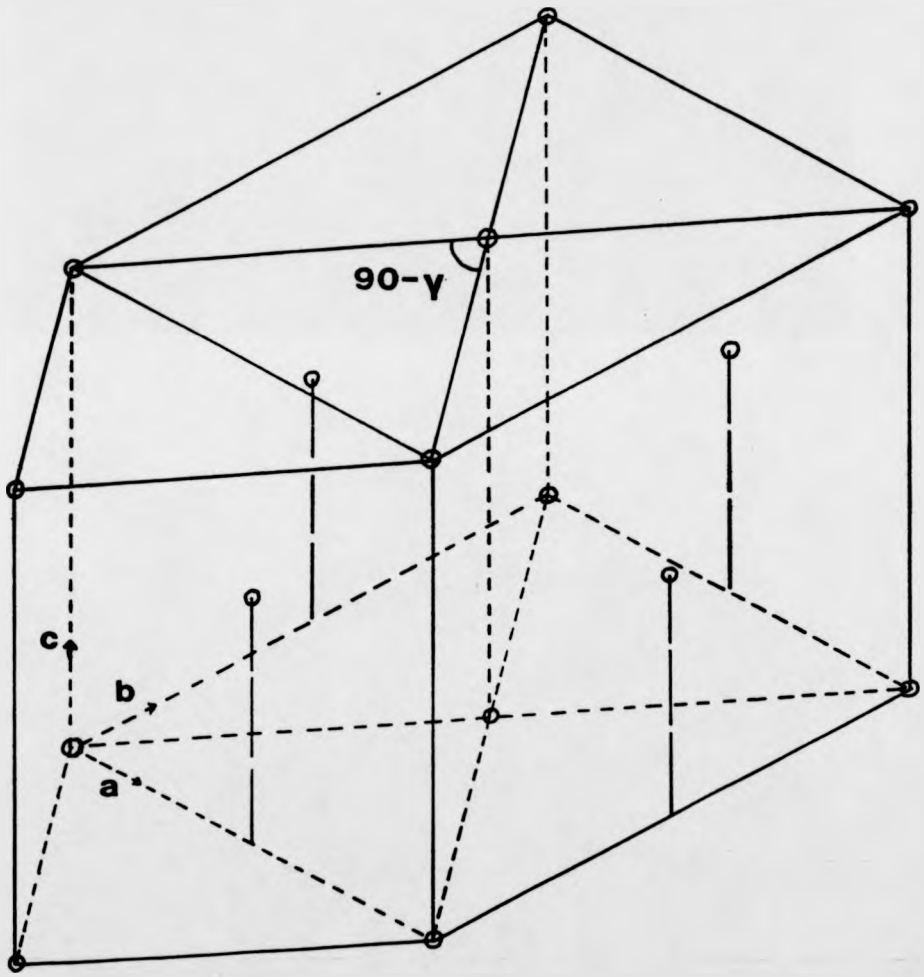

Figure 4.3 A schematic representation of the hydrogen chains which form along T-sites in the <110> directions and on {112} planes of the original bcc lattice.

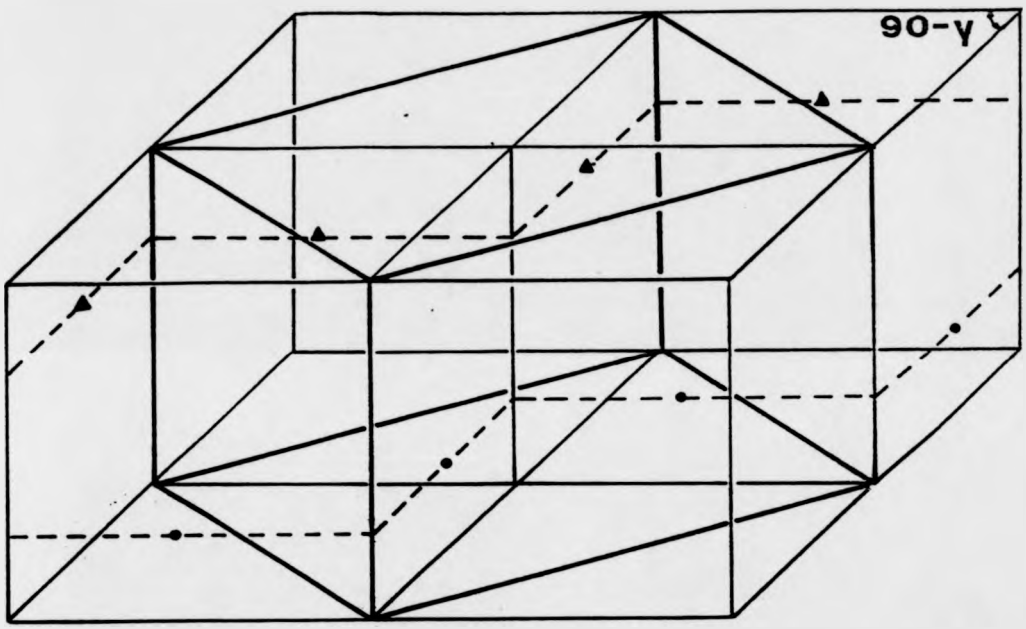

Figure 4.4 A schematic representation of the six inequivalent T-sites which exist in the β-NbH system. These inequivalent sites give rise to six possible chains of equivalent T-sites in which all sites have their principal symmetry axes parallel. The inequivalent chains give rise to separate domains which form in a 'single crystal' of the β-phase. Pairs of domains containing chains 1 and 2, 3 and 4, and 5 and 6 tend to twin in the formation of a multi-domain crystal.

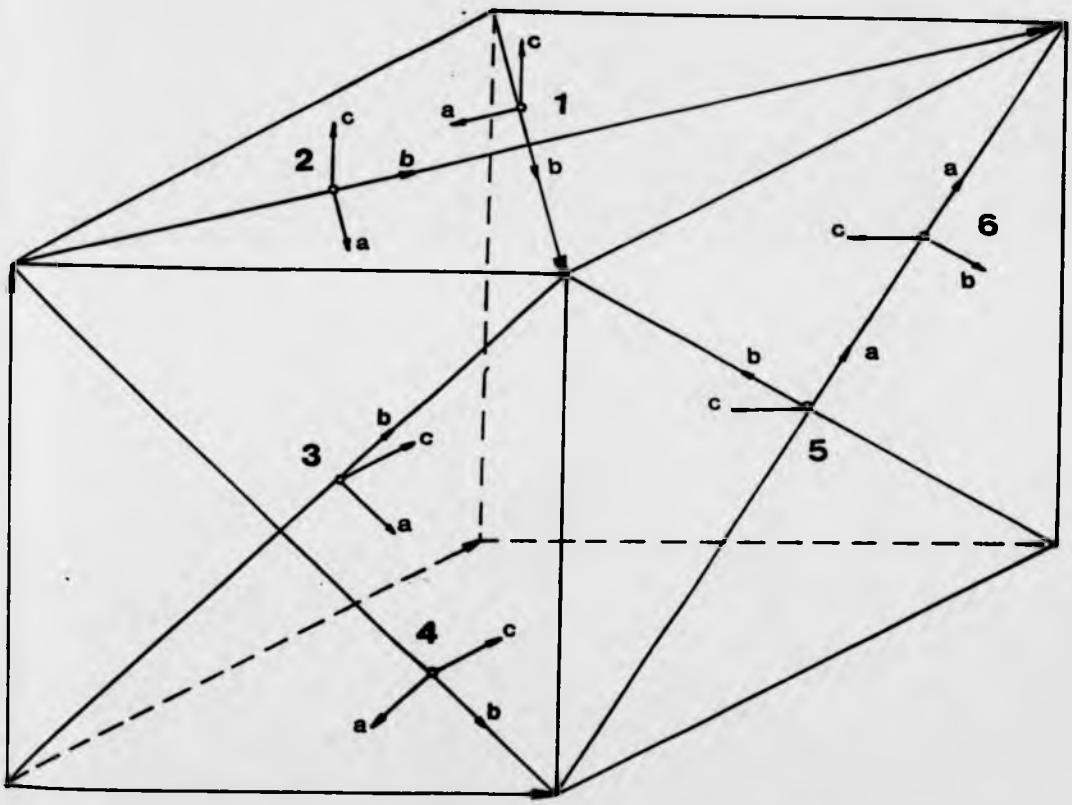

Figure 4.5 Hydrogen solubility curves show the equilibrium hydrogen concentration in niobium versus hydrogen pressure for the isotherms shown here in degrees Kelvin, after Wenzl and Welter [4.3].

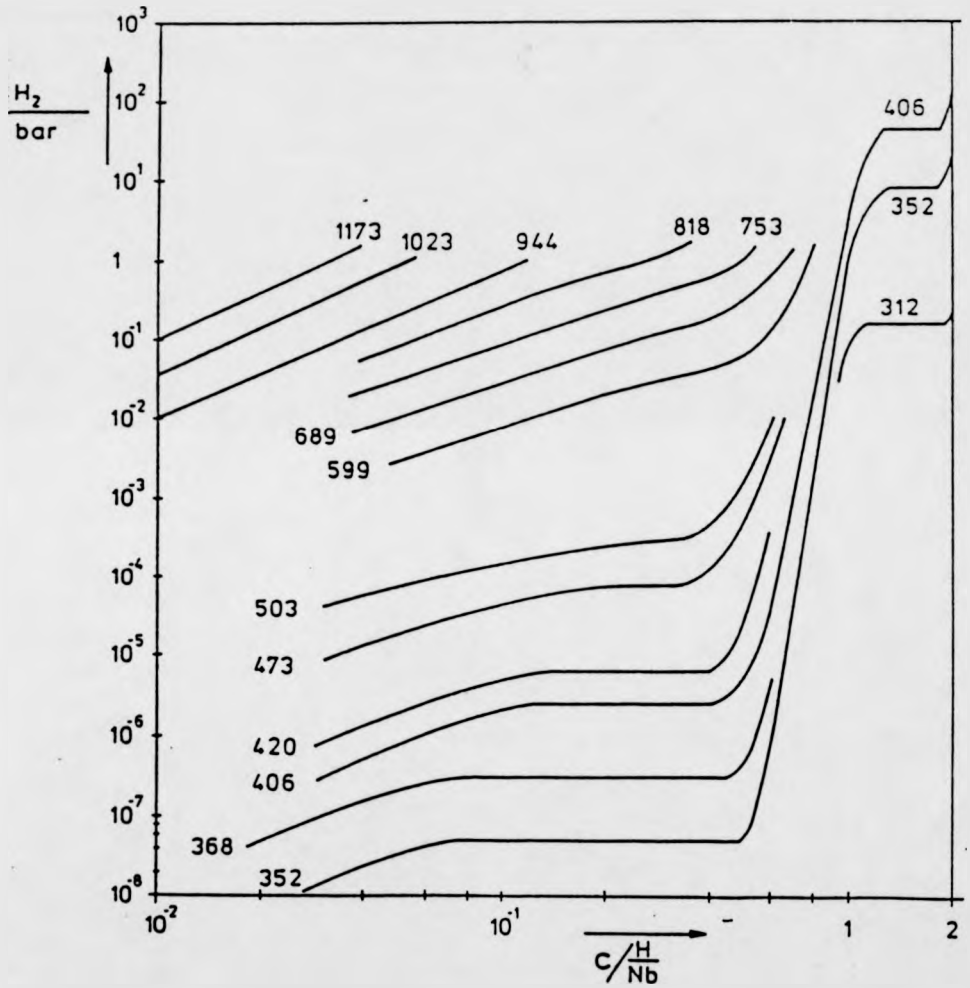

Figure 4.6 Theoretical predictions of the relaxation rates ($R_1 \alpha \lambda_L + \lambda_U$, see equation 4.4 after Sholl et al [4.10]) variation with the B_0 field direction for the three jump models presented in the text for a single domain, single crystal of β-NbH. The angle θ is that between B_0 and the [001] axis where the hydrogen chains lie along the [110] direction and the axis of rotation of the crystal is perpendicular to the $(1\bar{1}0)$ plane.

_____ model 1, ---------- model 2. _ _ _ _ _ model 3.

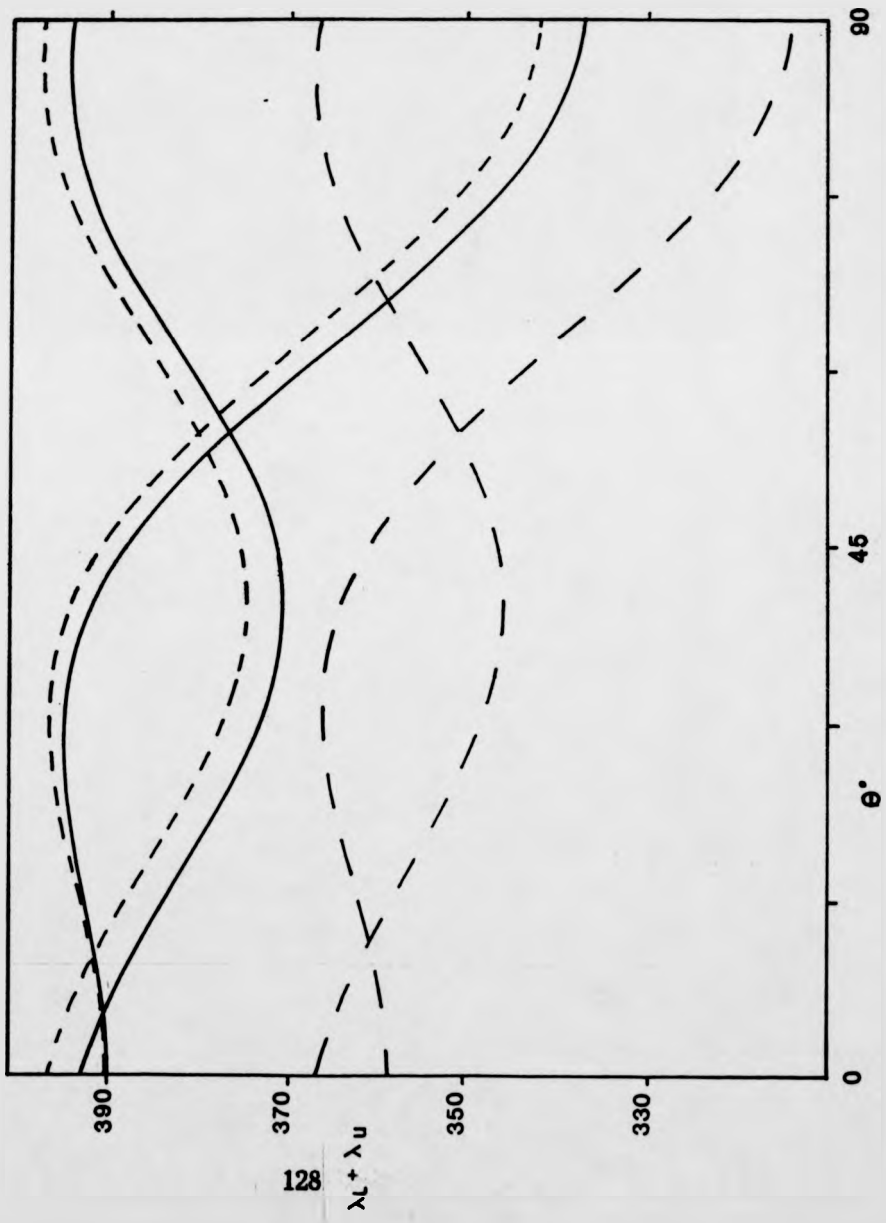

Figure 4.7 Normalised relaxation rate dependence on crystal orientation for all three models shown in figure 4.6 where the rates are weighted for equally populated domains within the crystal.

_____ model 1. ---------- model 2. _ _ _ _ _ model 3.

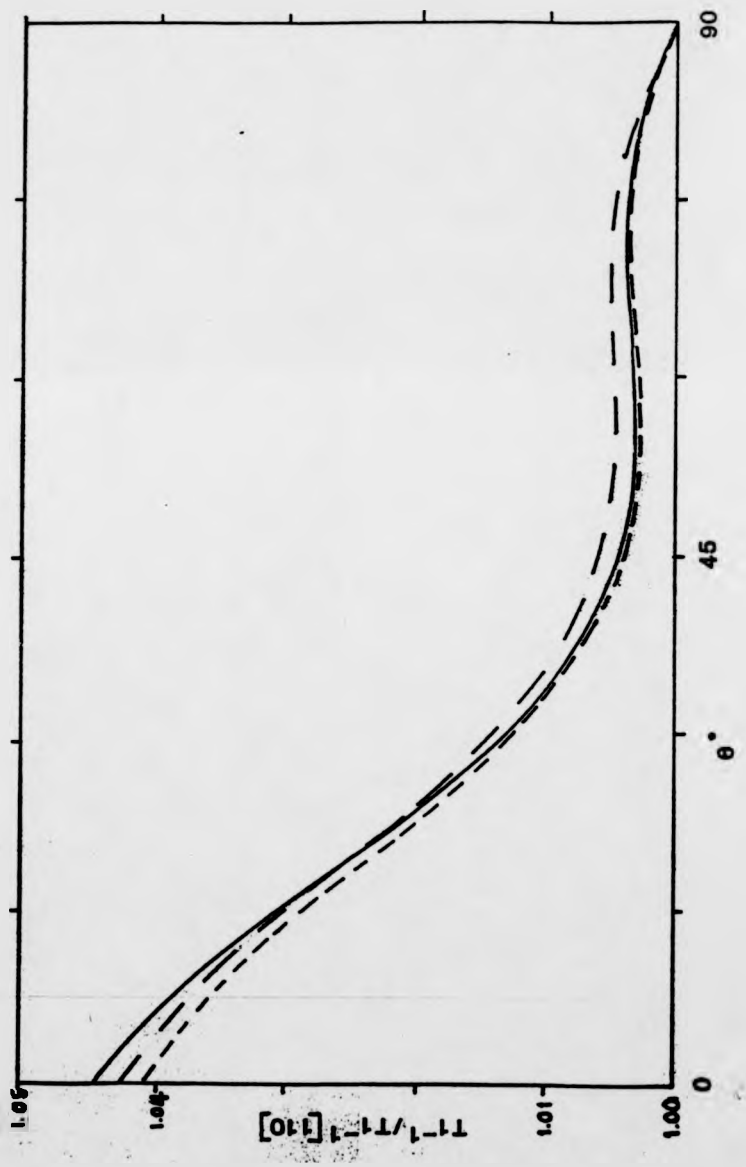

Figure 4.8 A schematic representation the cylindical crystal sample used to produce sample one, β-$NbH_{0.76}$, and sample three, β_1-$VH_{0.53}$. Rotating the crystal about its cylinder axis, which is parallel to the [110] direction, the B_0 field can be aligned with the [001], [$1\bar{1}1$] and [$1\bar{1}0$] crystal axes (of the original bcc lattice).

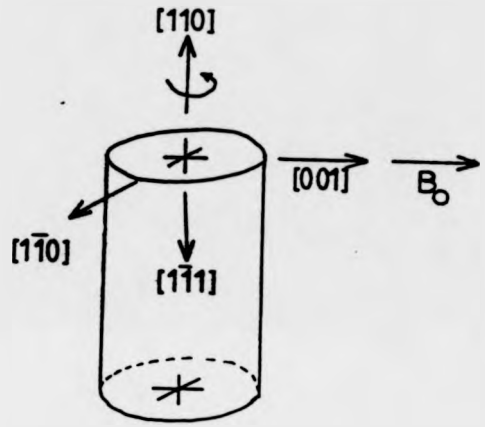

Figure 4.9 Experimental Knight shift results measured at 39.8MHz for sample one; the cylindrical single crystal β-$NbH_{0.76}$. The two resolvable proton lines reveal the variation of principal symmetry axis for the different hydrogen domains as the crystal orientation with respect to the B_0 field is varied.

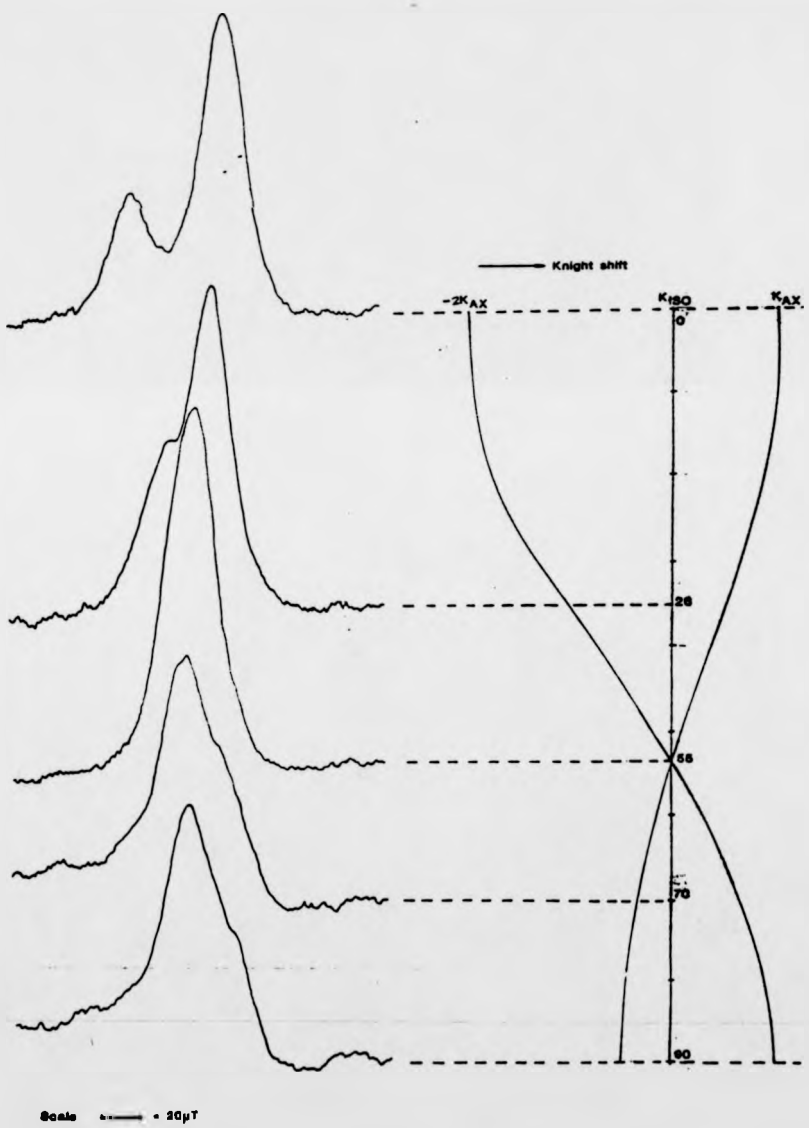

Figure 4.10 Experimental T_1 results for sample one, β-$NbH_{0.76}$ single crystal at 290K and 39.8MHz. Compare with the form of the relaxation rate dependence shown in figure 4.6.

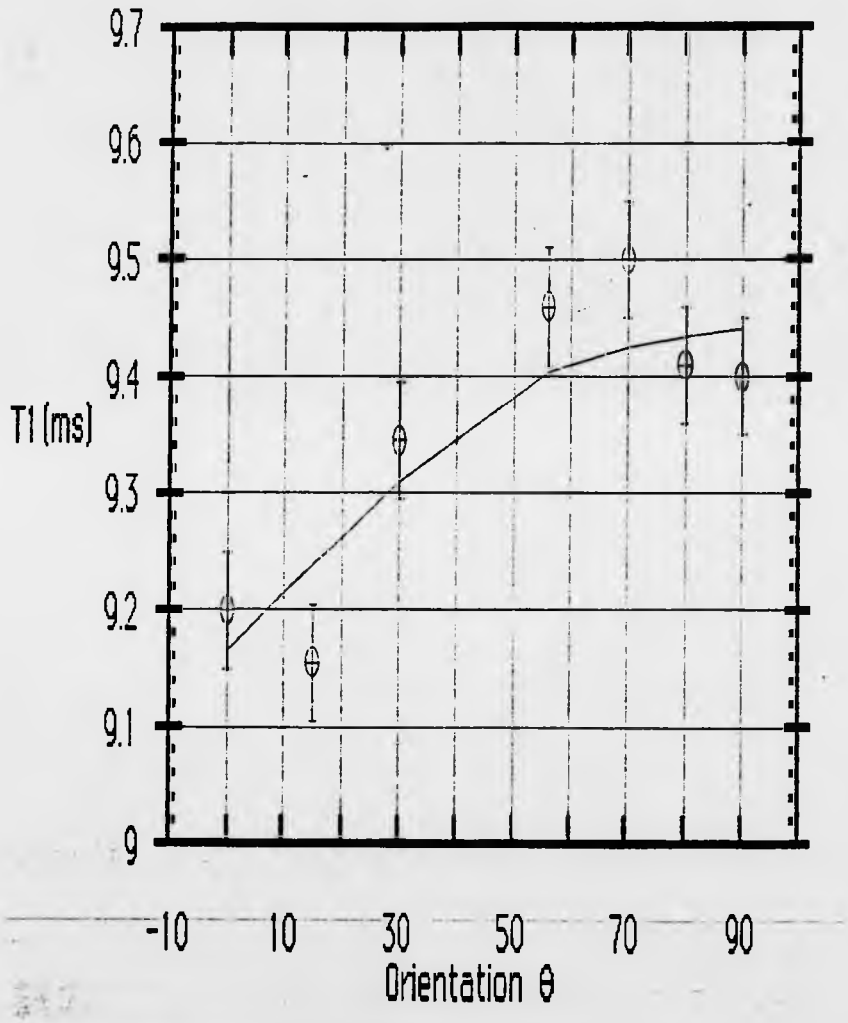

Figure 4.11 Experimental T_1 versus temperature results obtained from sample one, β-$NbH_{0.76}$, for three different crystal orientations with respect to B_0, at a frequency of 39.8MHz. Part A: here $\Theta = 0°$, that is B_0 aligned along the [001] axis of the original Nb bcc crystal lattice (see text and figure 4.8).

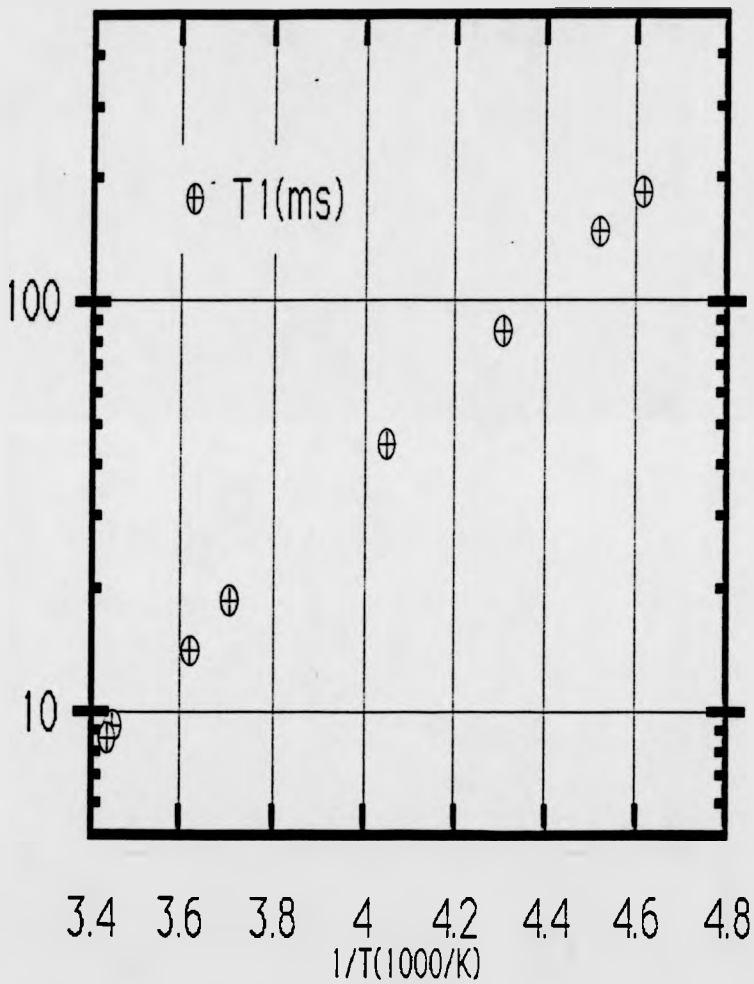

Figure 4.11 B β-$NbH_{0.76}$ $\Theta = 55°$

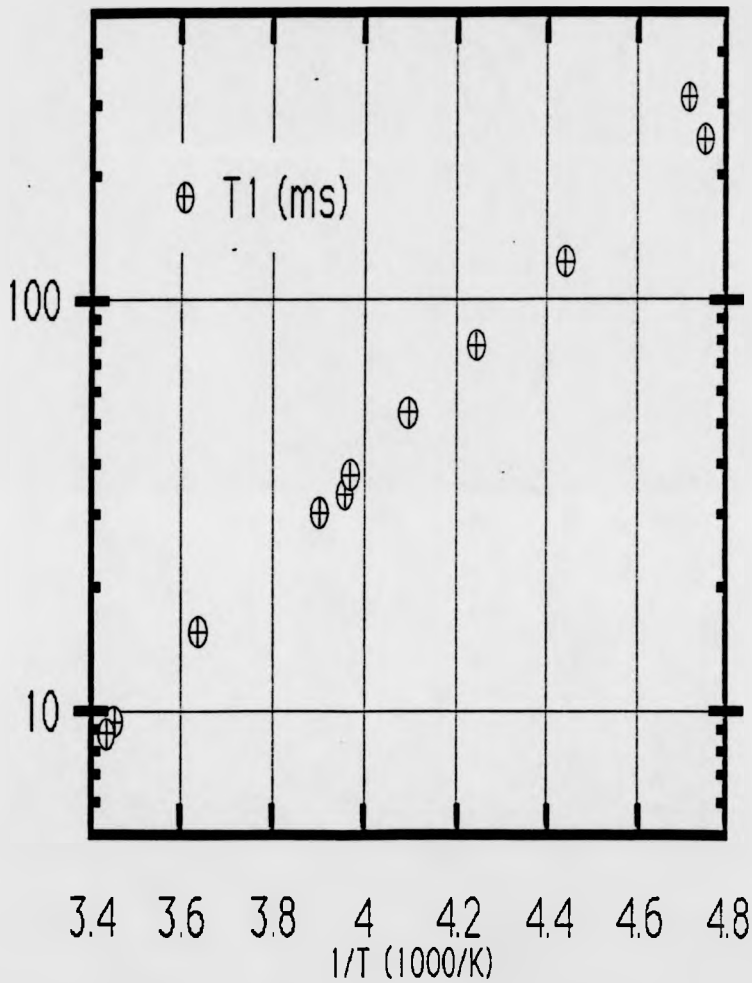

Figure 4.11 C β-$NbH_{0.76}$ $\Theta = 90°$, that is B_o aligned along the $[1\bar{1}0]$ crystal axis shown in figure 4.8.

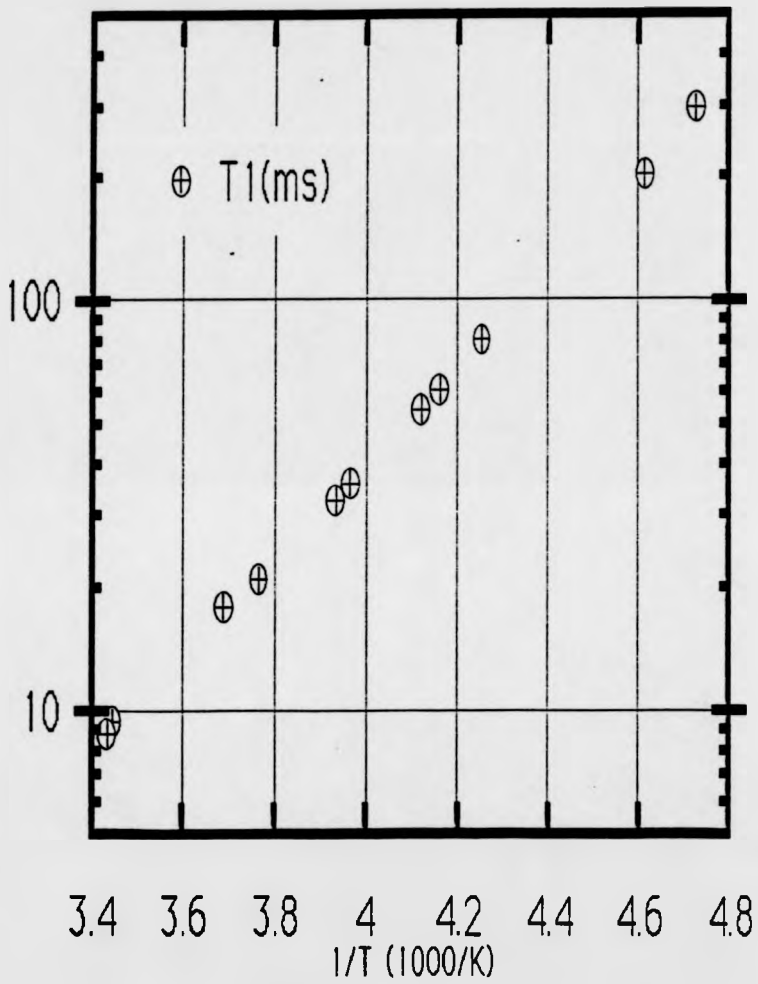

Figure 4.12 Experimental T_1 versus temperature results for sample one measured at 39.8MHz. The three crystal orientations shown seperately in figure 4.11 are shown together here for comparison.

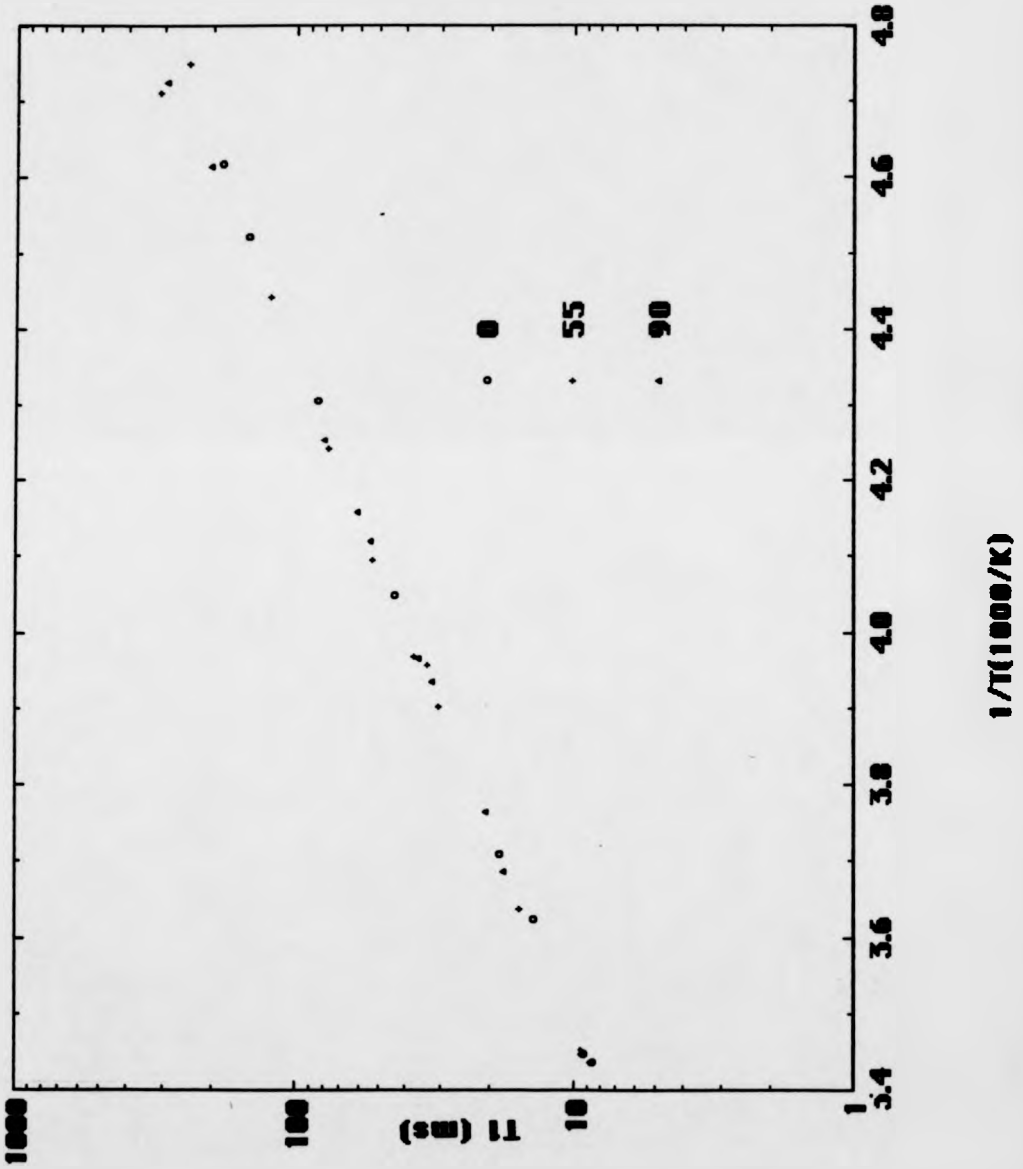

Figure 4.13 A schematic sectional side view of the hydriding device used in an attempt to form a single domain β-NbH sample by hydriding at high hydrogen pressures of up to $4x10^6$ Pa. An aperture in the top of the device allows exposure of the high pressure hydrogen atmosphere to only a single face of a disc sample. A single crystal disc of pure niobium is clamped between two body portions of the device. The portions each comprise a circular knife edge which contact the disc and prevent flow of hydrogen around the crystal. The cavity below the inner body portion is sealed from the hydrogen atmosphere using a bolt which locks a copper o-ring against two, upper and lower, knife edges. In theory therefore, the hydrogen is expected to flow from above the crystal and through it in a single direction. In practice the discs tended to form cracks presumably due to stresses created in the heat cycling.

1 upper aperture 2 single crystal disc 3 outer body portion
4 inner body portion 5 locking nut 6 copper o-ring

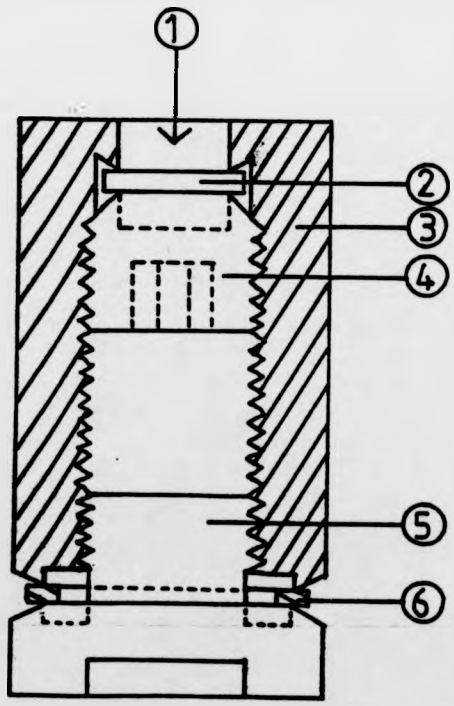

Figure 4.14 A schematic representation of the crystallographic orientation of sample two a β-$NbH_{0.75}$ single domain disc. The lattice vectors shown are for the original bcc niobium lattice.

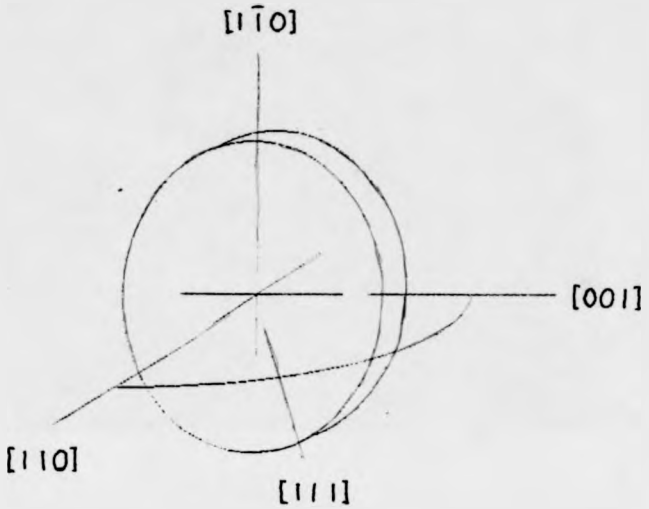

Figure 4.15 Knight shift results for sample two, a β-$NbH_{0.75}$ single domain disc, measured at 47MHz and room temperature. Measured lines at five orientations are shown. Additional observed centers of lines for different orientations are represented by dots while the solid line represents the fitted curve. The orientation dependence is in good agreement with equation 4.5 and the fitted line provides values of α=39ppm and $K_{a\perp}$=-19.5ppm.

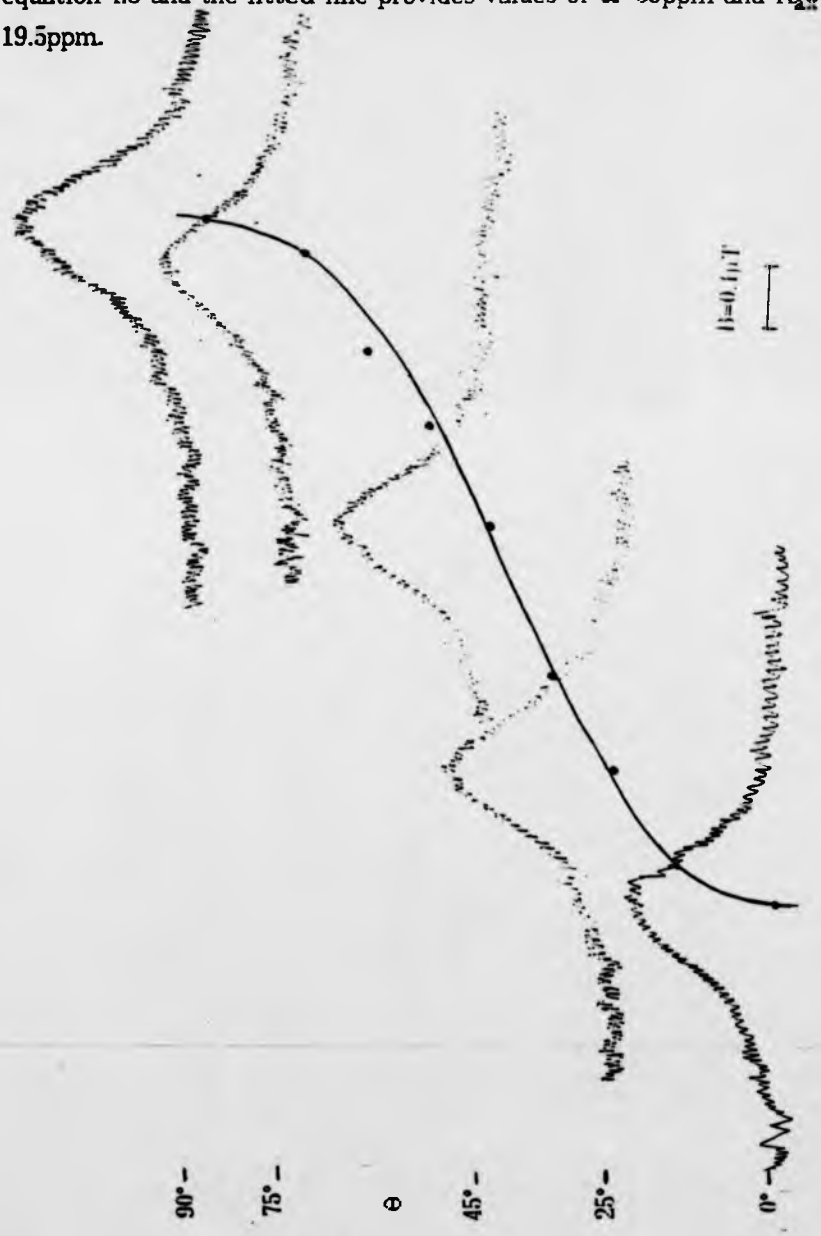

Figure 4.16 The temperature dependence of the ^1H relaxation time T_1 for certain orientations of the single domain disc of $NbH_{0.75}$. Part A: $\Theta=0°$.

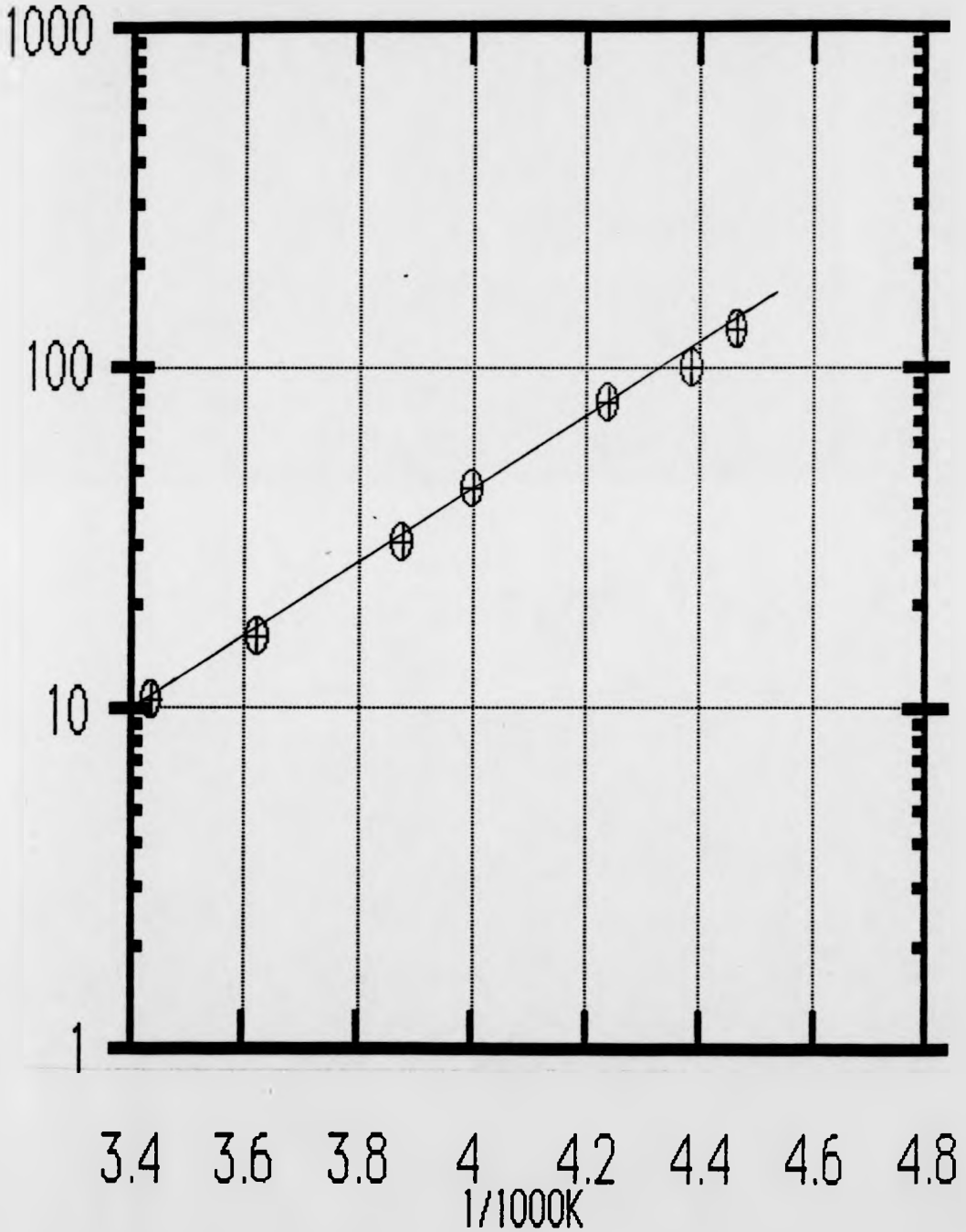

Figure 4.16 B $NbH_{0.75}$ disc Θ=35°

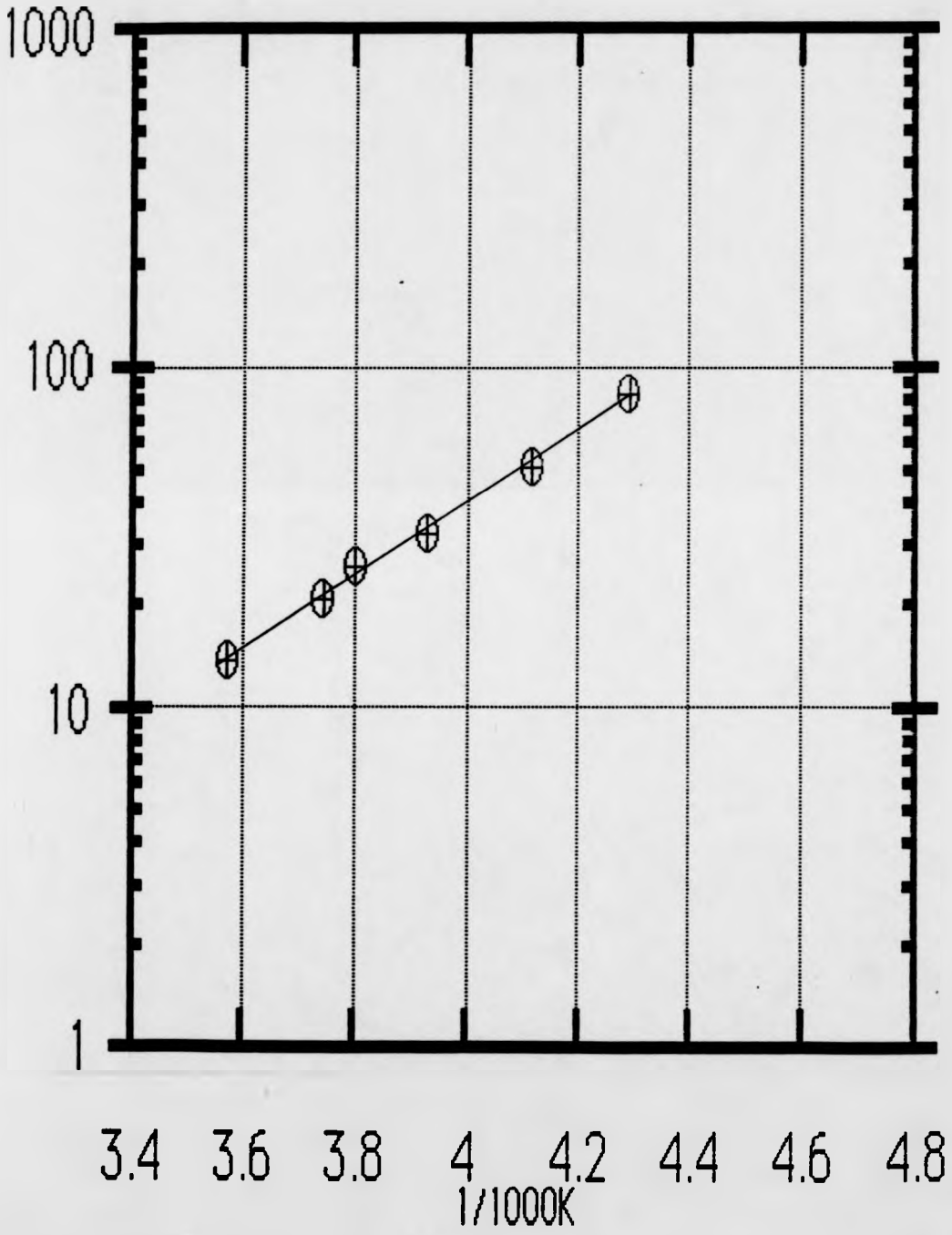

Figure 4.16 C $NbH_{0.75}$ disc Θ=90°

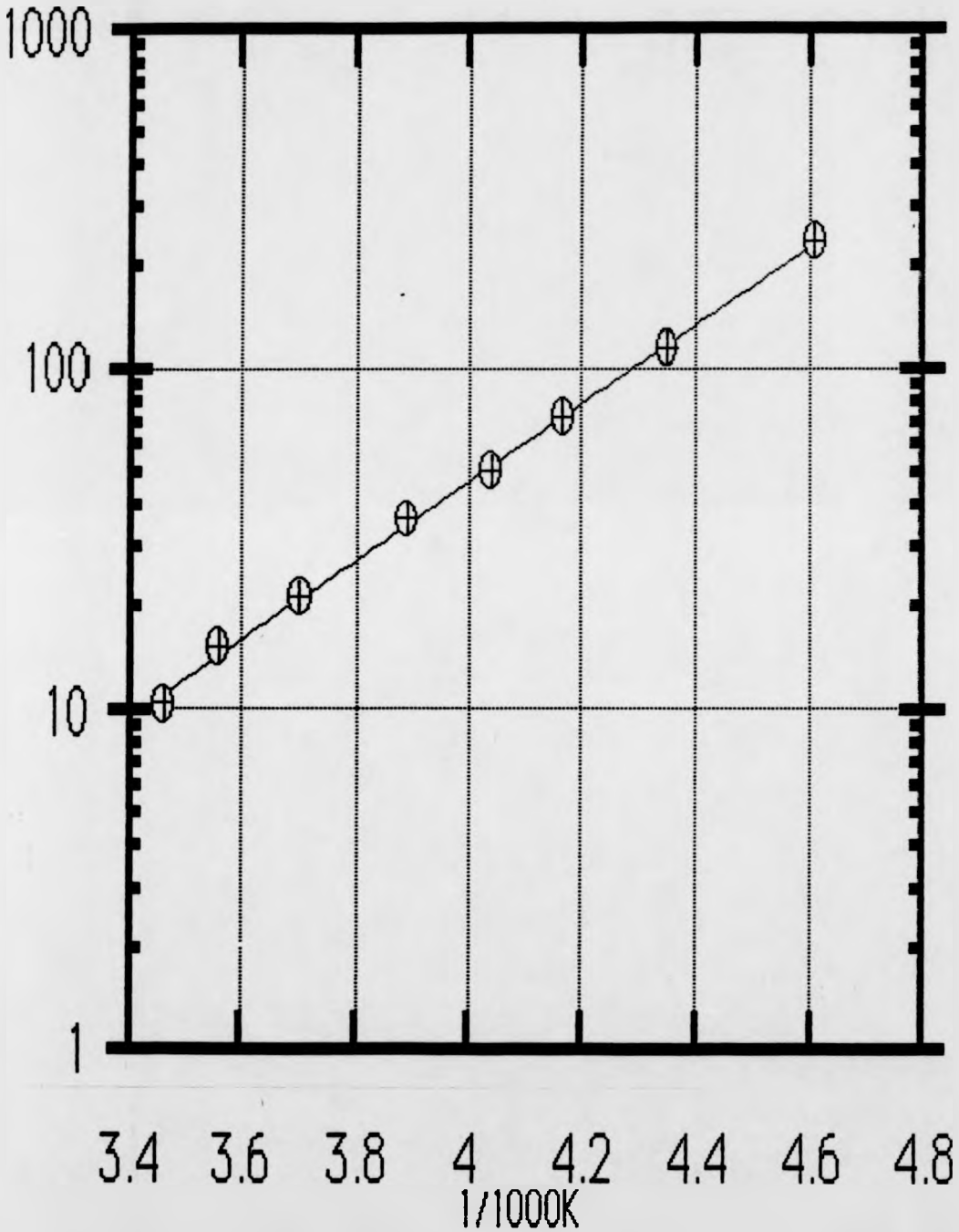

Figure4.16 D T_1 data for all three angles as shown seperately in parts A, B, and C supra, $NbH_{0.75}$ disc.

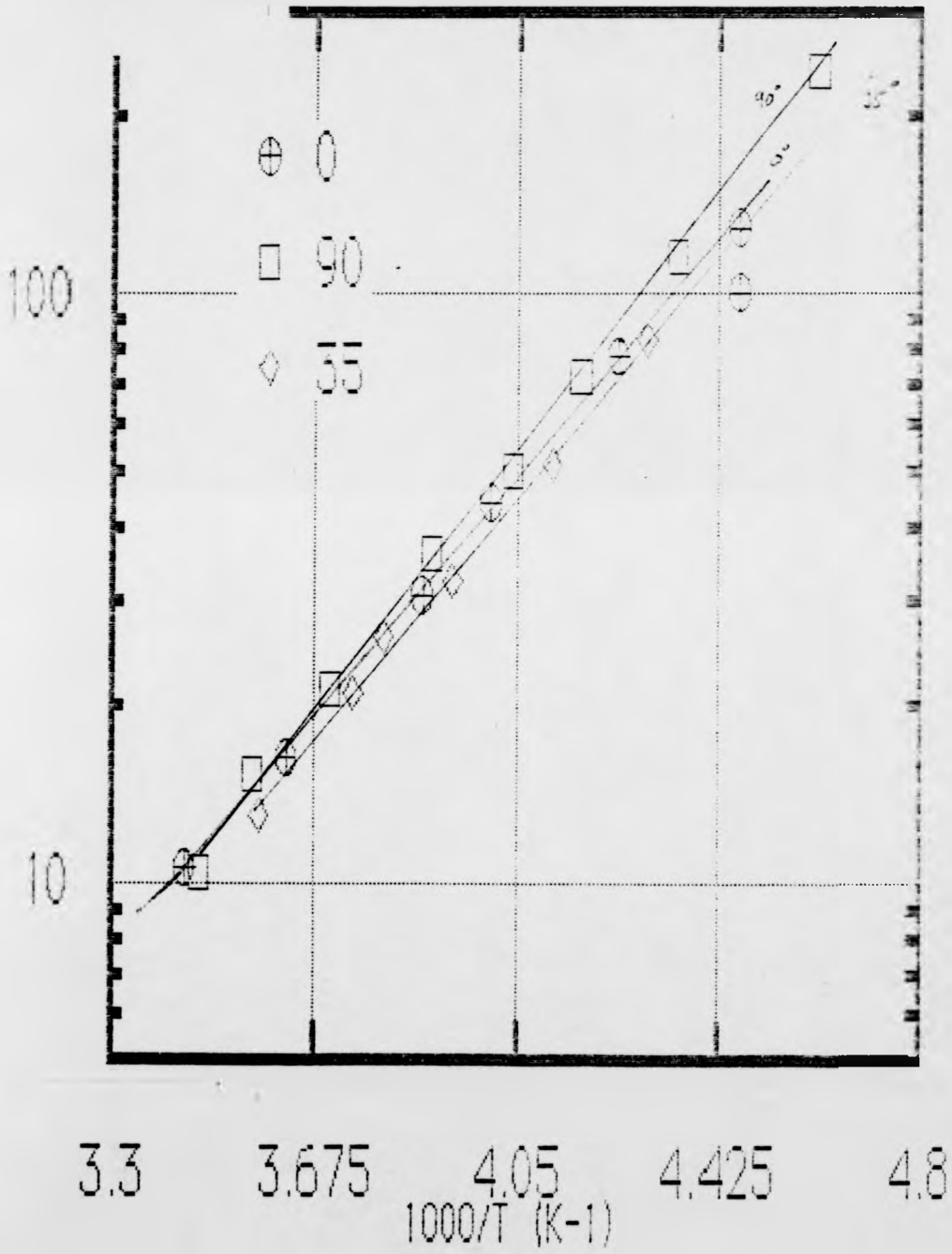

Figure 4.17 ^1H relaxation time T_1 versus crystal orientation for a range of temperatures for the single domain disc sample $NbH_{0.75}$. The data points shown here for Θ=0°, 35°, and 90° are interpolated from T_1 measurements made at those fixed angles as shown in figure 4.16. Additional T_1 measurements were made at fixed temperatures but over a small intermediate spread of orientations, the data points shown are for orientations Θ=30°, 45°, and 60°.

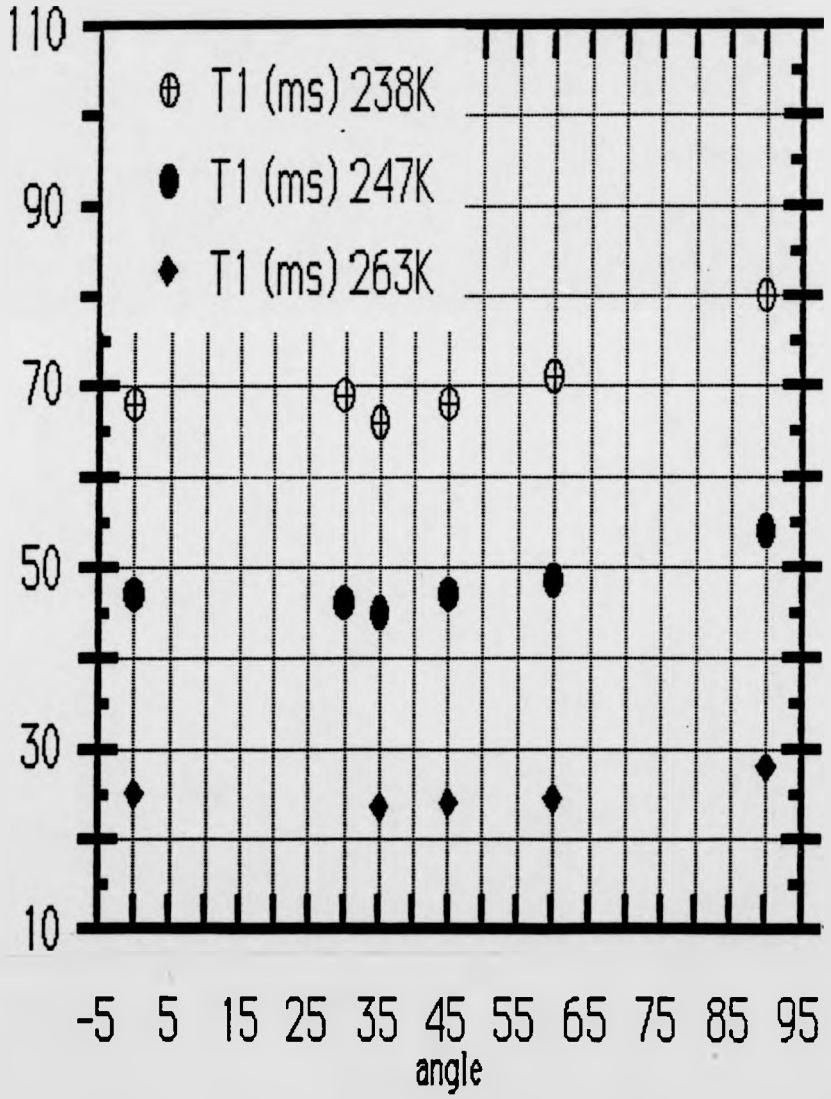

Figure 4.18 A larger scale representation of the T_1 data for the $NbH_{0.75}$ disc sample shown in figure 4.17 for the specific temperature of 238K. The angular form of the T_1 behaviour compares very favourably with theoretically predicted behaviour for all three models described in section 4.1.2 and shown in figure 4.6.

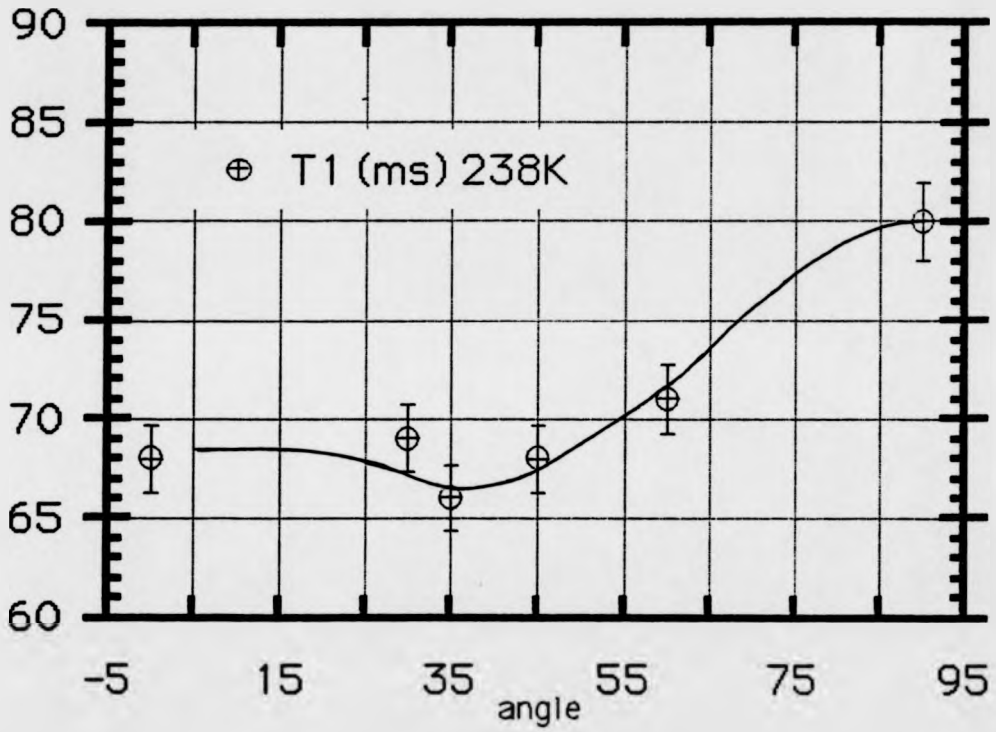

Figure 4.19 Phase diagram of the vanadium-hydrogen system after Schober and Pesch [4.27].

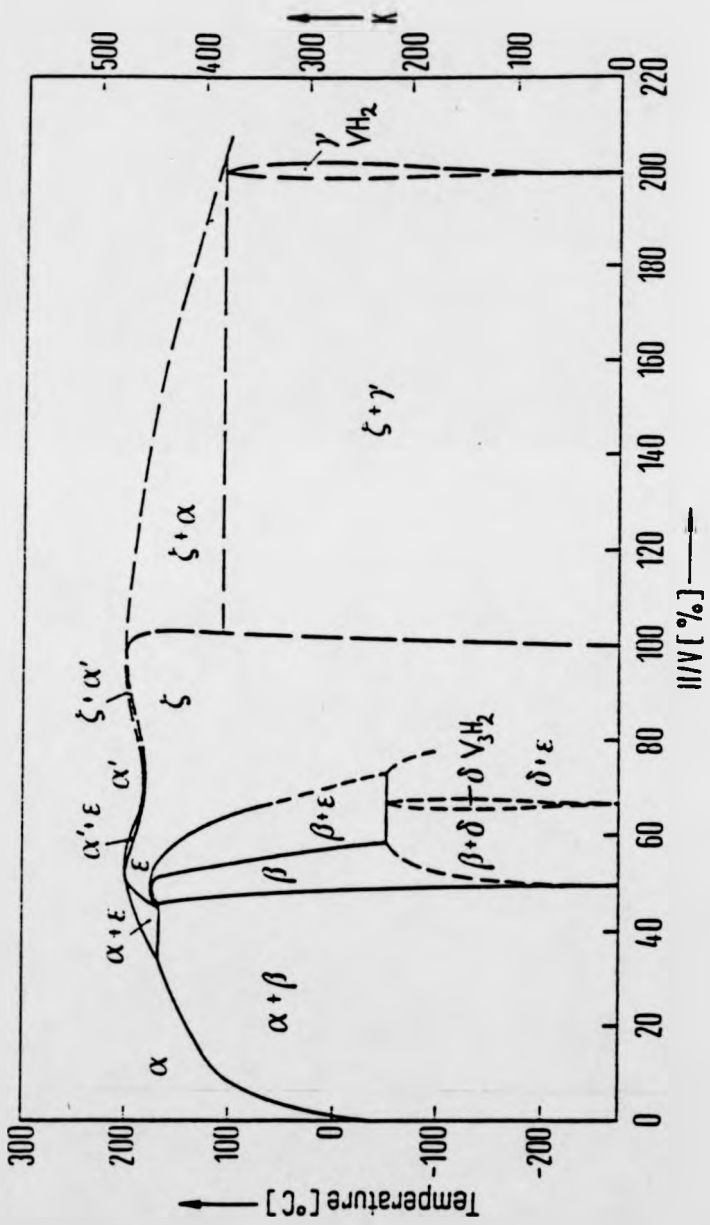

Figure 4.20 The structure of β_1-V_2H where the filled circles represent occupied O_{Z1} sites and the empty circles are empty O_{Z2} sites, the metal atoms are not shown. The hydrogens form layers of {1̄,0,1} type planes of occupied O_{Z1} sites separated by planes of unoccupied O_{Z2} sites in single domains.

The a, b and c lattice vectors represent the unit cell vectors of the fundamental body-centered vanadium lattice. and A, B and C are the unit cell vectors of the monoclinic vanadium lattice. The lattice parameters determined by Takano et al [4.42] are a=2.9969±0.0002Å, b=2.999±0.001Å, c=3.3058±0.0002Å, c/a=1.103, β=90.30°±0.04°, and γ_m=84.39° for the stoichiometric composition at 298K.

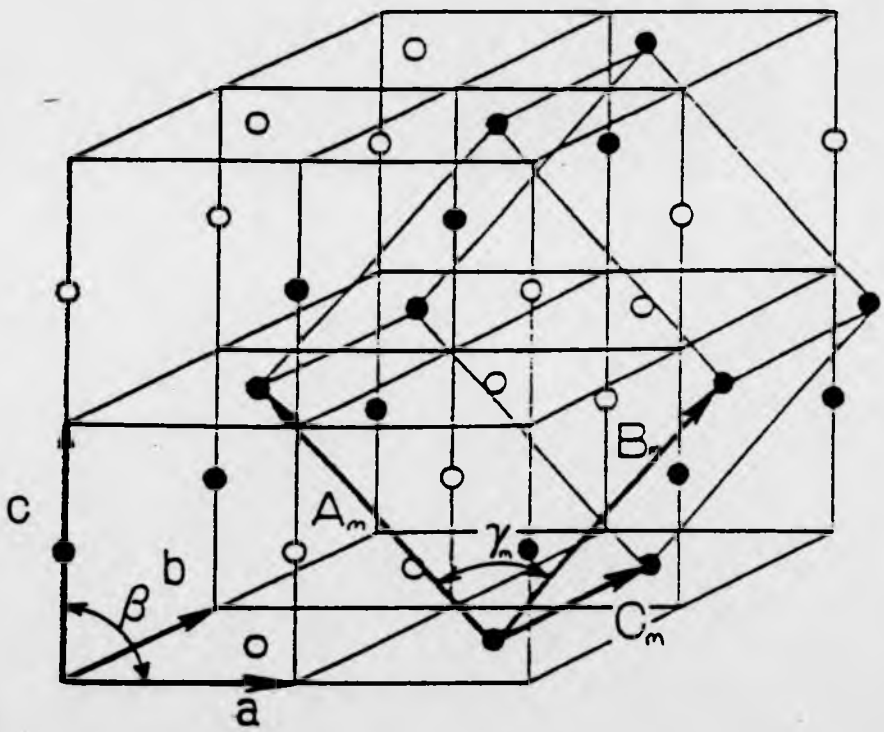

Figure 4.21 A schematic representation of three types of domain, A, B and C, formed in a bcc vanadium lattice, where the bcc axes are labelled a, b and c on the right of the crystal. The monoclinic (pseudotetragonal) A, B and C domains have their $[001]_m$ (or $[001]_T$) axis aligned along the a, b and c axis respectively of the original bcc lattice.

Sample 4 is a C domain crystal substantially as shown with approximate dimensions of length l= 30mm, depth d= 1mm, and breadth b= 12mm. The crystal was placed in the magnetic field with the bcc $[\bar{1}\bar{1}.0]$ axis perpendicular to B_0 such that the nmr coil cylinder-axis, the axis of rotation, was also aligned with the $[\bar{1}\bar{1}0]$ axis and therefore perpendicular to B_0.

The planes of hydrogen in the C domain are $(\bar{1}\bar{1}0)$ planes, as represented schematically by the shaded region, and the angle ψ described in the text varies from 0° for B_0 aligned with the $[\bar{1}10]$ axis to 90° for B_0 aligned with the [001] axis.

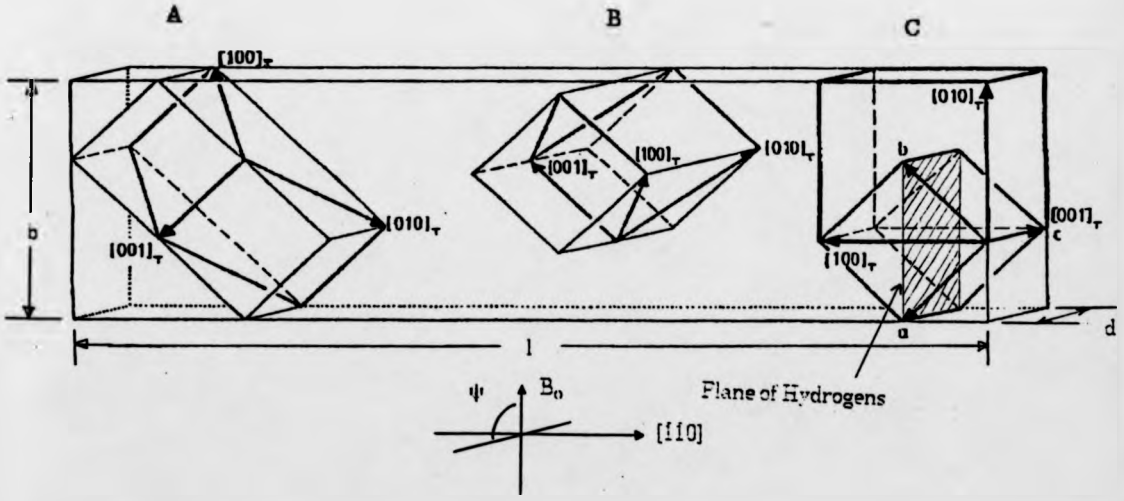

Figure 4.22 A pressure-composition-temperature diagram of the vanadium-hydrogen system, see for example Fromm and Gebhardt [4.46] and Mueller et al [4.50].

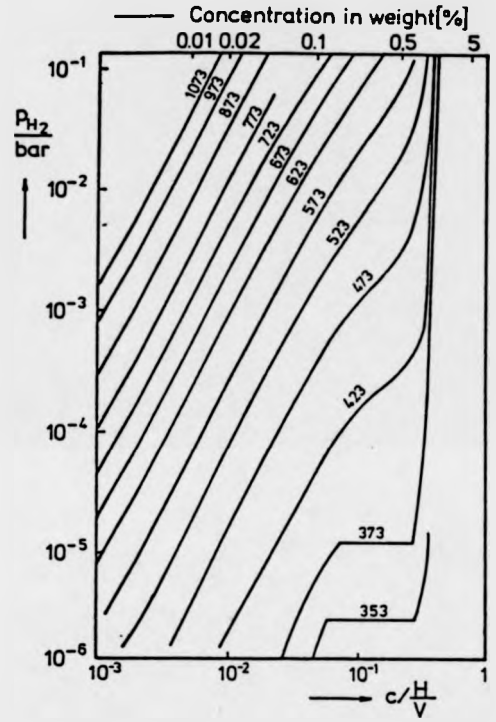

Figure 4.23 A schematic representation of an O_Z octahedral site occupied by hydrogens in the β_1-V_2H system. Note the slightly different values for a, b and c reported here by Asano et al [4.47] to those given above with reference to figure 4.20.

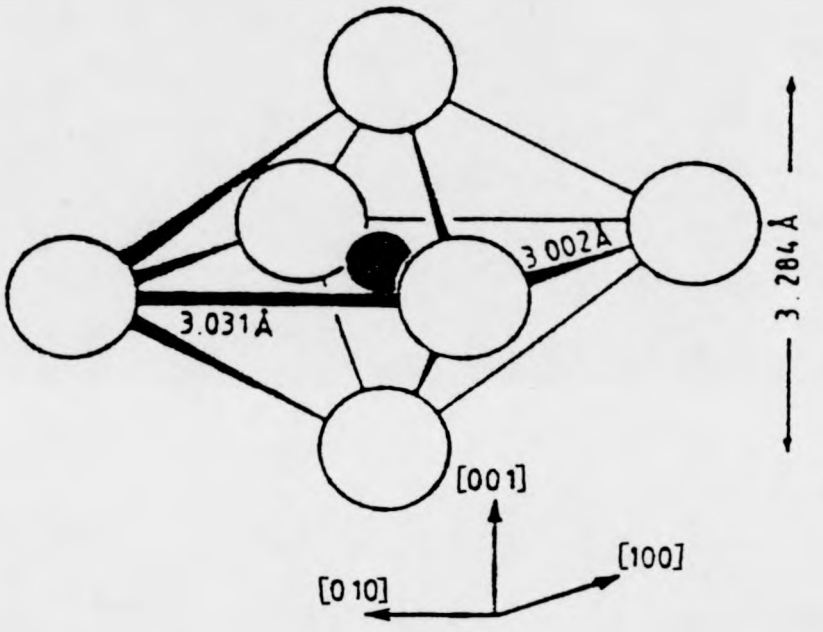

Figure 4.24 Jump vectors adopted by Richter et al [4.40] in determining the jump rates given in table 4.4. They consider only eight jumps to near neighbour O-site, four within the occupied plane, shown as $\underline{S}_1$, $\underline{S}_2$, $\underline{S}_3$ and $\underline{S}_4$, and four to the unoccupied plane $\underline{S}_1^o$, $\underline{S}_2^o$, $\underline{S}_3^o$ and $\underline{S}_4^o$.

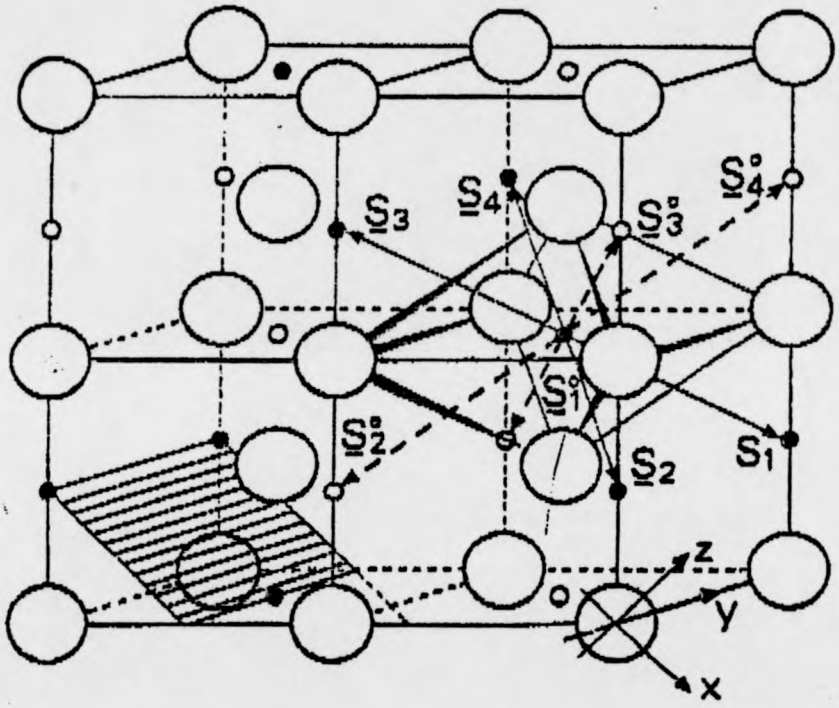

Figure 4.25 Sholl's theoretical predictions (in solid lines) for the behaviour of T_1 with (a) ψ (ie in the plane of hydrogens) at 390K and (b) Θ at the stated temperatures for a single domain β_1-V_2H crystal. Three data points observed by Hoke et al [4.41] are given for the ψ dependence in figure (a).

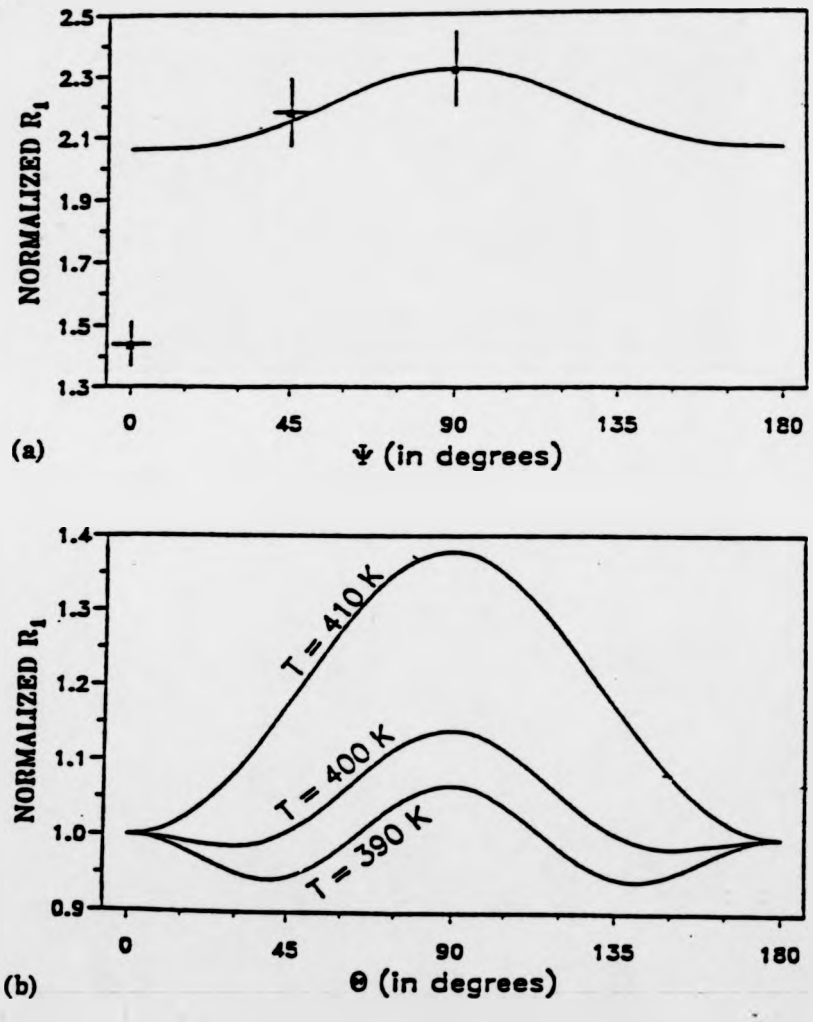

Figure 4.26 The proton lineshape variation with angle (Θ is the angle between the [001] axis and B_o) for a cylindrical partly crystalline sample of $VH_{0.53}$ (sample 3) measured at 298K and 47MHz. the field from left to right of the spectra shown is 2mT (ie full scale of ≈1795ppm). Four orientations are shown; from top Θ=0° ([001] parallel to B_o), 30°, 60° and 90° ([1$\bar{1}$0] parallel to B_o).

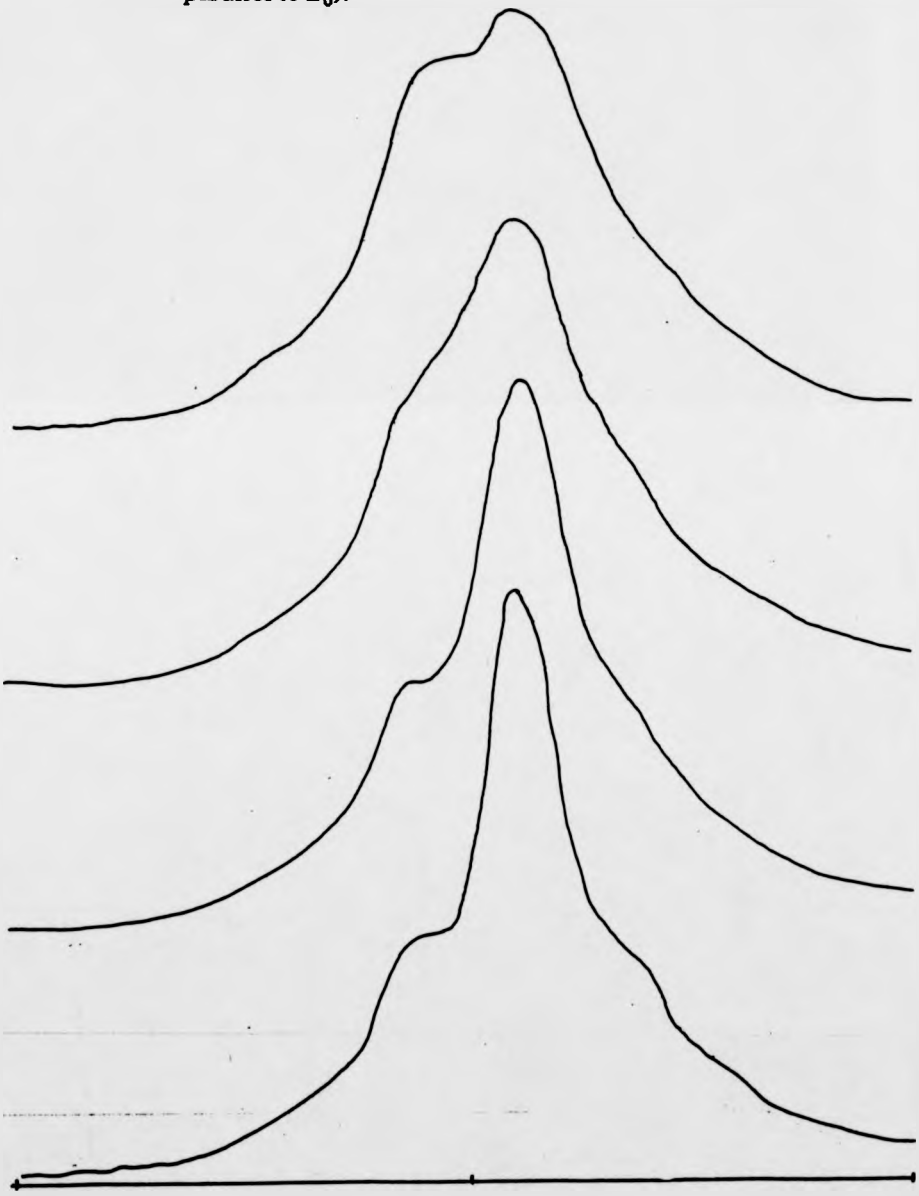

Figure 4.27 The lineshapes shown in figure 4.26 are shown fitted here using a Gaussian fitting program where in (a) $\Theta=0°$ and in (b) $\Theta=90°$. The parameters of the best-fit four lines shown are given in the text.

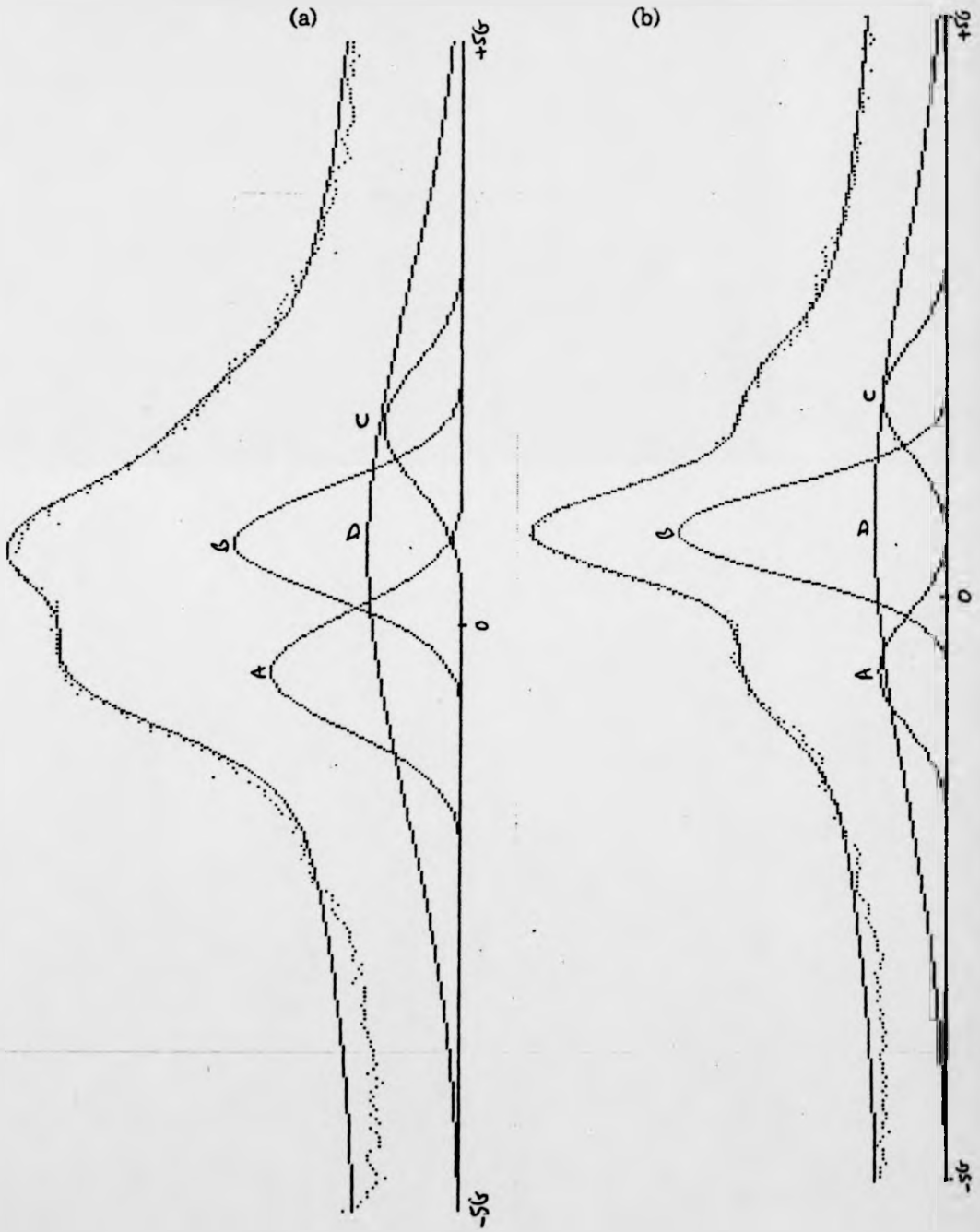

Figure 4.28 Proton spin-lattice relaxation times (ms) versus sample orientation for the $VH_{0.53}$ cylindrical sample measured at 298K and 47MHz. Angle θ=0° corresponds to the [001] crystal axis (see figure 4.8) parallel to B_o. The results shown are typical of the observed orientational behaviour of T_1.

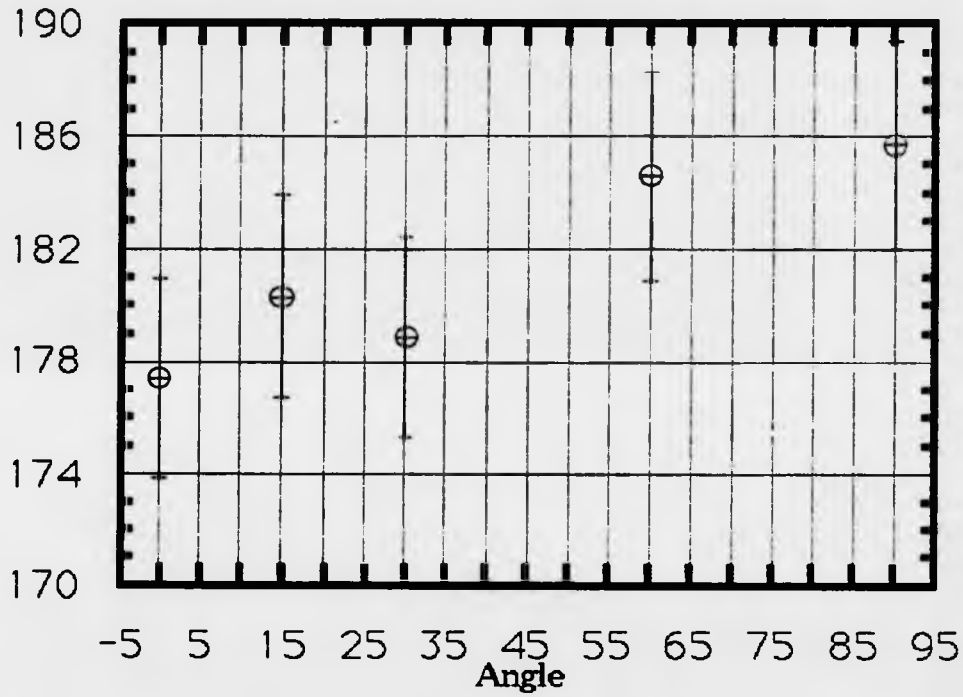

Figure 4.29 Proton T_1 (ms) versus reciprocal temperature for the $VH_{0.53}$ cylindrical sample measured at 47MHz. Only data for the crystal orientation $\Theta=0°$ is shown. Partly due to the difficulty of accurately measuring long T_1 (greater than hundreds of ms) but also due to the temperature dependence of the dipolar mechanism, minimal anisotropy in T_1 was observed at the lower temperatures. A value of $T_{1e}T=113$ (±5) sK is obtained from this data. Note also that the dipole contribution to T_1 in this temperature regime is complicated by the existence of diffusion on both the O_{Z1} and O_{Z2} sites and no value of E_a is determined but see the excellent work of Fukai and Kazama [4.45].

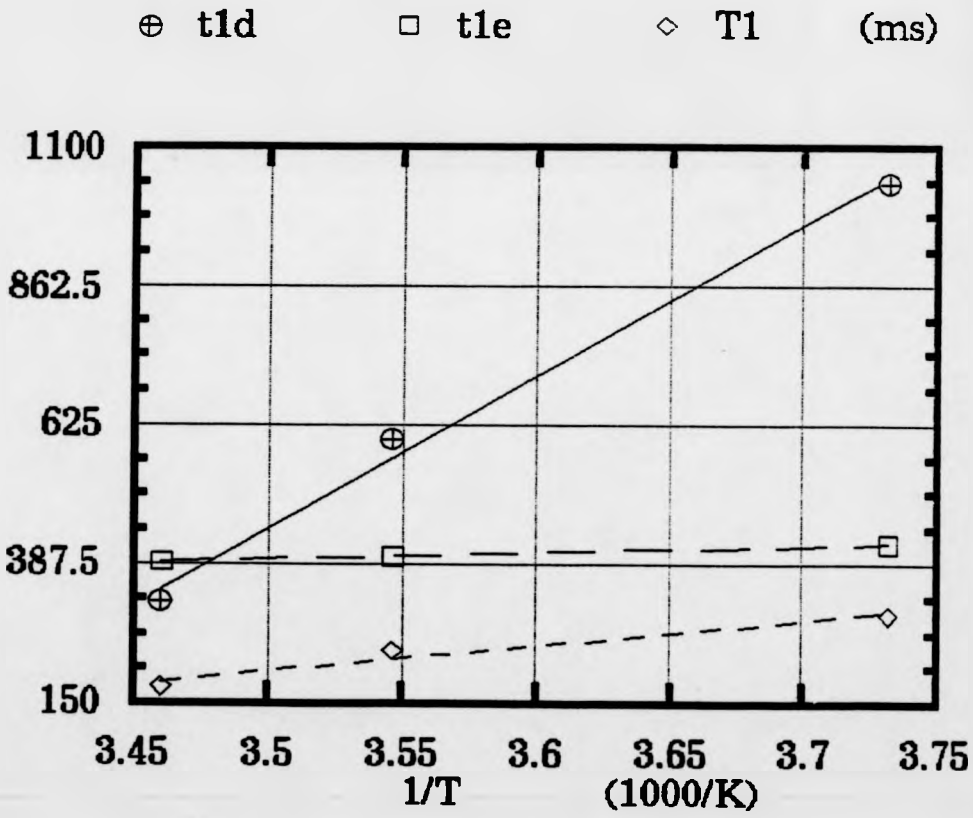

Figure 4.30 Orientation dependence of the proton line in the β-V_2H C-domain sample, measured at 19.8MHz and 285K. The upper line is for Θ=90°, ie [001] perpendicular to and the plate faces parallel to B_o, and subsequent lines show 10° increments in Θ to 0°.

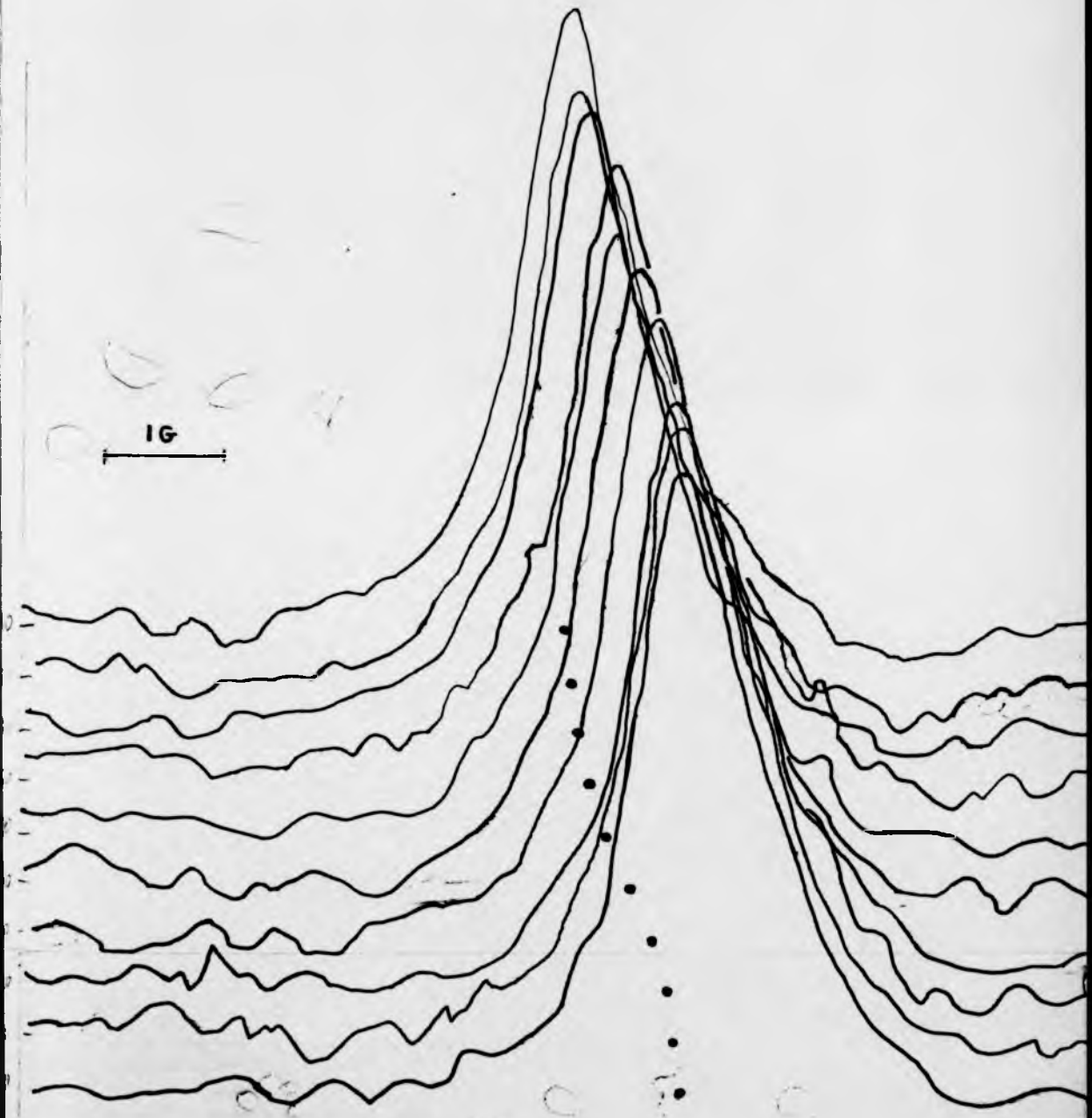

Figure 4.30 Orientation dependence of the proton line in the β-V_2H C-domain sample, measured at 19.8MHz and 285K. The upper line is for Θ=90°, ie [001] perpendicular to and the plate faces parallel to B_o, and subsequent lines show 10° increments in Θ to 0°.

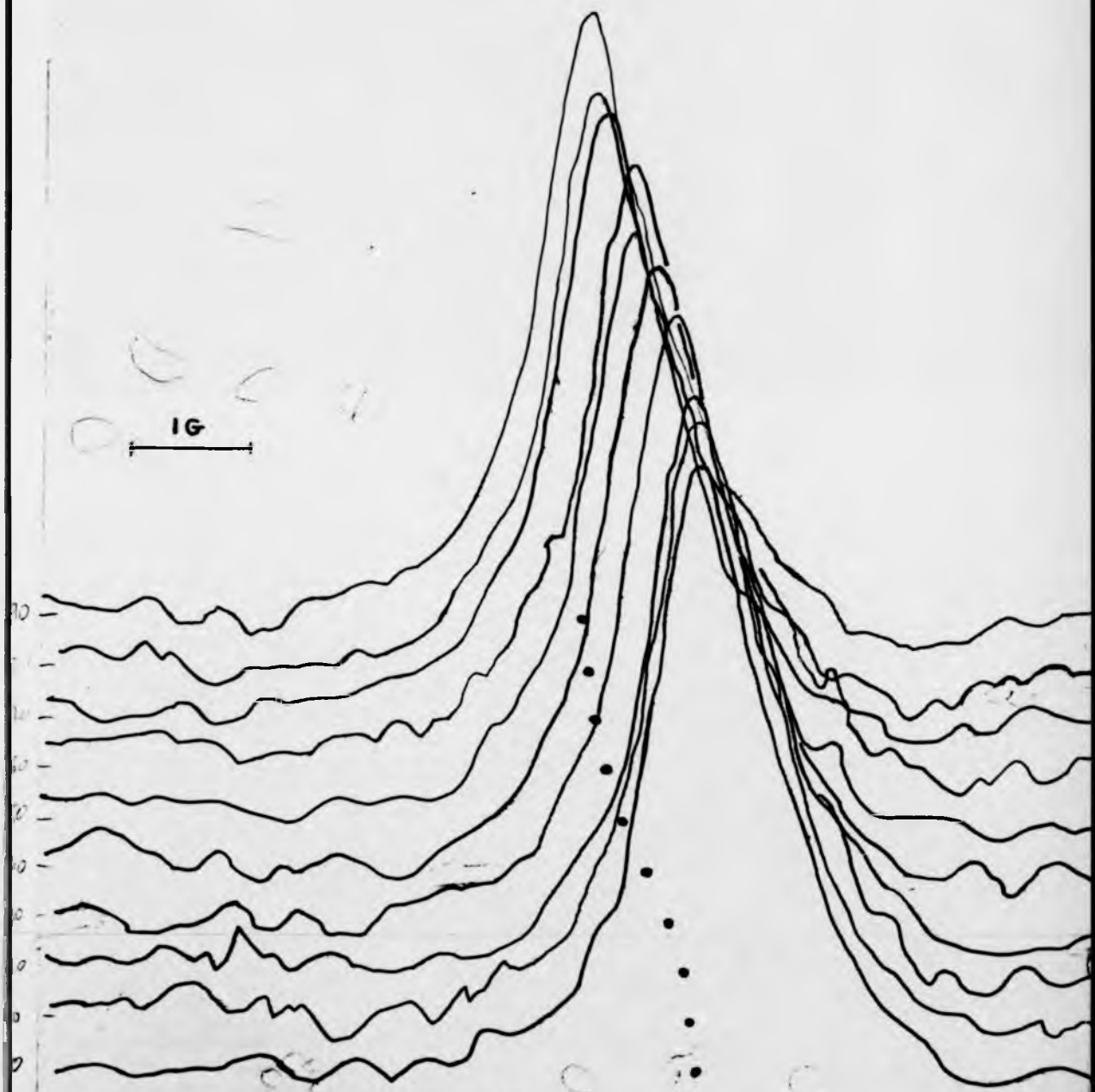

Figure 4.31 Orientation dependence of the proton T_1 (ms) in the β-V_2H C-domain sample, measured at 19.8MHz and 285K. The angle shown is ψ which is the angle between B_0 and the crystal [$\bar{1}$10] axis. The line is simply a guide to the eye.

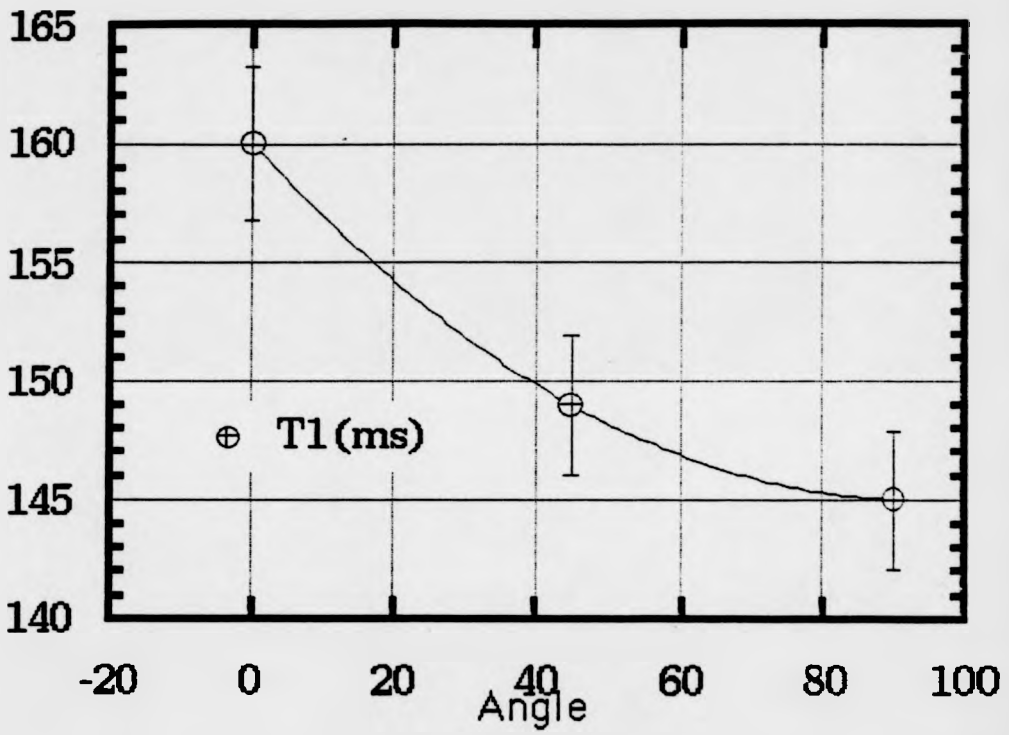

Figure 4.32 Phase diagram of the Yttrium-Hydrogen system after Khatamian and Manchester [4.53].

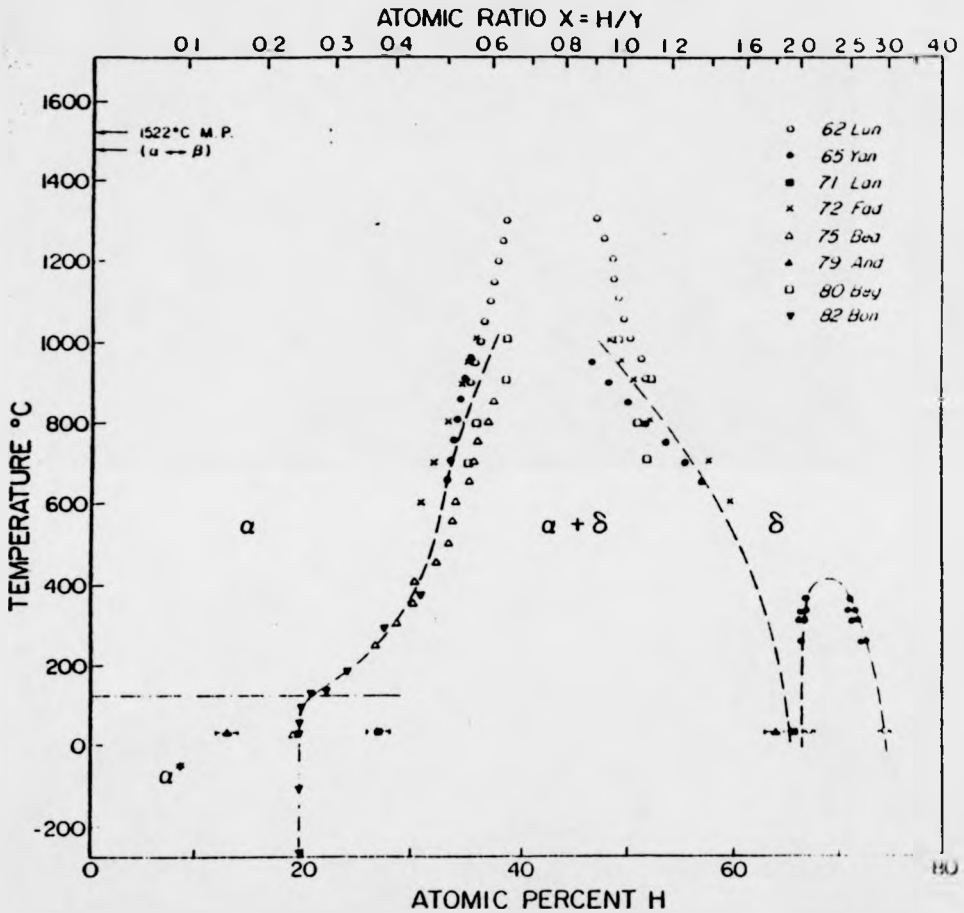

Figure 4.33 (a) A schematic perspective view of part of the hexagonal unit cell structure of the hcp α-YH_x system. For yttrium metal c=5.73Å, a=3.65Å and at RTP c/a=1.57 (close to the ideal ratio of 1.633). The metal atoms are shown as empty circles, O-sites as solid squares and T-sites as solid circles. Intersite jumps are also shown as described in the text.
(b) A schematic view of hydrogen ordering along the c-axis of α-YH_x at low temperatures (less than 170K) [4.55]. The metal atoms are shown as empty circles, and empty and occupied T-sites are respectively empty and filled squares.

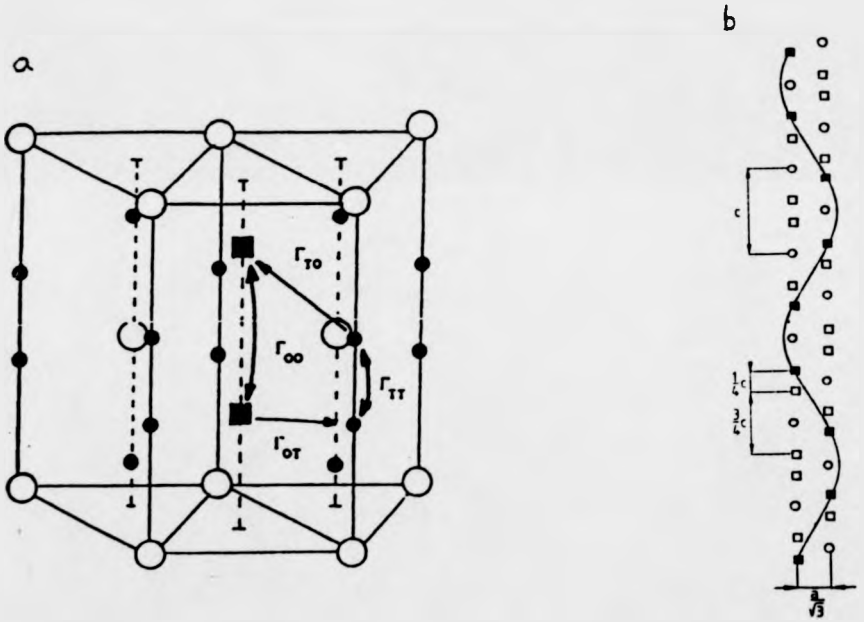

Figure 4.34 Pressure composition curve for the yttrium-hydrogen system. see [4.5 and 4.6]

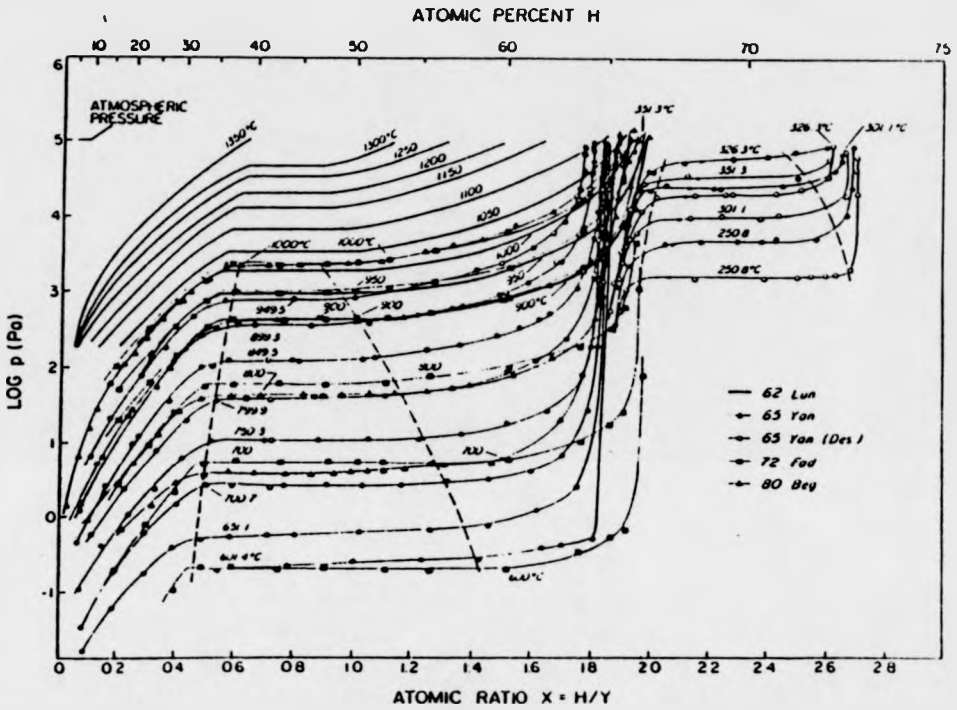

Figure 4.35 Theoretical R_1 v Θ dependence determined from expressions derived by Sholl [4.62] for the specific hydrogen jump models in the α-YHx system. Model 1 described in the text provides the R_1 v Θ dependence shown here.

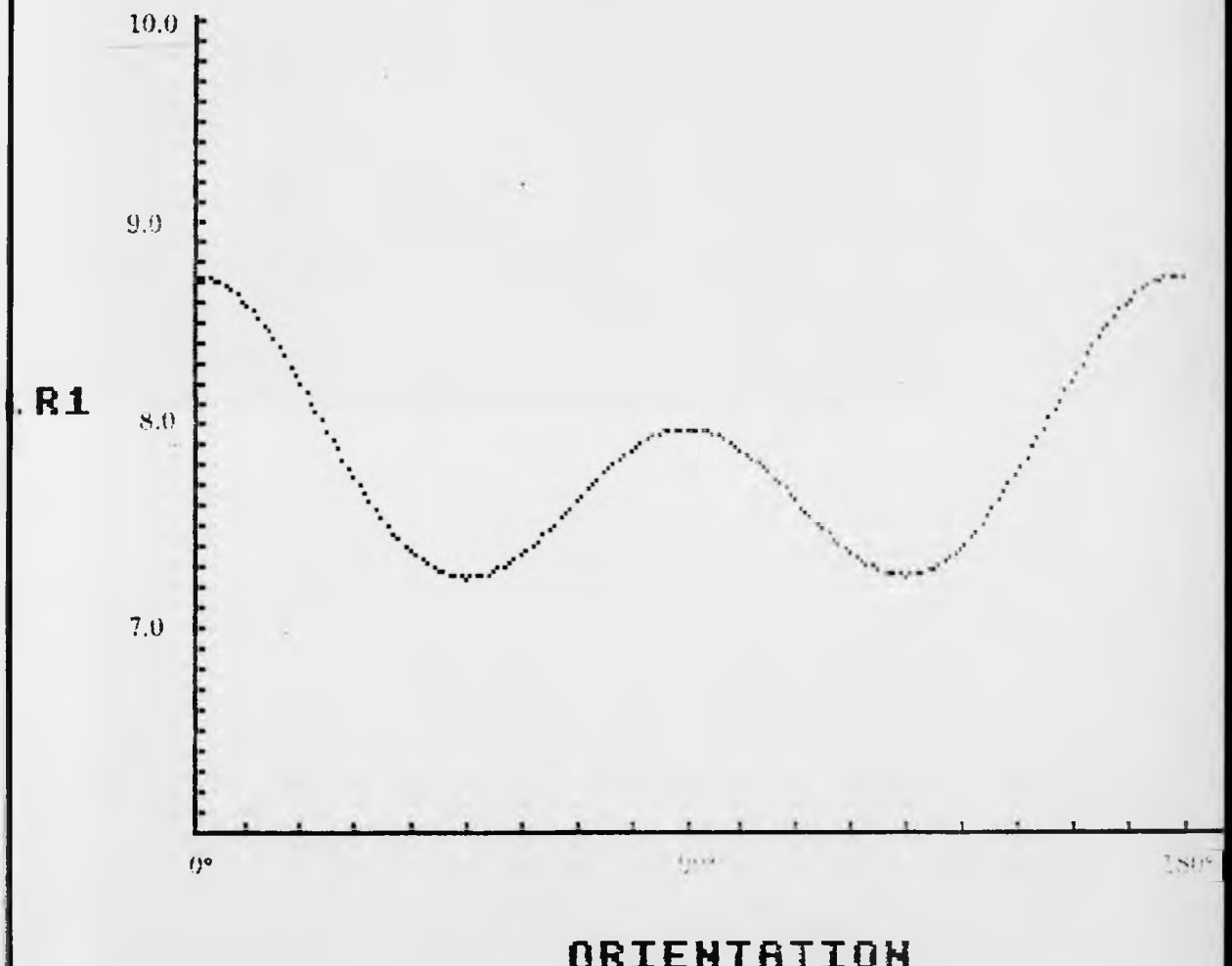

Figure 4.36 Further theoretical predictions to those shown in figure 4.35. for the behaviour of R_1 v Θ for model 2 described in the text. Here model 1 is shown for comparison with model 2 which is the bottom line (the data has not been normalised).

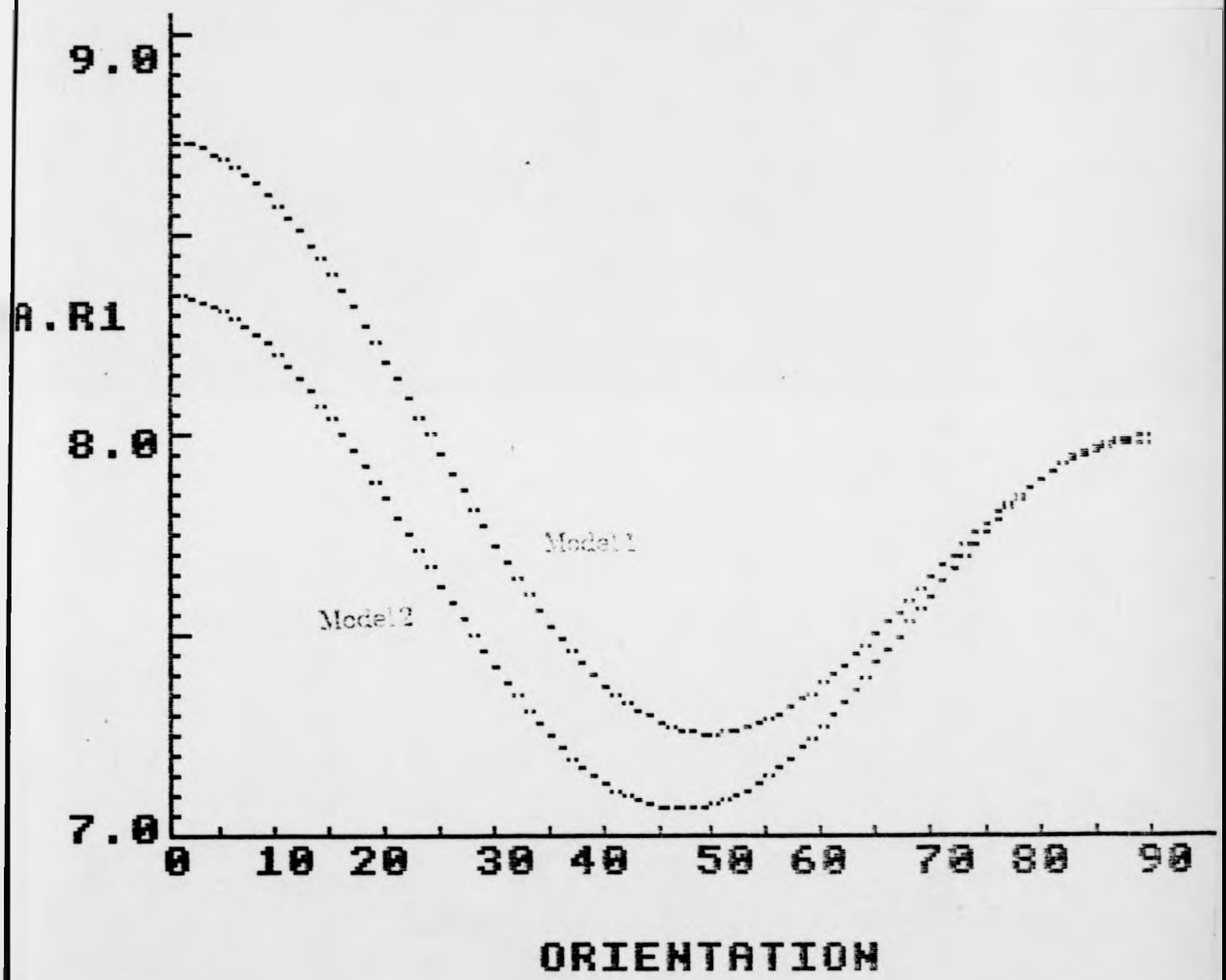

Figure 4.37 Theoretically predicted behaviour of R_1 v Θ for the hexagonal α-ScH system: (a) shows dependence for angle Θ between B_0 and the crystal c axis, (b) as for (a) but in the vicinity of the high temperature maximum in R_1 [4.41].

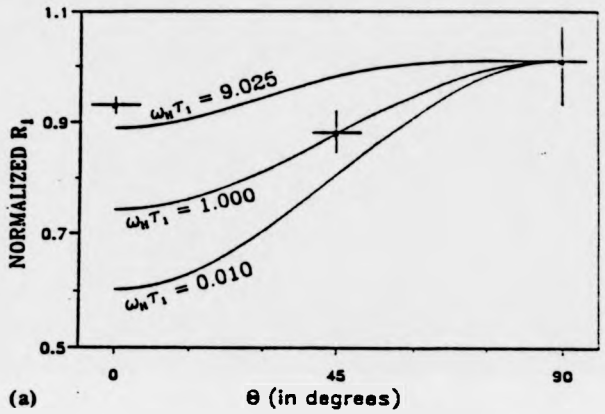

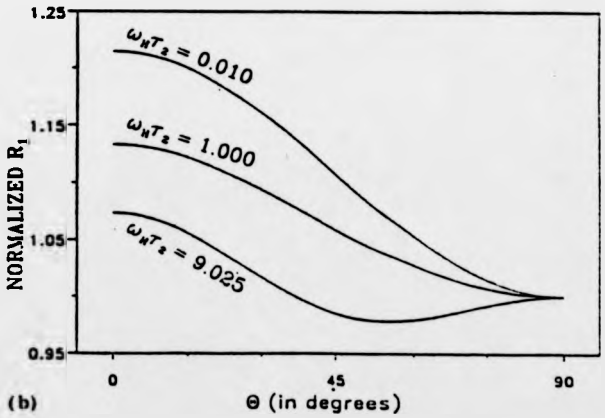

Figure 4.38 A schematic drawing of the α-YH_x single crystal cylinder orientation. The cylinder axis is aligned along a crystallographic b axis.

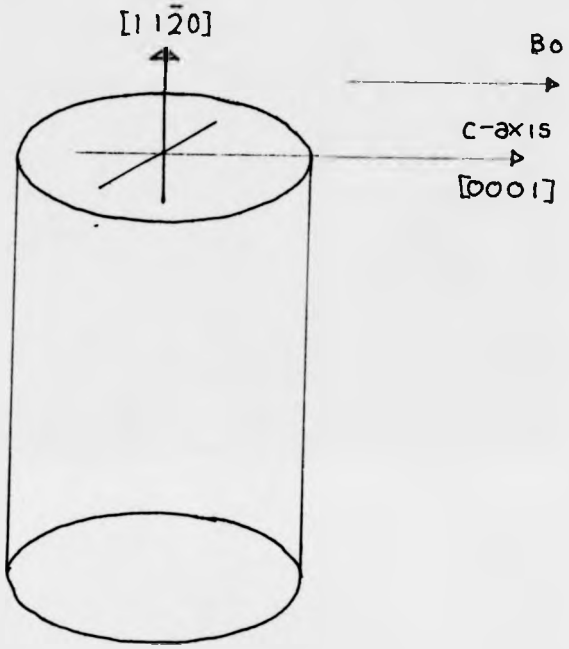

Figure 4.39 Experimentally observed Knight shift dependence for the α-$YH_{0.17}$ single crystal sample. Three orientations are shown, from the top they are; Θ=90° (c axis perpendicular to B_o), Θ=45° and Θ=0° (c axis parallel to B_o). The values of K_{ISO}=-58ppm and K_{AX}=-12ppm±4ppm were determined from these measurements.

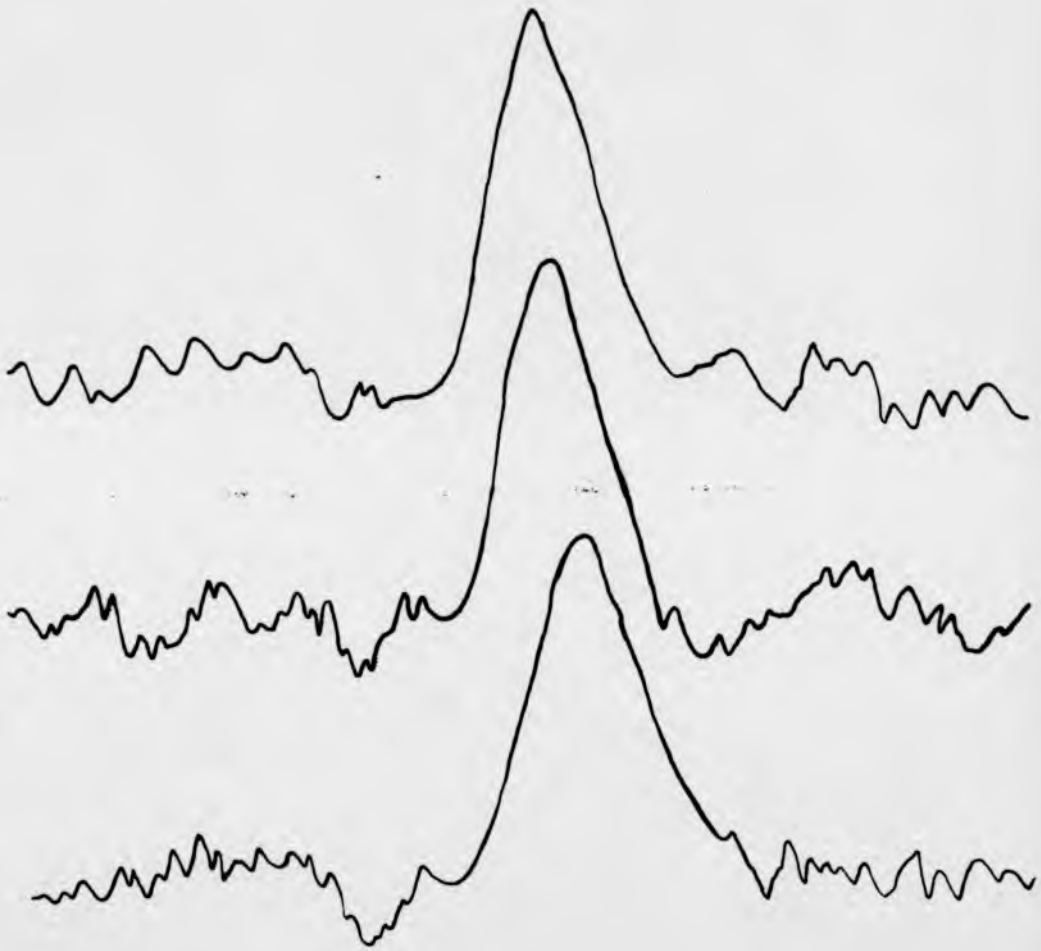

Figure 4.40 Experimentally observed T_1 (ms) orientation dependence for the α-$YH_{0.17}$ single crystal sample, measured at 47MHz and 290K. The angle Θ is the orientation of B_o with respect to the c-axis.

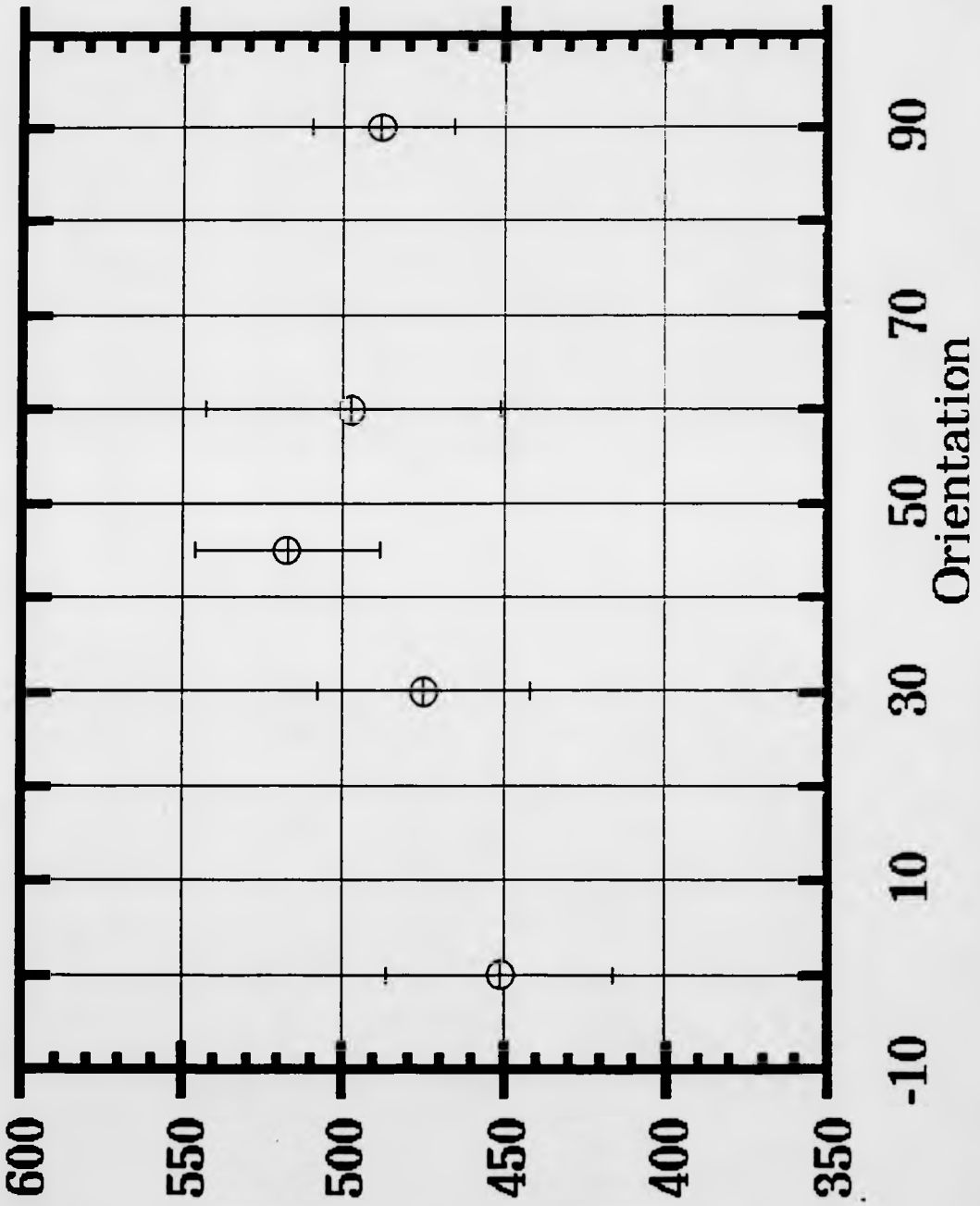

Figure 4.41 Experimentally observed T_1 (ms) orientation dependence for the α-$YH_{0.17}$ single crystal sample, measured at 47MHz and 173K.

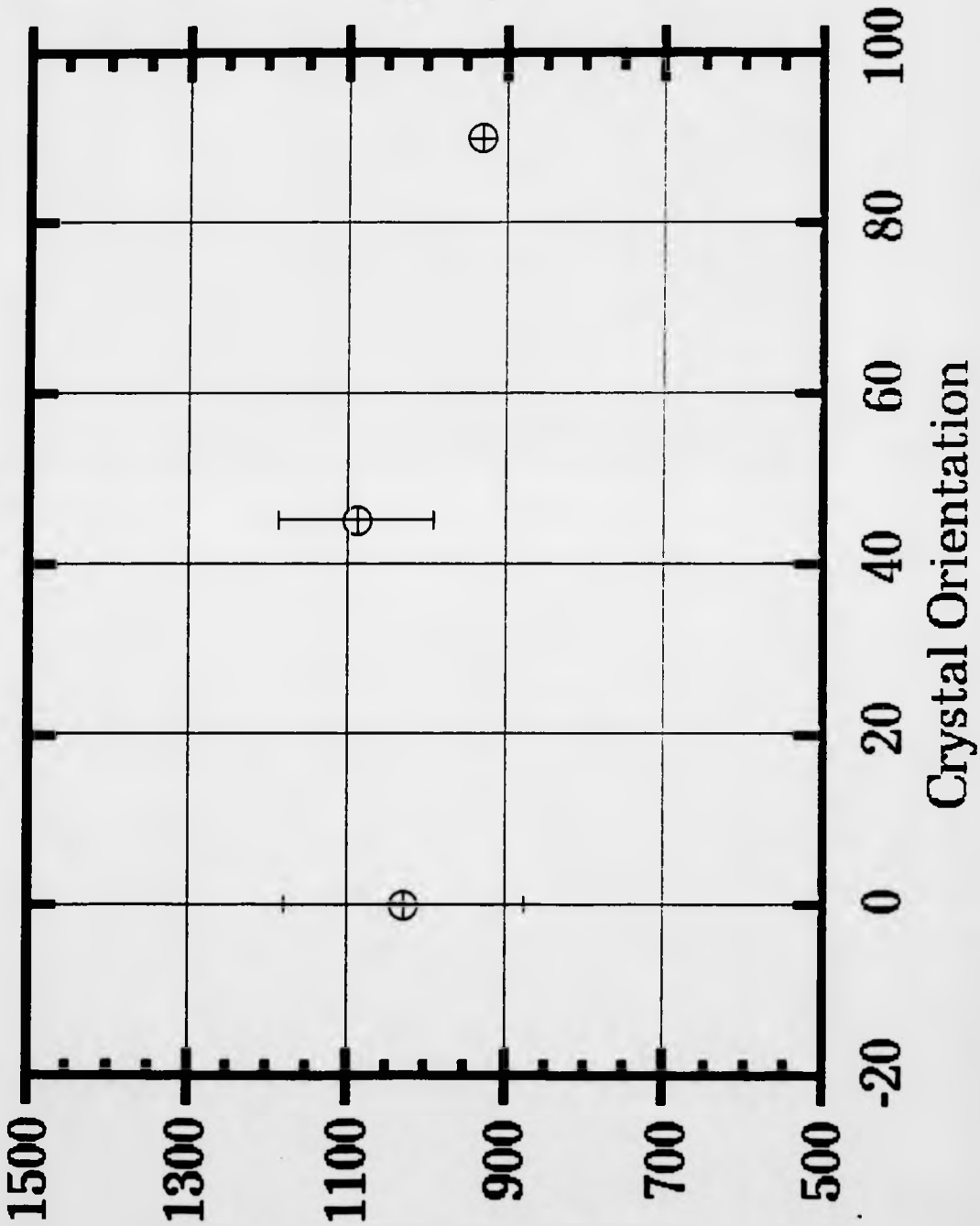

Figure 4.42 Experimentally observed T_1 (ms) orientation dependence for the α-$YH_{0.17}$ single crystal sample, measured at 47MHz and 77K.

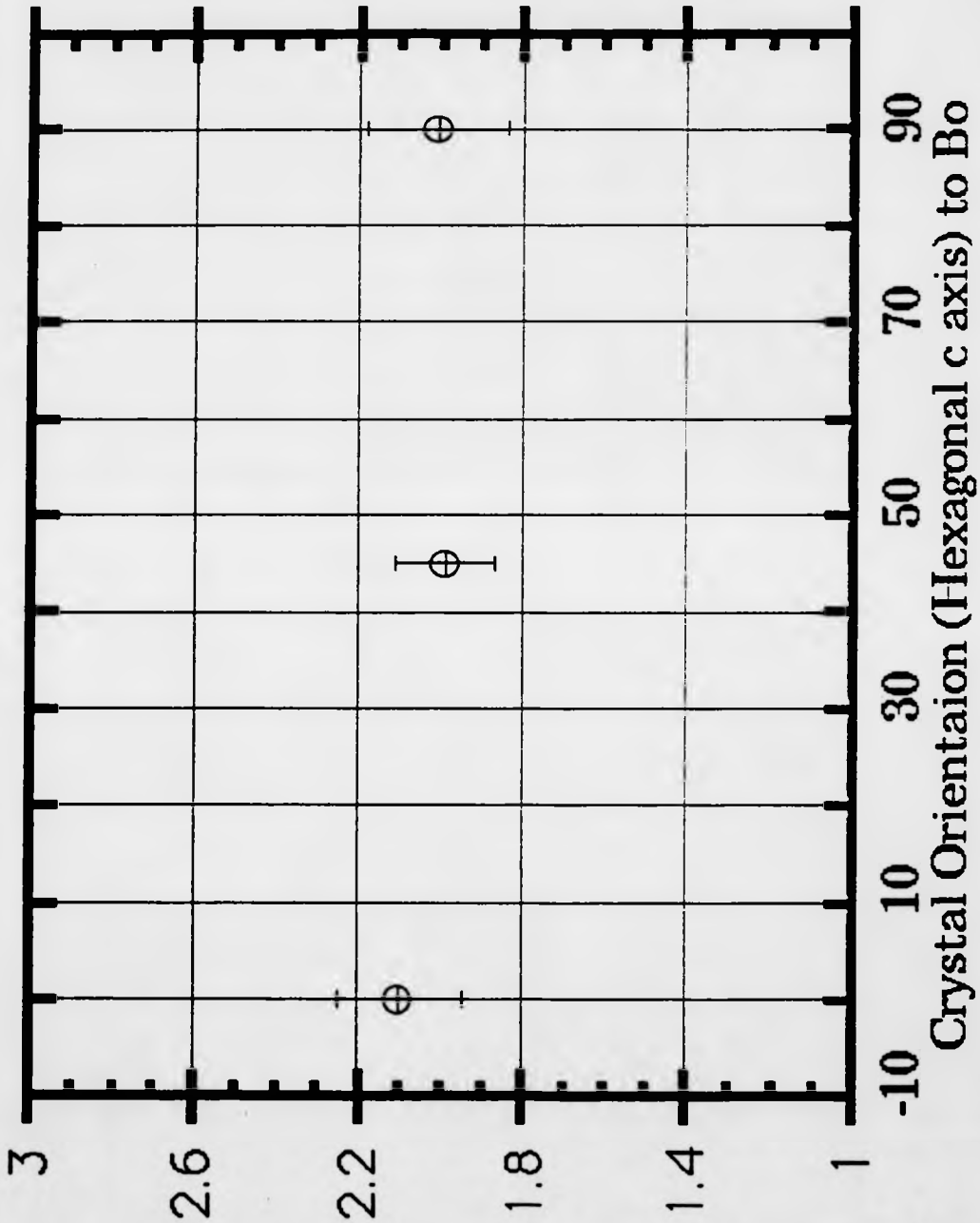

Chapter Five
QNS Investigation of the High Temperature T_1 Anomaly

5.1 The Anomaly

Anomalous behaviour of T_1 of certain nuclei in a range of metal-hydrogen systems was first reported in 1987 [5.1]. The observed effect is a decrease in T_1 below its predicted value at high temperatures. That is, at temperatures above the usual diffusion related (dipole-dipole or quadrupole) minimum in T_1, where the hyperfine interaction is expected to be the dominant relaxation mechanism, T_1 is observed to decrease considerably below the expected value extrapolated using the Korringa relation from low temperature measurements. The expected behavior of T_1 at high temperatures, that T_1 is dominated by the hyperfine interaction, was discussed in chapter two. The anomaly has been observed in two fundamentally different types of system and raises an interesting contradiction to previously existing theory.

The types of systems are first, Group 3 and 4 dihydrides, such as YH_x and ScH_x where $x \approx 2$, and second, Group 3 and 5 metal-hydrogen solid-solution phases, such as VH_x and NbH_x where $x \approx 0.2$.

Specifically, the anomaly has been observed in the proton T_1 at high temperatures in the dihydrides of Sc, Ti, Y, Zr and La [5.1, 5.2, 5.4, 5.21]. Similarly, the anomaly has been observed for deuterium in Y and Sc dideuterides, and indeed also for ^{45}Sc nuclei in ScH_{2-x} and ScD_{2-x} [5.1, 5.2, 5.4]. Both ^{45}Sc and ^{2}D possess a quadrupole moment (-0.22 and 0.0028 barns respectively) and the 'usual' motional relaxation rate maximum referred to above is due to the quadrupole mechanism as discussed in section 2.1.

In the solid-solution phase systems the anomaly has been observed for the proton T_1 in VH_x, NbH_x and TaH_x and alloys of these, but not for the T_1 of ^{51}V which behaved as expected at high temperatures [5.3]. For Group 3 hcp solid solution phase systems the anomaly has been observed for the ^{45}Sc T_1 but not for the spin-lattice relaxation time of the proton or deuterium [5.4]. Some T_1 data for systems which exhibit the anomaly is shown in figures 5.1 and 5.2. A corresponding reduction in T_2 is also seen in certain systems for example ^{1}H in YH_{2-x} [5.8] and ScH_{2-x} [5.17]. Indeed, the anomaly becomes more curious since recent nmr results show T_1 starting to increase again at the highest temperatures, as shown in figure 5.1b and as clearly seen in the most recent results of Han et al [5.21] from their study of ZrH_{2-x}. That is, there may exist

a true second minimum at high temperatures, higher than which the relaxation may again be dominated by T_{1e}.

Initial studies were directed towards ensuring that the effect was not an experimental flaw rather than a physical phenomenon within the sample. In this regard phase transition studies were made together with empirical calculations and studies to determine if for example gas loss from the sample was causing the effect. There are many problems associated with nmr studies at high temperatures and the results of the collaborative studies between Warwick and Ames is at the forefront of these studies. For a recent review of techniques of high temperature nmr studies and results of studies of different systems the reader is referred to reference [5.18].

Many possible explanations can be discounted on the available evidence and these are set out and explained elsewhere [5.1-4]. They include in summary: paramagnetic impurity effects, highly correlated hydrogen diffusion, substantial change in T_{1e} due to electronic structure transitions or variation in the temperature dependence of the Korringa product, diffusion effects of the host metal atoms or of impurity atoms (such as O or N), O-site occupation, chemical exchange with H in the gas phase, and formation of ortho-H_2 molecules on grain surfaces.

In chapter two it was shown how the relaxation rate depends on contributions from a variety of interaction mechanisms. In particular it was shown how atomic motion effects a modulation of both the dipole-dipole and quadrupole interaction which produces a distinctive T_1 variation with temperature. Essentially the motional relaxation mechanisms combine two features which can be expressed as

$$(T_1)^{-1} = A_i \, F_i(\omega_0, \omega_s, \tau_c) \qquad [5.1]$$

where A_i is that part of the interaction of the nuclear spin i with its surroundings that is caused to fluctuate in time by motion with a characteristic correlation time τ_c. The function F is the spectral density function which describes the fluctuation of the interaction strength in terms of the resonant frequency ω_0 of nucleus i, the resonant frequency ω_s of another nucleus, and the correlation time τ_c of the fluctuation.

Thus two variables exist variation of which could cause the anomaly. First, the interaction strength of the motionally modulated interaction may change. For example, in the case of the dipole-dipole interaction the mean separation

might be reduced, or for the quadrupole interaction in the case of the dihydride systems the efg at the nucleus might increase due to an increase in the number of interstitial vacancies. Second, the correlation time of the interaction might alter. For example, for the dipole-dipole interaction, since the anomaly occurs in the high temperature regime of the usual T_1 minimum, τ_c would need to increase thereby making the interaction more effective and reducing T_1.

Several factors point to the possibility that the anomaly is diffusion related. These factors include, for example, that the onset of the turn-down in T_1 occurs at lower temperatures in the solid-solution phases compared with the dihydride phases. Hydrogen diffusivity is, of course, much greater in the former systems at a given temperature. Indeed it is found that the onset of the anomaly occurs when the interstitial dwell time $\tau_d \sim 10^{-10}$s for all these systems. The anomaly is further characterised by a T_1 turn-down which exhibits an Arrhenius dependence having an activation energy between approximately 0.7 and 1.0 eV. It is also found that the critical onset temperature of the anomaly, T_c, for ^{2}D occurs at lower temperatures than for ^{1}H in the equivalent samples of the same composition. This could be due to the fact that the ^{2}D relaxation is primarily due to the quadrupolar mechanism and depends on both ^{2}D and vacancy diffusion, while the ^{1}H relaxation is dependent on ^{1}H motion only. In these dihydrides the particle hopping rate τ_d^{-1} is approximately equal to $c_v\tau_v^{-1}$ since the vacancy concentration $c_v \ll 1$ and hence $\tau_v \ll \tau_d$. Thus the BPP, or diffusional, T_1 minimum condition $\omega_0\tau_c \approx 1$ is satisfied at lower temperatures [5.2]. Further, there is some (but notably little) evidence of a frequency dependence in the anomalous behaviour of the proton T_1 in the dihydride phases, see figure 5.1a, which may point to a diffusional basis given the frequency dependence observed in the low-temperature regime as described by the BPP model. This effect is not observed for the solid-solution phases however.

Interstitial Clustering

To account for the anomaly it has been proposed that an analogy may be made to superionic conductors [5.1, 5.2]. A similar temperature dependent T_1 phenomenon observed in superionic conductors [5.5] has been explained by Hutchings et al [5.22] in terms of clustering of F^- ions in Frenkel pairs. Barnes et al [5.1] have proposed that in the case of metal-hydrogen systems, the otherwise highly mobile hydrogen ions cluster into groups having a finite

lifetime τ_{cl} greater than the correlation time (at the same temperature) of the relevant mechanism responsible for the nmr interaction which causes the lower temperature T_1 minimum. They particularly applied the model to the ScH $(D)_{2-x}$ system wherein the ^{45}Sc relaxation rate is dependent on the quadrupole interaction which can be written as

$$T_{1Q}^{-1} = \frac{24\pi^2 c_v}{49\omega_D} (e^2qQ/h)^2 \left(\frac{\omega_D\tau_v}{1+\omega_D^2\tau_v^2} + \frac{4\omega_D\tau_v}{1+4\omega_D^2\tau_v^2}\right) \qquad (5.2)$$

(compare with (2.20a) and eg (2.23)), where c_v is the vacancy concentration and τ_v the correlation time for a single vacancy hopping. This is a well known result for these systems where it was found that the quadrupole relaxation is determined by fluctuations in the electric field gradient caused by interstitial vacancy diffusion. In the case of hydrogen clustering in the ScH_x systems discussed by Barnes et al, it was proposed that $\tau_{cl} > \tau_v$ and that the clusters are relatively static during their lifetime (ie $\tau_c \approx \tau_{cl}$). Also, in order to account for the observed lack of frequency dependence of the high temperature minimum $\omega_0\tau_{cl} < 1$. The ^{45}Sc relaxation rate due to the clustering would then be dependent on the concentration of clusters n_{cl}, assuming each cluster was associated with a single Frenkel interstitial.

The effect of the clustering would be to create a maximum relaxation rate (comparable to that of the low temperature maximum rates) when the clustering concentration achieved a maximum. It can be shown that to agree with the experimentally observed values of T_1 the cluster concentration is required to be $n_{cl} \approx 0.2$ and the mean lifetime needs to be $\tau_{cl} \approx 10^{-7}$ to 10^{-3} s. The latter requirement contrasts with the otherwise good comparison of the MeH phenomenon to superionics (see eg [5.4]), where the lifetime of the clusters is predicted to be about 10^{-12} s. The requirement of long clustering times at a temperature where we expect the hydrogen to be highly mobile makes the model intuitively improbable, but nevertheless it remains a theoretical possibility.

Richards' model

The problem as it was first perceived was somewhat simpler than it now appears since the phenomenon was observed only in the sub-stoichiometric fcc dihydrides. An early explanation for the anomaly was presented by Richards [5.6] which accounted for the reduction in T_1 by an actual net decrease in the interstitial diffusivity and hence an increase in the correlation

time τ_c for the nuclear magnetic interaction. This solution has obvious appeal in its simplicity.

The basis for Richards' model comes from a theory he proposed to explain the variation in interstitial site occupation between different dihydrides where, for example, some O-site occupation is observed in YH_{2-x} at certain temperatures but not in ScH_{2-x} [5.7]. The model essentially provides an O-site blocking mechanism through the anharmonic vibration of hydrogen on T-sites neighbouring the O-site. In his more recent paper [5.6] Richards takes this model further to provide a mechanism whereby the T_1 anomaly in fcc dihydrides is explained by a decrease in hydrogen diffusion. He assumes a particle diffusion path between neighbouring T-sites via an intermediate O-site which is reasonable since the direct T-T jump requires a higher activation energy. A schematic representation of the jump model is shown in figure 5.3. In fcc dihydrides the hydrogens occupy T-sites which form a sc structure in the metal lattice: an extended sc lattice is not shown. Richards uses an over-barrier hopping model in which, in order to reach an O-site, the hydrogen must have sufficient energy to pass over the saddle-point or potential maximum. An adiabatic system is assumed and the potential barrier is represented as

$$U = \frac{z\Sigma_n \partial_n \exp[\frac{-E_n(T)}{kT}]}{\Sigma_n \exp[\frac{-E_n(T)}{kT}]} + U_A \qquad (5.3)$$

where $E_n(T)$ is the energy at the occupied T-site at equilibrium, $\partial_n = E_n(S) - E_n(T)$, $E_n(S)$ is the energy of the site when the hopping hydrogen is at the saddle-point, z is the number of hydrogens interacting equally with the hopping particle and U_A is the barrier potential in the absence of H-H interactions. Now, the particle hopping rate is proportional to the probability that a particle has sufficient energy to go over the saddle-point, that is

$$\nu = \nu_o \exp(\frac{-U_o}{kT}) \{\exp(\frac{-U_T}{kT})[\frac{1+Z_\nu(S)}{1+Z_\nu(T)}]\} \qquad (5.4)$$

where U_o is the zero temperature barrier potential which is assumed to be independent of temperature, whilst $U_T = U - U_o$ and the Z_ν are partition functions for the saddle-point and equilibrium configurations. The factor in the curly bracket in equation 5.4 is an additional factor to the basic Arrhenius expression given in section 1.3 due to the repulsion model. To account for the anomaly this factor must decrease at a greater rate than that at which the

$\exp(-U_o/kT)$ factor increases at high temperatures and thereby decrease the jump frequency. Richards assumes a simple model for the potential at the occupied T-sites and introduces a repulsion parameter J which modulates the potential depending on the position of the hopping proton. Thus values of $E_n(T)$ and $E_n(S)$ can be calculated and substituted into (5.3) and (5.4). Richards' model gives a very good fit to some experimental data as shown in figure 5.4. The experimental data shown are for $ScH_{1.83}$ where $U_o = E_a = 0.7$ eV and a value of J =0.15 eV is required to generate sufficient repulsion to create a fit. This value of J can be justified since it is generally accepted that nearest equilibrium separation is ~2,1Å in hydrides (the Switendick criteria). When the ^1H is at the O-site it is separated from surrounding T-sites by 2.08Å. Richards goes on to justify the apparent increase in T_1 at still higher temperatures due to a breakdown of his model in that the adiabatic assumption is no-longer correct or that indeed direct T-T site jumps may begin to be favourable. It was from the perspective of the initial nmr results and Richards' model that the following qns investigation was conducted.

5.2 Sub-stoichiometric dihydrides: $YH_{1.98}$

A study of $YH_{1.98}$ has been made in two separate neutron experiments using both IN6 and IN10 spectrometers at ILL. The aim of these experiments was to determine the ^1H diffusivity in the temperature range of the high temperature T_1 anomaly.

IN6 experiment

As shown in section 4.3 the YH_x system has a stable ∂-phase in the composition range $1.80 \leq x \leq 2.05$ at room temperature. The ∂-phase has an fcc structure (CaF_2 type) with lattice parameter a =5.2 ± 0.01 Å and a density ρ =4.29 gcm^{-3} and, as previously discussed, the hydrogen predominantly occupy T-sites. The high purity, fine powder samples used were prepared at the Ames Laboratory using a vapour decomposition technique. The sample container and method of transfer have previously been described in section 3.2, where for the IN6 experiment a=60mm, b=35mm, c=1mm and d=0.7mm. Dimension d was calculated to give an 85% neutron transmission coefficient through the sample allowing for a 50% packing factor. Approximately 5g of $YH_{1.98}$ was used. Whilst it can be shown that various experimental factors in the nmr experiments, such as evaporation of hydrogen from powder samples or loss of hydrogen through the quartz sample containers at the high temperatures of the study, could not explain the T_1 phenomena the sample

handling and transfer techniques, as well as sample cell structure used in these qns experiments were designed to minimise any such effects.

The relatively large thickness of the steel cell, required to prevent hydrogen loss at high temperatures, gave rise to a large amount of scattering and consequently good statistics in a given run were required in order to enable subtraction out of the noise from the actual signal. Typically, runs at a given temperature were in excess of six hours. The sample itself was found to have a transmission coefficient of 81%. A schematic diagram of the arrangement of neutron beam and sample cell is shown in figure 3.8 where the plane of the sample was placed obliquely at 135° to the beam and a 2mm Cd mask was placed in front of the sample to allow only a 4 x 2 cm window of neutrons onto the cell. An incident neutron wavelength of 5.1Å was used and for analysis the detectors were grouped into 37 sets between 2Θ scattering angles of 12° to 113°. A series of runs using the empty cell were carried out over the full temperature range and a standard measurement on a vanadium sample taken. The maximum temperature achieved was 1050K, which had several undesirable effects on the cell. After cooling, the main copper O-ring between the conflats was considerably distorted and made separation of the conflats extremely difficult. The bolts holding the conflats together had welded to the threaded holes of the bottom conflat. To avoid the latter problem the threading was removed and a nut and washer used to fasten longer bolts.

Data collected from a series of runs was corrected and analysed as previously described. The clear and disappointing conclusion being that the resolution of IN6 was not good enough to enable quantitative determination of the ^1H diffusivity. Some results are shown in figure 5.5 which shows $S(Q, \omega)$ versus energy about the elastic peak. The data clearly shows an increase in the qns FWHM with temperature. However, since this can only be resolved at $Q = 1.93$ $Å^{-1}$ no positive conclusions can be drawn about ^1H diffusion behaviour with temperature, though it does appear that D is increasing with temperature. The lack of quantitative results is due to the lack of resolution in the qns lineshape using IN6. The choice of IN6 for this experiment was in part determined by a prediction for $D \sim 4 \times 10^{-6}$ cm^2s^{-1} at 870K based on nmr T_1 data [5.8]. For the instrument set up used, IN6 has a resolution of ~100μeV about the elastic peak, this means that a diffusion coefficient of $D = 10^{-5}$ cm^2s^{-1} could be observed at $Q = 0.5$ $Å^{-1}$. The nmr data was interpreted using a simple BPP model and suggested that some analysable results could be achieved at high temperatures. However, a later calculation of D from diffusion measurements of hydrogen in α-YH_x obtained using neutron scattering [5.9]

and extrapolated to the dihydride composition using a simple blocking model gave a value of D ~2 x 10^{-7} cm^2s^{-1} at the same temperature. This value is considerably lower than original predictions and accounts for the inability to obtain quantitative qns diffusion results.

A typical inelastic scattering spectrum obtained from this series of runs is shown in figure 5.6. The figure shows low energy yttrium lattice modes at 13, 18 and 28 meV as well as the hydrogen vibrational modes. The first harmonic is seen at approximately 112 meV and the second at 224 meV. The first harmonic result is in agreement with the expression

$$E(R)=AR^{-3/2} \qquad (5.5)$$

known as the Ross equation [5.10], which equates the optic mode energy of the system to the hydrogen-to-metal distance R. The energy determined from these experiments yields a distance of approximately 2.25Å in agreement with the T-site to metal distance. Additionally, the second harmonic population was found to increase with temperature as expected and an anharmonic broadening of the first harmonic was observed. There was also a noticeable but slight decrease in the energy of the first harmonic with increasing temperature. These last two observations could imply an increase in the average H-Me distance with temperature and a possible double site occupation (for example a tendency towards some O-site occupation) or anharmonic oscillation within the T-site. However, a much more rigorous study of this high energy inelastic scattering regime would be required to make any quantitative analysis, for example by using the HET facility at ISIS [5.11, 5.12]. No such investigation has been carried out but should be considered by neutron spectroscopists since the results could shed much light on hydrogen behaviour at high temperatures and therefore on the anomaly itself.

IN10 experiment

Following the IN6 experiment a further qns study was performed using IN10 at a later date. On this high-resolution back-scattering spectrometer an incident wavelength of 6.27Å was used. The instrument is capable of resolving up to 0.3μeV at this wavelength. All 8 detectors were used in a range of 7.45°< 2Θ <129°. The sample holder had dimensions a=50mm, b=50mm, c=1mm and d=0.5mm (see figure 3.10), and the plane of the powder was placed obliquely to the beam at an angle of 100°. The empty cell and vanadium runs were done before loading approximately 5g of $YH_{1.98}$ into the

cell. Because of the much lower neutron flux on IN10 longer runs were required, typically a 12 hour run was made at each temperature with a stability of ±7K. Four temperatures were studied, namely 575K, 887K, 982K and 1079K. Data correction and analysis was carried out as previously explained.

Typical fitted data is shown in figure 5.7 where the experimental data points represent the number of neutron counts at a given energy. This figure shows only the qns line since the elastic lineshape and all other background counts have been removed. The solid line represents the best fit Lorentzian to the data from which the HWHM value for the qns peak is derived. The results for a temperature of 1079K are shown in figure 5.8 where E_{HWHM} is plotted versus Q^2 over a range of Q^2 from 0.169 to 0.773 $Å^{-2}$. The diffusion coefficient is calculated using results from the first 3 detectors, Q up to 0.1$Å^{-1}$, as represented by the best line fit shown. The diffusion coefficient observed at each temperature is shown in figure 5.9.

The results clearly show increasing diffusivity over the entire temperature range from 575K to 1079K which is well into the T_1 anomaly region since the onset is T_c ~950K. Fitting the data to an Arrhenius expression we find that E_a =0.33 ± 0.09 eV and D_0 =0.7 (±0.4) x 10^{-4} cm^2s^{-1}. The incontrovertible conclusion is that the mean hydrogen diffusivity does not decrease above T_c. Hence Richards' model is incorrect. These results were the first of their kind to disprove this theory [5.14].

These results must be considered in the light of the existing nmr T_1 data which is shown in figure 5.1a, from which we know that T_c occurs at approximately 1000K and 900K when measured at 40 and 12.3 MHz respectively. Using equation 1.3 we find that the qns data give a value of t_j ~ 0.6 x 10^{-10} s in this temperature region assuming a T-T distance of approximately 2.6Å. This is in good agreement with the general form of the T_1 data, discussed in section 5.1 that T_c occurs for t_d ~ 10^{-10} s.

The overall result is in good agreement with other recent data on similar systems studied by Stuhr et al [5.13] also using qns, as shown in figure 5.10, and a study using the nmr alternating pulsed-field-gradient technique [5.19] at Warwick reported by Barnfather et al [5.14], see figure 5.11.

The YH_{2-x} study by Stuhr et al was also conducted on IN10 using a range of hydrogen concentrations, $1.80 \leq x \leq 1.97$, near to the stoichiometric dihydride concentration. Their results, as shown in figure 5.12, indicate that the

hydrogen diffusivity increases with increasing concentration and they conclude that there is an increasing occupation of O-sites. In fact, this trend in diffusivity is well known from nmr results, see for example Markert and Cotts [5.15], but of course cannot in itself account for the T_1 anomaly. In any case, increasing diffusivity with concentration at a given temperature is not observed in ScH_{2-x} and there is no reason to suppose that O-site occupation increases in this material. Nevertheless a T_1 anomaly occurs in ScH_{2-x} so that it seems unlikely that the anomaly is associated with O-site occupation.

5.3 Solid-solution phase systems: $Nb_{0.75}V_{0.25}H_{0.20}$

A study of $Nb_{0.75}V_{0.25}H_{0.20}$ has been made using the back-scattering tof spectrometer IN10. The aim was to observe the nature of the ^1H diffusivity in the temperature range of the T_1 anomaly. This particular alloy composition was chosen because it does not undergo a phase transition from α to β in the region of 350K and also a clear onset of the T_1 anomaly is observed at around 500K as shown in figure 5.2b. This contrasts with the α-phases of the non-alloy systems which do undergo such a phase transition and where the actual onset of the T_1 turn-down is very gradual over a range of about 250K. The high purity, fine powder sample used was prepared at the Ames Laboratory by a vapour decomposition technique. An identical arrangement of the IN10 spectrometer and sample was used for this study as for the $YH_{1.98}$ sample, with λ_o=6.27Å and 8 detectors in the range $0.07 \leq Q \leq 2$ Å^{-1} ($7.45° \leq 2\theta \leq 129°$) with a sample to beam angle of 100°. The sample cell needed a much thicker powder chamber because of the lower concentration of hydrogen in this sample which results in a lower average cross-section per nucleus. Consequently the cell dimensions were a=50mm, b=50mm, c=1mm and d=1.5mm (see figure 3.10). Again, long runs were used to obtain good count statistics and measurements made at four temperatures, 286K, 417K, 559K and 809K, with an error of the order of ±7K.

A typical fitted set of data is shown in figure 5.13 where number of neutron counts versus energy is shown for a single detector for a single sample temperature. The results of linefitting such data for three detectors and a sample temperature of 809K are shown in figure 5.14 where E_{HWHM} is plotted against Q^2. The diffusion coefficients determined from the data are shown in figure 5.15 for all temperatures.

These results again show an increase in diffusivity with temperature. Indeed, an Arrhenius fit to the data, as shown in figure 5.15, yields values of

E_a =0.16 ± 0.02 eV and D_o =1.8 (±0.4) x 10^{-4} cm^2s^{-1}. Clearly the T_1 anomaly cannot be explained in terms of a decrease in diffusivity in these systems either. This result is in reasonable agreement with other recent diffusivity measurements reported by Han et al [5.3] who used an nmr field-gradient technique, after Cotts et al [5.20], to measure diffusion coefficients. Their results are shown in figure 5.16 for $Nb_{0.75}V_{0.25}H_{0.23}$ which yield values of E_a =0.20 eV/atom and D_o =8.6 x 10^{-6} cm^2s^{-1}.

The conclusion from these results is that there is no net decrease in hydrogen diffusivity with temperature above the critical temperature T_c~500K. The anomaly is not due to a net decrease in hydrogen diffusivity and there is no apparent anomalous effect in the diffusivity since it appears to obey a simple Arrhenius dependence.

5.4 Discussion and Conclusions

Richards' model is not able to explain the anomaly, nevertheless phenomenologically he was able to obtain a good fit to T_1 data by assuming a second activated process competing with known processes. His theory provided a net decrease of hydrogen diffusion which has been shown to be invalid in light of the data presented above. From their own results of hydrogen diffusion data Stuhr et al propose O-site occupation as an explanation of the T_1 anomaly which would only appear applicable for the YH_{2-x} system in order to explain the dependence of diffusion coefficient on hydrogen concentration. This proposal to explain the T_1 anomaly was already virtually discounted [5.1], prior to their suggestion, because it was not possible to produce a realistically large τ due to slow hydrogen diffusion on the O-sites either by a realistic model or by fitting to experimental data.

Two explanations of the phenomena which have been proposed since publication of these results which are not consistent with Richards' model are a two state model which incorporates the clustering model discussed earlier and hydrogen pairing.

Two-state model

Han et al [5.3] have proposed a two state diffusion mechanism to account for the anomaly based on the work of Lottner et al [5.24]. It involves two characteristic (correlation) times for hydrogen diffusion where the hydrogens move rapidly between a mobile state and a rest state. The model allows for the occupation time of the rest state to be much longer than in the mobile state

and T_{1d} results from a combination of contributions associated with each characteristic time. This partitioning is similar to that used by Boyce et al [5.5] when describing ionic conductors.

Han et al consider two forms of the model: the first in which the fraction of the interstitials in the mobile state is very small («1), and the second where the rest state is defined as a trap for one or more hydrogens. From their analysis they conclude that for the first model the dwell time in the immobile state increases with temperature and that it is likely that the fraction of time each interstitial is in the immobile state also increases with temperature. The immobile state is therefore the excited state for the system which could be a state such as that proposed earlier of immobile clustering of hydrogens excited from their interstitial sites. Their analysis provides results consistent with qns results for NbH_x and is also appropriate for the anomalous T_1 behaviour of ^1H, ^2D and ^{45}Sc. It does however, raise a problem in that where one intuitively expects the clusters to break up at higher temperatures the model requires the clustering lifetime to increase.

The second model is found to require a large but not unfeasible density of trapping sites such as dislocations or other imperfections. However, it provides a relaxation mechanism which is frequency dependent. This of course is not found to be the case from experiment. Neither model is entirely satisfactory therefore, and sufficient questions remain for further models to be investigated.

Hydrogen Pairing

The most recent explanation of the anomaly to be proposed is that of hydrogen pairing by Cotts [5.23]. From the basis of equation 5.1 and available experimental data Cotts is able to provide a possible explanation of the T_1 anomaly observed for ^2D and also ^{45}Sc but for ^1H the requisite restrictions on the pairing hydrogens make the explanation less likely.

The observed T_1^{-1} are expressed by Cotts as a linear sum of components $(T_1^{-1})_m + (T_1^{-1})_e + (T_1^{-1})_x$, where m denotes motion and x the anomaly phenomenon. The pairing state is taken to be an excited state of lifetime τ_x which occurs randomly with mean time τ_u. In the regime $T \gg T_c$ where $\tau_d^{-1} \geq 10^{11}\ s^{-1}$, and since the activation energy of the process is greater than 0.5eV, it is likely that $\tau_x \ll \tau_u$. This process would not affect the tracer diffusion

coefficient and also provides a T_1 behaviour which is frequency independent, since $\omega\tau_x \ll 1$, and which obeys an Arrhenius temperature dependence consistent with observation. Cotts derives the following expression:

$$(T_1^{-1})_x = \Gamma_x^2 \tau_x \exp(-U_x/k_B T) \qquad (5.6)$$

From available data it is possible to determine that $\Gamma_x \geq 2.5 \times 10^7$ s^{-1} assuming $\tau_x \leq \tau_d$. Thus a very large interaction strength is required which is considerably greater than that due to dipole-dipole interactions within the Switendick criterion that H-H separation is less than 2.1Å in a hydride system (this criterion yields $\Gamma_{dip} \leq 10^5$ s^{-1}). Cotts determines that for ^1H in $ScH_{1.38}$ H-H separation is required to be less than 0.746Å which is the H-H separation in an H_2 molecule. For $Nb_{0.75}V_{0.25}H_{0.23}$, however, the separation is estimated to be less than 0.39Å.

The requirement of these small dipole separations is compounded by a further requirement that only small orientational variation of paired dipoles occurs within the lifetime of the pair. Despite this the nuclear dipole interaction in H-H pairs may be a candidate for the unknown relaxation mechanism but in the words of Cotts, "just barely". The requirements go against one's intuition and do not sit easily without further experimental verification.

Conclusion

It is apparent that none of the theories proposed to date satisfactorily explains the anomaly across the broad range of systems in which it is observed. Further study is therefore needed of these systems in order to provide a tenable explanation of the still anomalous T_1 behaviour. A particularly useful experimental study, for example, would be a coherent elastic neutron scattering experiment of various deuteride systems which could tell us something about location of ^2D within a system. It is apparent that the spatial as well as temporal behaviour of the interstitial particles is of great significance in the explanation of their behaviour in the T_1 anomaly regime.

From a broader perspective, this study of the T_1 anomaly highlights both a weakness and a strength of nmr as a technique for studying the solid state. The possible weakness is that the anomaly remains unexplained because the observables of nmr are so sensitive to a large number of different interactions and physical phenomena. However, surely it is also a strength of the

technique that this sensitivity exists and that therefore an anomaly was observed thus revealing the existence of an underlying physical behaviour within a material which might otherwise remain undetected.

References

5.1 Barnes R G, Jerosch-Herold M, Shinar J, Borsa F, Torgeson D R, Lucas A J, Styles G A and Seymour E F W, Phys Rev B, **35** 890-893, (1987).

5.2 Barnes R G, Borsa F, Jerosch-Herold M, Han J W,Belhoul M, Shinar J, Torgeson D R, Peterson D T, Styles G A and Seymour E F W, J Less Common Metals, **129**279-285,(1987)

5.3 Han J W, Lichty L R, Torgeson D R, Seymour E F W, Barnes R G, Billeter J L and Cotts R, Phys Rev B, **40**9025-9034,(1989)

5.4 Barnes R G, Z Phys Chem NF, **164**841-851,(1989)

5.5 Boyce J B, Mikkleson Jr, J F and O'Keefe M, Solid State Comm, **21** 955,(1977)

5.6 Richards P M, Phys Rev B, **36**7417-7421,(1987)

5.7 Richards P M, J Sol Stat Chem, **43** 5, (1982)

5.8 Belhoul M, PhD Thesis, University of Warwick, (1983)

5.9 Anderson et al, J Less Common Metals, **101**404-418,(1984)

5.10 Ross D K, Z Phys Chem NF, **114**221-230,(1979)

5.11 Dianoux A J, private communication.

5.12 Ross D K, private communication.

5.13 Stuhr U, Schereth M, Steinbinder D and Wipf H, Z Phys Chem NF, **164** 929,(1989)

5.14 Barnfather K J, Seymour E F W, Styles G A, Dianoux A J, Barnes R G and Torgeson D R, Z Phys Chem NF, **164**935-940,(1989)

5.15 Markert J and Cotts R, J Less-Common Metals, **129**358,(1987)

5.16 Khatamian , Phys Rev B, **21**2622,(1980)

5.17 Jerosh-Herold M, PhD Thesis, Iowa State University, (1986)

5.18 Stebbins J F, Chem Rev, **91**1353-1373,(1991)

5.19 Karlicek R F and Lowe I J, J Magn Res, **37**75(1980)

5.20 Cotts R M, Hoch M J R, Sun T and Markert J T, J Magn Res, **83**252,(1989).

5.21 Han J W, Torgeson D R, Barnes R G and Peterson D T, Phys Rev B, **44** 1-8,(1991)

5.22 Hutchings M T, Clausen K, Dickens M H, Hayes W, Kjems J K, Schnabel P G and Smith C, J Phys C, **17**3903,(1984).

5.23 Cotts R M, J Less-Common Metals, **172-174**467-474,(1991).

5.24 Lottner V, Heim A and Springer T, Z Physik B, **32**157-165,(1979).

Figure 5.1a Temperature dependence of the proton spin-lattice relaxation time in $ScH_{1.83}$ (at 12.2 MHz) and $YH_{1.98}$ (at 12.2 and 40 MHz), as reported by Barnes et al [5.2]. The temperatures at which the anomalous turn-down begins are indicated by arrows. The data for $YH_{1.98}$ show clearly the normal frequency dependence of the proton T_1 at the low temperature minimum and a weak frequency dependence at T_c. The solid curve shows the temperature dependence of the conduction electron contribution T_{1e} for $YH_{1.98}$ extrapolated from low temperatures.

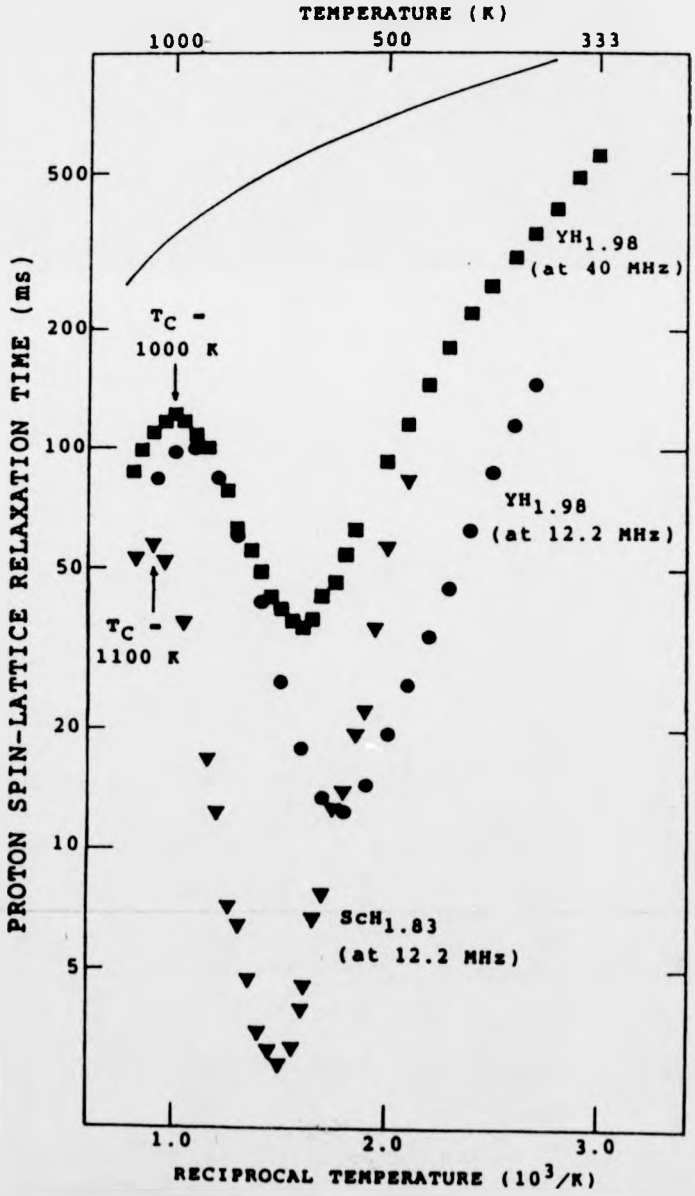

Figure 5.1b Temperature dependence of both ^{1}H and ^{45}Sc T_1^{-1} in the same sample of $ScH_{1.88}$. Different scales of relaxation rate are shown for each nuclei for ease of presentation. The anomalous effect is clearly seen for ^{45}Sc nuclei and at a lower temperature than for ^{1}H nuclei. This graph is taken from Barnes' Stuttgart review paper [5.4].

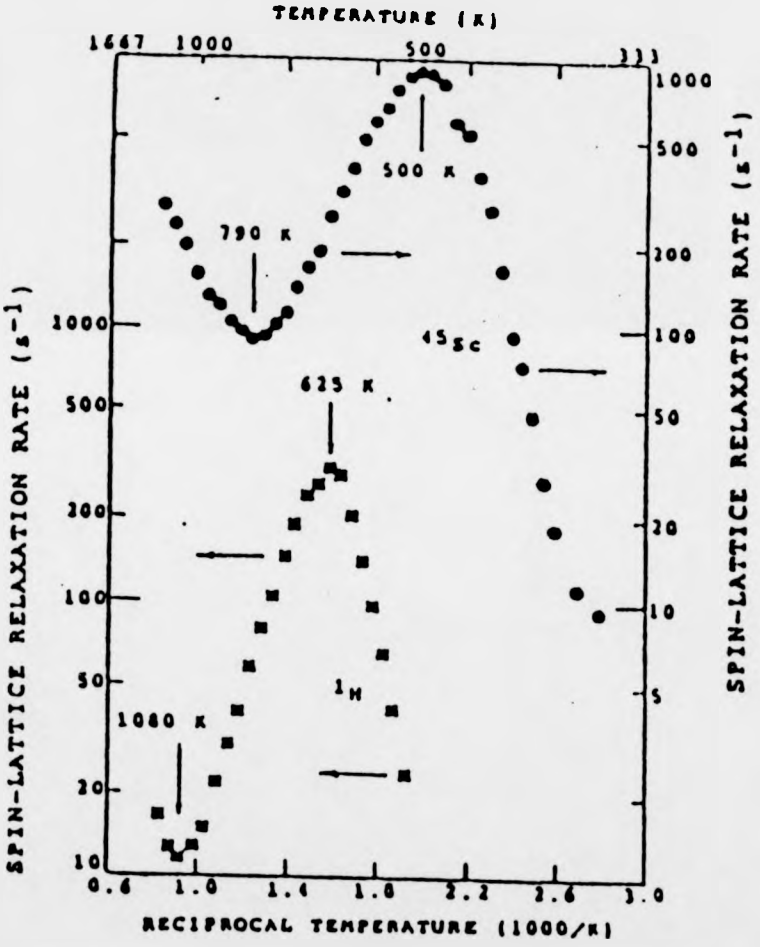

Figure 5.2a Temperature dependence of ^1H spin-lattice relaxation time in $VH_{0.20}$, $NbH_{0.21}$ and $TaH_{0.20}$ after Han et al [5.3]. (Presumably measured at 12.2MHz, though this is not stated in their paper.) The rapid change in T_1 near 2.8×10^{-3} K^{-1} and 2.5×10^{-3} K^{-1} for $NbH_{0.21}$ and $VH_{0.20}$ respectively, is due to the α-β phase transition which for the $TaH_{0.20}$ system occurs at a lower temperature than shown here.

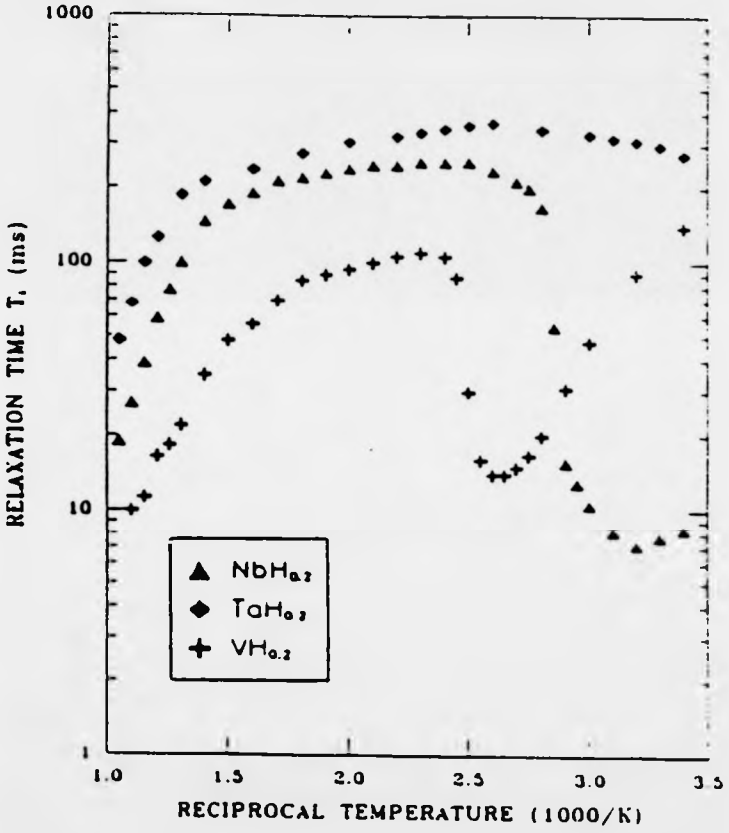

Figure 5.2b ^1H T_1 in $Nb_{0.75}V_{0.25}H_{0.23}$ versus reciprocal temperature, after Han et al [5.3]. No frequency dependence is observed at the turn-down which is much more clearly resolved here compared to the non-alloy system data shown in figure 5.2a. The critical temperature is about 500K.

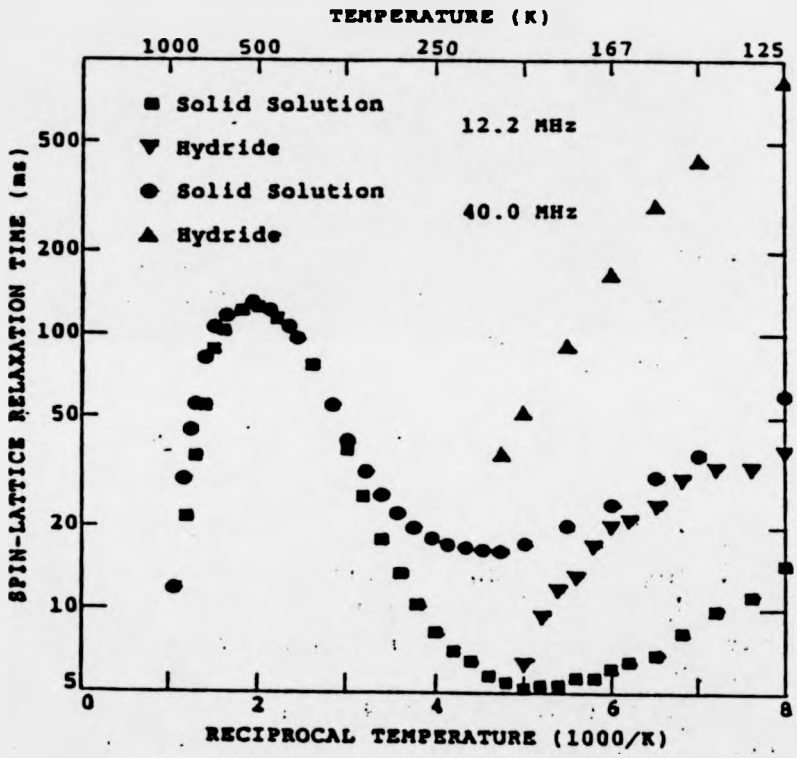

Figure 5.3 Schematic representation of a proton hopping path between neighbouring T-sites via an O-site in an fcc sub-stoichiometric MeH system. The drawing presented by Richards [5.6], tries to show the effect of increased repulsion at the o-site due to large anharmonic vibrational motion of protons at neighbouring t-sites. The nominal hopping particle is represented by an open circle and its 'intended' destination by an open square. The point marked s represents the centre of a face of a tetrahedron formed by metal atoms (not shown) and would be the likely saddle point in the absence of hydrogen interactions.

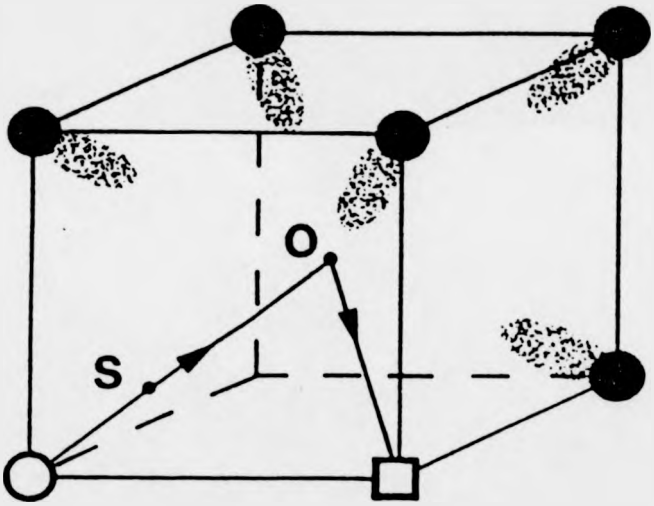

Figure 5.4 Richards was able to obtain a good fit to experimental data using his theory of repulsion due to large vibration, as shown in this graph taken from his paper [5.6]. The experimental data are normalised T_1 for ^{45}Sc in $ScH_{1.83}$ taken from reference [5.1]. The solid line is that derived from equation 5.1 using potentials also derived theoretically. Both theory and experimental data are normalised to unity at their maximum values.

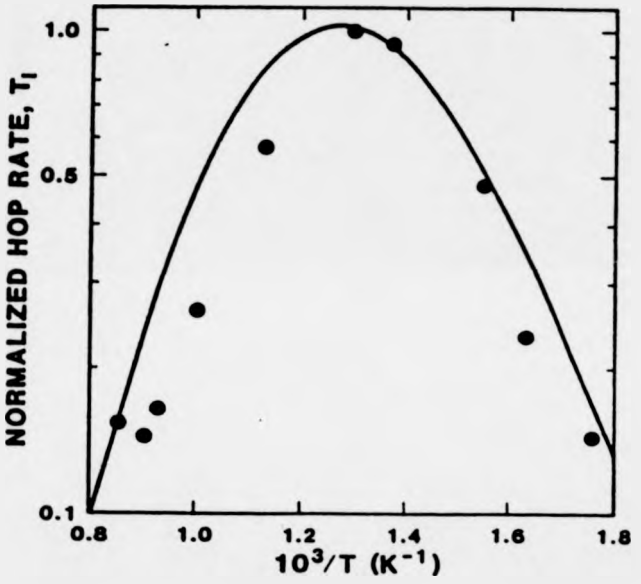

Figure 5.5 IN6 experimental data is show here with apparent broadening of the elastic lineshape due to quasielastic scattering of neutrons from hydrogen in $YH_{1.98}$ at various temperatures. Note that only 1% of the total elastic peak is shown and that Q (=1.93Å) is very large. The lines shown, from broadest to narrowest, were measured at 1025K, 900K, 500K, and 300K.

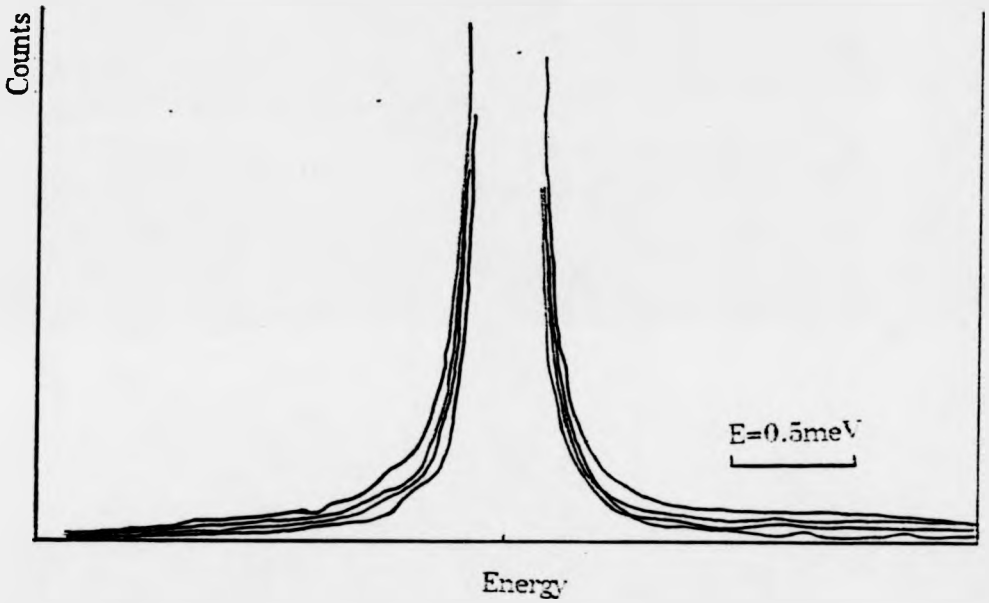

Figure 5.6 IN6 experimental data showing an inelastic neutron scattering lineshape from $YH_{1.98}$ measured at 500K. Three distinct low energy Y lattice modes can be seen as well as high energy hydrogen vibrational modes at about 112 meV and 224 meV.

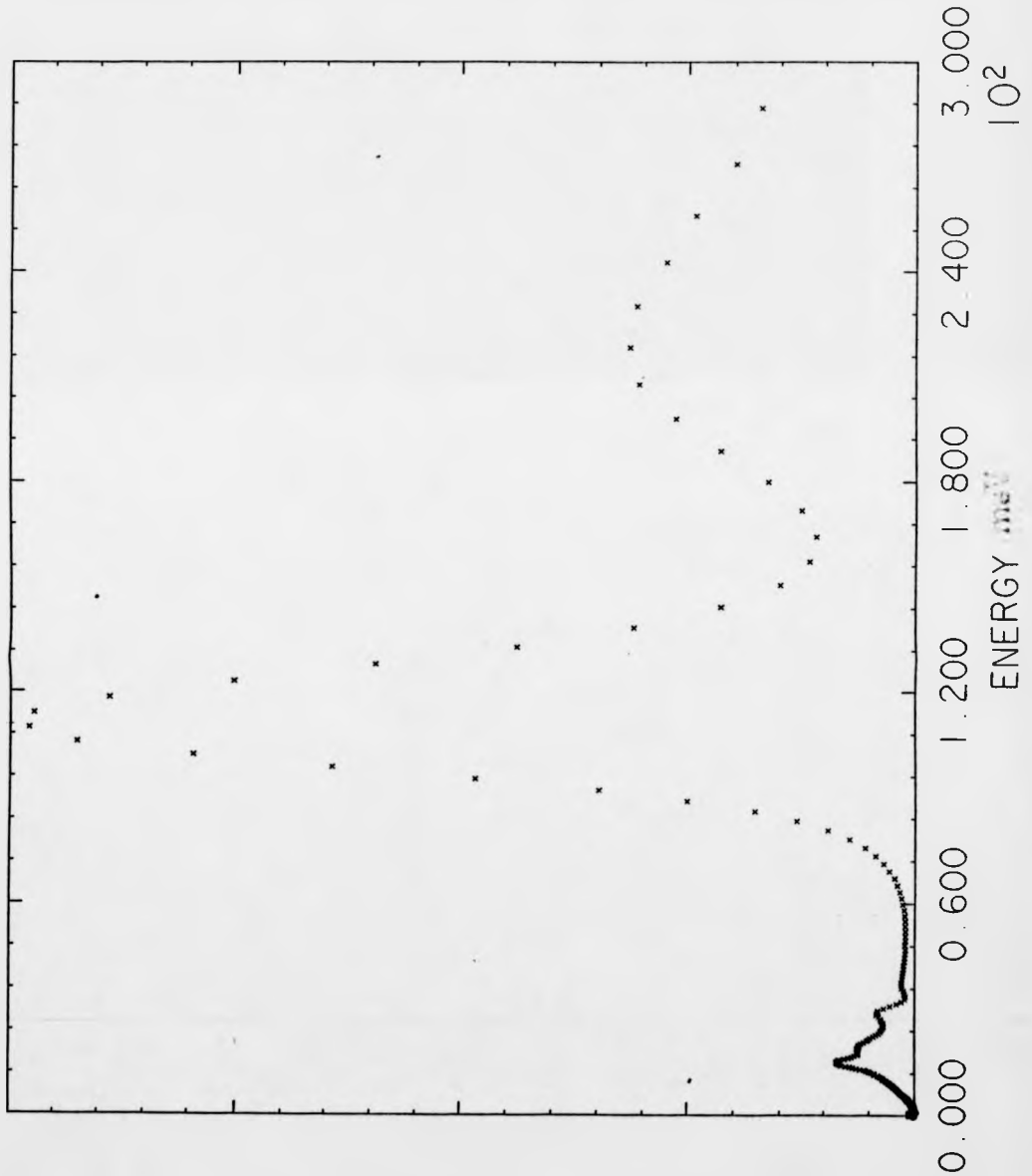

Figure 5.7 Typical IN10 experimental data of neutron counts versus energy from a qens study of $YH_{1.98}$. The spectrum is centered on the elastic energy value and is shown corrected as described in the text having subtracted, inter alia, the elastic line and scattering from the sample cell.

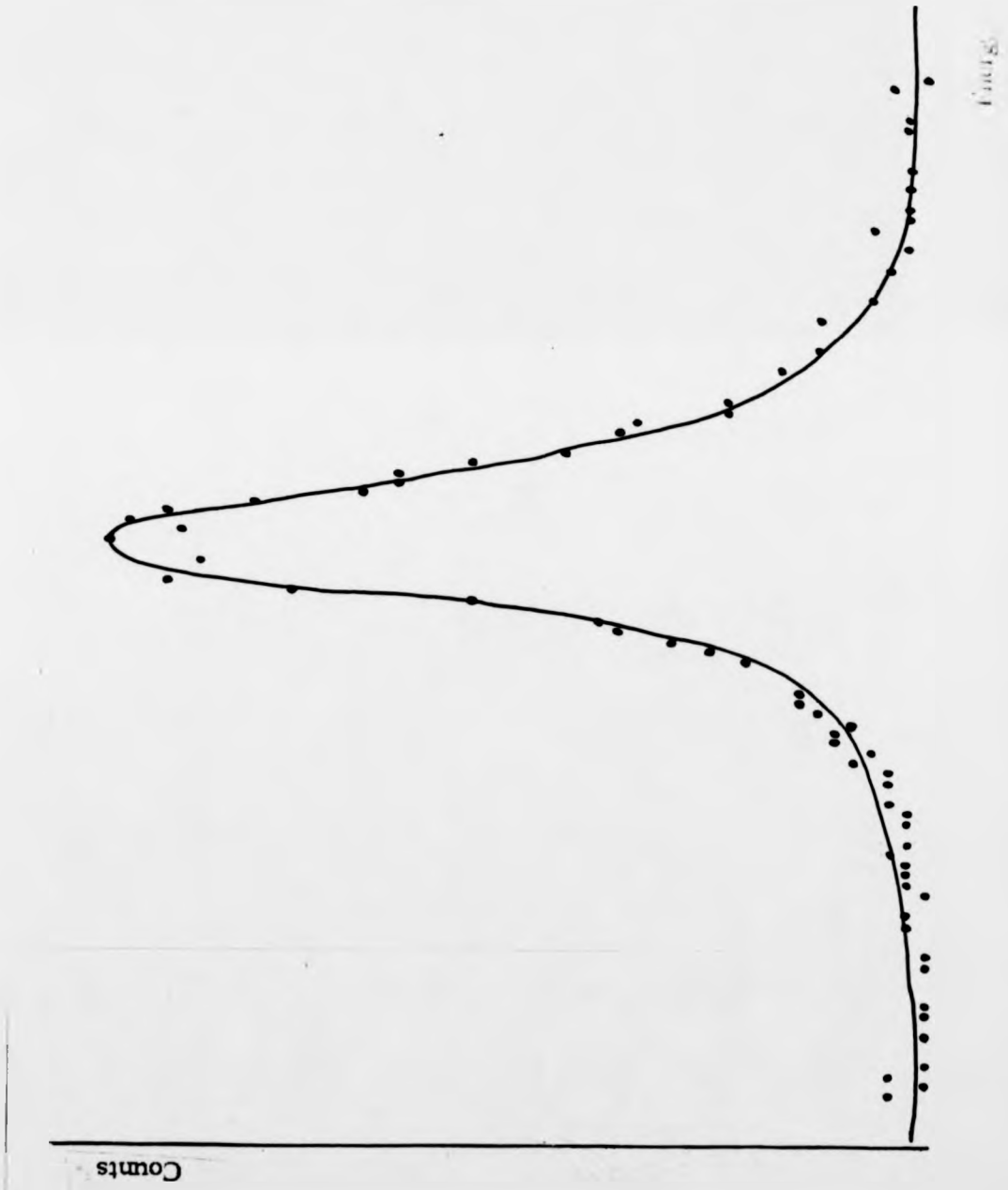

Figure 5.8 Measured energy half-width at half-maximum of the qns lineshape versus Q^{-2} for $YH_{1.98}$ at 1079K The fitted line is a best fit to the first three data points only.

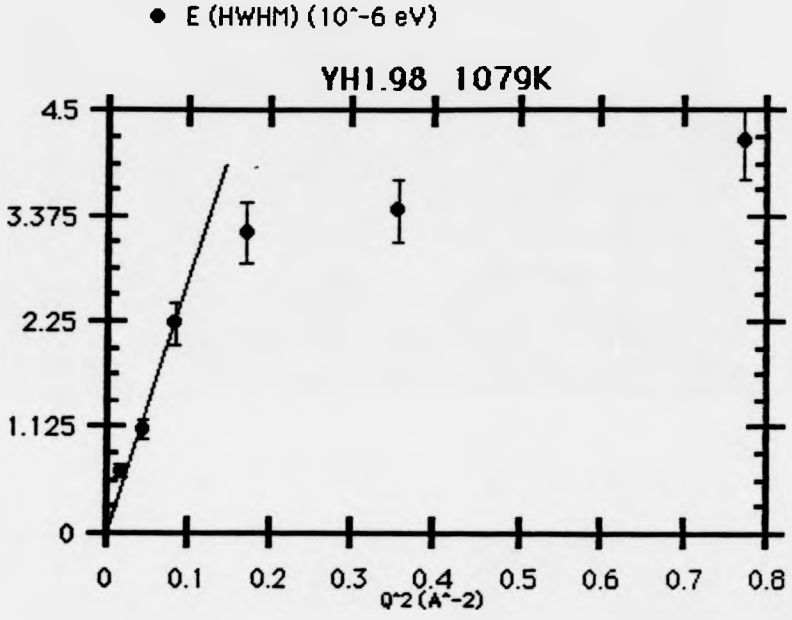

Figure 5.9 Hydrogen diffusion coefficient versus reciprocal temperature for $YH_{1.98}$ measured from a qns study using IN10. The best fit curve to the four data points shows an increasing hydrogen diffusivity which extends substantially monotonically into the T_1 anomaly temperature regime. The best fit yields an activation energy of E_a =0.33 ± 0.09 eV and a diffusion constant of D_o = 0.7 (±0.4) x 10^{-4} cm^2s^{-1}.

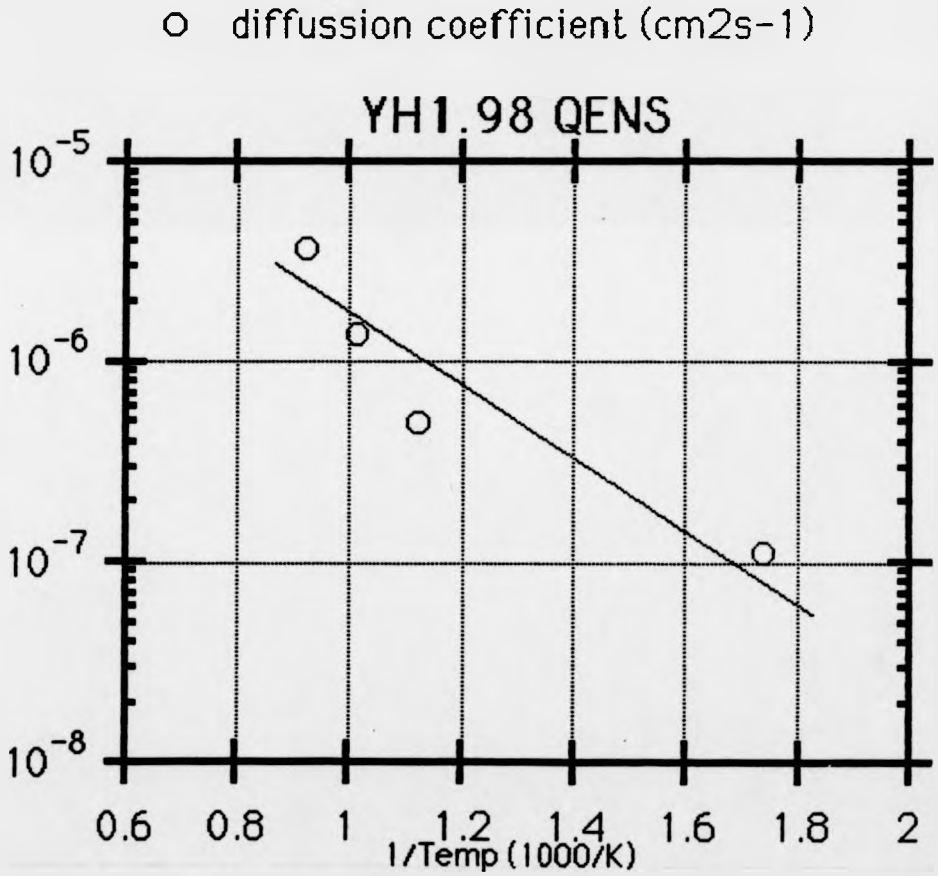

Figure 5.10 The data shown here was obtained shortly after the present study by Stuhr et al [5.13]. Hydrogen diffusion coefficients versus reciprocal temperature is presented for $YH_{1.97}$. Hydrogen diffusivity is clearly seen to increase in the anomaly temperature regime in good agreement with the present results. They obtained values of $E_a = 0.35 \pm 0.07$ eV and $D_o = 3.4\ ^{+2.3}_{-1.2} \times 10^{-4}$ $cm^2 s^{-1}$.

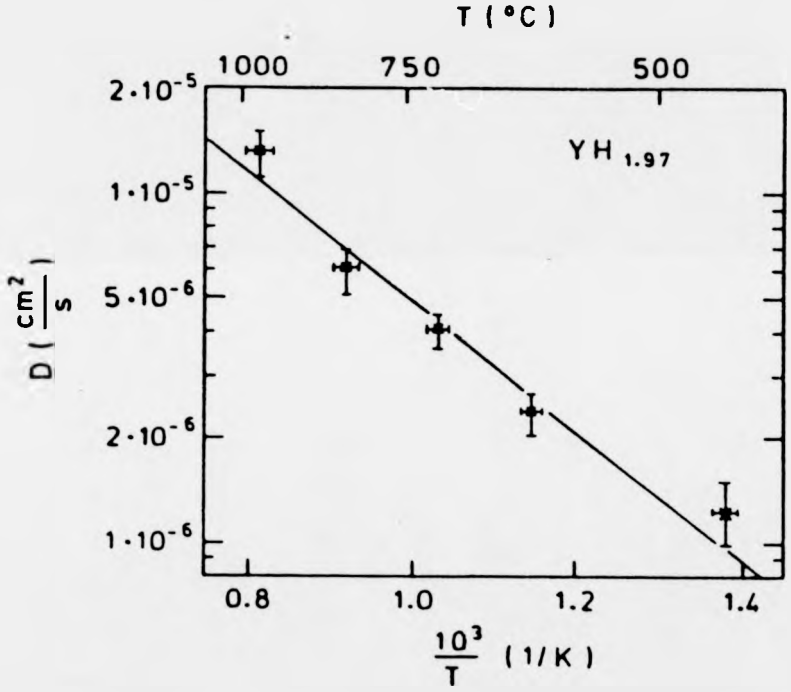

Figure 5.11 Further evidence of the increasing diffusivity of hydrogen in the anomaly regime has been obtained by alternating pulsed-field-gradient studies [5.14].

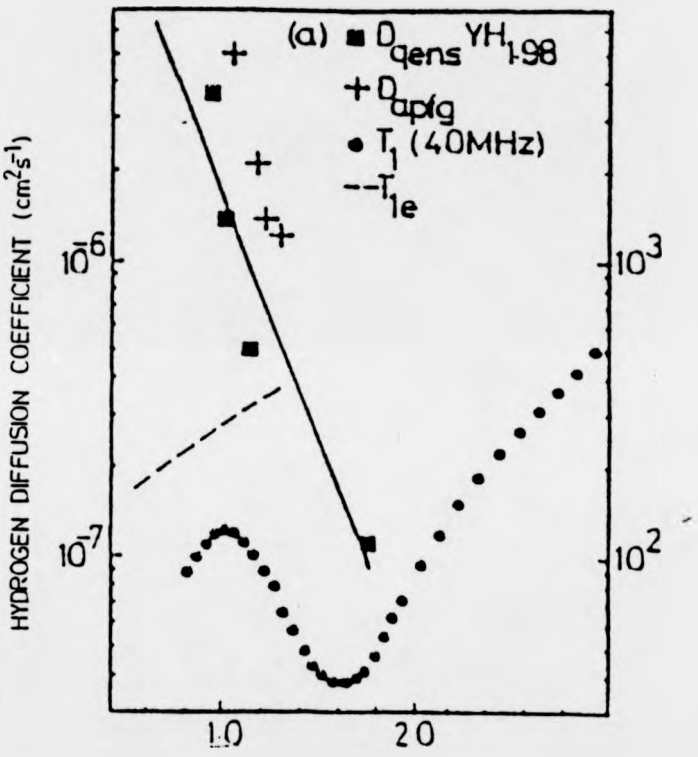

Figure 5.12 Stuhr et al [5.13] measured the effect of hydrogen concentration on diffusivity. Diffusion coefficients are shown here at two temperatures and for hydrogen to yttrium ratios of 1.80, 1.92 and 1.97 to 1. Different ordinate scales are shown for the different temperatures.

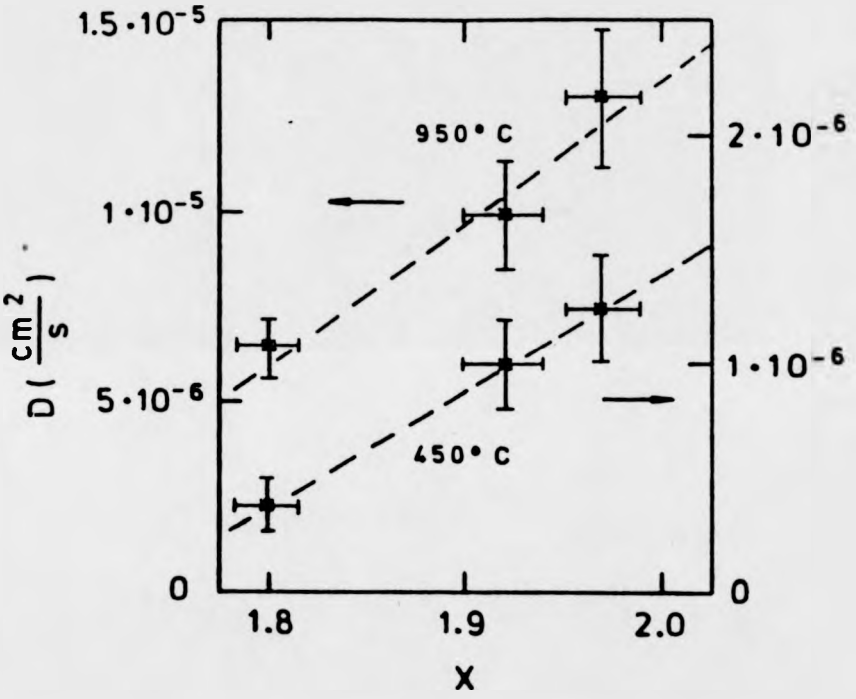

Figure 5.13 Typical IN10 results of fitted qns data for $Nb_{0.75}V_{0.25}H_{0.20}$. Corrected neutron counts are shown against energy with deviation of experimental data from the fitted curve shown inset.

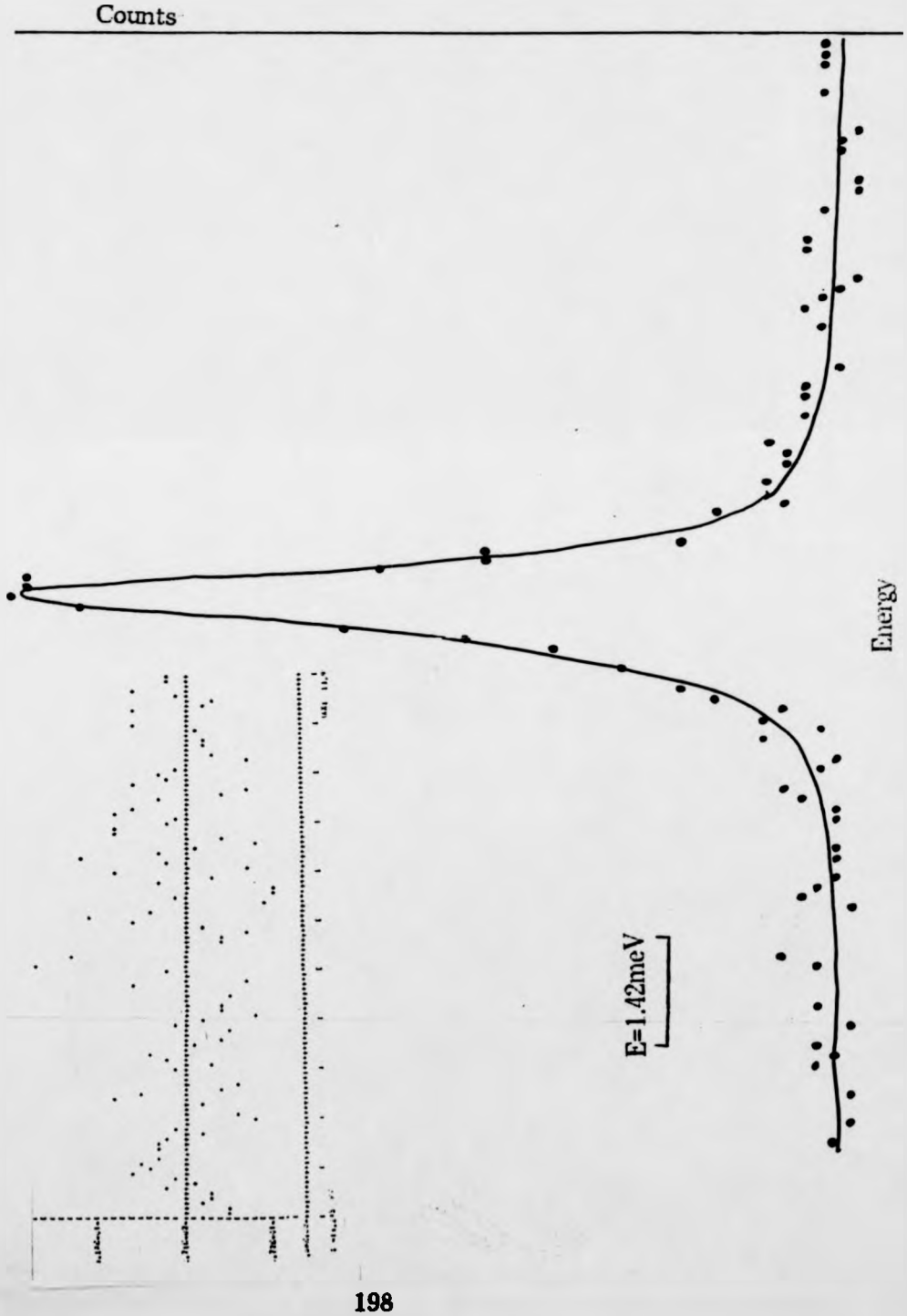

Figure 5.14 Values of half-width energy at half maximum of the fitted spectra are shown at low Q^2 for the $Nb_{0.75}V_{0.25}H_{0.20}$ sample at 809K which is well above T_c for this system.

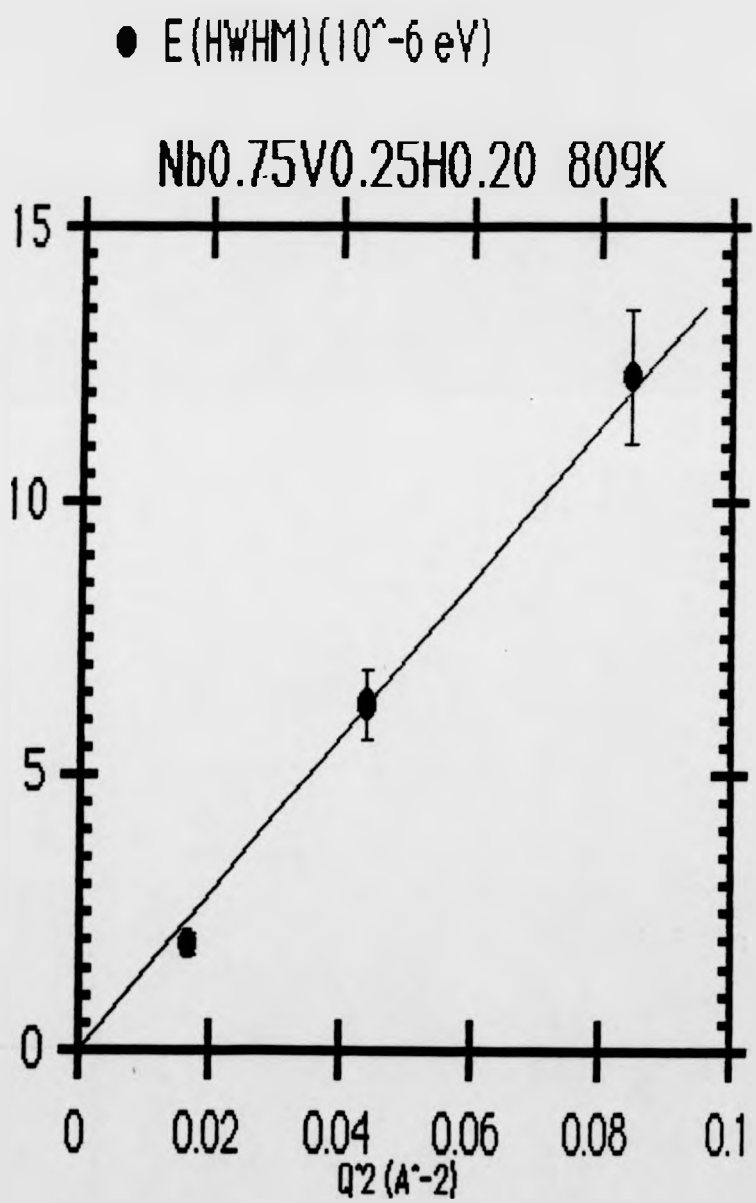

Figure 5.15 Diffusion coefficient versus reciprocal temperature for $Nb_{0.75}V_{0.25}H_{0.20}$ obtained from a qns study using IN10. Hydrogen diffusivity is clearly seen to continue increasing above the critical temperature (T_c =500 K) of the T_1 anomaly. Values of E_a =0.16 ± 0.02 eV and D_o =1.76 ±0.4 x 10^{-4} cm^2s^{-1} were obtained.

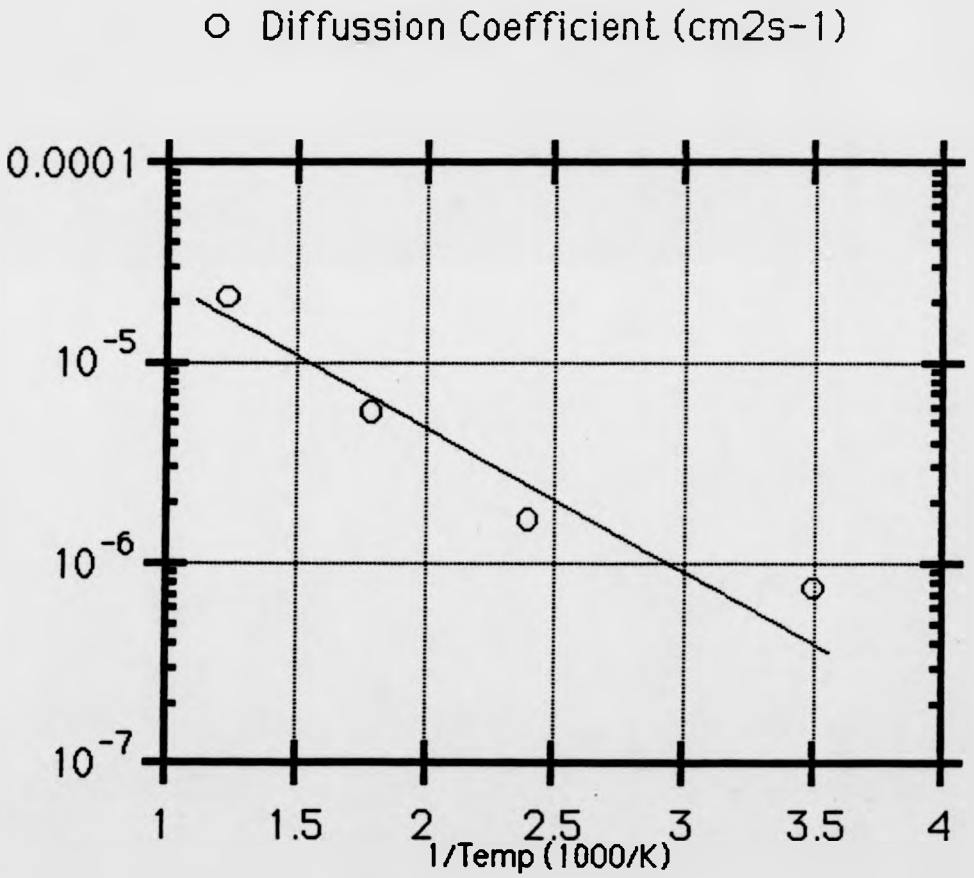

Figure 5.16 Han et al [5.3] reported results of hydrogen diffusion coefficient versus reciprocal temperature obtained using an nmr stimulated spin-echo alternating pulsed-field-gradient technique [5.20]. The graph shows diffusion coefficients versus reciprocal temperature for $Nb_{0.75}V_{0.25}H_{0.23}$. T_1 for the the same sample is also shown. They also found diffusivity increased in the anomaly regime and the results fitted to the Arrhenius expression yield E_a =0.20 eV and D_o =8.6 x 10^{-4} cm^2s^{-1}.